The syntheses and reactivities of niobium cyclopentadienyl arylimido complexes bearing the 2,6-di-iso-propylphenyl (Dipp) imido substituent

ROUSE, STEPHEN,JOHN

Durham University

Department of Chemistry

The syntheses and reactivities of niobium cyclopentadienyl arylimido complexes bearing the 2,6-di-*iso*-propylphenyl (Dipp) imido substituent

Thesis submitted for the degree of

Doctor of Philosophy

by

Stephen J. Rouse

April 2021

Statement of originality

This thesis is based on work conducted by the author, in the Department of Chemistry at Durham University, during the period October 2015 to April 2021. All the work described in this thesis is original, unless otherwise acknowledged in the text or in the references. None of this work has been submitted for any another degree in this or any other university.

Signed: 

S. Rouse

Date: 21/04/2021

In loving memory of

my great-aunt

Jacqueline White

(1933 – 2018)

and

my grandfather

Dr Andrew Craig

(1934 – 2018)

ABSTRACT

The work in this thesis focusses on the syntheses and reactivities of niobium cyclopentadienyl arylimido complexes featuring the 2,6-di-*iso*-propylphenyl (Dipp) imido substituent. The steric and electronic effects of the $DippN^{2-}$ arylimido moiety are exploited in order to achieve new reactivities of half-sandwich and *bis*(cyclopentadienyl) niobium complexes. CHAPTER 1 outlines the structure, bonding and resulting typical reactivities of RN^{2-} ligands of transition metal imido complexes, with particular focus on systems where the imido substituent R is an aryl group. The potential reactivities and applications of niobium cyclopentadienyl imido systems $[Cp'_2Nb^{V}(NR)]^+$ and $Cp'Nb^{III}(NR)$ towards small molecule activation are outlined based on those reported for analogous zirconocene systems $Cp'_2Zr^{IV}(NR)$ and Cp'_2Zr^{II}, respectively.

The syntheses of the cyclopentadienyl complexes $CpNbCl_2(NDipp)$ (**2**; 39% yield) and $Cp_2NbCl(NDipp)$ (**3**; 71% yield) from $NbCl_3(NDipp)(DME)$ (**1**; DME = 1,2-dimethoxyethane) are described in CHAPTER 2. The subsequent reduction chemistry of the mono(cyclopentadienyl) complex **2** is explored in the absence of strong σ-donors and π-acceptors, with the envisaged coordination of dinitrogen. The synthesis of the corresponding mono(fluorenyl) derivative $FluNbCl_2(NDipp)$ (**6**) is discussed.

The work in CHAPTER 3 explores the removal of the chloride ligand from the niobocene imido complex **3**, both *via* electrophilic abstraction and nucleophilic displacement, with the syntheses of the derivatives $Cp_2Nb(ClGaCl_3)(NDipp)$ (**9**), $Cp_2NbMe(NDipp)$ (**11**) and $Cp_2Nb(NDipp)(PCO)$ (**12**) being described. The reaction between complex **3** and $GaCl_3$ (3 equivalents) is demonstrated to form the unusual aryl–gallium π-bonding species $Cp_2Nb(ClGaCl_3)(N\{Dipp{\cdot}Ga_2Cl_6\})$ (**10**).

The reactivity of the d^0 niobocene arylimido complex **3** towards electrophilic addition is investigated in CHAPTER 4. Protonation of complex **3** exclusively occurs at the N-atom to afford the amido species $[Cp_2NbCl(NHDipp)]^+$ (**13**$^+$), isolable as either its triflate salt (75% yield) or *tetrakis*{3,5-*bis*(trifluoromethyl)phenyl}borate (68% yield) salts. The reaction of complex **3** with the larger trityl (Tr^+) electrophile is found to result in electrophilic aromatic substitution at the *para*-position of the aryl imido substituent, with the formation of the niobocene imido complex $Cp_2NbCl(NDipp^{Tr})$ (**17**; $Dipp^{Tr}$ = 2,6-^{i}Pr$_2$C$_6$H$_2$-4-Tr; 29% yield).

The unusual oxidative coupling of the niobium(V) complex **3** is probed in CHAPTER 5, where the reaction with $AgBAr^F_4$ (Ar^F = 3,5-*bis*{trifluoromethyl}phenyl) is demonstrated to afford the diphenoquinoidal diketimido salt $[\{Cp_2NbCl\}_2(N\{2,6\text{-}^iPr_2C_6H_2\}_2N)][BAr^F_4]_2$ ([**18**][BAr^F_4]$_2$; 91% yield). The paramagnetic character of [**18**][BAr^F_4]$_2$ is investigated both computationally (DFT)

and experimentally (Evans' method). Additionally, the reduction of the diketimido complex [**18**][BAr^F_4]$_2$ to the neutral biphenyl diimido species {Cp_2NbCl}$_2$(N{2,6-^{i}$Pr_2C_6H_2$}$_2$N) (**20**; ~30% yield) is outlined.

The overall conclusions of this thesis are presented in CHAPTER 6 along with areas for future study. Finally, the experimental details (CHAPTER 7), APPENDICES and REFERENCES are presented.

ACKNOWLEDGEMENTS

First of all, I would like to say a huge thank you to my supervisor, Dr Phil Dyer. Thank you for all your help and support over the years – your words of wisdom, encouragement and otherwise(!) have been very much appreciated. I know it's been a long haul (although I'm sure you'll say "Pfft… no stamina!" to that!), so thank you so much for being incredibly patient and not giving up on me! (And for badgering me when necessary!)

To the rest of the Dyer Group, both past and present: *Afternoon* (as Claire so aptly put it!). Thank you to you all for making my time in the lab so enjoyable – through your company, singing (in)abilities when a 'tune' came on the radio, and the continuous supply of edible goodies in the office! And of course, for all the cups of tea (or "cheeky ones", as they will be forever known); on that note, I can officially announce my long-awaited top three "best brew" makers as: Ben Smith (no competition with the *ISO 3103* standard!), Amy Buckley (that course you went on served you well!) and Claire Brodie (for a non-tea drinker, top notch!). Additional special thanks go to Jas, Anna and Michael L for showing me the ropes and being so welcoming when I joined; to Michael H and Alana for being very tolerant desk neighbours; to Dominikus for all the advice and for *trying* to teach me some German (although *ich verstehe nur Bahnhof*…); to Eder Olivas for all the motivational messages and chats; and to Claire for being the best lab/glovebox buddy!

I would also like to thank everyone who has been of technical support to me during my Ph.D., including: Juan Aguilar and Catherine Heffernan for all their chats, humour and, of course, NMR expertise; Peter Stokes and Dave Parker for helping me with the *i*ASAP+ (even though it didn't always like to work for my complexes!); Emily Unsworth for the elemental analyses (and for allowing your air-sensitive CHN kit to take up residence in our glovebox for weeks on end…); Andrei Batsanov for characterising my beautiful crystals (and for not being afraid to tell me when they are "completely shapeless"); Mark Fox for all your help with the DFT calculations and for putting up with my (many!) questions; Connor Sibbald for showing me the ropes on using the SPS and for all the 'banter' and coffee supplied; and Aaron Brown and Malcolm Richardson for their brilliant glassblowing skills to keep the Dyer Group well-stocked up on (mostly salvaged!) glassware!

Thank you as well to all the friendly faces about the department who have helped keep my sanity in check over the years! While too numerous to mention everyone, a special thanks to Annette Passmoor (the best storekeeper of all time – sorry Tony!), Val Watson (the best lab attendant and Musgrave Room tea-maker), and Emma Knighton and Kerry Strong (for letting me hide out in your prep room and scrounge countless bits of equipment from the teaching lab!).

And last but not least, I would like to thank my friends and family, in particular to my mum, dad and grandma for their hospitality and support while I've been writing up; to Angus for being the best (and most tolerant) flatmate while we were in Durham; and to everyone from *Durham University Choral Society* and *Penrith Singers* for cheering me up through music and good company! Wouldn't have gotten through it without you all! ☺

CONTENTS

ABBREVIATIONS

°	degrees
°C	degrees Celsius
$\%V_{bur}^{X}$	percentage buried volume determined at atom X
$\angle_{A–B–C}$	angle A–B–C
2,6-Lut	2,6-lutidine
Å	ångström(s) (1×10^{-10} m)
Ar	aryl group
Ar^{F}	3,5-*bis*(trifluoromethyl)phenyl
ASAP+	positive-ion atmospheric solids analysis probe
atm	standard atmosphere
ATR	attenuated total reflectance
B3LYP	Becke three-parameter Lee–Yang–Parr functional
Cent	centroid (of a Cp'-ring, unless otherwise defined)
COSY	correlation spectroscopy
Cp	cyclopentadienyl
Cp*	pentamethylcyclopentadienyl
Cp'	cyclopentadienyl derivative
$Cp^{\dagger}$	tetramethylcyclopentadienyl
Cp^{R}	R-monosubstituted cyclopentadienyl
CSD	*Cambridge Structural Database*
Cy	cyclohexyl
Da	dalton(s)
$d_{A–B}$	distance between atoms A and B
DABCO	1,4-diazabicyclo[2.2.2]octane
DCE	1,2-dichloroethane
DCM	dichloromethane
DFT	density functional theory
diox	1,4-dioxane
Dipp	2,6-di-*iso*-propylphenyl
Dippp	2,6-*bis*(2,6-di-*iso*-propylphenyl)phenyl
$Dipp^{Tr}$	2,6-di-*iso*-propyl-4-tritylphenyl
DME	1,2-dimethoxyethane
Dmp	2,6-dimethylphenyl
dppe	1,2-*bis*(diphenylphosphino)ethane
dppm	*bis*(diphenylphosphino)methane
DPQ	diphenoquinoidal
$DPQH_2$	4,4'-dihydrodiphenoquinoidal
dtbpe	1,2-*bis*(di-*tert*-butylphosphino)ethane
EPR	electron paramagnetic resonance
equiv.	equivalent(s)
E_{red}	reduction potential
eV	electron volt
Fc	ferrocene
Flu	(9-)fluorenyl
FMO	frontier molecular orbital
G	Gibbs free-energy
h	hour(s)
HOMO	highest-occupied molecular orbital
Hz	hertz
*i*ASAP+	inert ASAP+
Ind	indenyl
Ind'	indenyl derivative
IR	infra-red
$^{n}J_{A–B}$	*n*-bond coupling constant between nuclei A and B
k	reaction rate
L	neutral ligand (2-electron donor)
LA	Lewis acid
LUMO	lowest-unoccupied molecular orbital
m/z	mass-to-charge ratio
Mes	mesityl (2,4,6-trimethylphenyl)
Mes*	2,4,6-tri-*tert*-butylphenyl
min	minute(s)
MO	molecular orbital
mol%	percentage by moles
MS	mass spectrometry
Naphth	naphthalene
NBO	natural bond orbital
NMR	nuclear magnetic resonance
NOESY	nuclear Overhauser effect spectroscopy
Ph^{F}	pentafluorophenyl
pK_a	Brønsted acidity
pK_{aH}	Brønsted acidity of the conjugate acid
ppm	parts per million
PSYCHE	pure shift yielded by chirp excitation
py	pyridine
R	alkyl group (unless otherwise stated)
RDS	rate-determining step
RMS	root-mean-square
RT	room temperature
r_{vdW}	van der Waals' radius
S	total spin quantum number
S_EAr	electrophilic aromatic substitution
SHE	standard hydrogen electrode
SMD	solvent model based on density
S_N1	unimolecular nucleophilic substitution
S_N2	bimolecular nucleophilic substitution
SOMO	singly-occupied molecular orbital
Tf	triflyl (trifluoromethylsulfonyl)
THF	tetrahydrofuran

TMS	trimethylsilyl
Tol	*p*-tolyl (4-methylphenyl)
Tr	trityl (triphenylmethyl)
vol%	percentage by volume
WBI	Wiberg bond index
WCA	weakly-coordinating anion
wt%	percentage by weight
X^-	anionic ligand (1-electron donor)
XRD	X-ray diffraction
δ	chemical shift
θ	fold angle; angle between two defined planes
μ_B	Bohr magneton
μ_{eff}	effective magnetic moment
$\mu_{s.o.}$	spin-only magnetic moment
ν	frequency
$\nu_{½}$	full width at half maximum frequency
$\phi_{A–B–C–D}$	dihedral angle; angle made by bonds A–B and C–D

COMPOUND NUMBERING

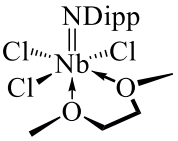

1

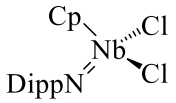

2

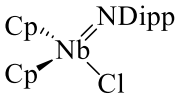

3

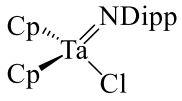

3_{Ta}

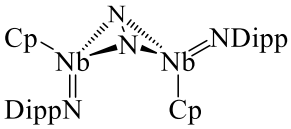

4

5

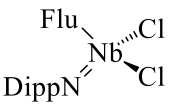

6

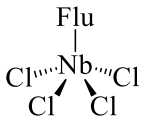

7

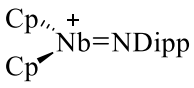

8^+

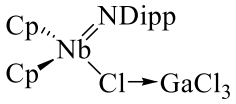

9

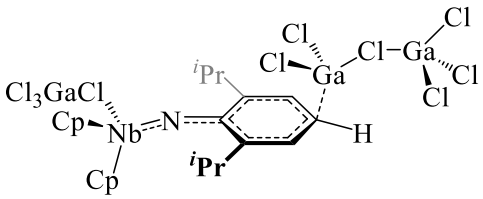

10

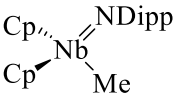

11

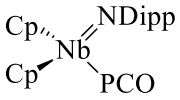

12

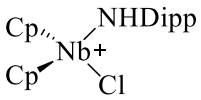

13^+

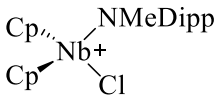

$14a^+$

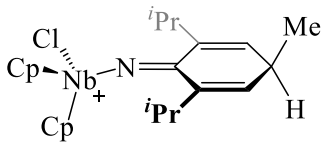

$14b^+$

15

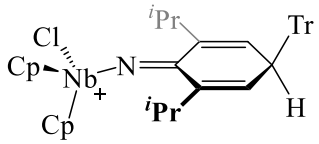

16^+

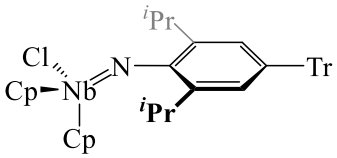

17

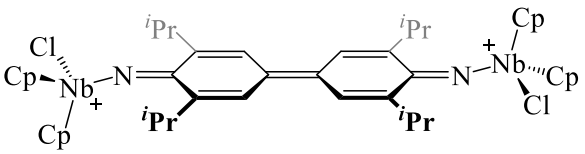

18^{2+}

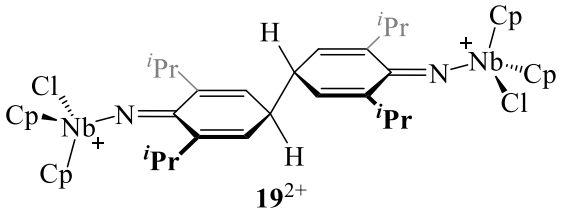

19^{2+}

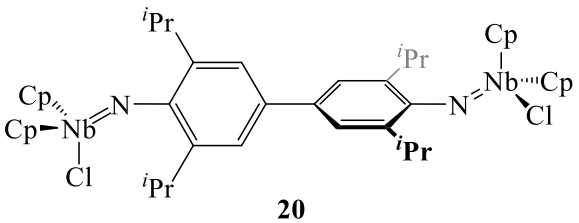

20

CHAPTER 1:

Introduction

Transition metal imido complexes, which contain the "M(NR)" motif, constitute one of the richest classes of compounds, both in the variety of structural possibilities and the diversity of the chemistry associated with them.[1,2] Indeed, complexes containing this ligand have been proposed as intermediates in a variety of processes including ammoxidation,[3–6] alkene oligomerisation,[7–10] and even enzymatic transformations.[11,12]

1.1. Structure and bonding of transition metal imido complexes

1.1.1. Overview of the coordination modes of imido ligands

In recent decades, the use of imido (RN^{2-}) ligands in transition metal complexes has grown, in part due to the ease with which the steric and electronic properties of the complexes can be tuned by simply varying the imido substituent R.[13] The imido moiety is isoelectronic with oxo (O^{2-}) and nitrido (N^{3-}) ligands, where each of these ligands are capable of forming multiple-bonds with metal centres. As such, imido ligands are considered both strong σ- and π-donors,[14] which are able to stabilise transition metal centres in their highest oxidation states as discrete complexes, *e.g.* $Li_2[Cr^{VI}(N^tBu)_4]$ and $Os^{VIII}(N^tBu)_4$.[15]

Imido ligands can adopt a variety of different coordination modes and hence can accommodate a range of different electronic requirements of the transition metal centre(s) to which they are bonded (FIGURE 1.1).[14] The most frequently encountered bonding mode is the so-called terminal imido coordination. This corresponds with either the formation of an M=N double-bond (X_2-coordination) or, with additional donation of the heteroatom lone-pair, a M≡N triple-bond (LX_2-coordination) if vacant π-symmetry orbitals are available on the metal centre.* In addition to terminal coordination, imido ligands are known to adopt at least three different bridging coordination modes in transition metal complexes as shown in FIGURE 1.1.

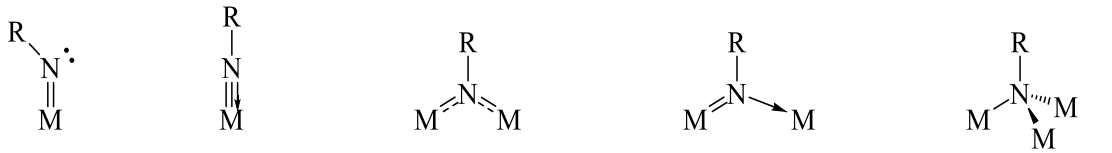

FIGURE 1.1: The five coordination modes of imido ligands with transition metal centres.[14]

* According to the neutral electron-counting formalism, LX_2- and X_2-ligands contribute four and two electrons, respectively.[16]

1.1.2. Terminal imido coordination: Structural and orbital considerations

Since the identification of both LX_2- and X_2-coordination modes of terminal imido ligands, key structural differences in the crystallographically-determined complexes have been used to distinguish between these two multiply-bonded motifs. Historically, the M–N–C bond angle has been used as a key indicator of the coordination mode, with "linear" (~165–180°) and "bent" (<165°) geometries being attributable to LX_2- and X_2-ligands, respectively.[14] These assignments were hypothesised to be due to the hybridisation of the imido N-atom, namely sp-hybridisation for LX_2 (and hence a M≡N triple-bond) and sp^2-hybridisation for X_2 (*i.e.* a M=N double-bond) coordination modes, as shown in FIGURE 1.2. Such geometric differences were exemplified in the solid-state structures of the *bis*(imido) complexes $OsO_2(N^tBu)_2$ (**A**)[17] and $Mo(NPh)_2(\kappa^2\text{-}S_2CNEt_2)_2$ (**B**),[18] which formally must each contain one LX_2- and one X_2-imido ligand in order to achieve a stable 18-electron configuration.

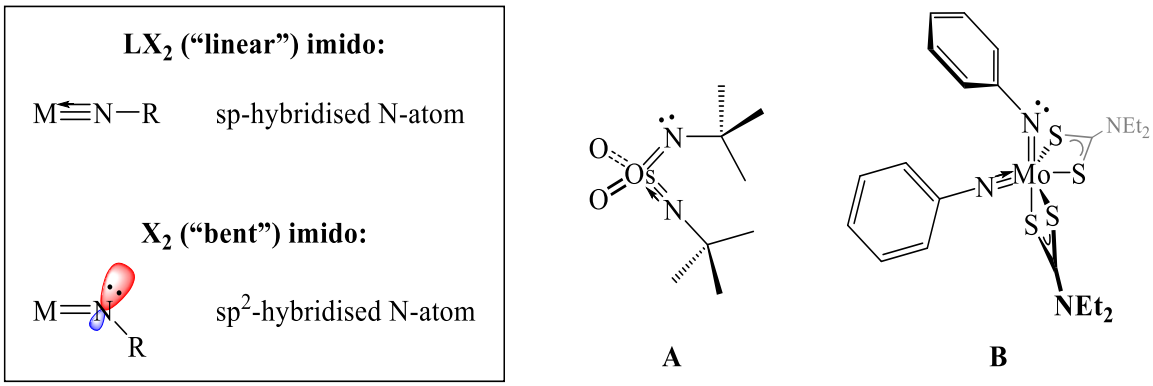

FIGURE 1.2: Hybridisation arguments for the formation of "linear" LX_2- and "bent" X_2-imido complexes,[14] alongside the crystallographically-determined 18-electron *bis*(imido) complexes **A** and **B** that conform to these arguments.[17,18]

However, discrepancies in the proposed relationship between imido coordination modes and M–N–C bond angles were later reported by Schrock and co-workers for their planar *tris*(imido) complex $Os(NDipp)_3$ (**C**; Dipp = 2,6-di-*iso*-propylphenyl).[19] The structure of complex **C** was determined crystallographically to feature three "linear" imido ligands. However, if each ligand adopted an LX_2-coordination to osmium, this would amount to a formally 20-electron complex. To circumvent this formulation, Schrock and co-workers proposed that one imido ligand in fact adopts a "linear" X_2-coordination, where the N-atom was sp-hybridised with its lone-pair contained within a non-bonding p-orbital (FIGURE 1.3). It was proposed that there was no electronic preference for this hybridisation of the X_2-imido within complex **C**, but instead this conformation was a result of intramolecular and intermolecular steric interactions (or crystal-packing forces). A similar conclusion was reached following the computational studies of the "bent" and hypothetical "linear" geometries of the X_2-imido ligand of complex **B**.[20]

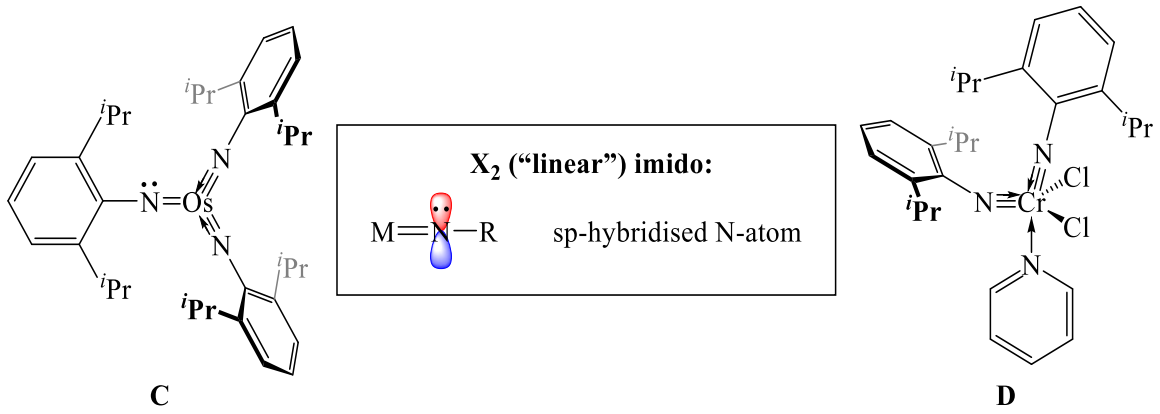

FIGURE 1.3: Examples of crystallographically-determined imido complexes featuring "linear" X_2 (**C**)[19] and "bent" LX_2 (**D**)[21] coordination modes, where the former is attributable to a nitrogen lone-pair in a non-bonding p-orbital.

Furthermore, crystal-packing forces have also been attributed to variations in the M–N–C bond angles of complexes featuring LX_2-imido ligands, where angles anywhere between ~150 and 180° could be accommodated for this 4-electron donor without an electronic penalty.[22] This is exemplified in the solid-state structure of $CrCl_2(NDipp)_2(py)$ (**D**; py = pyridine), which contains both "linear" (~169°) and "bent" (~148°) LX_2-imido ligands for the complex to attain an 18-electron configuration (FIGURE 1.3).[21]

As a result of the structural diversity observed, today M–N–C bond angles within imido complexes are only used as an indication of the metal–nitrogen bond order. Instead, M–N bond lengths have been found to be a more reliable method for determining the nature of an imido ligand's coordination mode.[23] As expected, a shorter M–N interatomic distance is associated with a higher metal–heteroatom bond order; the M–N bond for an LX_2-imido ligand may be ~0.03 Å shorter than its X_2-counterpart.[20] This is demonstrated with the aforementioned Group VI *bis*(imido) complexes **B** and **D**, where the $\Delta d_{M–N}$ value is ~0.035 Å for the LX_2,X_2-imido complex **B**[18] compared with ~0.019 Å for the LX_2,LX_2-complex **D**.[21]

1.1.3. Terminal *vs*. bridging imido coordination

In addition to having an impact on M–N–C bond angles, structural factors are significant in determining whether imido ligands adopt terminal or bridging coordination modes to transition metal centres. While crystal-packing forces are difficult to predict, the tendencies of imido ligands to adopt a bridging coordination are strongly dependent on the steric bulk of the imido substituent (and associated steric demands of the rest of the complex): namely, imido ligands with smaller substituents are more likely to adopt μ_2- and μ_3-bridging modes compared to those with bulkier substituents. The impact of the steric demands of an imido substituent is evident from the proportion of transition metal imido complexes deposited in the *Cambridge Structural Database* (CSD)[24] featuring either μ_2- or μ_3-NR ligands (for a given alkyl or aryl substituent, R), as shown in FIGURE 1.4.

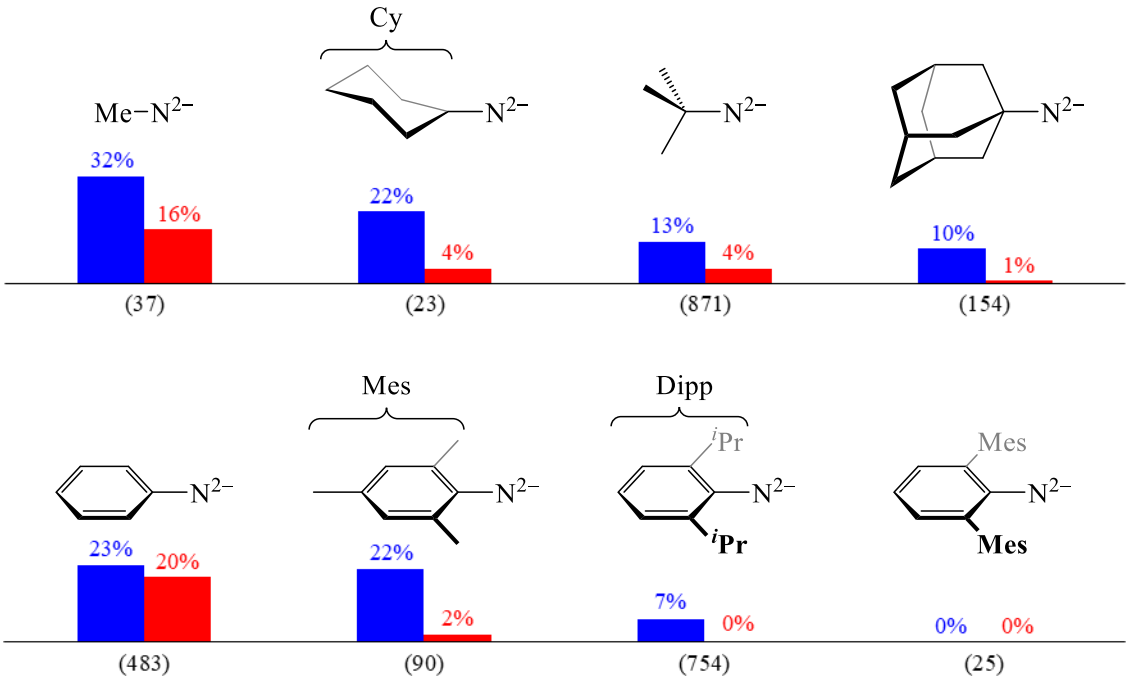

FIGURE 1.4: Examples of imido ligands (RN^{2-}) and the proportions in which μ_2-NR (blue) and μ_3-NR (red) bridging coordination modes are adopted in transition metal imido complexes deposited in the CSD. Numbers in parentheses denote the total number of complexes featuring the ligand in any coordination mode (including terminal). Alkylimido (TOP ROW) and arylimido (BOTTOM ROW) ligands are arranged in order of increasing steric bulk (LEFT to RIGHT).

While it is clear that steric effects strongly influence the terminal *vs.* bridging coordination of an imido ligand, the electronic requirements of the metal centre(s) within the complex also play a key role. For electronically unsaturated monomeric imido complexes, dimerisation of the complex may lead to its stabilisation through the formation of a metal–metal bond (for non-d^0-metals) due to the significant reduction in the intermetallic distance. Due to the generally low d^n-configuration of early transition metals, doubly-bridging imido motifs are more commonly found within such systems.[14] This is exemplified with the isolation of the 18-electron dimeric complex $\{Cp^*Cr^{IV}Br(\mu\text{-NCy})\}_2$ (**E**; Cp* = C_5Me_5 and Cy = cyclohexyl) instead of its hypothetical 16-electron monomeric counterpart (SCHEME 1.1).[25]

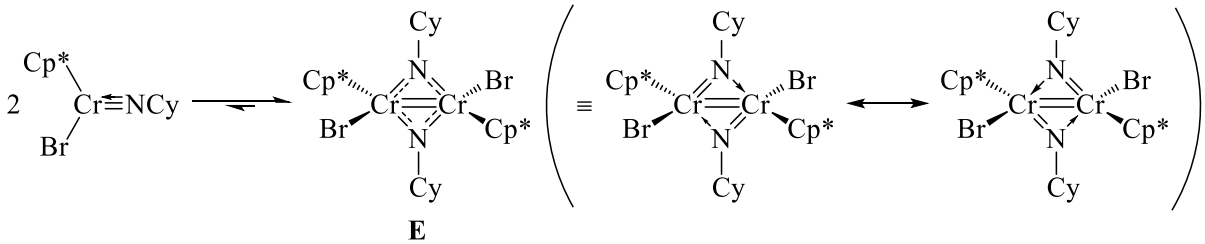

E

SCHEME 1.1: Dimerisation of the hypothetical 16-electron terminal imido complex Cp*CrBr(NCy) to the isolable 18-electron doubly-bridging imido complex $\{Cp^*CrBr(\mu\text{-NCy})\}_2$ (**E**).[25] The resonances forms of symmetric-bridging **E** are also shown.

In addition to steric and electronic stabilisation, the formation of dimeric complexes containing a bridging imido moiety can lead to the coordinative saturation of the transition metal centre. As this usually results in a reduced reactivity scope for μ-imido complexes, the variety of reactions available to terminal imido ligands will be the focus of the following sections.

1.2. General reactivity at the RN^{2-} moiety of transition metal imido complexes

The reactivity of imido complexes reported in the literature is extensive. This section will, however, focus specifically on the chemistry that results from the variable electron-density about the imido nitrogen atom. Attention will be drawn to the reactivity of imido complexes in which the highest-occupied molecular orbital (HOMO) is either localised at the N-atom as a lone-pair (SECTION 1.2.1), within a metal–heteroatom π-bond (SECTIONS 1.2.2 & 1.2.3) or, for a few electron-rich arylimido complexes, delocalised onto the pendant aromatic ring (SECTIONS 1.2.4 & 1.2.5). Despite the variable LX_2- and X_2-coordination modes involved with these reactivities, for clarity, the structures of all complexes featuring terminal imido ligands will be depicted as a double-bonded ligands (*i.e.* M=NR) from hereafter, irrespective of the actual metal–nitrogen bond order.

1.2.1. Brønsted and Lewis basicity of the imido N-atom

As with most nitrogen-containing species, a common property of terminal imido complexes is the basicity of the N-atom resulting from the presence of a lone-pair of electrons. As expected, this characteristic is most notable for X_2-coordinated imido ligands rather than their LX_2-counterparts, since in the former the lone-pair is not involved in π-bonding to the metal centre of the complex (SECTION 1.1.2). The basicity of imido ligands is exemplified in derivatives of the d^0 tungsten(VI) *tris*(imido) complex $W(NDipp)_3$ (**F**). Here, the corresponding methylated species $[WMe(NDipp)_3]^-$ ($[\mathbf{F}\text{-Me}]^-$) is readily protonated by the weak Brønsted acid $[HNMe_3]BPh_4$ ($pK_a = 9.76$)[26] to afford the neutral amido complex $WMe(NDipp)_2(NHDipp)$ (**G**; SCHEME 1.2i).[27] In addition to reacting with Brønsted acids, the imido N-atom of the neutral derivative $W(NDipp)_3(PMe_3)$ ($\mathbf{F}\cdot PMe_3$) demonstrates Lewis basicity and undergoes selective *N*-alkylation by RI {R = Me or $SiMe_3$ (TMS)} to produce $WI(NDipp)_2(NRDipp)$ (**H**), following the displacement of PMe_3 by the generated I^- anion (SCHEME 1.2ii).

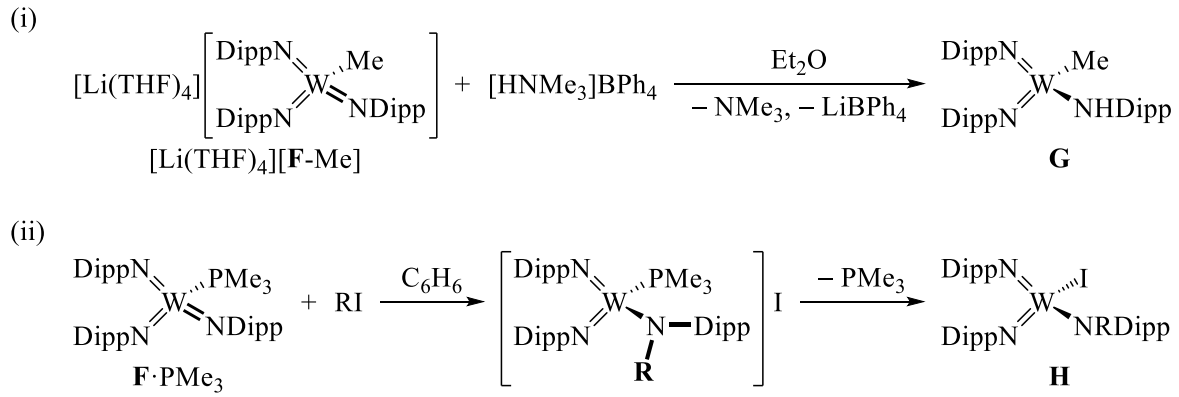

SCHEME 1.2: Reported basicities of derivatives of $W(NDipp)_3$ (**F**): (i) *N*-protonation of $[Li(THF)_4][\mathbf{F}\text{-Me}]$ and (ii) *N*-alkylation of $\mathbf{F}\cdot PMe_3$ (R = Me or TMS).[27]

Typically, the nitrogen lone-pair is less available when the imido ligand coordinates to multiple metal centres, so for dinuclear complexes featuring both terminal and bridging imido moieties, electrophilic attack occurs typically at the terminal imido ligand. An example of this type of reactivity is demonstrated by the dirhenium(VI) complex $Re_2(\mu\text{-}N^tBu)_2(N^tBu)_4$ (**I**) reported by Wilkinson and co-workers. This complex is selectively protonated by TfOH (Tf = SO_2CF_3) at one terminal $^tBuN^{2-}$ ligand to form the triflate salt $[Re_2(\mu\text{-}N^tBu)_2(N^tBu)_3(NH^tBu)]OTf$ ([**I**·H]OTf; SCHEME 1.3).[28] Interestingly, the nucleophilicity of complex **I** at the terminal imido ligands extends to reactions with "softer" Lewis acids, namely CuOTf and AgOTf,* resulting in the multinuclear adducts $Re_2(\mu\text{-}N^tBu)_2(N^tBu)_2(N\{CuOTf\}^tBu)_2$ (**I**·2CuOTf) and $\{Re_2(\mu\text{-}N^tBu)_2(N^tBu)_4\}_2\{Ag_2(\mu\text{-}OTf)_2\}$ ($\{$**I**·AgOTf$\}_2$), respectively. In contrast, a Lewis adduct was not afforded from the reaction between AgOTf and the lighter homologue of complex **I**, namely $Mn_2(\mu\text{-}N^tBu)_2(N^tBu)_2$. Instead, a single-electron transfer process takes place to afford the oxidised monocationic complex.[30]

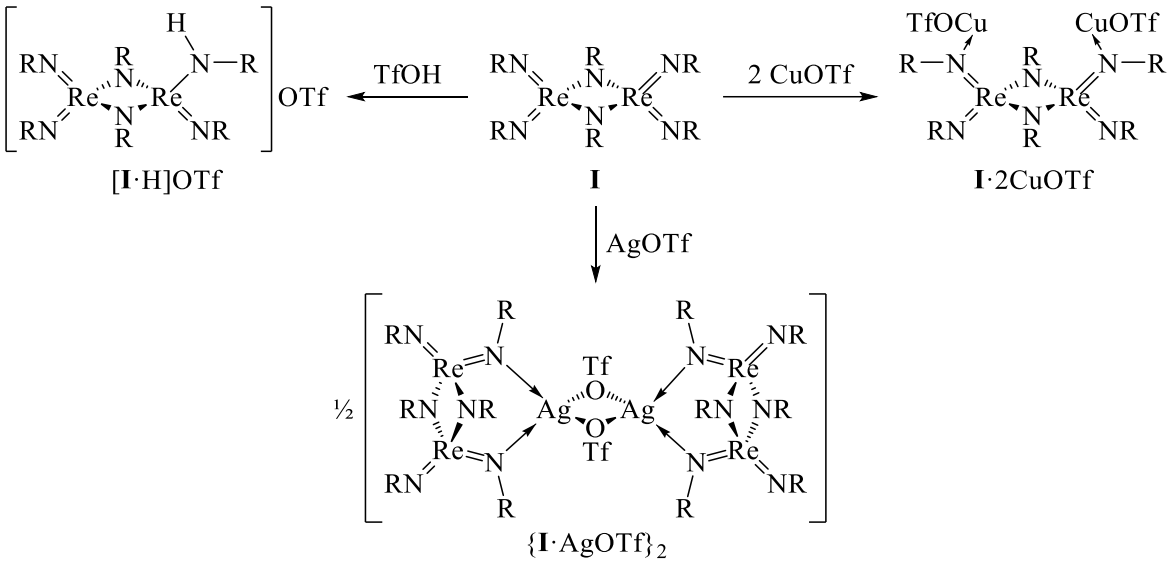

SCHEME 1.3: Reported reactivity of complex **I** (R = ^{t}Bu) with electrophiles TfOH, CuOTf and AgOTf.[28] For clarity, the μ-*O,O'*-triflate ligand is abbreviated to >OTf.

Compared to the dirhenium(VI) complex **I**, $ReCl_3(NMe)(PPh_3)_2$ (**J**) is remarkably stable to protonolysis, given that complex **J** can be recovered quantitatively after heating at reflux for 2 h in HCl-saturated benzene (SCHEME 1.4).[31] In fact, complex **J** demonstrates unusually acidic methyl H-atoms, as in the presence of pyridine (py), the ketimido complex $ReCl_2(N{=}CH_2)(PPh_3)_2(py)$ (**K**) is formed in 68% yield following the elimination of HCl.[32] The stability of complex **J** to protonation (even under the harsh conditions described in SCHEME 1.4) may be attributed to the imido ligand adopting an LX_2-coordination mode in order to form an electronically saturated 18-electron complex. This difference in the Brønsted basicities of complexes **I** and **J** suggests that, for imido complexes whose molecular

* Calculated chemical hardness values: η_H = 12.84 eV, η_{Cu} = 6.49 eV and η_{Ag} = 6.27 eV.[29]

structures cannot be crystallographically determined, the ease of *N*-protonation may be used to indicate the availability of the nitrogen lone-pair (and hence the M–N bond order).

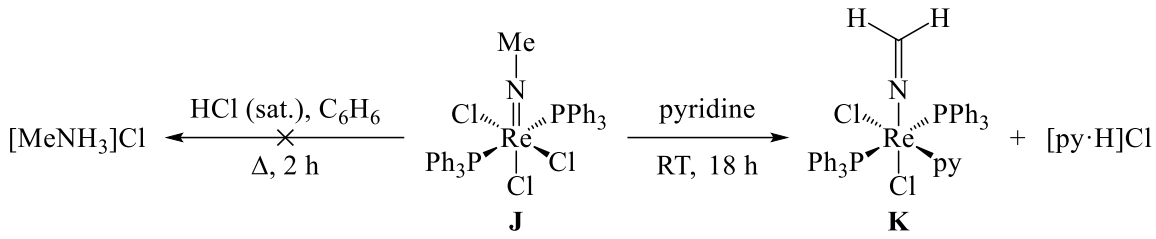

SCHEME 1.4: Reactivity of the 18-electron imido complex $ReCl_3(NMe)(PPh_3)_2$ (**J**) with acids[31] and bases.[32]

1.2.2. [2 + 2] cycloaddition of unsaturated species to M=N multiple-bonds

While LX_2-bound imido ligands are less susceptible to electrophilic attack at the N-atom, the involvement of the heteroatom lone-pair in bonding to the metal centre makes the metal–nitrogen bond more π-rich, which can enable the [2 + 2] cycloaddition of other unsaturated species. The first crystallographic evidence for the occurrence of this reactivity across M=N bonds was reported by Glueck *et al.* with the formation of the κ^2-*N,O*-carbamate complex Cp*Ir{OC(O)N^{t}Bu} (**L$_I$**) from the reaction between the late transition metal complex Cp*Ir(N^{t}Bu) (**M**) and CO_2 (SCHEME 1.5i).[33] In contrast, the reaction between complex **M** and the electron-rich alkynes MeC≡CMe and MeC≡CPh was unsuccessful (even at 85 °C). This difference in reactivity has tentatively been attributed to the lower bond polarity of the alkynes compared to the C=O units in CO_2, resulting in poorer interaction with the polar $Ir^{\delta+}=N^{\delta-}$ bond. By lowering the frontier molecular orbital (FMO) energies of the alkyne through use of electronegative substituents, RC≡CR (R = CO_2Me) was found to react with complex **M** at room temperature. However, rather than isolating the expected iridium(III) [2 + 2] cycloaddition product Cp*Ir{C(R)C(R)N^{t}Bu} (**L$_{II}$**), the iridium(I) η^4-pyrrole complex Cp*Ir(η^4-C_4R_4N^{t}Bu) (**N**) was instead obtained (SCHEME 1.5i). Glueck *et al.* later rationalised that the azametallacyclobutene **L$_{II}$** likely formed as an intermediate during the synthesis of complex **N**, but rapidly underwent further [2 + 2] cycloaddition with another equivalent of alkyne, followed by reductive elimination, to produce the ring-closed pyrrole ligand and the formally reduced metal centre (SCHEME 1.5ii).[34]

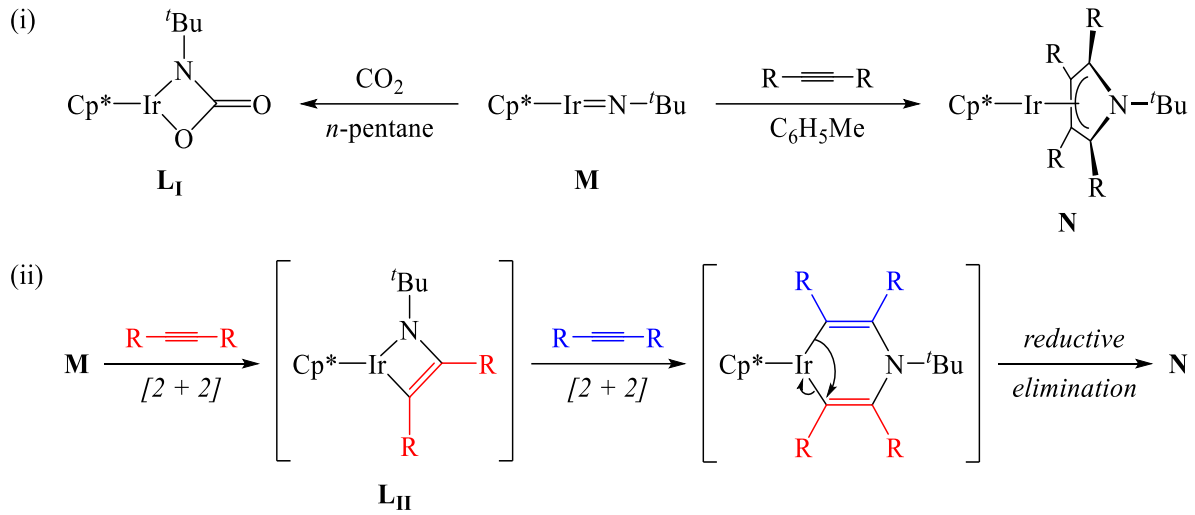

SCHEME 1.5: (i) [2 + 2] cycloaddition reactions of complex **M** with CO_2 and RC≡CR (R = CO_2Me).[33] (ii) Proposed mechanism for the formation of the iridium(I) η^4-pyrrole complex **N** *via* four- and six-membered azametallacycles.[34]

Later, Horton and co-workers reported that the early transition metal imido complex V(NHSi^{t}Bu$_3$)(NSi^{t}Bu$_3$)$_2$(OEt$_2$) (**O**) also reacts with alkynes, although as found for the reaction with complex **M**, the [2 + 2] cycloaddition product was not isolable.[35] Instead, the reaction between complex **O** and the symmetric alkyne C_2R_2 (*e.g.* R = Me or Et) forms the 1-azaallyl complex V{CH$_2$CMe$_2$Si^{t}Bu$_2$[η^3-NC(R)CHR]}(NHSi^{t}Bu$_3$)(NSi^{t}Bu$_3$) (**P**), as confirmed crystallographically for R = Et (SCHEME 1.6). NMR spectroscopic analysis of the reaction between complex **O** and C_2Me_2 revealed that the [2 + 2] cycloaddition product, namely the azametallacyclobutene V{C(Me)C(Me)NSi^{t}Bu$_3$}(NHSi^{t}Bu$_3$)(NSi^{t}Bu$_3$) (**Q$_I$**), is initially formed following the dissociation of Et$_2$O. While **Q$_I$** is isolable as a solid at –60 °C, rapid C–H metallation at a ^{t}Bu-group occurs upon dissolution to afford the 1-azaallyl complex **P** (SCHEME 1.6).

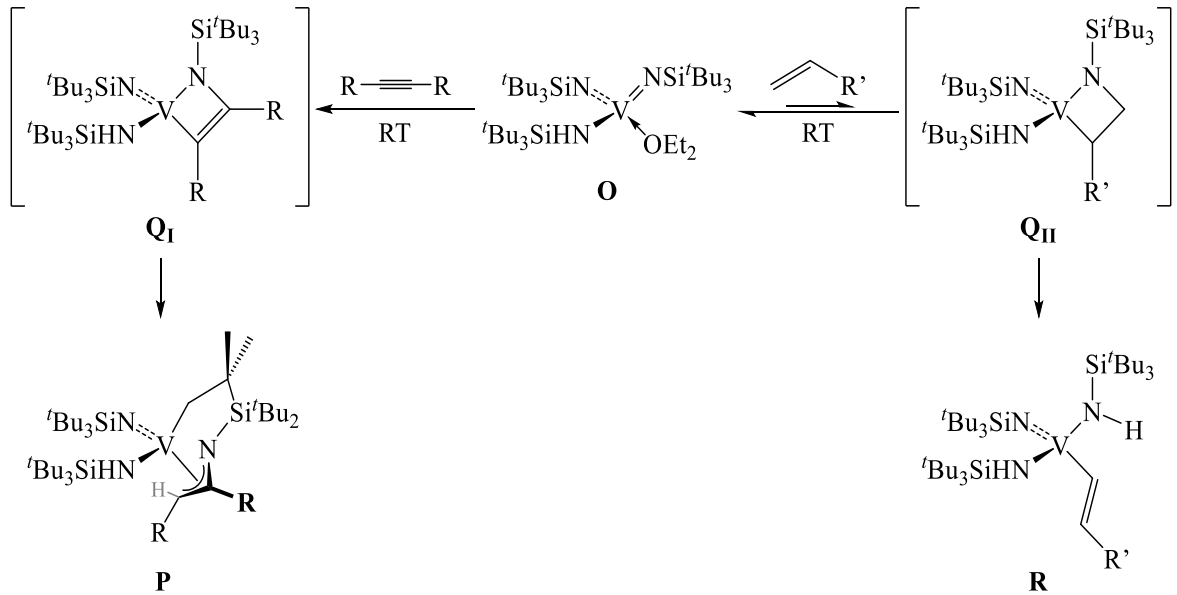

SCHEME 1.6: [2 + 2] cycloaddition of alkynes C_2R_2 (R = Me or Et) and alkenes C_2H_3R' (R' = H or Me) to complex **O**.[35]

As observed to occur with alkynes, the addition of alkenes C_2H_3R' (R' = H or Me) to complex **O** results in C–H activation, although this time at the vinyl positions of the substrate with the formation of the

alkenyl amido complexes V(CH=CHR')(NHSi^{t}Bu$_3$)$_2$(NSi^{t}Bu$_3$) (**R**; SCHEME 1.6). NMR spectroscopic monitoring of the reaction between the complex **O** and ethene revealed that the [2 + 2] cycloaddition product V{CH$_2$CH$_2$N(Si^{t}Bu$_3$)}(NHSi^{t}Bu$_3$)(NSi^{t}Bu$_3$) (**Q$_{II}$**) formed in equilibrium with the imido complex, before slowly being converted to the alkenyl complex **R**. By increasing the pressure of ethene to 20 bar then cooling the reaction mixture to –70 °C, Horton and co-workers were able to isolate complex **Q$_{II}$** as the first example of an azametallacyclobutane complex formed from the [2 + 2] cycloaddition of an alkene to an imido ligand.

1.2.3. 1,2-addition reactions across imido M=N double-bonds

While the formation of the alkenyl complex **R** *via* the [2 + 2] cycloaddition of an alkene to the imido complex **O** (SCHEME 1.6) is unusual, the somewhat related 1,2-addition of molecules possessing a reactive R–H bond (*e.g.* R = H, aryl or alkyl) across imido M=N bonds is more prevalent. This reactivity is particularly observed for d^0 imido complexes, which cannot undergo oxidative addition of R–H to the metal centre due to the transition metal being in its highest available oxidation state.

Wolczanski and co-workers initially reported that heating a benzene solution of the zirconium *tris*(amido) complex ZrCy(NHSi^{t}Bu$_3$)$_3$ (**S$_I$**-Cy; Cy = cyclohexyl) afforded the phenyl derivative Zr(NHSi^{t}Bu$_3$)$_3$Ph (**S$_I$**-Ph) and cyclohexane.[36] The formation of these two products was consistent with the thermolytic elimination of CyH from complex **S$_I$**-Cy to form the mono(imido) derivative Zr(NHSi^{t}Bu$_3$)$_2$(NSi^{t}Bu$_3$) (**T$_I$**) as a transient species, followed by the 1,2-addition of PhH across the Zr=N bond of **T$_I$** (SCHEME 1.7). Furthermore, when the imido complex **T$_I$** is formed in the presence of H$_2$ or CH$_4$, the 1,2-addition product Zr(NHSi^{t}Bu$_3$)$_3$R (**S$_I$**-R; R = H or Me) was obtained, providing the first example of dihydrogen and methane activation across a M=N bond in the literature.[*] While the 14-electron imido complex **T$_I$** was not isolable, its transient formation was verified by the thermolysis of **S$_I$**-R (R = H, Me, Cy or Ph) in THF, where the complex was trapped as its 16-electron THF-adduct Zr(NHSi^{t}Bu$_3$)$_2$(NSi^{t}Bu$_3$)(THF) (**T$_I$**·THF).

[*] It is unclear whether the imido complex **T$_I$** was the first example of 1,2-addition of PhH across a M=N bond, as this reactivity was reported concurrently for another zirconium imido complex, Cp$_2$Zr(N^{t}Bu).[61] The reactivity of this system will be discussed in SECTION 1.3.1.

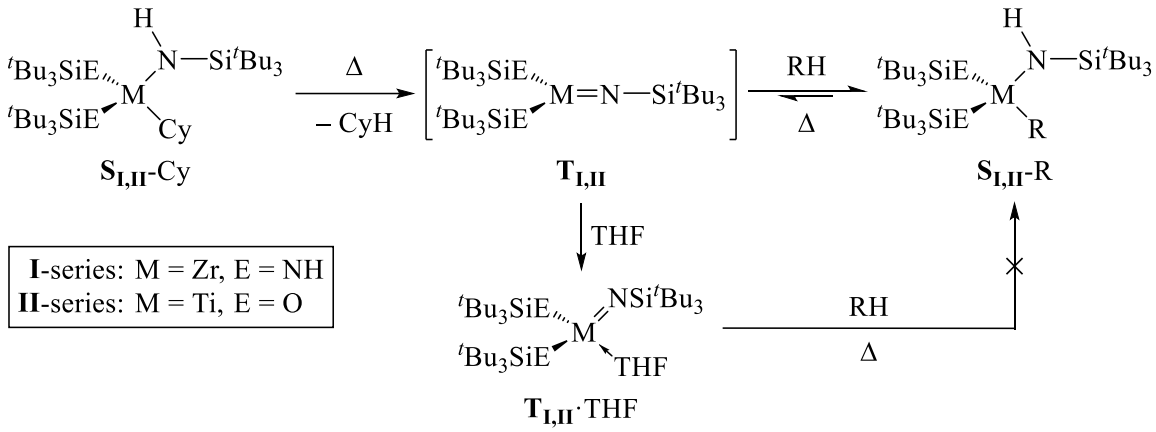

SCHEME 1.7: Transient formation of the Group IV imido complexes $\mathbf{T_I}$ (M = Zr, E = NH) and $\mathbf{T_{II}}$ (M = Ti, E = O), which undergo 1,2-addition reactions with RH to form $\mathbf{S_I}$-R (R = H, Me or Ph)[36] and $\mathbf{S_{II}}$-R (R = H, Me, Et, ^{n}Bu, ^{neo}Hex, *c*-C_3H_5, *c*-C_4H_7, *c*-C_5H_9, Bn, $CH_2C_6H_3$-3,5-Me_2, $CH_2CH{=}CH_2$, $CH_2CH{=}CHMe$, Ph, Tol or $CH{=}CH_2$),[37,38] respectively.

Wolczanski and co-workers later improved the substrate scope for C–H activation through use of a titanium siloxy variant of the amido precursor $\mathbf{S_I}$-Cy, namely TiCy(NHSi^{t}Bu$_3$)(OSi^{t}Bu$_3$)$_2$ ($\mathbf{S_{II}}$-Cy). Thermolysis of $\mathbf{S_{II}}$-Cy was proposed to proceed *via* the transient formation of the imido complex Ti(NSi^{t}Bu$_3$)(OSi^{t}Bu$_3$)$_2$ ($\mathbf{T_{II}}$),[37] which was similarly trapped irreversibly as its THF-adduct Ti(NSi^{t}Bu$_3$)(OSi^{t}Bu$_3$)$_2$(THF) ($\mathbf{T_{II}}$·THF) as confirmed crystallographically.[38] The transient imido complex $\mathbf{T_{II}}$ was demonstrated to activate not only H_2, CH_4 and benzene, but also a range of alkyl (both primary and secondary), benzyl, allyl, vinyl and aryl C–H bonds, with the formation of Ti(NHSi^{t}Bu$_3$)(OSi^{t}Bu$_3$)$_2$R ($\mathbf{S_{II}}$-R; SCHEME 1.7), where C–H bonds with a higher s-character were generally found to have a lower activation energy.[37,38]

A large kinetic isotope effect was observed for the reaction between the imido complex $\mathbf{T_{II}}$ and RH/RD, which suggested that the 1,2-addition reaction proceeded *via* a concerted rate-determining step (RDS), with a four-centre transition-state involving the metal centre, N- C$^\alpha$- and H/D-atoms.[38] Computational analysis of the 1,2-addition of RH (R = alkyl) to the Ti=N bond of complex $\mathbf{T_{II}}$ supported this concerted mechanism.[39] However, prior to the RDS, the σ-alkane complex Ti(NSi^{t}Bu$_3$)(OSi^{t}Bu$_3$)$_2$(RH) ($\mathbf{T_{II}}$·RH) was computed to form as an intermediate (SCHEME 1.8). Further calculations indicate that this σ-alkane complex is formed purely from a $\sigma_{R-H}\rightarrow d\sigma_{Ti}$ agostic interaction, since $d\pi_{Ti}\rightarrow\sigma^*_{C-H}$ back-bonding is not possible for a d^0 titanium(IV) centre (due to its vacant metal-based orbitals). However, the σ^*_{C-H} orbital of RH is involved in the RDS of the 1,2-addition reaction, where $\pi_{Ti-N}\rightarrow\sigma^*_{C-H}$ back-donation leads to the ultimate cleavage of the C–H bond. The stepwise donation/back-donation has also been computed for the oxidative addition of RH to late transition metals;[40] however, due to electrostatic repulsion between the filled metal-based orbitals and σ_{C-H}, formation of the σ-alkane complex (rather than C–H cleavage) is normally the rate-determining step.[41]

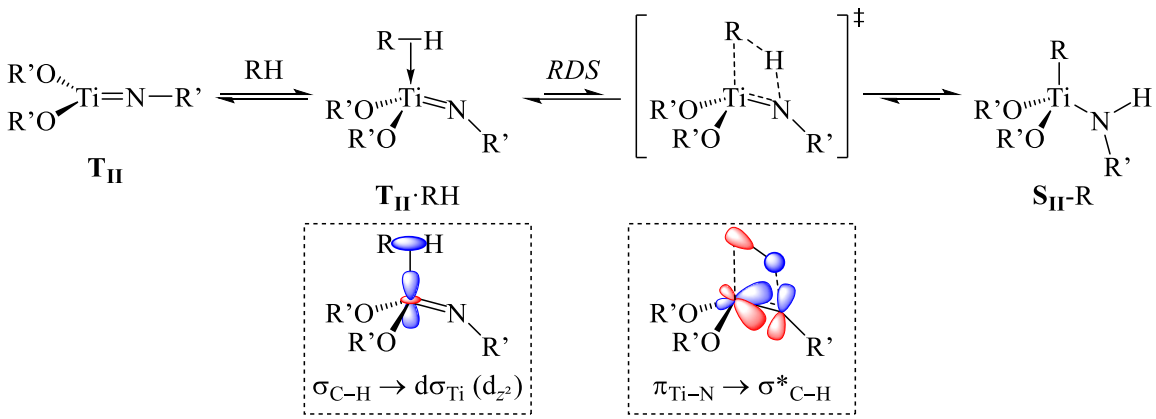

SCHEME 1.8: Computed mechanism for the 1,2-addition of RH (R = alkyl) to the transient imido complex $\mathbf{T_{II}}$ (R' = Si^{t}Bu$_3$), where the significant MO interactions within intermediate $\mathbf{T_{II}}$·RH and the transition-state are shown below the corresponding structures.[39,42]

By examining the molecular orbitals (MOs) involved in the 1,2-addition of RH across the Ti=N bond in complex $\mathbf{T_{II}}$ (SCHEME 1.8), Wolczanski was able to deduce the requirements for early transition metal imido complexes to activate C–H bonds.[42] Firstly, the electrophilic site (usually the lowest-unoccupied MO, LUMO) must be localised on the early transition metal centre, and should preferably resemble a directional d_{z^2} orbital, to enable the initial σ-coordination of RH through $\sigma_{C-H} \rightarrow d\sigma_M$ donation. Secondly, the HOMO of the imido complex must have significant M=N π-bond character and be oriented in the same plane as the LUMO; this facilitates back-donation into the σ^*_{C-H} orbital of RH and hence C–H bond cleavage. Indeed, there are many other examples of transient d^0 imido complexes of early transition metals following these two criteria that have been reported to be capable of activating C–H bonds, including complexes of scandium(III),[43–46] tantalum(V)[47] and tungsten(VI).[48] However, no such reactivity has been explored for niobium(V) imido complexes in the literature.

1.2.4. Electrophilic addition to arylimido ligands

As outlined in each of the three previous subsections, the reactivity of imido complexes is dominated by the high electron-density about the N-atom. While electrophile attack predominantly occurs at the heteroatom (SECTION 1.2.1), if there are ancillary ligands with significant steric bulk surrounding the metal centre, such reactivity may be inhibited. However, if the imido complex contains a sufficiently electron-rich metal centre and also an aryl *N*-substituent, the electron density may be donated onto the arene *via* resonance to enable reactivity at the less hindered *ortho*- or *para*-positions of the aryl substituent (SCHEME 1.9).

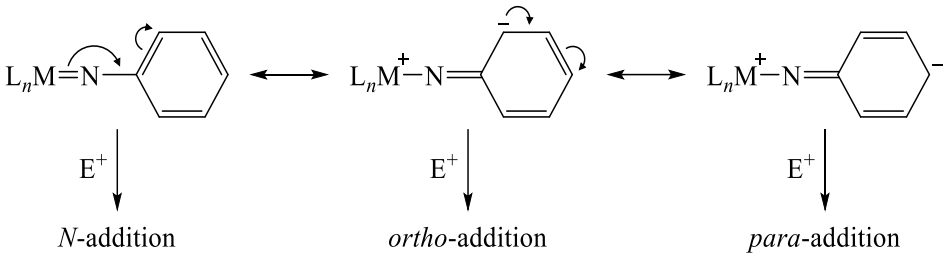

SCHEME 1.9: Selected resonance forms of a generic arylimido complex and their reactivity with an electrophile (E^+).

As considerable steric bulk is required to prevent electrophilic attack of the N-atom, *ortho*-aryl attack is also usually kinetically hindered. Indeed, to date, only electrophilic addition has been reported to occur at the *para*-position of the aryl substituent. Such electrophilic addition to the *para*-position of an aryl imido substituent was first reported by Sharp and co-workers in the dinuclear rhodium(I) d^8 complex $Rh_2(\mu\text{-NTol})(CO)_2(\mu\text{-dppm})_2$ (**U$_I$**; Tol = *p*-tolyl and dppm = *bis*{diphenylphosphino}methane), where the addition product $[Rh_2(\mu\text{-N}\{\text{Tol-4-CH}_2\text{Cl}\})(CO)_2(\mu\text{-dppm})_2]Cl$ ([**U$_I$**-4-CH_2Cl]Cl) was afforded from a DCM solution of **U$_I$**.[49] Electrophilic addition to **U$_I$** is not limited to DCM as an electrophile, with Sharp and co-workers later reporting the more rapid *para*-addition of MeX (X = OTf or I) and $PhCH_2Cl$ (SCHEME 1.10).[50]

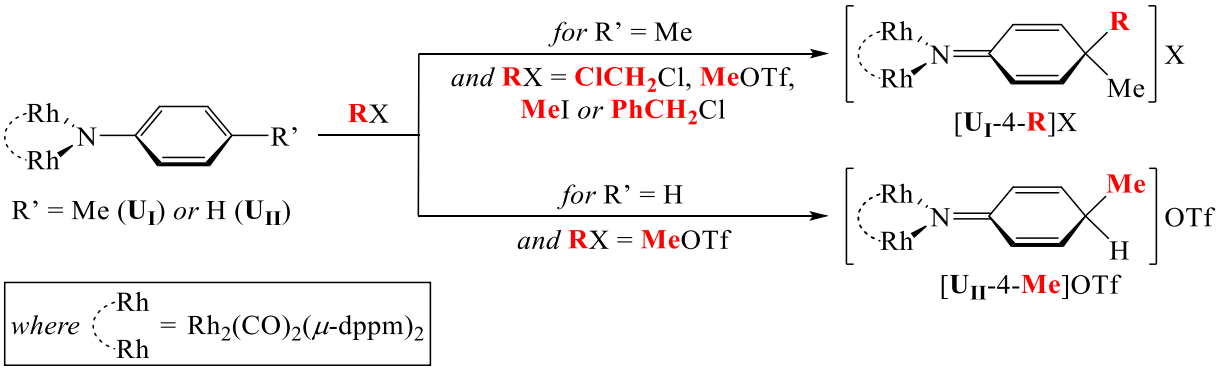

SCHEME 1.10: Reported *para*-addition of $Rh_2(\mu\text{-NTol})(CO)_2(\mu\text{-dppm})_2$ (**U$_I$**) and $Rh_2(\mu\text{-NPh})(CO)_2(\mu\text{-dppm})_2$ (**U$_{II}$**) with electrophiles RX.[49,50] For clarity, the electrophilic R-group is designated in red.

The phenylimido derivative $Rh_2(\mu\text{-NPh})(CO)_2(\mu\text{-dppm})_2$ (**U$_{II}$**) was also found to be reactive towards electrophilic addition at the *para*-position of the aryl imido substituent, although only for the strongest electrophile of the four used, namely MeOTf (SCHEME 1.10).[50] Compared to **U$_I$**, the reduced reactivity of the imido complex **U$_{II}$** may be attributed to the absence of a σ-donating methyl group at the *para*-position, resulting in a lower electron-density at the same position. Aside from these two dirhodium systems described by Sharp, no other arylimido complexes appear to meet the aforementioned steric and electronic requirements for preferential electrophilic attack at the *para*-aryl position rather than the N-atom.

1.2.5. Oxidative coupling of arylimido ligands

While the dirhodium phenylimido complex **U$_{II}$** is less susceptible to electrophilic attack than its tolylimido counterpart (SECTION 1.2.4), the absence of a *para*-substituent on the phenyl ring enables the electron-rich complex to undergo alternative reactivity to **U$_{I}$**. Following the addition of an equimolar quantity of ferrocenium hexafluorophosphate ($FcPF_6$) to the phenylimido complex **U$_{II}$**, Sharp and co-workers report that a bimolecular oxidative coupling at the *para*-aryl position occurred to afford the dicationic diketimido complex $[\{Rh_2(CO)_2(\mu\text{-dppm})_2\}_2(\mu,\mu\text{-N}\{C_6H_4\}_2N)][PF_6]_2$ ([**V**][PF_6]$_2$; SCHEME 1.11).[51] Crystallographic analysis of [**V**][PF_6]$_2$ revealed that the backbone of the diketimido ligand adopted a planar, fully-conjugated diphenoquinoidal (DPQ) arrangement, indicating that the H-atoms at the *para*-positions had been lost during oxidative coupling of **U$_{II}$**. These H-atoms were likely lost through deprotonation by unreacted **U$_{II}$** present in the reaction mixture, which was supported by the isolation of the amido salt $[Rh_2(\mu\text{-NHPh})(CO)_2(\mu\text{-dppm})_2]PF_6$ ([**U$_{II}$**·H]PF_6) alongside the diketimido derivative [**V**][PF_6]$_2$ in a 2:1 molar ratio (SCHEME 1.11).

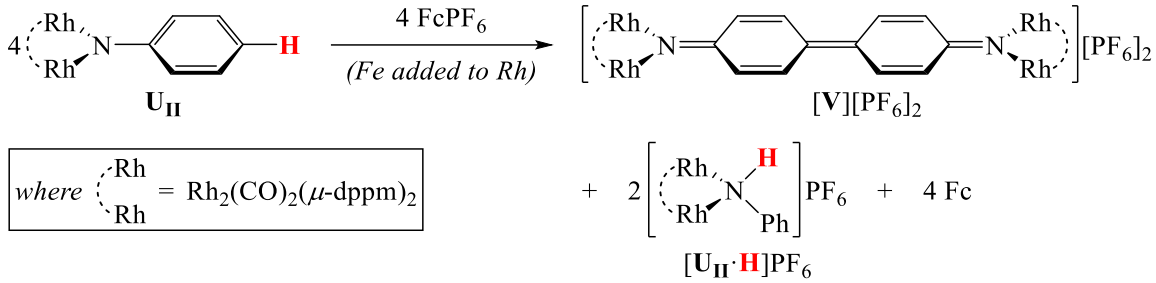

SCHEME 1.11: Formation of the diphenoquinoidal (DPQ) diketimido salt $[\{Rh_2(CO)_2(\mu\text{-dppm})_2\}_2(\mu,\mu\text{-N}\{C_6H_4\}_2N)][PF_6]_2$ ([**V**][PF_6]$_2$) from the addition of equimolar $FcPF_6$ to the phenylimido complex **U$_{II}$**.[51]

As two of the four equivalents of complex **U$_{II}$** were found to be acting as a base instead of being oxidised (SCHEME 1.11), the complete oxidation of the imido complex was ensured by slowly adding **U$_{II}$** to $FcPF_6$ (instead of *vice versa*), in order to maintain an excess of the oxidant throughout the reaction. Following this approach, it was possible to isolate the less-conjugated, 4,4'-dihydrodiphenoquinoidal ($DPQH_2$) diketimido salt $[\{Rh_2(CO)_2(\mu\text{-dppm})_2\}_2(\mu,\mu\text{-N}\{4,4'\text{-Ph}_2\}N)][PF_6]_2$ ([**W**][PF_6]$_2$) in 92% yield (SCHEME 1.12); again, the structure of the product was confirmed crystallographically. This dicationic $DPQH_2$ diketimido complex was proposed to have formed from the homocoupling of two radical cations, $[Rh_2(\mu\text{-NPh})(CO)_2(\mu\text{-dppm})_2]^{\bullet+}$ (**U$_{II}$**$^{\bullet+}$), with the localisation of the positive charge at the N-atom of **U$_{II}$**$^{\bullet+}$ to minimise electrostatic repulsion during dimerisation. Such a coupling mechanism differs slightly from a classical 'Scholl-type' radical mechanism often invoked for the coupling of simple arene derivatives (*e.g. ortho*-terphenyls).[52] Indeed, Scholl coupling proceeds *via* the heterocoupling of a radical cation with a neutral, unoxidised species (*i.e.* **U$_{II}$**$^{\bullet+}$ with neutral imido complex **U$_{II}$** in this system)[53] rather than the homocoupling of two radical cations.

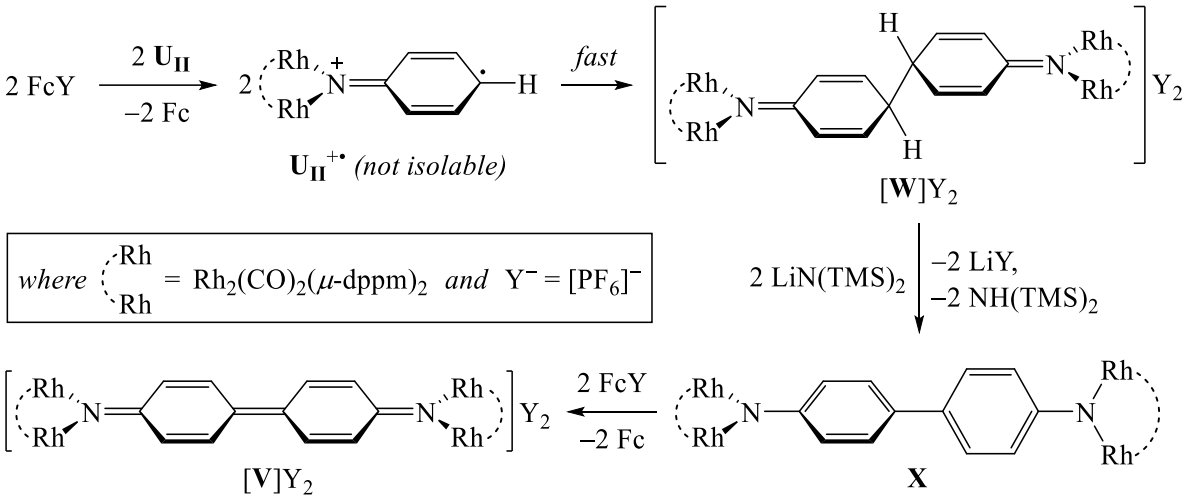

SCHEME 1.12: Synthesis of the DPQ diketimido complex [**V**][PF_6]$_2$ from the oxidative coupling of the imido complex $\mathbf{U_{II}}$, *via* the isolable 4,4'-dihydrodiphenoquinoidal ($DPQH_2$) diketimido and biphenyl diimido derivatives [**W**][PF_6]$_2$ and **X**, respectively. The proposed transient radical cation $\mathbf{U_{II}}^{\bullet+}$ is also shown for the first step.[51]

Following treatment of the $DPQH_2$ diketimido complex [**W**][PF_6]$_2$ with two equivalents of $LiN(TMS)_2$, Sharp and co-workers demonstrated the successful deprotonation at the two *para*-positions of the dicationic complex. This reaction afforded the neutral diimido complex {$Rh_2(CO)_2(\mu$-dppm)$_2$}$_2$(μ,μ-N{C_6H_4}$_2$N) (**X**; SCHEME 1.12) in 90% yield. Subsequently, the addition of two equivalents of $FcPF_6$ to the diimido derivative **X** was shown to result in the oxidation of the complex, with the formation of the DPQ diketimido complex [**V**][PF_6]$_2$ (94% yield). This stepwise synthesis of the diketimido complex [**V**][PF_6]$_2$ was also proposed as the mechanism by which the oxidative coupling of imido complex $\mathbf{U_{II}}$ occurred under the original reaction conditions (SCHEME 1.11), albeit in the absence of external base $LiN(TMS)_2$. To further validate that the pathway described in SCHEME 1.12 proceeds without the base, the deprotonation of the $DPQH_2$ diketimido complex [**W**][PF_6]$_2$ was demonstrated by the addition of two equivalents of the imido complex $\mathbf{U_{II}}$, affording the expected neutral diimido species **X** and two equivalents of the amido salt [$\mathbf{U_{II}}$·H]PF_6.

Unlike with electrophilic addition (SECTION 1.2.4), the oxidative coupling of arylimido complexes is not limited to the dirhodium system of Sharp and co-workers. Indeed, Harrold and Hillhouse demonstrated that the nickel(II) complex $L_2Ni(NDippp)$ (**Y**; L_2 = *bis*{3-*tert*-butyl-4,5-dimethylimidazol-2-yliden-1-yl}methane and Dippp = 2,6-*bis*{2,6-di-*iso*-propylphenyl}phenyl) undergoes oxidative coupling in the presence of the ferrocenium salt $FcBPh^F_4$ (Ph^F = C_6F_5) to form [{L_2Ni}$_2$(N{2,6-$Dipp_2C_6H_2$}$_2$N)][BPh^F_4]$_2$ ([**Z**][BPh^F_4]$_2$) in 89% yield (SCHEME 1.13).[54] The X-ray crystallographic analysis of the dicationic complex $\mathbf{Z}^{2+}$ confirmed the presence of a diketimido ligand with a DPQ backbone, indicating the loss of the H-atoms at the *para*-positions during oxidative coupling.

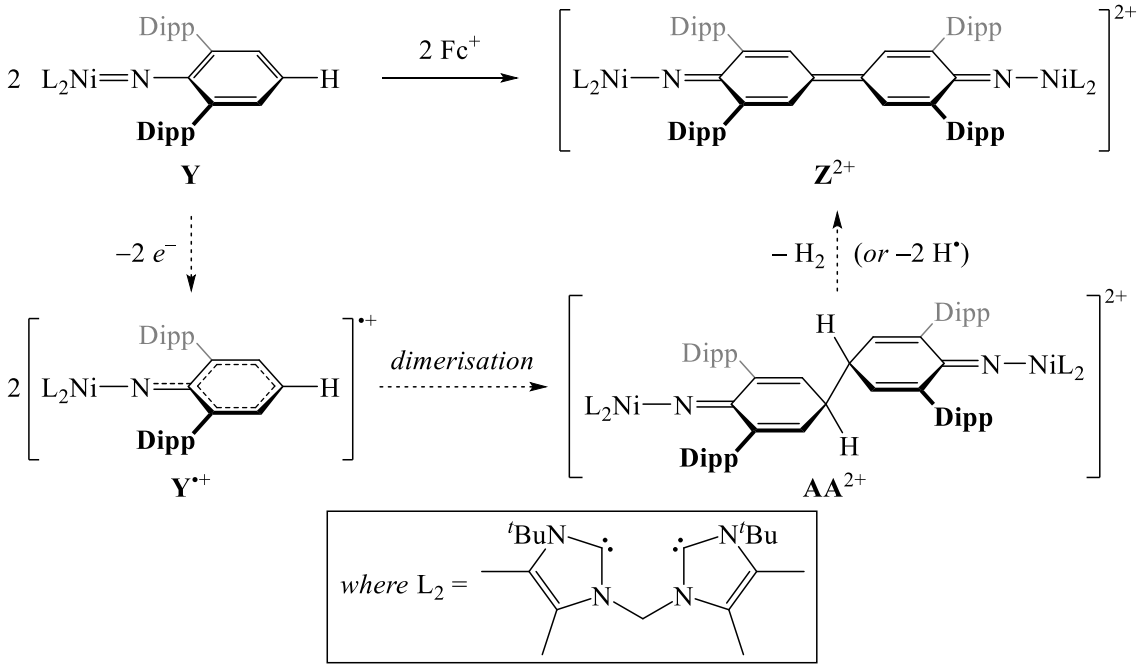

SCHEME 1.13: Oxidative coupling of the arylimido complex **Y** with equimolar $FcBPh^F_4$ to form the DPQ diketimido complex [**Z**][BPh^F_4]$_2$; the proposed mechanism is shown as dashed arrows. [BPh^F_4]$^-$ counteranions are omitted for clarity.[54]

While an amido by-product was observed for the oxidative coupling of dirhodium imido complex $\mathbf{U_{II}}$, no such *N*-protonated species was detected alongside the formation of the nickel diketimido complex [**Z**][BPh^F_4]$_2$. Instead, Harrold and Hillhouse proposed that the H-atoms at the *para*-positions were lost as dihydrogen (or H$^\bullet$ radicals)* to form the diketimido complex $\mathbf{Z}^{2+}$, with the oxidative coupling of the nickel imido complex **Y** proceeding according to SCHEME 1.13 (dashed route).[54] The ~2:2:1 stoichiometry of the imido complex **Y**, the ferrocenium oxidant and the product $\mathbf{Z}^{2+}$ agreed with this mechanism. Despite adapting the reaction conditions however, the proposed radical cation [L_2Ni(NDippp)]$^{\bullet+}$ ($\mathbf{Y}^{\bullet+}$) and the $DPQH_2$ diketimido dication [{L_2Ni}$_2$(N{4,4'-Dippp$_2$}N)]$^{2+}$ ($\mathbf{AA}^{2+}$) intermediates were not isolable, indicating their marked instability towards homocoupling and dehydrogenation, respectively.

The instability of the radical cation $\mathbf{Y}^{\bullet+}$ has been explained by density functional theory (DFT) analysis. Harrold and Hillhouse computed the radical cation has coplanar "L_2Ni" and aryl moieties, which enables the delocalisation of its singly-occupied MO (SOMO) over the N-, C^{ortho}- and C^{para}-atoms (FIGURE 1.5).[54] In turn, this facilitates the coupling of two radical cations at the *para*-aryl position. Comparatively, the *bis*(phosphine) analogue [Ni(N{2,6-$Mes_2C_6H_3$})(dtbpe)]$^{\bullet+}$ ($\mathbf{AB}^{\bullet+}$; dtbpe = 1,2-*bis*{di-*tert*-butylphosphino}ethane and Mes = 2,4,6-trimethylphenyl) is unable to adopt a coplanar "P_2Ni"/aryl geometry due to its unfavourable Mes···^{t}Bu steric interactions.[55] Consequently, radical cation $\mathbf{AB}^{\bullet+}$ is stable and thus isolable, since its unpaired electron is confined to a sterically-protected $\pi_{Ni–N}$-orbital rather than delocalised across the aryl ring (FIGURE 1.5).

* The authors state they "have not successfully ascertained the fate of the eliminated hydrogen equivalents".[54]

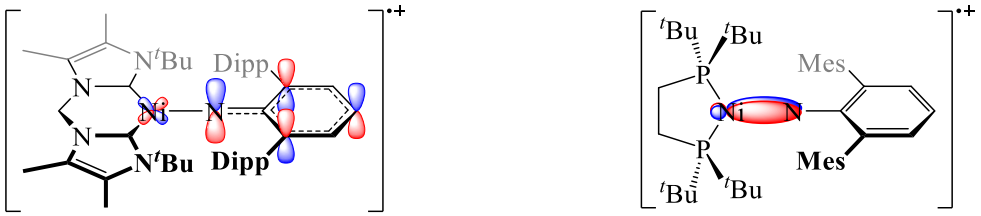

Y$^{\bullet+}$ **AB**$^{\bullet+}$

FIGURE 1.5: Computed SOMOs of the nickel radical cations **Y**$^{\bullet+}$ (unstable)[54] and **AB**$^{\bullet+}$ (stable and isolable).[55]

While the potential intermediate **V**$^{2+}$ in the nickel *bis*(NHC) system may have been unstable to dehydrogenation (SCHEME 1.13), the most recent literature example of arylimido oxidative coupling exclusively resulted in the isolation of the DPQH$_2$ diketimido dication. Aldrich *et al.* demonstrated that the addition of AgBAr$^F_4$ (Ar^F = 3,5-*bis*{trifluoromethyl}phenyl) to Ru(NDipp)(dppe)(PMe$_3$) (**AC**; dppe = 1,2-*bis*{diphenylphosphino}ethane) affords the DPQH$_2$ diketimido derivative [{Ru(NCMe)(dppe)(PMe$_3$)}$_2$(N{4,4'-Dipp$_2$}N)][BAr$^F_4$]$_2$ ([**AD**][BAr$^F_4$]$_2$) in 78% yield when the reaction is performed in 50 vol% MeCN (SCHEME 1.14).[56] Notably, no reaction between the imido complex **AC** and AgBAr$^F_4$ occurs in the absence of MeCN, demonstrating that coordination of the solvent is essential for stabilising the DPQH$_2$ diketimido dication as an 18-electron complex.* Potentially due to its electronic saturation, no subsequent reactivity of the DPQH$_2$ diketimido complex **AD**$^{2+}$ (*e.g.* deprotonation or dehydrogenation) has been reported.

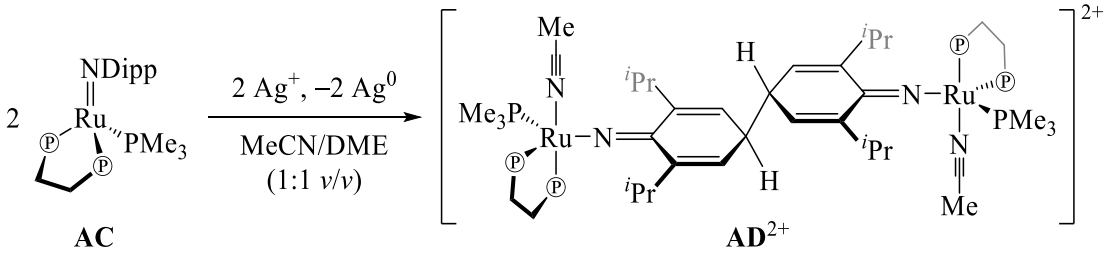

AC **AD**$^{2+}$

SCHEME 1.14: Oxidative coupling of the ruthenium arylimido complex **AC** to the DPQH$_2$ diketimido derivative **AD**$^{2+}$ using AgBAr$^F_4$. For clarity, [BAr$^F_4$]$^-$ counteranions are omitted and PPh$_2$ is abbreviated to Ⓟ; DME = 1,2-dimethoxyethane.[56]

While the steric bulk of the ancillary ligands is rather variable between the arylimido complexes **U$_{II}$**, **Y** and **AC**, the electronic requirements for oxidative coupling at the *para*-aryl position is more consistent between the three systems. Similar to the requirements for electrophilic addition to the same position, oxidative dimerisation appears to be exclusive to arylimido complexes containing electron-rich metal centres (*i.e.* late transition metals in low oxidation states). Consequently, such reactivity would not be expected for the arylimido complexes of early transition metals, despite there being no formal change in oxidation state of the metal centre during oxidative coupling.

* Each N-atom of the DPQH$_2$ diketimido ligand of [**AD**][BAr$^F_4$]$_2$ likely adopts an LX-coordination mode.

1.3. Reactivity of neutral zirconocene imido complexes and their cationic Group(V) metallocenium analogues

1.3.1. The first zirconocene imido system, $Cp_2Zr(N^tBu)$

Zirconocene complexes containing an imido ligand, $Cp'_2Zr(NR)$ (**AE**; Cp' = a cyclopentadienyl derivative), are systems of interest for catalytic applications exploiting the reactive nature of the metal–heteroatom multiple-bond towards small molecules. Since the low-lying metal-based orbitals in "bent" *bis*(cyclopentadienyl) complexes are restricted to occupying a plane orthogonal to the "Cp'_2M" wedge (*yz*-plane in FIGURE 1.6), the imido ligand in complex **AE** is only able to act as an X_2 ligand and, as such, the 16-electron zirconocene imido complex is electronically unsaturated.[57] As a result of this electronic and coordinative unsaturation, zirconocene imido complexes are isolable as their 18-electron dimeric complexes $\{Cp'_2Zr(\mu\text{-}NR)\}_2$, although only for systems in which the steric constraints allow for metal–metal bridging of the imido ligand (*e.g.* for Cp' = C_5H_5 {Cp} and R = Tol[58] or C_6H_4-4-^{t}Bu).[59]

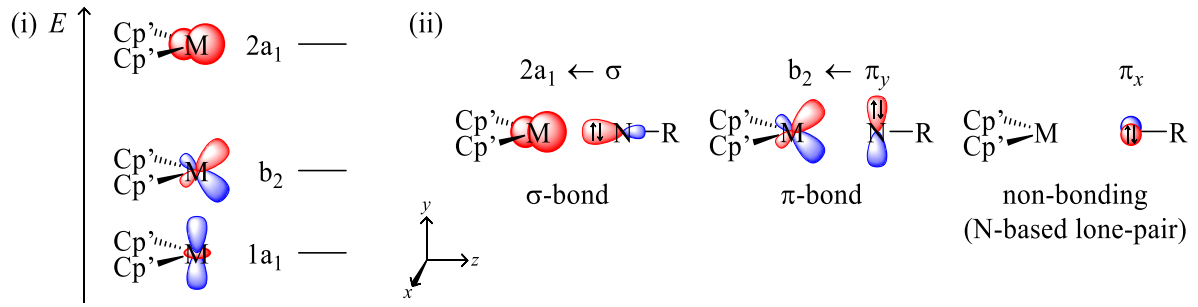

FIGURE 1.6: (i) Computed low-lying metal-based orbitals in the Cp'_2M^{n+} fragment available for bonding (for a d^0 metal).[57] (ii) Bonding interactions between Cp'_2M^{n+} and RN^{2-} accounting for the X_2 coordination mode of the imido ligand.[60]

The first monomeric zirconocene imido complex to be generated *in situ* was $Cp_2Zr(N^tBu)$ (**AE$_I$**) by Bergman and co-workers following the thermolysis of the amido derivative $Cp_2Zr(NH^tBu)R'$ {R' = NH^tBu (**AF$_I$**) or Me (**AG$_I$**-Me)}.[61] When thermolysis of **AF$_I$** or **AG$_I$**-Me was performed in THF, the monometallic imido complex **AE$_I$** was isolable as its 18-electron base-adduct $Cp_2Zr(N^tBu)(THF)$ (**AE$_I$**·THF). However, the formation of **AE$_I$** in benzene leads to the C–H activation of the solvent resulting in the amido complex $Cp_2Zr(NH^tBu)Ph$ (**AG$_I$**-Ph; SCHEME 1.15). Furthermore, in the presence of an electron-rich alkyne $R^1C{\equiv}CR^2$ (R^1 = Me or Ph and R^2 = Me or Ph), complex **AE$_I$** undergoes a [2 + 2] cycloaddition forming the azametallacyclobutene complex $Cp_2Zr\{C(R^1)=C(R^2)N(^tBu)\}$ (**AH$_I$**). This reactivity of the transient imido complex **AE$_I$** is similar to that of Wolczanski's zirconium complex $Zr(NHSi^tBu_3)_2(NSi^tBu_3)$ (**T$_I$**) described in SECTION 1.2.3 (SCHEME 1.7).[36] However, in contrast to complex **T$_I$**, the zirconocene imido complex **AE$_I$** is unable to activate the less reactive $C(sp^3)$–H bonds of alkanes such as methane.[61]

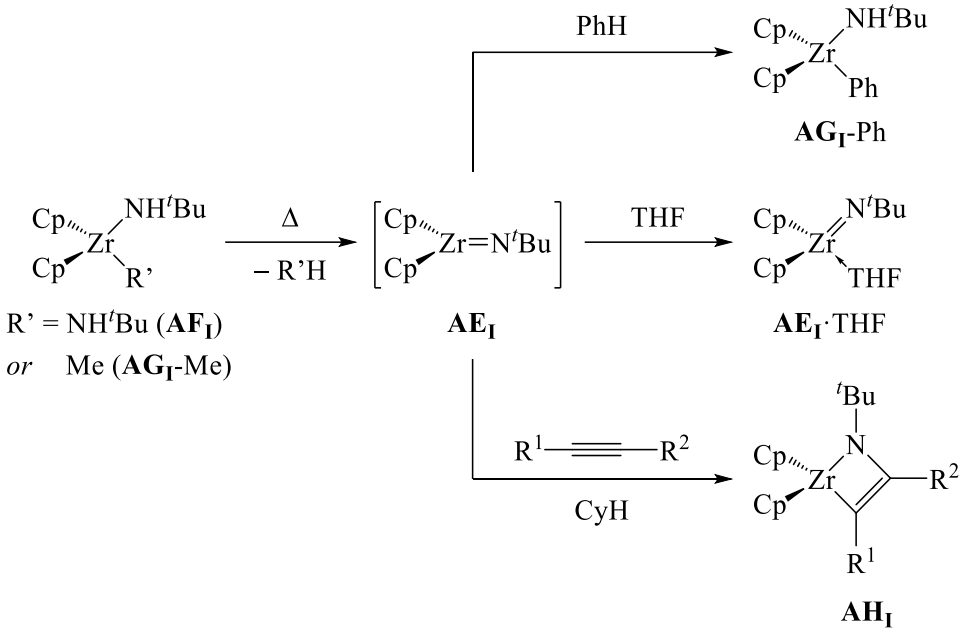

SCHEME 1.15: Thermolysis of $\mathbf{AF_I}$ or $\mathbf{AG_I}$-Me leading to the first reported transient zirconocene imido complex $\mathbf{AE_I}$, which subsequently reacts with benzene, THF and $R^1C{\equiv}CR^2$ ($R^1 = R^2$ = Me or Ph; or R^1 = Ph and R^2 = Me).[61]

While the THF molecule is irreversibly bound within Wolczanski's complex $\mathbf{T_I}$·THF (SCHEME 1.7),[36] ^{1}H NMR spectroscopic analysis of the zirconocene imido complex $\mathbf{AE_I}$·THF revealed that the THF-adduct exists in equilibrium with its base-free form $\mathbf{AE_I}$ (ΔG_{dissoc} = +25 kJ mol^{-1}).[62] As a consequence of this equilibrium, complex $\mathbf{AE_I}$·THF provides a more facile route to transient $\mathbf{AE_I}$ than the aforementioned thermolysis of $\mathbf{AF_I}$. Indeed, $\mathbf{AE_I}$·THF remains susceptible to the 1,2-addition of benzene and the [2 + 2] cycloaddition of alkynes, with the latter being possible at room temperature (SCHEME 1.16).[59] Furthermore, Bergman and co-workers revealed that $\mathbf{AE_I}$·THF could undergo reversible room-temperature [2 + 2] cycloadditions with ethene and norbornene,[59] along with the C(sp^2)–H activation of norbornene,[60,63] cyclopentene,[60,63] indene[64] and ferrocene[64] at elevated temperatures (SCHEME 1.16), further advancing the chemistry of this zirconocene imido system.

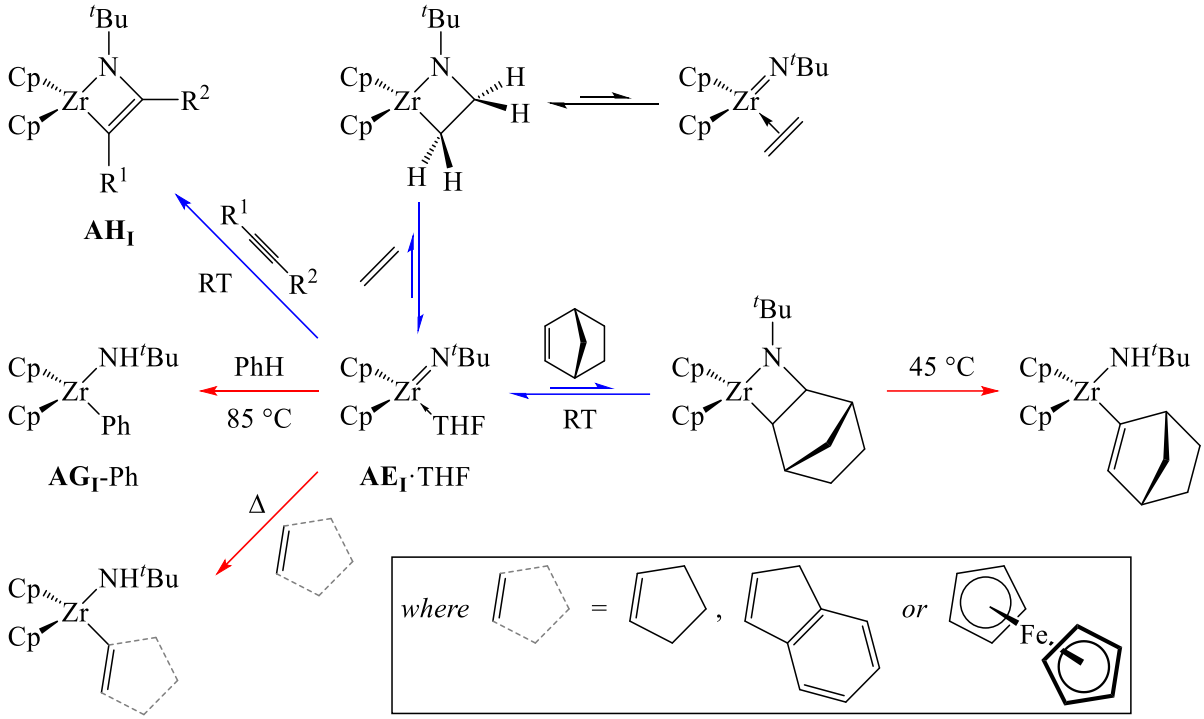

SCHEME 1.16: Reported [2 + 2] cycloaddition (blue)[59] and C–H activation (red)[63,64] reactions of $\mathbf{AE_I}$·THF with various substrates.

1.3.2. Catalytic hydroamination of alkynes by Cp'$_2$Zr(NR) complexes

By changing the imido substituent of the initial zirconocene imido system $\mathbf{AE_I}$, Bergman and co-workers found that additional reactivity could be achieved for the analogous complex featuring a 2,6-dimethylphenyl (Dmp) imido substituent, $Cp_2Zr(NDmp)$ ($\mathbf{AE_{II}}$). Similar to the *tert*-butylimido derivative, the thermolysis of $Cp_2Zr(NHDmp)_2$ ($\mathbf{AF_{II}}$) generates the transient complex $\mathbf{AE_{II}}$, which in the presence of alkyne $R^1C{\equiv}CR^2$ ($R^1 = R^2$ = Ph or Tol) undergoes a [2 + 2] cycloaddition reaction to afford the azametallacyclobutene $Cp_2Zr\{C(R^1)=C(R^2)N(Dmp)\}$ ($\mathbf{AH_{II}}$). However, the subsequent treatment of complex $\mathbf{AH_{II}}$ ($R^1 = R^2$ = Ph) with anhydrous $DmpNH_2$ affords the enamine $R^1HC=C(NHDmp)R^2$ ($\mathbf{AI_{II}}$) when the reaction was performed at 45 °C (SCHEME 1.17). If the same reaction is performed at room temperature, protonation of a C-atom on azametallacyclobutene $\mathbf{AH_{II}}$ occurs to form an isolable enamido complex $Cp_2Zr\{N(Dmp)C(R^2)=CHR^1\}(NHDmp)$ ($\mathbf{AJ_{II}}$), which subsequently undergoes α-elimination at 45 °C to produce $\mathbf{AI_{II}}$ and the transient imido complex $\mathbf{AE_{II}}$ (SCHEME 1.17; dashed route).

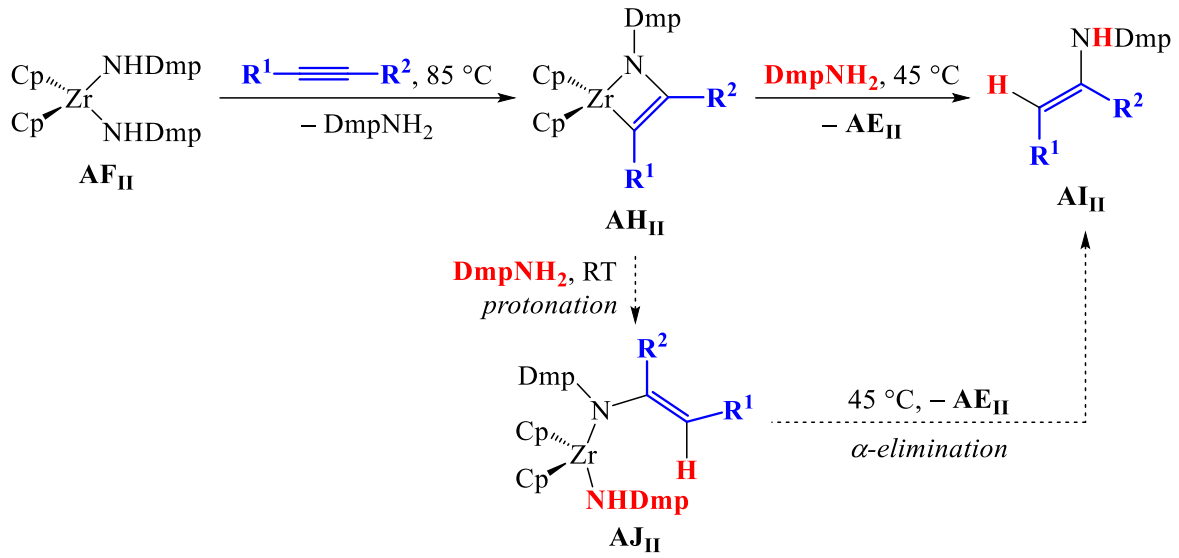

SCHEME 1.17: Formation of the azametallacyclobutene $\mathbf{AH_{II}}$ ($R^1 = R^2 = Ph$) and its subsequent reactions with $DmpNH_2$ to afford the enamine $\mathbf{AI_{II}}$.[65]

When considering the synthesis of $\mathbf{AH_{II}}$ from the transient imido complex $\mathbf{AE_{II}}$ and $R^1C{\equiv}CR^2$, the overall transformation described in SCHEME 1.17 can be regarded as a stoichiometric alkyne hydroamination reaction to afford the enamine $\mathbf{AI_{II}}$. Furthermore, with the regeneration of the imido complex $\mathbf{AE_{II}}$ in the final α-elimination step, Bergman and co-workers subsequently demonstrated the catalytic hydroamination of an alkyne (~10 equivalents) with $DmpNH_2$ at elevated temperatures, using $Cp_2Zr(NHDmp)_2$ ($\mathbf{AF_{II}}$; 3 mol%) as the pro-catalyst (SCHEME 1.18).[65,66] This catalysis was achievable for a range of symmetric ($R^1 = R^2$ = Me or Ph) and asymmetric (R^2 = Me and R^1 = Ph, ^{n}Pr or ^{i}Pr) alkynes, with reasonable regioselectivity towards $R^1HC{=}C(NHDmp)R^2$ ($\mathbf{AI_{II}}$) over its isomer $R^2HC{=}C(NHDmp)R^1$ ($\mathbf{AI_{II}'}$). The synthesis of the minor enamine product $\mathbf{AI_{II}'}$ was attributed to the reversibility of the [2 + 2] cycloaddition step (SCHEME 1.18ii) at high temperatures, which enables the formation of the less thermodynamically-stable azametallacyclobutene $Cp_2Zr\{C(R^2){=}C(R^1)N(Dmp)\}$ ($\mathbf{AH_{II}'}$). In turn, this azametallacyclobutene is more easily protonated to its enamido derivative than its isomer $\mathbf{AH_{II}}$ (SCHEME 1.18iii) due to steric factors.[66]

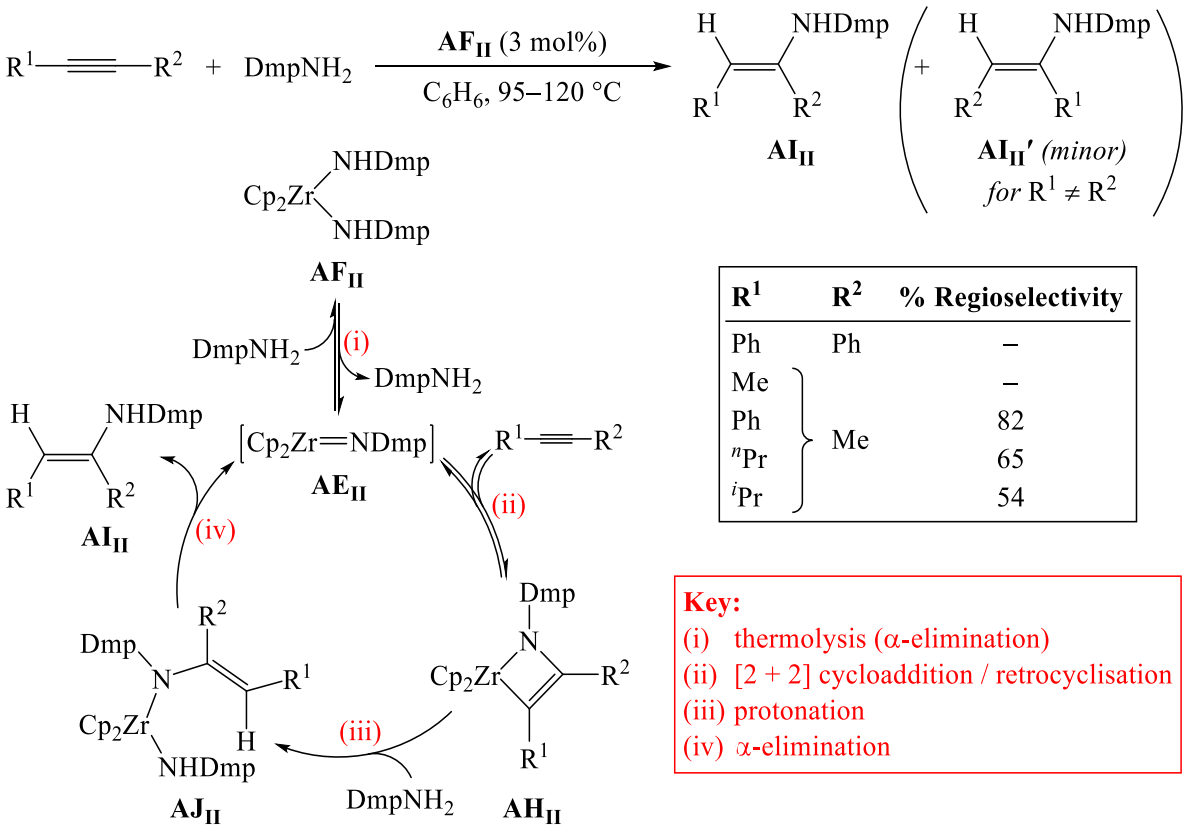

R¹	R²	% Regioselectivity
Ph	Ph	–
Me	Me	–
Ph		82
^{n}Pr		65
^{i}Pr		54

SCHEME 1.18: Overall reaction and the catalytic cycle for the hydroamination of alkynes with $DmpNH_2$ to form the enamine **AI$_{II}$** using the pro-catalyst **AF$_{II}$**.[65,66]

In addition to the extensively-explored $DmpNH_2$/**AF$_{II}$** system, the catalytic hydroamination of symmetric alkynes ($R^1 = R^2$ = Me or Ph) has also been demonstrated with $^{t}BuNH_2$ and the initial zirconocene imido complex $Cp_2Zr(N^{t}Bu)$ (**AE$_{I}$**), the latter forming transiently from the pro-catalyst $Cp_2Zr(NH^{t}Bu)_2$ (**AF$_{I}$**).[65] However, alkyne hydroamination appears to be limited to less sterically bulky $RNH_2/Cp_2Zr(NHR)_2$ systems; indeed, neither stoichiometric nor catalytic enamine synthesis was demonstrated using the $^{t}BuMe_2SiNH_2/Cp_2Zr(NHSi^{t}BuMe_2)_2$ (**AF$_{III}$**) system with its large trialkylsilyl groups.[65] While the reaction between the transient imido species $Cp_2Zr(NSi^{t}BuMe_2)$ (**AE$_{III}$**) and the alkyne $R^1C{\equiv}CR^2$ ($R^1 = R^2$ = Ph) can be demonstrated to produce the azametallacyclobutene complex $Cp_2Zr\{C(R^1)=C(R^2)N(Si^{t}BuMe_2)\}$ (**AH$_{III}$**), the subsequent approach of the amine $^{t}BuMe_2SiNH_2$ is inhibited by unfavourable steric interactions.[65]

Furthermore, the substrate scope for hydroamination to date is fairly limited for zirconocene imido systems. Despite employing temperatures of up to 160 °C, hydroamination of neither ethene, norbornene nor allylbenzene could be achieved using the $DmpNH_2$/**AF$_{II}$** system.[65] The lack of catalytic (or stoichiometric) hydroamination of C=C bonds is likely to be attributable to the instability of the azametallacyclobutane intermediates, on account of the high degree of reversibility for [2 + 2] cycloaddition reactions between alkenes and transient imido species **AE$_{II}$**.

1.3.3. C–H activation of alkanes by Cp'$_2$Zr(NR) complexes

While extensive C–H activation of arenes and alkenes has been demonstrated with the transient zirconocene imido complex $Cp_2Zr(N^tBu)$ (**AE$_I$**), alkyl–H activation is limited to the more-reactive benzylic C(sp^3)–H bonds of mesitylene.[64] By substituting the two cyclopentadienyl ligands with the tethered counterpart *rac*-1,2-ethylene-1,1'-*bis*(tetrahydroindenyl) ({Cp'$_2$}$^{2-}$), Bergman and co-workers found that the transient imido complex {Cp'$_2$}Zr(N^{t}Bu) (**AE$_{IV}$**) activated a variety of R'–H (R' = alkyl) bonds to form {Cp'$_2$}Zr(NH^{t}Bu)R' (**AG$_{IV}$**-R'; SCHEME 1.19) in excellent yields (90–98%).[67] However, C(sp^3)–H activation by **AE$_{IV}$** is limited by the steric bulk of the alkane, with activation only possible at the terminal position of an ethyl group within the alkane (highlighted in blue; SCHEME 1.19).* However, if sterically-accessible C(sp^2)–H bonds were also available within the R'H molecule, C–H activation preferentially occurred at these positions, as observed with the selective activation at the vinylic position of 1-hexene.[67]

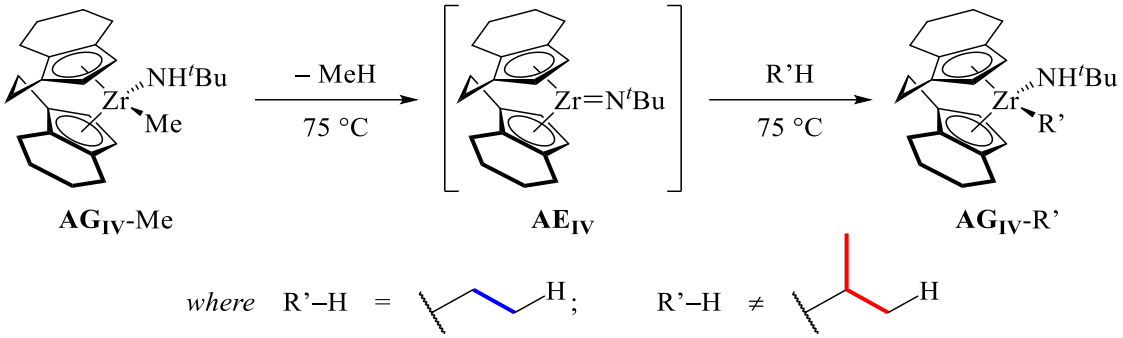

SCHEME 1.19: C–H activation of alkanes (R'H) achieved by the transient imido complex {Cp'$_2$}Zr(N^{t}Bu) (**AE$_{IV}$**); where R' = hexyl (*n*-, *iso*- or *neo*-), 3-methylpentyl or *n*-pentyl.[67]

Limited examples of C(sp^3)–H activation were later reported with the mixed zirconocene system Cp*CpZr(N^{t}Bu) (**AE$_V$**), which demonstrated reactivity with R'H (R' = ^{n}Hex, *cis*-2,3-dimethylcyclopropyl or TMS) to afford the amido complexes Cp*CpZr(NH^{t}Bu)R' (**AG$_V$**-R').[68] Since the transient imido complex **AE$_V$** was also shown to react with various sp^2- and sp-hybridised R'H substrates, through competition studies Bergman and co-workers were able to deduce a reactivity series for C–H activation. As found for Wolczanski's imido systems (SECTION 1.2.3), smaller R'–H substrates with greater s-character undergo C–H activation at a faster rate.[68] Furthermore, electron-withdrawing R'-substituents have a lower activation energy for R'–H activation, as observed from the comparison between R' = Ar^F and C_6H_3-3,5-^{i}Pr$_2$ substrates. While the s-character and electron-withdrawing ability of R' are more generally associated with a more stable carbanion R'$^-$, no correlation between the pK_a and rate of C–H activation for R'H was found; this in turn suggested a concerted 1,2-addition pathway.[42]

* C(sp^3)–H activation at the terminal positions of *iso*-propyl groups (highlighted in red; SCHEME 1.19) within 2,3-dimethylbutane and 2,4-dimethylpentane was unsuccessful and only led to the decomposition of the zirconocene imido complex **AE$_{IV}$**.[67]

Similarly to Wolczanski's Group IV imido complex Ti(NSi^{t}Bu$_3$)(OSi^{t}Bu$_3$)$_2$ (**T$_{II}$**; SCHEME 1.8), alkyl R'–H activation by transient Cp'$_2$Zr(NR) (**AE**) is proposed to occur *via* the formation of the σ-alkane complex Cp'$_2$Zr(NR)(η^2-R'H) (**AE**·R'H), followed by the concerted formation of Zr–R' and N–H bonds to produce Cp'$_2$Zr(NHR)R' (**AG**-R').[42] Therefore, as before, in order for the required orbital overlap between complex **AE** and R'H, the LUMO of the zirconocene imido complex must be localised on the metal centre as a d_{z^2} orbital, whereas the HOMO should possess significant metal–nitrogen π-bond-character (FIGURE 1.7i). Furthermore, the 1,2-addition of alkanes R'–H across M=N bonds was computed to be promoted by more electrophilic metal centres,[42] which may explain the improved reactivity of Wolczanski's more electronically unsaturated 14-electron complex **T$_{II}$** (SECTION 1.2.3) than Bergman's 16-electron complexes Cp'$_2$Zr(NR).

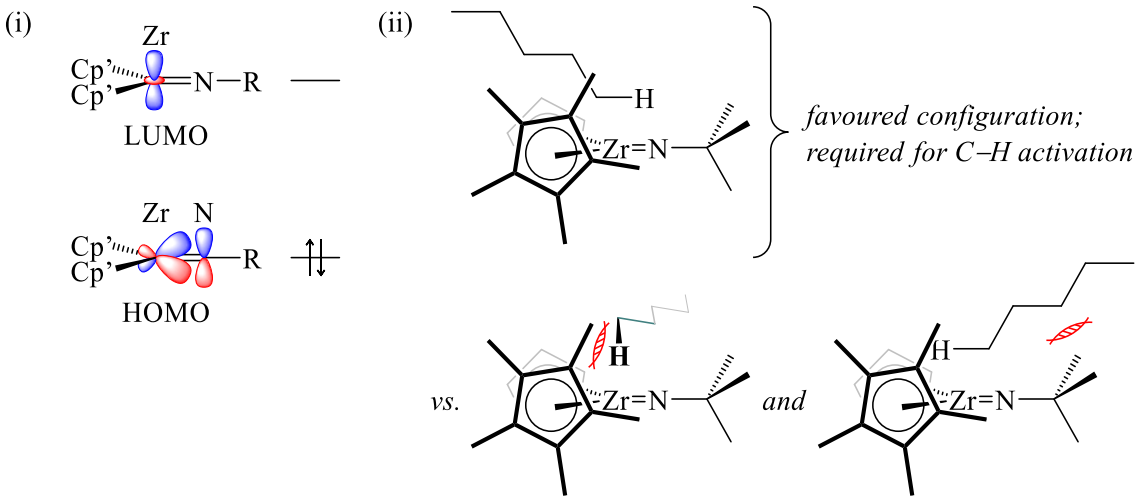

FIGURE 1.7: (i) FMOs of the transient 16-electron zirconocene imido complex Cp'$_2$Zr(NR) (**AE**) required for the 1,2-addition of alkanes. (ii) Steric interactions between Cp*CpZr(N^{t}Bu) (**AE$_V$**) and *n*-pentane leading to C–H activation.[42]

It is notable, however, that electronic effects do not completely explain the difference in the ability of the three zirconocene *tert*-butylimido complexes (*i.e.* **AE$_I$**, **AE$_{IV}$** and **AE$_V$**) to activate C(sp^3)–H bonds. Although the metal centre in the *bis*(cyclopentadienyl) complex **AE$_I$** is more electrophilic than its tethered and mixed zirconocene counterparts (**AE$_{IV}$** and **AE$_V$**, respectively),* it is the only complex of the three not to react with alkanes. Thus, the enhanced reactivity of complexes **AE$_{IV}$** and **AE$_V$** towards 1,2-addition of alkanes likely arises from the increased steric bulk of the Cp'-ligands, which orients the R'–H bond to be parallel to the Zr=N bond (FIGURE 1.7ii) and leads to a lower activation energy for C(sp^3)–H activation.[42]

Although C–H activation has been achieved for limited alkane (R'H) substrates using transient zirconocene imido complexes Cp'$_2$Zr(NR) (**AE**), the subsequent reactivity of the produced alkyl amido complex Cp'$_2$Zr(NHR)R' (**AG**-R') has yet to be explored. Wolczanski notes that following the C(sp^3)–H activation of an alkane, the migratory insertion chemistry of the resulting alkyl ligand may be

* The Cp-ligand is considered a weaker σ-donor than its alkylated counterparts Cp* and the tethered *bis*(tetrahydroindenyl) {Cp'$_2$}.

exploited to result in terminal functionalisation of the original alkane.[69] However, a suitable system was not identified.[42] For example, addition of carbon monoxide to the alkyl complex **AG**-R' may result in overall alkane carbonylation, with the production of commodity aldehyde R'C(O)H and regeneration of the imido complex **AE**, hence giving rise to a catalytic cycle (SCHEME 1.20). To date, alkane carbonylation has only been demonstrated with late transition metal complexes under irradiation[70] or in the presence of dihydrogen,[71] so the direct synthesis of aldehydes R'C(O)H from R'H and CO under ambient conditions is highly desirable.

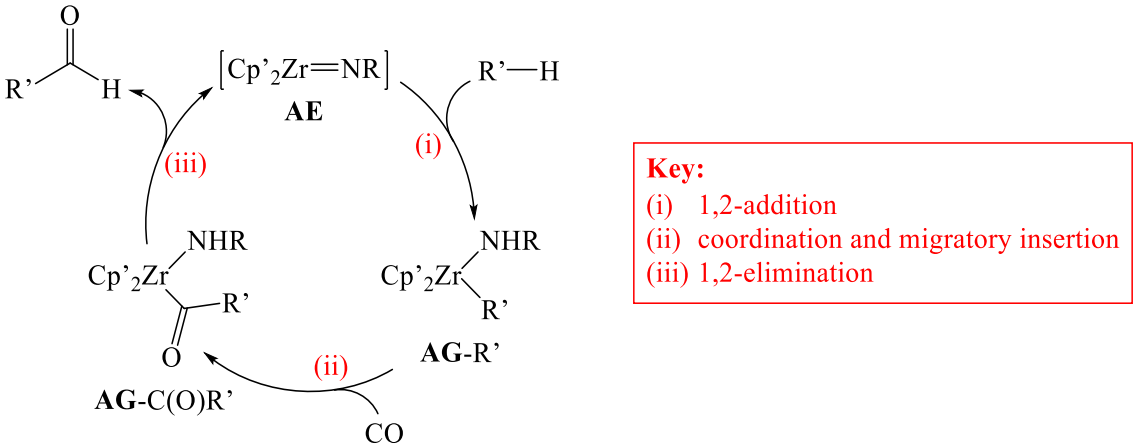

SCHEME 1.20: Potential alkane carbonylation reaction, catalysed by the general transient zirconocene imido complex **AE**.

1.3.4. The reactivity of Group V metallocenium imido cations, $[Cp'_2M(NR)]^+$

As an increase in electrophilicity at the metal centre of the zirconocene imido complexes $Cp'_2Zr(NR)$ (**AE**) was calculated to promote C(sp^3)–H activation over the metal–nitrogen multiple-bond (SECTION 1.3.3),[42] it might be expected that the cationic Group V metallocenium analogues, $[Cp'_2M(NR)]^+$ (**AK**$^+$), are more reactive than their neutral Group IV counterparts. This reactivity was first explored in the tantallocenium derivative $[Cp^*_2Ta(N^tBu)]^+$ (**AK$_I^+$**), which was generated *in situ* following hydride abstraction from $Cp^*_2TaH(N^tBu)$ (**AK$_I$**-H) and isolated as the 18-electron THF-adduct $[Cp^*_2Ta(N^tBu)(THF)]BPh^F_4$ ([**AK$_I$**·THF]BPh^F_4) in 82% yield (SCHEME 1.21).[72] The ability of [**AK$_I$**·THF]$^+$ to undergo 1,2-additions across the Ta=N bond was demonstrated by its reactions with H_2 and terminal alkynes (propyne and phenylacetylene) forming $[Cp^*_2Ta(NH^tBu)R']^+$ ([**AL**-R']$^+$; R' = H, C≡CMe or C≡CPh) in good yields (up to 88%).

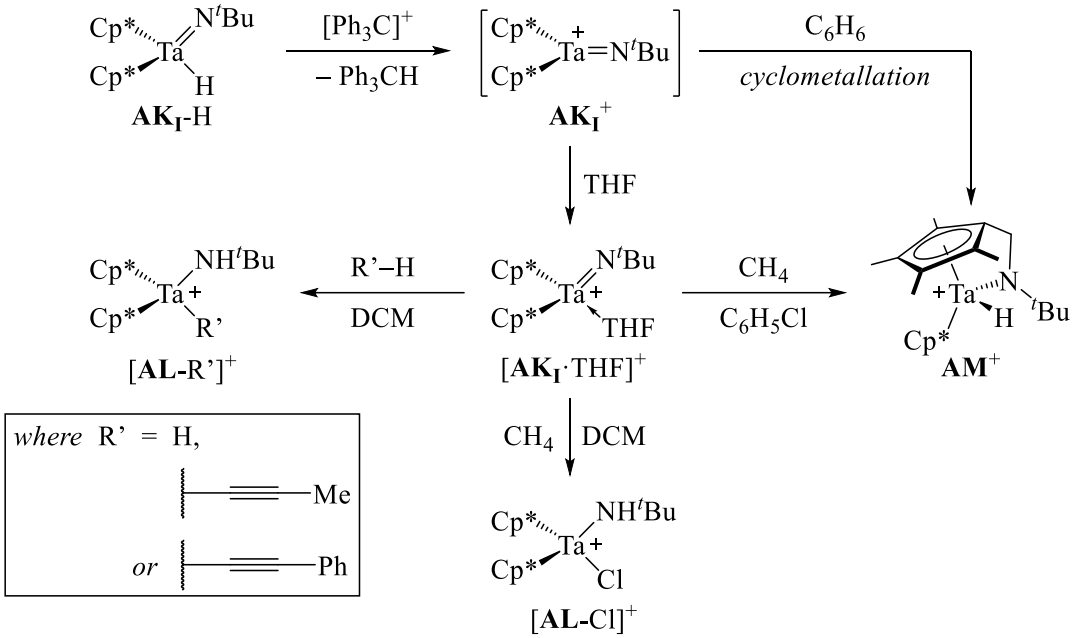

SCHEME 1.21: Synthesis and subsequent 1,2-addition reactions of the tantallocenium imido cationic complex [$\mathbf{AK_I}$·THF]BPh^F_4; $[BPh^F_4]^-$ counteranions are omitted for clarity.[72]

The C(sp^3)–H activation of methane by [$\mathbf{AK_I}$·THF]$^+$ was unsuccessful, however. When the reaction with methane was attempted in DCM, the tantallocenium imido cation [$\mathbf{AK_I}$·THF]$^+$ reacted with the solvent to afford [Cp*$_2$TaCl(NH^{t}Bu)]$^+$ ([**AL**-Cl]$^+$; SCHEME 1.21). In chlorobenzene, on the other hand, [$\mathbf{AK_I}$·THF]$^+$ underwent intramolecular C–H activation with a methyl group on a Cp*-ligand to result in the cyclometallated complex [Cp*Ta{η^5-C$_5$Me$_4$CH$_2$N(^{t}Bu)}H]BPh^F_4 ([**AM**]BPh^F_4), as confirmed by X-ray crystallographic analysis. Notably, transient generation of the imido complex $\mathbf{AK_I}^+$ in benzene also resulted in the metallocycle [**AM**]BPh^F_4, rather than the C(sp^2)–H activation of Ph–H typically observed with its neutral Cp'$_2$Zr(NR) analogues $\mathbf{AE_{I–V}}$.[61,65,67,68] This preference for intramolecular C–H activation may explain the reduced reactivity of the tantallocenium imido cation $\mathbf{AK_I}^+$ towards intermolecular 1,2-addition reactions compared to its neutral Group IV counterparts.

If unsubstituted cyclopentadienyl ligands are used within Group V metallocenium imido complexes [Cp'$_2$M(NR)]$^+$ (*i.e.* Cp' = Cp), the competing cyclometallation should be avoided and hence such complexes may be reactive towards intermolecular C(sp^2)–H and C(sp^3)–H activation. Thus, it may be anticipated that this enhanced reactivity might be exhibited by the Cp-derived niobocenium imido complex [Cp$_2$Nb(N^{t}Bu)(XC$_6$D$_5$)]$^+$ ([$\mathbf{AK_{II}}$·XC$_6$D$_5$]$^+$; X = Cl or Br) generated *in situ* by Humphries *et al.* following the methyl abstraction from Cp$_2$NbMe(N^{t}Bu) ($\mathbf{AK_{II}}$-Me; SCHEME 1.22).[73] However, only the [2 + 2] cycloaddition reactions with alkenes were attempted by this group, with monitoring of the reaction between [$\mathbf{AK_{II}}$·XC$_6$D$_5$]$^+$ and ethene (1 atm) performed by ^{1}H NMR spectroscopy. This led to the identification of a new species formed in equilibrium with [$\mathbf{AK_{II}}$·XC$_6$D$_5$]$^+$ and ethene, although the δ_H and $^1J_{C–H}$ values (4.10 ppm and 167 Hz, respectively) of the new CH_2 signals were consistent with

the formation of the η^2-alkene complex $[Cp_2Nb(N^tBu)(\eta^2\text{-}C_2H_4)]^+$ ($[\mathbf{AK_{II}}\cdot C_2H_4]^+$) rather than the [2 + 2] cycloaddition product $[Cp_2Nb\{CH_2CH_2N(^tBu)\}]^+$ ($\mathbf{AN}^+$; SCHEME 1.22).*

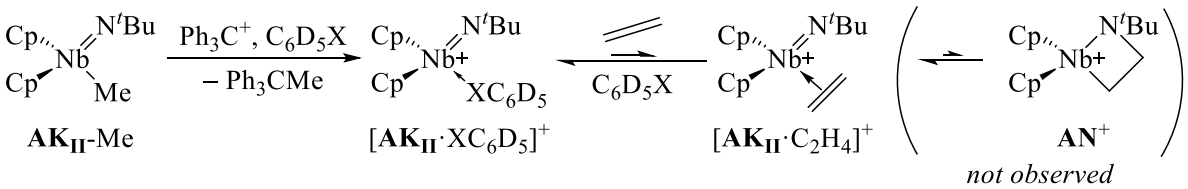

SCHEME 1.22: Synthesis of niobocenium imido complex $[\mathbf{AK_{II}}\cdot XC_6D_5]BPh^F_4$ (X = Br or Cl) and its reaction with ethene; $[BPh^F_4]^-$ counteranions are omitted for clarity.[73]

The inability of the transient cation $[Cp_2Nb(N^tBu)]^+$ ($\mathbf{AK_{II}}^+$) to react with ethene to form azametallacyclobutane $\mathbf{AN}^+$ differs markedly from the reactivity of its neutral, isoelectronic analogue $Cp_2Zr(N^tBu)$ ($\mathbf{AE_I}$; SCHEME 1.16).[59] This may suggest that while a more electrophilic metal centre may promote C–H activation of alkanes, [2 + 2] cycloaddition of unsaturated species across metal–nitrogen double-bonds may, in fact, be inhibited. However, only limited reactivity of the transient imido complex $\mathbf{AK_{II}}^+$ has been explored to date, so suitable π-systems for [2 + 2] cycloaddition (and R'–H substrates for 1,2-addition) across the Nb=N bond of the niobocenium imido complex may yet still be identified.

* The δ_H and $^1J_{C–H}$ values of $[\mathbf{AK_{II}}\cdot C_2H_4]^+$ (corresponding to the CH_2 groups) were similar to those reported for unbound ethene in the same sample (5.23 ppm and 160 Hz, respectively).[73] Typically, the corresponding values of azametallacyclobutanes are smaller (δ_H = 3.08–3.22 ppm and $^1J_{C–H}$ = 147–152 Hz)[35,37] due to a decrease in s-character compared to the free alkene (sp^3 *vs.* sp^2).

1.4. Reactivity of reduced zirconocene(II) systems and their relationship to niobium(III) half-sandwich imido complexes

While transient zirconocene imido complexes Cp'$_2$Zr(NR) have demonstrated reactivity in the hydroamination of alkynes and alkane C–H activation (SECTION 1.3), elsewhere, the reactivity of the imido-free zirconocene(II) fragment Cp'$_2$Zr (**AO**) has also been of interest with regards to dinitrogen fixation. Industrially, the reduction of dinitrogen to ammonia is achieved using the Haber–Bosch process (SCHEME 1.23),[74] however the high operating temperatures and pressures required by this heterogeneous system makes finding a homogeneous catalytic process highly desirable.

$$N_2 + 3\,H_2 \xrightleftharpoons[100\text{–}300\ \text{atm},\ 400\text{–}550\ ^\circ\text{C}]{\text{Fe catalyst/alkali metal}} 2\,NH_3$$

SCHEME 1.23: Industrial synthesis of ammonia using the Haber–Bosch process.[74]

1.4.1. Dinitrogen fixation by reduced zirconocene systems

Around half a century ago, Manriquez and Bercaw explored the reactivity of the chemistry of the transient Cp*$_2$Zr (**AO$_I$**) species, formed from the sodium amalgam reduction of its dichloride complex Cp*$_2$ZrCl$_2$ (**AO$_I$**-Cl$_2$). Under an atmosphere of N_2, reduction of **AO$_I$**-Cl$_2$ afforded the end-on bridging dinitrogen complex {Cp*$_2$Zr(η^1-N$_2$)}$_2$(μ,η^1,η^1-N$_2$) (**AP**; SCHEME 1.24),[75] which was confirmed as the first zirconocene dinitrogen complex reported in the literature following the crystallographic determination of its structure.[76] However, the coordinated dinitrogen within complex **AP** is not significantly activated, as the subsequent hydrogenation of the complex simply affords three equivalents of N_2 along with zirconocene(IV) dihydride Cp*$_2$ZrH$_2$ (**AO$_I$**-H$_2$; SCHEME 1.24) following the oxidative addition of H_2.[77,78]

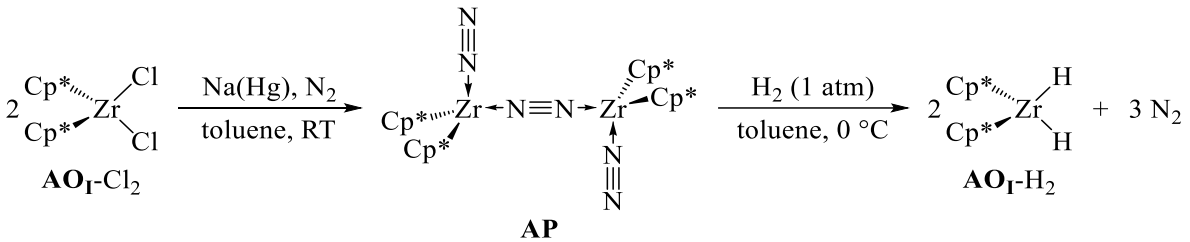

SCHEME 1.24: Reduction of **AO$_I$**-Cl$_2$ to produce the first zirconocene(II) dinitrogen complex **AP**,[75] which is hydrogenated to zirconocene(IV) dihydride complex **AO$_I$**-H$_2$.[77,78]

Compared to the end-on bridging ligation, dinitrogen adopting a side-on bridging coordination mode is generally considered to result in a more activated N_2 moiety, due to greater orbital overlap between the metal d-orbitals and $\pi_{N–N}$ and $\pi^*_{N–N}$ MOs.[79] By reducing the steric bulk of the cyclopentadienyl ligands, Chirik and co-workers were able to achieve this side-on bridging coordination of dinitrogen for the

tetramethylcyclopentadienyl ($Cp^{\dagger}$) derivative of the zirconocene system $\mathbf{AO_I}$.[80] The dinitrogen complex $\{Cp^{\dagger}_2Zr\}_2(\mu,\eta^2,\eta^2\text{-}N_2)$ (**AQ**) is produced following the sodium amalgam reduction of $Cp^{\dagger}_2ZrCl_2$ ($\mathbf{AO_{II}}\text{-}Cl_2$; SCHEME 1.25), where X-ray crystallographic analysis verified the end-on bridging mode of the ligand. Unlike complex **AP**, the μ,η^2,η^2-dinitrogen complex **AQ** was found to react with dihydrogen to produce the bridging diazene complex $\{Cp^{\dagger}_2ZrH\}_2(\mu,\eta^2,\eta^2\text{-}N_2H_2)$ (**AR**), which similarly was confirmed crystallographically. Furthermore, at elevated temperatures further hydrogenation of complex **AR** occurred, resulting in the formation of ammonia alongside the dihydride complex $Cp^{\dagger}_2ZrH_2$ ($\mathbf{AO_{II}}\text{-}H_2$; SCHEME 1.25), albeit in poor yields (10–15%).

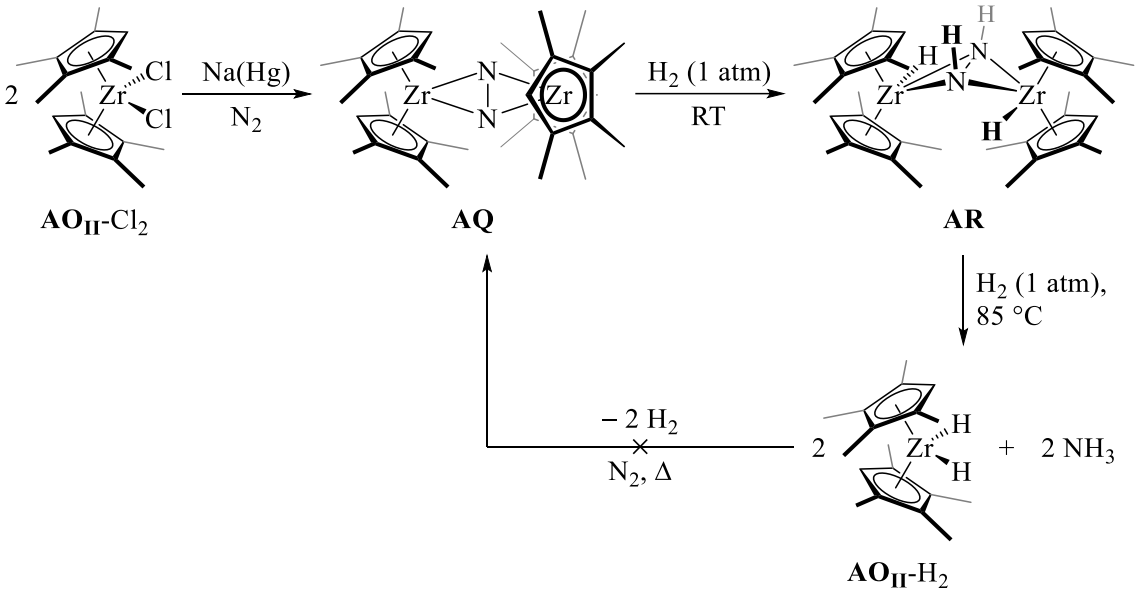

SCHEME 1.25: Reduction of $\mathbf{AO_{II}}\text{-}Cl_2$ to the μ,η^2,η^2-dinitrogen complex **AQ**, which is sequentially hydrogenated to the diazene complex **AR** and the dihydride complex $\mathbf{AO_{II}}\text{-}H_2$.[80]

While Chirik and co-workers demonstrated the stoichiometric synthesis of ammonia from complex $\mathbf{AO_{II}}\text{-}Cl_2$, unfortunately this zirconocene system was not found to be suitable for the catalytic reduction of dinitrogen. This is due to the fact that once dihydride complex $\mathbf{AO_{II}}\text{-}H_2$ formed, the dinitrogen complex **AQ** (or any other intermediate) could not be regenerated *via* the reductive elimination of H_2, even at elevated temperatures (SCHEME 1.25).[80] This may be attributable to the thermodynamic instability of the proposed transient reductive elimination product, $Cp^{\dagger}_2Zr$ ($\mathbf{AO_{II}}$), which is electronically unsaturated as a 14-electron complex. Indeed, zirconocene(II) derivatives have never been isolated without the presence of a good σ-donor or π-acceptor such as trimethylphosphine.[81]

Concurrent to their investigation of the $Cp^{\dagger}_2Zr$ system, Chirik and co-workers found that indenyl (Ind) derivatives of cyclopentadienyl ligands are more capable of stabilising the electronically unsaturated zirconium(II) centres.[82] As confirmed crystallographically, the group found that indenyl ligands are able to adopt an unusual η^9-coordination mode in the *bis*(indenyl)zirconium(II) complexes (η^5-Ind')(η^9-Ind')Zr ($\mathbf{AO_{III}}$; Ind' = C_9H_5-1-R^1-3-R^2, where R^1 and R^2 are alkyl or trialkylsilyl groups), leading to the stabilisation of electronically saturated 18-electron complexes.[83] However, these

bis(indenyl) complexes were too stable to react with dinitrogen, so Chirik and co-workers attempted the synthesis of the mixed zirconocene complex Cp*(η^9-Ind')Zr (**AO$_{IV}$**; Ind' = C_9H_5-1-R-3-R'; where either R = R' = Me, ^{i}Pr or TMS; or R' = Me and R = ^{i}Pr or ^{t}Bu), with the presence of only one indenyl ligand envisaged to lead to a compromise on stability.[84]

The sodium amalgam reduction of Cp*(η^5-Ind')ZrCl_2 (**AO$_{IV}$**-Cl_2) under an atmosphere of argon was found to produce the desired 18-electron complexes **AO$_{IV}$** in up to 99% yield (SCHEME 1.26), where the η^9-hapticity of the Ind'-ligand was confirmed crystallographically (for R = R' = ^{i}Pr).[84] Furthermore, for R' = Me, **AO$_{IV}$** forms the end-on bridging dinitrogen complexes {Cp*(μ,η^5,η^2-Ind')Zr}$_2$(μ,η^1,η^1-N_2) (**AS**; Ind' = C_9H_5-1-R-3-Me and R = Me, ^{i}Pr or ^{t}Bu) on exposure to an atmosphere of N_2 (SCHEME 1.26), where the indenyl ligands adopt an unusual η^5,η^2-bridging mode. Crystallographic characterisation of the dinitrogen complex **AS** (for R = ^{i}Pr) found that the short Zr–C and long C–C bond lengths of the η^2-coordinated indenyl ligand were consistent with the formation of metallacyclopropyl moieties within the complex. This in turn indicated that the zirconium(II) centres had reduced the η^2-alkene moiety (*i.e.* L → X_2) instead of the desired bridging dinitrogen ligand, leading to no significant activation (or lengthening) of the N≡N triple-bond. Consequently, the hydrogenation of **AS** has not been reported by Chirik and co-workers and therefore catalytic ammonia synthesis has not yet been attained using a Cp'$_2$Zr-derived system.

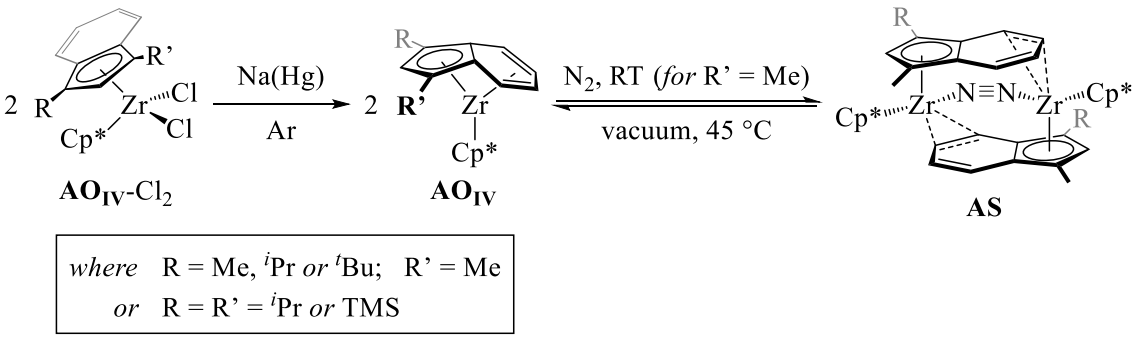

SCHEME 1.26: Reduction of the dichloride complex **AO$_{IV}$**-Cl_2 to the η^9-indenyl complex **AO$_{IV}$**, which reacts with N_2 to form the μ,η^1,η^1-dinitrogen complex **AS**.[84]

Potentially, the undesirable η^5,η^2-bridging mode of the indenyl ligand in dinitrogen mono(indenyl) complexes may be preventable by increasing the steric bulk of the mixed zirconocene system, which, in turn, could lead to an increased activation of the N_2-ligand. However, as for cyclopentadienyl ligands, the modification of the substituent groups on indenyl ligands provides a synthetic challenge.[85] Consequently, it is highly desirable to find an alternative ligand to Cp' and Ind' that can be modified more easily (both sterically and electronically), and yet still retains the fundamental coordinative features of cyclopentadienyl ligands and their derivatives.

1.4.2. The *pseudo*-isolobal relationship between zirconocene and niobium half-sandwich imido complexes

While the imido moiety may appear structurally rather different to the cyclopentadienyl ligand, in the early 1990s it was noted that the two ligands are electronically quite similar to each other.[86] As shown in FIGURE 1.8, both Cp^- and RN^{2-} ligands possess three filled FMOs available for coordination to a metal centre, namely one σ-orbital and two degenerate π-orbitals, which are of similar symmetry and energy between the two ligands.[13,87] While cyclopentadienyl ligands also possess two antibonding δ*-orbitals capable of accepting electron density from metal centres, these high-energy MOs can largely be ignored for early transition metal complexes with low d^n-configurations, where metal–cyclopentadienyl π-backdonation is usually minimal.[88]

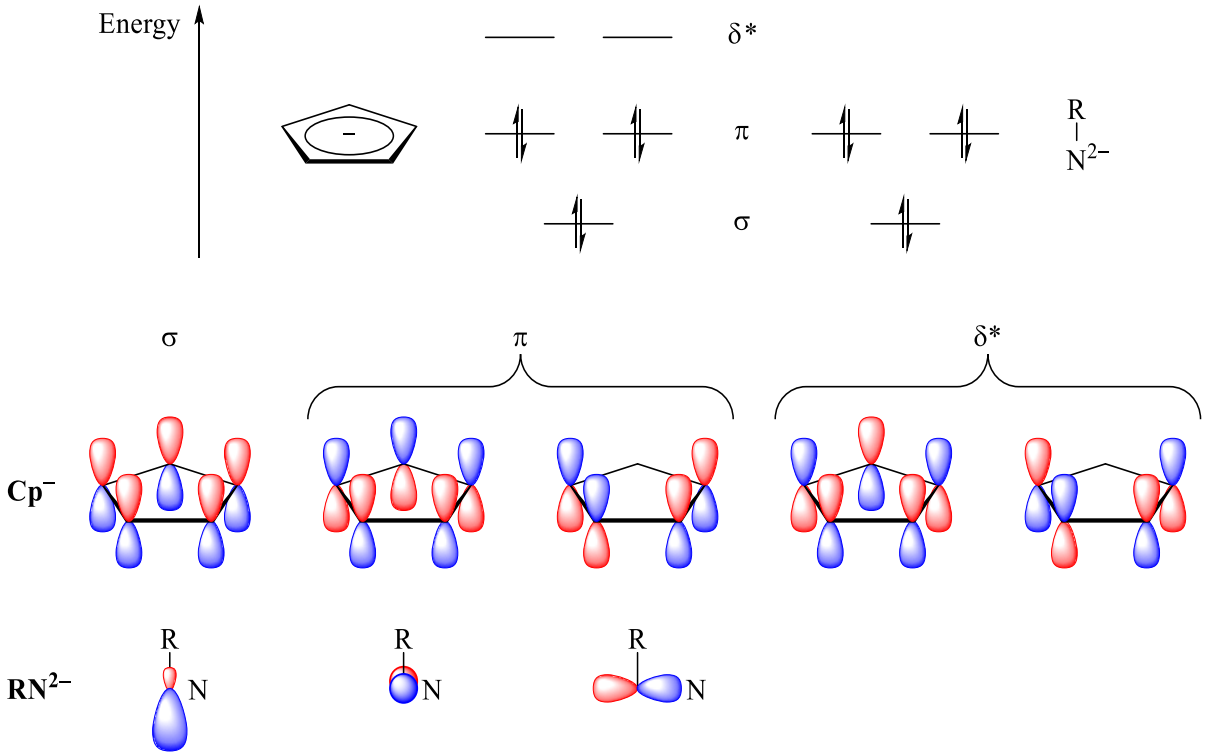

FIGURE 1.8: The electronic similarities between the FMOs of cyclopentadienyl (Cp^-) and imido (RN^{2-}) ligands.[13,88]

As a consequence of their similar FMOs, Cp^- and LX_2-bound RN^{2-} ligands may be considered *pseudo*-isolobal to each other, since both adopt a 1σ,2π-coordination mode. Therefore, accounting for the different charges of the two ligands, Gibson and co-workers extended the analogy to propose that Group V half-sandwich imido complexes "Cp'M^V(NR)" may be considered *pseudo*-isolobal to Group IV metallocene (sandwich) complexes (SCHEME 1.27i).[89] This was confirmed by computational analysis of the $[CpNb(NR)]^{2+}$ fragment,[89] with the FMOs of the fragment computed to be very similar to those of the Group IV metallocene moiety $[Cp_2M]^{2+}$ (see FIGURE 1.6i).[57] Furthermore, the similar reactivities of zirconocene and niobium half-sandwich imido complexes, with regard to diphenylation and

subsequent formation of η^2-benzyne complexes (SCHEME 1.27ii),[90–92] helped to validate the *pseudo*-isolobal relationship between the two systems.

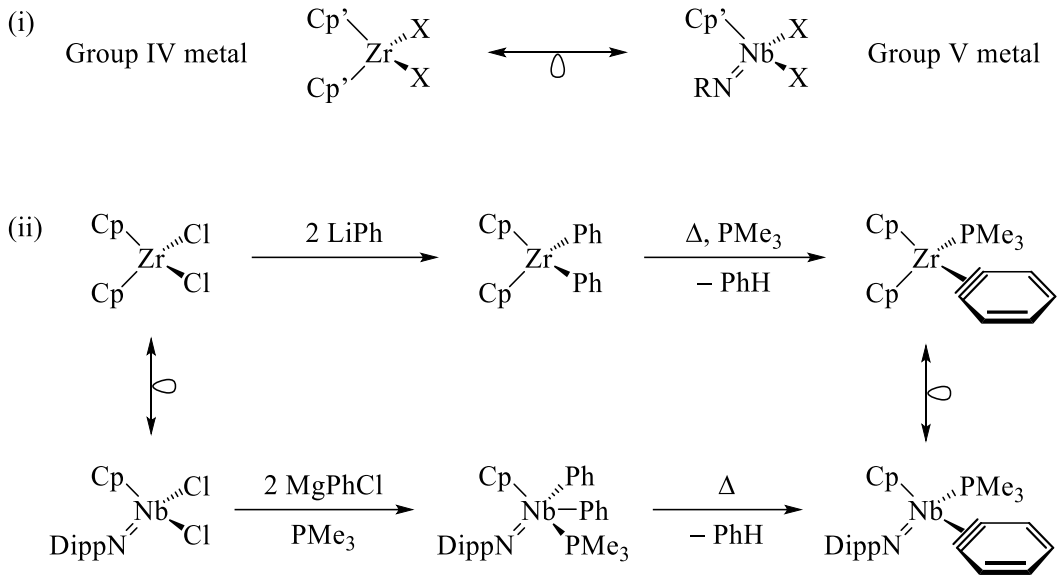

SCHEME 1.27: (i) The proposed *pseudo*-isolobal analogy between Group IV metallocene and Group V half-sandwich imido complexes.[89] (ii) Example of the similar reactivities reported for zirconocene and niobium half-sandwich imido complexes.[90–92]

As a consequence of the *pseudo*-isolobal analogy, it might be anticipated that niobium half-sandwich imido systems may also be capable of the dinitrogen fixation chemistry as demonstrated by the zirconocene system $\mathbf{AO_{II}}$ of Chirik and co-workers (SECTION 1.4.1).[80] Due to issues regenerating the dinitrogen complex **AQ** by the reductive elimination of H_2 from dihydride $\mathbf{AO_{II}}$-H_2, this zirconocene system was unable to catalytically synthesise ammonia. In contrast to zirconocene systems, the steric and electronic properties of "Cp'Nb(NR)" are more easily varied due to the wealth of commercially-available primary amine (RNH_2) precursors to imido ligands. Therefore, through tuning of the imido ligand, it may be possible to develop a niobium half-sandwich imido system capable of catalysing dinitrogen fixation (SCHEME 1.28).

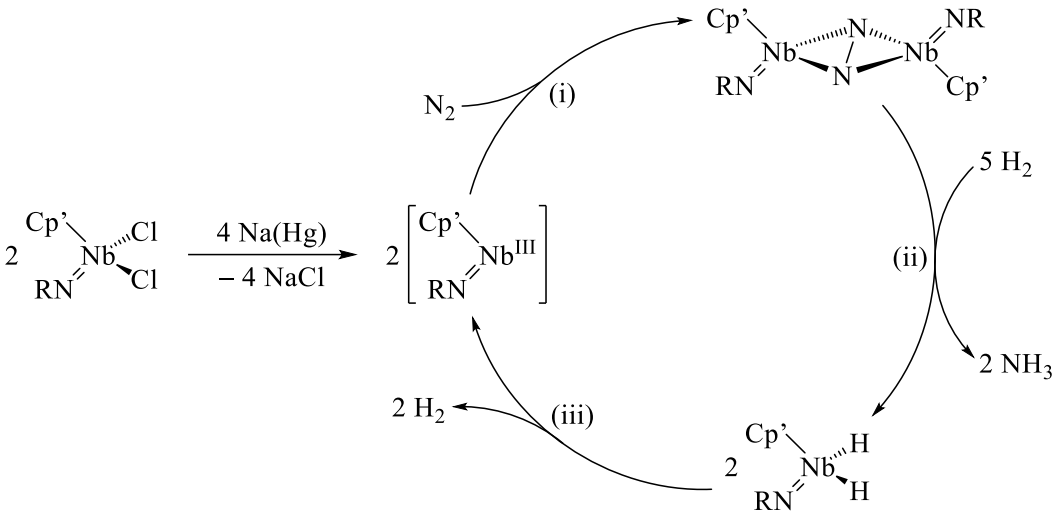

SCHEME 1.28: Proposed reduction of the pro-catalyst Cp'$NbCl_2$(NR) and the catalytic synthesis of ammonia, *via* the (i) coordination of dinitrogen, (ii) hydrogenation, and (iii) reductive elimination of dihydrogen.

Furthermore, the alternative reaction pathways available to imido ligands may provide alternative routes to the hydrogenation step in the proposed catalytic cycle (SCHEME 1.28ii). In addition to the aforementioned reactivity of imido ligands towards 1,2-addition of H_2 across the M=N bond (SECTION 1.2.3), RN^{2-} ligands may be able to act as an H-atom reservoir through the 1,2-hydride shifting between the metal centre and the heteroatom. This reactivity is exemplified in the interconversion between the rhenium(VII) complex $ReH(NDipp)_3$ (**AT**) and the rhenium(V) complex $Re(NDipp)_2(NHDipp)$ (**AU**), where the latter is trappable as $Re(NDipp)_2(NHDipp)L$ (**AU**·L) in the presence of a π-acceptor (L = alkynes, alkenes, aldehydes or phosphines; SCHEME 1.29).[86,93] In turn, these two reactivities affording amido (RHN^-) ligands may in turn facilitate the synthesis of ammonia at lower temperatures compared to the zirconocene systems of Chirik, especially if the subsequent transfer of the amido H-atom to the coordinated dinitrogen ligand can be achieved.

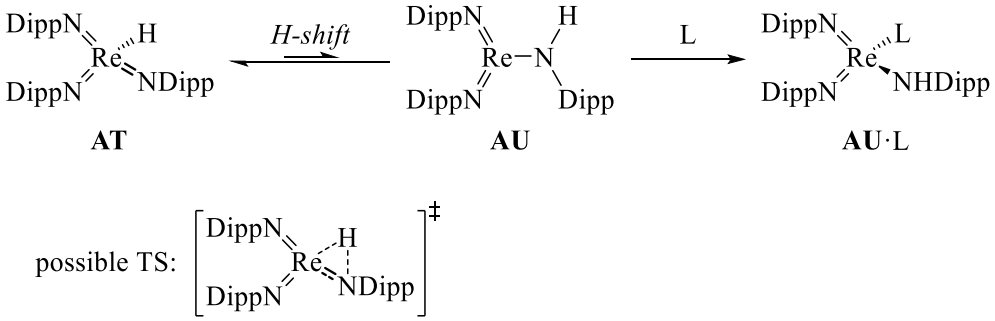

SCHEME 1.29: Metal–nitrogen hydride-shift between the hydride complex **AT** and the amido complex **AU**, where the latter is trappable by the coordination of a π-accepting ligand (L = C_2H_2, C_2Me_2, C_2H_4, norbornene, O=CH^{t}Bu or PMe_3).[86,93]

1.5. Thesis aims

With the envisaged catalytic applications outlined in SECTIONS 1.3.4 & 1.4.2, this thesis will aim to explore the reactivities of the niobium cyclopentadienyl imido species $Cp'Nb^{III}(NR)$ and $[Cp'_2Nb^{V}(NR)]^+$ generated *in situ* from their niobium(V) chloride precursors. For these coordinatively and electronically unsaturated reactive complexes, it is imperative that bridging of the imido ligand does not compete with the coordination of small molecules. Therefore, the 2,6-di-*iso*-propylphenyl (Dipp) imido derivative will be the focus of this work, since only two niobium complexes featuring μ-NDipp are known, namely $\{CpNb(\mu\text{-NDipp})X\}_2$ (X = Me or κ^2-BH_4).[94,95] Additionally, this imido substituent has a distinctive ^{1}H NMR spectroscopic signature, thus facilitating the monitoring of these new reactions involving the $DippN^{2-}$ ligand. Furthermore, the work here will endeavour to manipulate the electron-density about this arylimido ligand within the electronically saturated system $Cp_2NbCl(NDipp)$, with the aim of discovering new reactivities for d^0 transition metal imido complexes.

CHAPTER 2:

Synthesis and reduction of niobium cyclopentadienyl arylimido ($DippN^{2-}$) complexes

2.1. Chapter introduction

As outlined in SECTION 1.4.2, it is of interest to explore the reduction chemistry of niobium half-sandwich imido systems, $Cp'NbCl_2(NR)$, to investigate whether *pseudo*-isolobal analogues of Chirik's dinitrogen complex $\{Cp^{\dagger}{}_2Zr\}_2(\mu,\eta^2,\eta^2\text{-}N_2)$ (**AQ**; $Cp^{\dagger} = C_5HMe_4$)[80] can be generated. To prevent the undesirable bridging of the imido ligand in the reduced niobium(III) half-sandwich imido complexes (SECTION 1.5), 2,6-di-*iso*-propylphenylimido ($DippN^{2-}$) derivatives will be the focus of this work.

Various aspects of the chemistry of $Cp'NbCl_2(NDipp)$ complexes have been described to date, with several cyclopentadienyl variants, namely Cp' = Cp, Cp* and C_5H_4TMS (Cp^{TMS}), having been reported in the literature.[89,96] As with many other alkyl[89,97–99] and aryl[89,100,101] imido derivatives, $Cp'NbCl_2(NDipp)$ can be synthesised by the sequential addition of the cyclopentadienyl and imido ligands to $NbCl_5$ (SCHEME 2.1; red route). However, this route to $Cp'NbCl_2(NDipp)$ has several problems associated with it. Firstly, the cyclopentadienyl intermediate $Cp'NbCl_4$ formed in the first step is poorly soluble like its $NbCl_5$ precursor, making its purification and isolation challenging. Additionally, the subsequent reaction of $Cp'NbCl_4$ with DippNH(TMS) is problematic as the silylamine is usually a non-volatile, viscous oil, making its removal non-trivial following the reaction.

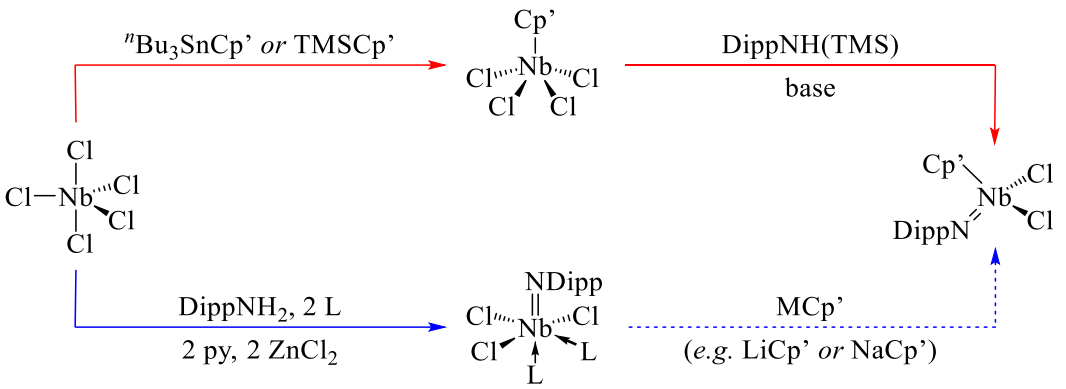

SCHEME 2.1: Two routes to $Cp'NbCl_2(NDipp)$ from $NbCl_5$, *via* either $Cp'NbCl_4$ (red route)[89,96] or $NbCl_3(NDipp)L_2$ (blue route).[102] The dashed arrow denotes a proposed, but unreported, synthetic step.

An alternative route for the synthesis of $Cp'NbCl_2(NDipp)$ would be to incorporate the imido moiety prior to the cyclopentadienyl ligand (SCHEME 2.1; blue route), *i.e.* first preparing $NbCl_3(NDipp)L_2$.[102] Indeed, several niobium half-sandwich imido complexes have been synthesised according to this strategy, including $CpNbCl_2(N^tBu)$, $Cp^{TMS}NbCl_2(N^tBu)$ and $CpNbCl_2(NTol)$ (Tol = *p*-tolyl), in high overall yields (of up to 84%).[103] Establishing a route to $Cp'NbCl_2(NDipp)$ *via* $NbCl_3(NDipp)L_2$ would be advantageous over the established syntheses as this complex is soluble (unlike $Cp'NbCl_4$), hence readily purifiable by recrystallisation. Furthermore, as the synthesis of $NbCl_3(NDipp)(DME)$ (**1**; DME = 1,2-dimethoxyethane) is reportedly quantitative,[102] using this strategy could help improve the yields of $Cp'NbCl_2(NDipp)$ complexes if suitable cyclopentadienide reagents (MCp') can be found.

2.2. Synthesis of $CpNbCl_2(NDipp)$

As no $Cp'NbCl_2(NDipp)$ complexes have been synthesised to date from $NbCl_3(NDipp)(DME)$ (**1**), the unsubstituted cyclopentadienyl derivative $CpNbCl_2(NDipp)$ (**2**) was chosen as the initial synthetic target. Notably, Antiñolo *et al.* have successfully synthesised other imido variants of $CpNbCl_2(NR)$ (R = Tol or ^{t}Bu) in high yields (72 and 84%, respectively) from the reaction between NaCp and $NbCl_3(NR)L_2$ (SCHEME 2.2).[103] Therefore, the use of the same cyclopentadienide salt appeared to be a plausible route to the Dipp-derivative complex **2** from the precursor **1**.

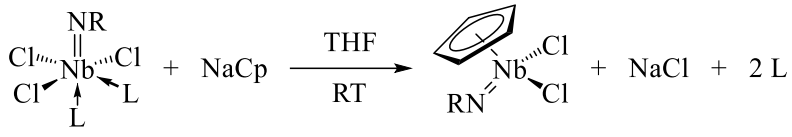

R	L
Tol	½ DME
^{t}Bu	pyridine

SCHEME 2.2: Reported synthesis of $CpNbCl_2(NR)$ (R = Tol or ^{t}Bu) from reaction of $NbCl_3(NR)L_2$ with NaCp.[103]

2.2.1. Reaction between $NbCl_3(NDipp)(DME)$ and NaCp

Sodium cyclopentadienide was prepared through reaction of sodium sand and freshly-cracked CpH in THF and isolated as the Lewis adduct NaCp·THF.[104] In a procedure analogous to that of Antiñolo *et al.*,[103] THF was added to an equimolar mixture of solids NaCp·THF and complex **1**[*] and the resulting solution stirred. Following extraction into hexanes, the previously unreported *bis*(cyclopentadienyl) complex $Cp_2NbCl(NDipp)$ (**3**) was isolated exclusively (29% yield based on NaCp·THF), rather than the desired monosubstituted complex **2**. The identity of the product was determined by ^{1}H NMR spectroscopic analysis; the other products of the reaction were insoluble and therefore could not be identified.

At first, it was believed that the formation of complex **3** may have been a result of inefficient dissolution of the two reagents. Therefore, the reaction was repeated by adding a solution of NaCp·THF dropwise to a cold solution of complex **1**, but once again, complex **3** was isolated (in 74% yield based on NaCp·THF) as the major product (SCHEME 2.3). Alterations to the reaction temperature (varying from –40 to 0 °C), the speed of addition of the NaCp solution to the niobium solution (~10 to ~30 min) and the solvent (toluene instead of THF) made no difference to the identity of the product formed.

[*] $NbCl_3(NDipp)(DME)$ (**1**) was synthesised quantitatively according to the aforementioned literature procedure.[102]

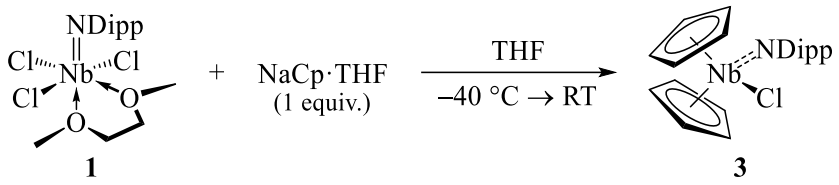

SCHEME 2.3: The reaction between an equimolar ratio of complex **1** and NaCp·THF, exclusively yielding the *bis*(cyclopentadienyl) complex **3** rather than the desired half-sandwich imido complex CpNbCl$_2$(NDipp) (**2**).

As expected, the *bis*(cyclopentadienyl) complex **3** is isolated in improved yields (71% based on niobium) from the reaction of complex **1** with two equivalents of NaCp·THF; this enabled further spectroscopic characterisation of the complex to be achieved. Along with the satisfactory elemental analysis of complex **3**, the complex proved sufficiently air- and moisture-stable for the successful determination of its accurate mass by positive-ion atmospheric solids analysis probe (ASAP+) mass spectrometry. Additionally, following recrystallisation of complex **3** from hot hexanes, single crystals suitable for an X-ray diffraction (XRD) study were obtained. The resulting molecular structure is shown in FIGURE 2.1.

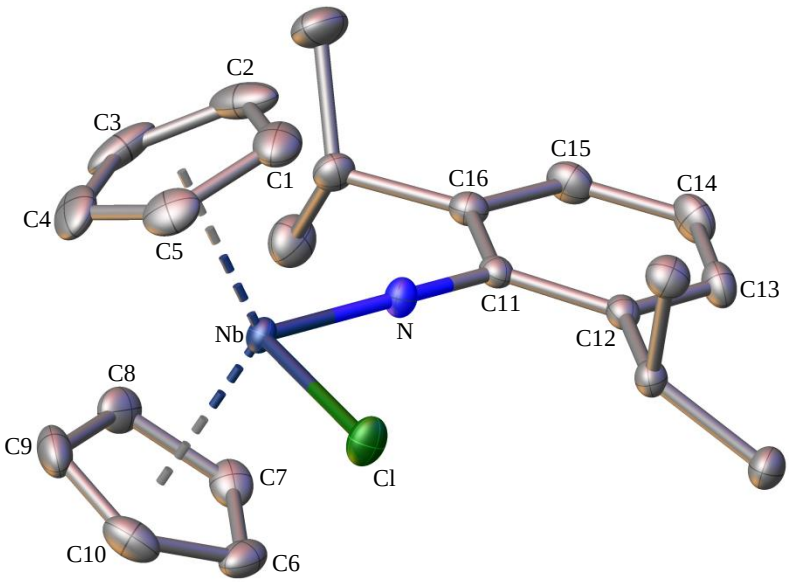

FIGURE 2.1: Experimentally-determined molecular structure of Cp$_2$NbCl(NDipp) (**3**); thermal ellipsoids are shown at 50% probability and H-atoms are omitted for clarity.

Compared to the reported molecular structure of the target mono(cyclopentadienyl) complex **2**,[89] the niobium–nitrogen bond in complex **3** is longer by ~0.03 Å (TABLE 2.1). This difference in Nb=N bond length, together with a shortened N–C^{ipso} bond (also by ~0.03 Å), is consistent with the imido ligand of complex **3** adopting an X$_2$-coordination mode (compared with the LX$_2$-coordination associated with complex **2**).* This X$_2$-coordination of the DippN^{2-} ligand therefore suggests that complex **3** is an electronically-saturated 18-electron species, which combined with the coordinative saturation of the

* While the more linear Nb–N–C moiety in complex **3** is often assigned to LX$_2$-coordination, this is likely due to crystal packing effects associated with the bulky *bis*(cyclopentadienyl) complex rather than hybridisation effects.[20]

metal centre may account for the complex's enhanced air- and moisture-stability compared to the 16-electron complex **2**. This degree of stability was reported for an *ansa*-derivative of complex **3**, {Cp'$_2$}NbCl(NDipp) ({Cp'$_2$} = *ansa*-{$Me_2C(C_5H_4)_2$}), which contains a crystallographically similar niobium–imido motif to complex **3** (TABLE 2.1).[105]

TABLE 2.1: Selected experimentally-determined interatomic distances (Å) and angles (°) of the niobium–imido moiety of complex **3**, along with those of literature complexes **2** and {Cp'$_2$}NbCl(NDipp) ({Cp'$_2$} = *ansa*-{$Me_2C(C_5H_4)_2$}).[89,105]

	Cp_2NbCl(NDipp) (3)	**$CpNbCl_2$(NDipp) (2)**	**{Cp'$_2$}NbCl(NDipp)**
$d_{Nb–N}$	1.7932(9)	1.761(6)	1.7984(14)
$d_{N–C11}$	1.3794(14)	1.408(9)	1.385(3)
$\angle_{Nb–N–C11}$	170.99(8)	165.6(5)	167.49(14)

The formation of the *bis*(cyclopentadienyl) imido complex $Cp_2MCl(NDipp)$ from reaction of $MCl_3(NDipp)(DME)$ with a single equivalent of NaCp·THF was not exclusive to M = Nb. Indeed, the analogous reaction between the tantalum complex $TaCl_3(NDipp)(DME)$ and one equivalent of NaCp·THF was found to produce $Cp_2TaCl(NDipp)$ (**3_{Ta}**), rather than $CpTaCl_2(NDipp)$, as confirmed herein through ^{1}H NMR spectroscopic analysis of the crude product.*

A similar double incorporation of the Cp'-moiety has been reported by Antiñolo *et al.* for the equimolar reaction between $NbCl_3(N^tBu)(py)_2$ (py = pyridine) and $LiCp^{TMS}$ at low temperature in THF, where after 2 h the *bis*(cyclopentadienyl) complex $Cp^{TMS}{}_2NbCl(N^tBu)$ is formed exclusively.[103] However, if the same reaction is instead performed at room temperature, a ~1:1 mixture of monosubstituted $Cp^{TMS}NbCl_2(N^tBu)$ and disubstituted $Cp^{TMS}{}_2NbCl(N^tBu)$ is produced after 24 h. The same stoichiometry of products was also found to result from reaction of $NbCl_3(N^tBu)(py)_2$ with isolated $Cp^{TMS}{}_2NbCl(N^tBu)$ over the same time period. Together, these observations suggest that the *bis*(cyclopentadienyl) complex Cp'$_2$MCl(NR) initially forms as the kinetic product of the equimolar reaction between $NbCl_3(NR)L_2$ and an ionic source of Cp'$^-$, following which an exchange reaction between $NbCl_3(NR)L_2$ and Cp'$_2$MCl(NR) occurs to afford Cp'$NbCl_2$(NR). This proposed overall mechanism for the reaction between $NbCl_3(NR)L_2$ and Cp'$^-$ is summarised in SCHEME 2.4.

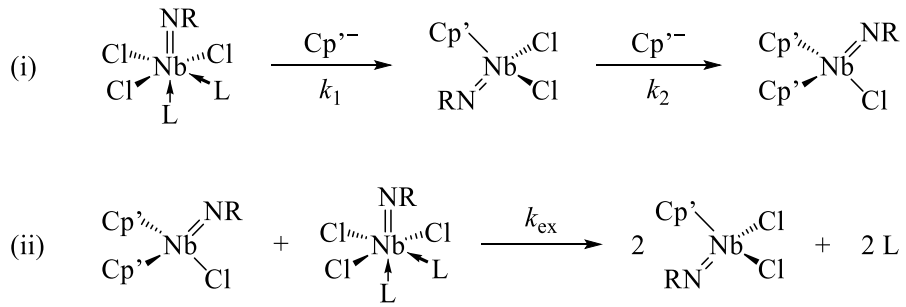

SCHEME 2.4: Proposed mechanism for the equimolar reaction between $NbCl_3(NR)L_2$ and an ionic source of Cp'$^-$, proceeding *via* (i) formation of Cp'$_2$NbCl(NR), followed by (ii) ligand exchange between Cp'$_2$NbCl(NR) and $NbCl_3(NR)L_2$.

* While the *bis*(cyclopentadienyl) complex **3_{Ta}** has not been reported in the literature, $CpTaCl_2(NDipp)$ has been previously synthesised and characterised.[101]

The initial formation of the disubstituted product $Cp'_2NbCl(NR)$ (SCHEME 2.4i) indicates that the second substitution step is more rapid than the first (*i.e.* $k_2 > k_1$). This may be explained by the fact that generally four-coordinate complexes contain less sterically crowded metal centres than six-coordinate complexes, and so the former complexes are usually more susceptible to nucleophilic substitution reactions. Indeed, the lesser degree of steric bulk surrounding the Nb-atom of $Cp'NbCl_2(NR)$ compared to that of $NbCl_3(NR)L_2$ is evidenced by a ~5% decrease in the determined percentage buried volumes ($\%V_{bur}^{Nb}$; TABLE 2.2). Here, the parameter $\%V_{bur}^{Nb}$ is defined as the percentage of volume occupied by the atoms within a sphere of radius 3 Å centred at the Nb-atom and is calculated using the free web application *SambVca 2.1*.[106] Ordinarily, $\%V_{bur}^{M}$ is used as a measure of an individual ligand's steric bulk (*e.g.* RN^{2-} ligands)[10] by centring the sphere at the transition metal (M) and removing all other ligands from the complex. However, herein, all ligands within niobium's primary coordination sphere were included in the calculations of $\%V_{bur}^{Nb}$ in order to quantify the total steric bulk around the metal centres. Typical steric maps generated by *SambVca 2.1*[106] are shown in FIGURE 2.2, with the molecular orientations shown beneath.

TABLE 2.2: Percentage buried volumes at niobium ($\%V_{bur}^{Nb}$) calculated[106] for crystallographically-determined complexes of $NbCl_3(NR)L_2$, $Cp'NbCl_2(NR)$ and $Cp'_2NbCl(NR)$. Sphere radius = 3.0 Å; Nb- and H-atoms removed prior to calculation.

$NbCl_3(NR)L_2$	**$\%V_{bur}^{Nb}$**	**$Cp'NbCl_2(NR)$**	**$\%V_{bur}^{Nb}$**	**$Cp'_2NbCl(NR)$**	**$\%V_{bur}^{Nb}$**
$NbCl_3(NDipp)(DME)$ (**1**) [ref: 107]	95	$CpNbCl_2(NDipp)$ (**2**) [ref: 89]	90	$Cp_2NbCl(NDipp)$ (**3**)	96
$NbCl_3(N^tBu)(py)_2$ [ref: 108]	94	$Cp^{TMS}NbCl_2(N^tBu)$ *(a)*	88	$Cp^{TMS}{}_2NbCl(N^tBu)$ *(a)*	95
		$CpNbCl_2(N^tBu)$ [ref: 89]	88	$Cp_2NbCl(N^tBu)$ [ref: 109]	94

(a) Computed (B3LYP/3-21G*) gas-phase structures, as experimental solid-state structures have not been reported.

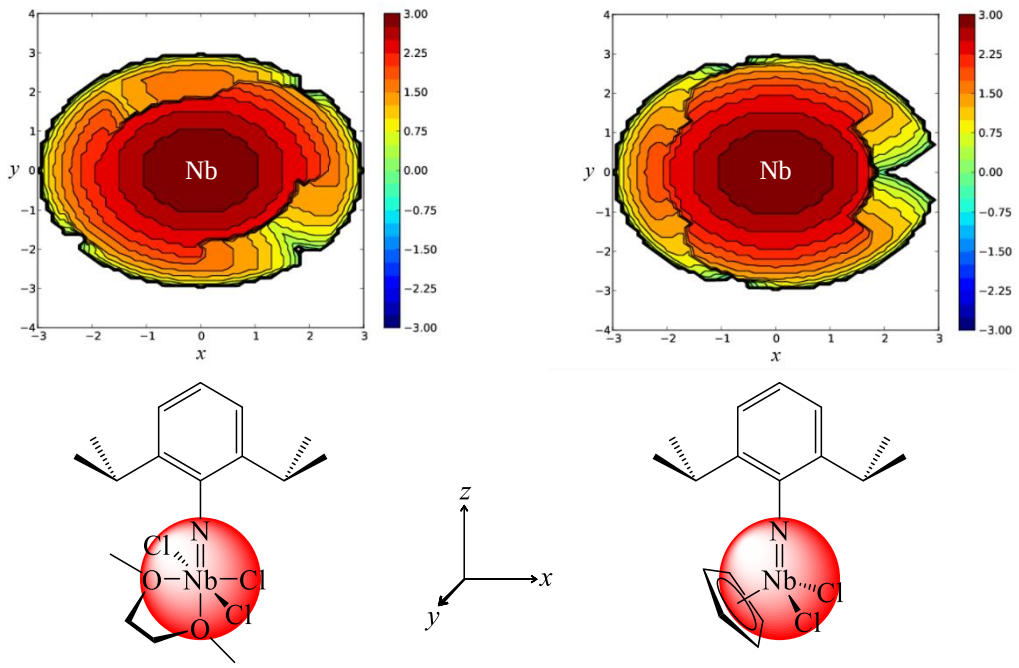

FIGURE 2.2: TOP: Steric maps of $NbCl_3(NDipp)(DME)$ (**1**; LEFT) and $CpNbCl_2(NDipp)$ (**2**; RIGHT) generated by *SambVca 2.1*,[106] as viewed down the Nb=N bond. BOTTOM: Schematic depiction of the centring of the spheres (radius = 3.0 Å) at the niobium atoms of the complexes.

In addition to having an impact on k_1 and k_2, steric factors are likely to affect the rate of ligand exchange between $NbCl_3(NR)L_2$ and $Cp'_2NbCl(NR)$ (k_{ex}; SCHEME 2.4ii), as the two complexes must attain close proximity for Cp'^-/Cl^- exchange between the metal centres. This is supported by the data in TABLE 2.2, where ligand exchange was not found to occur between the two bulkiest complexes **1** and **3** ($\%V_{bur}^{Nb}$ = 95 and 96%, respectively). In contrast, the reaction between the less sterically hindered *tert*-butylimido derivatives, namely $NbCl_3(N^tBu)(py)_2$ and $Cp^{TMS}{}_2NbCl(N^tBu)$ ($\%V_{bur}^{Nb}$ = 94 and 95%, respectively), was reported to take place.[103]

While k_{ex} is constant for a given system, the rates of substitution (k_1 and k_2; SCHEME 2.4i) are likely to be dependent on the nature of the Cp-source employed in the reaction with complex **1**. For instance, the use of a more covalent Cp-reagent may encourage the reaction with complex **1** to proceed *via* a transmetallation mechanism,[110] rather than a purely nucleophilic substitution pathway (as with NaCp). If the relative rates of substitution can be inverted (*i.e.* $k_1 > k_2$), it should be possible to ultimately prevent the irreversible formation of the *bis*(cyclopentadienyl) complex **3** and thus enable the isolation of the monosubstituted derivative **2**. To that end, an alternative cyclopentadienyl reagent to NaCp was sought.

2.2.2. Reaction between $NbCl_3(NDipp)(DME)$ and TlCp

Since the reaction of complex **1** with one equivalent of NaCp·THF resulted in the undesired formation of the *bis*(cyclopentadienyl) complex **3**, use of an alternative Cp-source was explored as a route to mono(cyclopentadienyl) complex **2**. Thus, the reactions of the more covalent cyclopentadienyl source

thallium(I) cyclopentadienide were explored. TlCp forms a polymeric chain of alternating thallium and cyclopentadienyl moieties in the solid state (FIGURE 2.3), which results in its low solubility (and its corresponding low reactivity) in most organic solvents.[111] While this Cp-source is kinetically unreactive, the reaction between TlCp and metal halides is thermodynamically driven by the production of an extremely insoluble thallium(I) halide salt.[112]

FIGURE 2.3: The polymeric structure of thallium(I) cyclopentadienide (TlCp).[111]

In the area of transition metal imido chemistry, TlCp has proved a suitable reagent for the transfer of a single cyclopentadienyl ligand to $CrCl_3(N^tBu)(DME)$, with the formation of a Group VI analogue of **2**, $CpCrCl_2(N^tBu)$, in reasonable yield (50%).[113] In contrast, the reaction between NaCp and $CrCl_3(N^tBu)(DME)$ was found to produce unidentifiable chromium(III) species. Therefore, in this system the covalency of TlCp was exploited as it is less reducing than its ionic sodium analogue. Similarly, the alkylidene analogue of **2**, $CpNb(=CH^tBu)Cl_2$, can only be synthesised from reacting $Nb(CH_2{}^tBu)_2Cl_3$ with TlCp (albeit in only 15% yield), as the reaction with NaCp also leads to an unknown mixture of components.[114]

Although TlCp is normally substituted for NaCp to circumvent problems with reduction, it was envisaged that the more covalent, and hence less reactive, thallium(I) species may prevent the double transfer of the Cp-ligand to the niobium centre in its reaction with complex **1**. To this end, complex **1** was reacted with one equivalent of TlCp (SCHEME 2.5). In contrast to the reaction between complex **1** and NaCp·THF (SCHEME 2.3), the desired half-sandwich imido complex **2** was produced from the reaction with TlCp, albeit in a moderately low yield (39%). However, no disubstituted complex **3** was isolable from the thallium(I) reaction, which indicated that the rate of reaction between **2** and TlCp (k_2; SCHEME 2.4) was sufficiently inhibited by using this covalent cyclopentadienyl source instead of NaCp·THF.

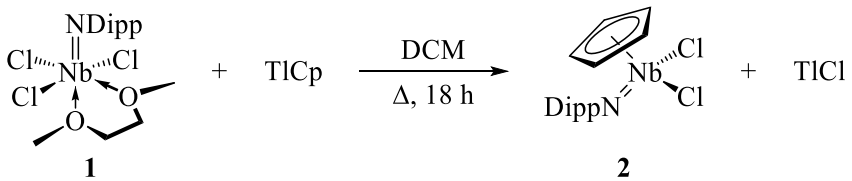

SCHEME 2.5: Synthesis of monosubstituted **2** from complex **1** and TlCp.

Due to time-constraints, the reaction described in SCHEME 2.5 was not optimised. Furthermore, due to the toxicity of thallium, there remains a drive to use alternative covalent cyclopentadienyl transfer reagents, such as TMSCp or $MgCp_2$, for the synthesis of the half-sandwich imido complex **2** from complex **1** at larger scales.

2.3. Reduction chemistry of $CpNbCl_2(NDipp)$

As outlined in SECTION 1.4.1, the reduction of $Cp^{\dagger}{}_2ZrCl_2$ (**AO_{II}**-Cl_2; $Cp^{\dagger} = C_5HMe_4$) by Chirik and co-workers is shown to yield the dinitrogen complex $\{Cp^{\dagger}{}_2Zr\}_2(\mu,\eta^2,\eta^2\text{-}N_2)$ (**AQ**), which in turn reacts stoichiometrically with dihydrogen to produce ammonia.[80] Since a *pseudo*-isolobal relationship has been established between $CpNbCl_2(NDipp)$ (**2**) and **AO_{II}**-Cl_2 (SECTION 1.4.2), it was envisaged that the niobium(III) dinitrogen complex $\{CpNb(NDipp)\}_2(\mu,\eta^2,\eta^2\text{-}N_2)$ (**4**) could similarly be afforded from the reduction of complex **2**. DFT analysis performed herein* indicated that the lowest-energy structure of dinitrogen complex **4** is the butterfly complex displayed in FIGURE 2.4. While the experimentally-determined structure of **AQ** has a considerably more planar "M_2N_2" framework than that of computed **4** (as quantified by the fold angle, θ, between planes M1–N1–N2 and M2–N1–N2), the two dinitrogen complexes have similar M–N and N–N interatomic distances (TABLE 2.3). Furthermore, natural bond orbital (NBO) analyses of the two structures† suggest that a similar degree of activation of the dinitrogen ligand could be achieved with complex **4**, based on the comparable M–N Wiberg bond indices (WBIs) of the two complexes.

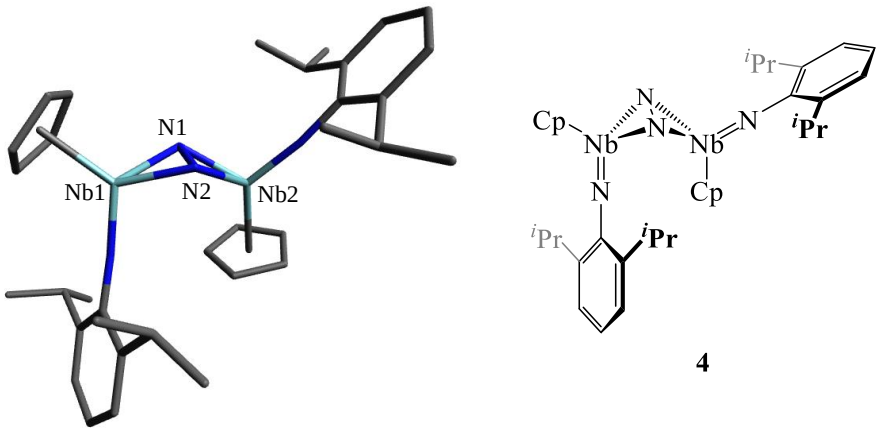

4

FIGURE 2.4: Computed (B3LYP/3-21G*) structure of $\{CpNb(NDipp)\}_2(\mu,\eta^2,\eta^2\text{-}N_2)$ (**4**), with H-atoms removed for clarity.

TABLE 2.3: Selected interatomic distances (Å) and angles (°) for the computed structure of complex **4** and the experimentally-determined[80] structure of complex **AQ**; computed WBIs are shown in parentheses.

	$\{CpNb(NDipp)\}_2(\mu,\eta^2,\eta^2\text{-}N_2)$ (4)	**$\{Cp^{\dagger}{}_2Zr\}_2(\mu,\eta^2,\eta^2\text{-}N_2)$ (AQ)**
θ [(a)]	135.7	0.00
$d_{M–N}$ [(b)]	2.072 (0.982)	2.1248(7) (0.949)
$d_{N1–N2}$	1.547 (1.032)	1.377(4) (1.057)

[(a)] Fold angle between planes M1–N1–N2 and M2–N1–N2.
[(b)] Average of $d_{M1–N1}$, $d_{M1–N2}$, $d_{M2–N1}$ and $d_{M2–N2}$.

* The input geometry for $\{CpNb(NDipp)\}_2(\mu,\eta^2,\eta^2\text{-}N_2)$ (**4**) was created by superimposing the "CpNb(NDipp)" and "N_2" fragments from the crystallographically-determined structures of complexes **2**[89] and **AQ**,[80] respectively.

† The crystallographically-determined[80] molecular structure of **AQ** was optimised by DFT prior to NBO analysis. The resulting gas-phase structure was found to be very similar to the experimental structure (root-mean-square {RMS} distance = 0.3633 Å and maximum distance = 0.7098 Å).

While the dinitrogen complex **4** has never been produced to date, the reduction chemistry of the niobium half-sandwich imido complex **2** has been briefly explored by Mountford and co-workers.[101] Initially, the group established that reduction of complex **2** using magnesium (reduction potential, E_{red} = –2.37 V *vs.* the standard hydrogen electrode, SHE)[115] in the presence of PMe_3 yields a niobium(III) species, isolable as the Lewis adduct $CpNb^{III}(NDipp)(PMe_3)_2$ (SCHEME 2.6).[101] However, in the absence of σ-donating/π-accepting ligands, only the one-electron reduction of complex **2** is achieved using the milder reducing agent $NaBH_4$ (E_{red} = –0.48 V *vs.* SHE),[115] which affords the dimeric niobium(IV) species $\{CpNb(\kappa^2\text{-}BH_4)(\mu\text{-}NDipp)\}_2$ (SCHEME 2.6).[95] As Chirik and co-workers found with the reduction of zirconocene(IV) $\mathbf{AO_{II}}$-Cl_2, both a strong reductant and the absence of other competing donor species are required to encourage the coordination of dinitrogen within the zirconocene(II) product **AQ**.[80] Therefore, a similar strategy was adopted to attempt the synthesis of the dinitrogen complex **4** from the half-sandwich imido complex **2**.

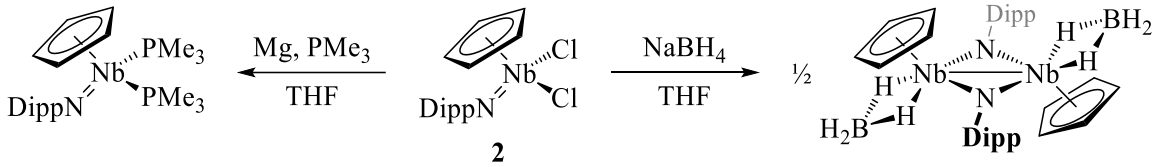

SCHEME 2.6: Reported reduction reactions of complex **2** to produce either niobium(III)[101] or niobium(IV)[95] species.

2.3.1. Reduction of $CpNbCl_2(NDipp)$ using alkali metal-based reducing agents

The reduction of complex **2** was initially attempted using two equivalents of sodium amalgam, Na(Hg), using conditions analogous to those reported by Chirik and co-workers for the reduction of zirconocene $\mathbf{AO_{II}}$-Cl_2.[80] Following the reduction reaction, the free amine $DippNH_2$ was isolable in near-stoichiometric amounts, indicating that degradation of complex **2** had occurred instead of its reduction to the dinitrogen complex **4** (SCHEME 2.7). As the rigorous exclusion of air and moisture was maintained throughout the reaction and work-up, the degradation pathway of complex **2** is unclear; furthermore, the niobium-containing products(s) of the reaction could not be identified.

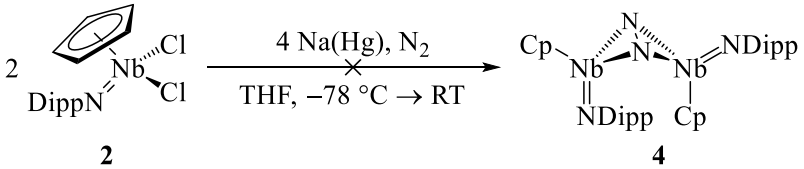

SCHEME 2.7: The attempted reduction of **2** using Na(Hg) under one atmosphere of dinitrogen.

In order to investigate whether the reactivity of the reducing agent may have been an issue for the reaction in SCHEME 2.7, the reduction of **2** was also attempted using sodium naphthalenide (NaNaphth). Along with being soluble compared to its amalgam analogue, the radical anion $Naphth^{\bullet-}$ is also a

stronger reducing agent than Na(Hg) (E_{red} = –2.70 V and –1.96 V *vs.* SHE, respectively).* However, following the reaction between complex **2** and two equivalents of NaNaphth, a near-stoichiometric amount of $DippNH_2$ was once again isolated alongside naphthalene. Residual water in the reaction mixture is unlikely to have led to the protonation of the imido ligand in complex **2**, since hydrolysis of $Naphth^{\bullet-}$ is known to result in 1,2-dihydronaphthalene (SCHEME 2.8),[118] which was not detected herein. Therefore, as with the attempted reduction using Na(Hg) (SCHEME 2.7), the decomposition pathway for complex **2** remains unknown.

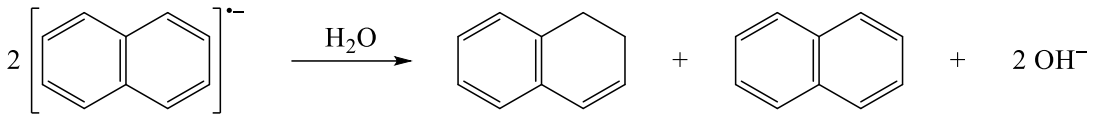

SCHEME 2.8: The reported hydrolysis of $Naphth^{\bullet-}$ to 1,2-dihydronaphthalene and naphthalene.[118]

The use of potassium graphite (KC_8) was also attempted as a reducing agent (E_{red} < –2.70 V)† for complex **2**, since it has been successfully used in the reported synthesis of the dinitrogen complex $\{(L_2X_2)Nb\}_2(\mu,\eta^1,\eta^1\text{-}N_2)$ from $(L_2X_2)NbCl$ ($L_2X_2^{2-}$ = $^{-}N\{SiMe_2CH_2P(Ph)CH_2SiMe_2\}_2N^{-}$).[121] However, no reaction was observed between **2** and KC_8 in hexanes, with the niobium(V) reactant being recovered quantitatively following the removal of the graphitic component by filtration. Changing the reaction solvent from hexanes to THF stimulated a reaction between complex **2** and KC_8, although as found using reductants Na(Hg) or NaNaphth, $DippNH_2$ was near-quantitatively afforded following extraction into hexanes. However, further ^{1}H NMR spectroscopic analysis of the hexanes-soluble product indicated the additional presence of a new species as a minor component (~12 mol%) alongside the free amine (~88 mol%). The new species was found to have signals attributable to a Dipp-moiety (*iso*-propyl signals at δ_H = 3.83 and 1.31 ppm) alongside a Cp-ligand (δ_H = 5.50 ppm) in a 1:1 ratio (FIGURE 2.5).

* The reported[116] E_{red} values (*vs.* ferrocene, Fc) have been adjusted for the SHE by the addition of 0.400 V.[117]

† While naphthalene (E_{red} = –2.70 V)[119] is reportedly reducible by potassium graphite, the exact E_{red} value of KC_8 is challenging to determine due to the decrease in %K over the course of reaction affecting its reducing strength.[120]

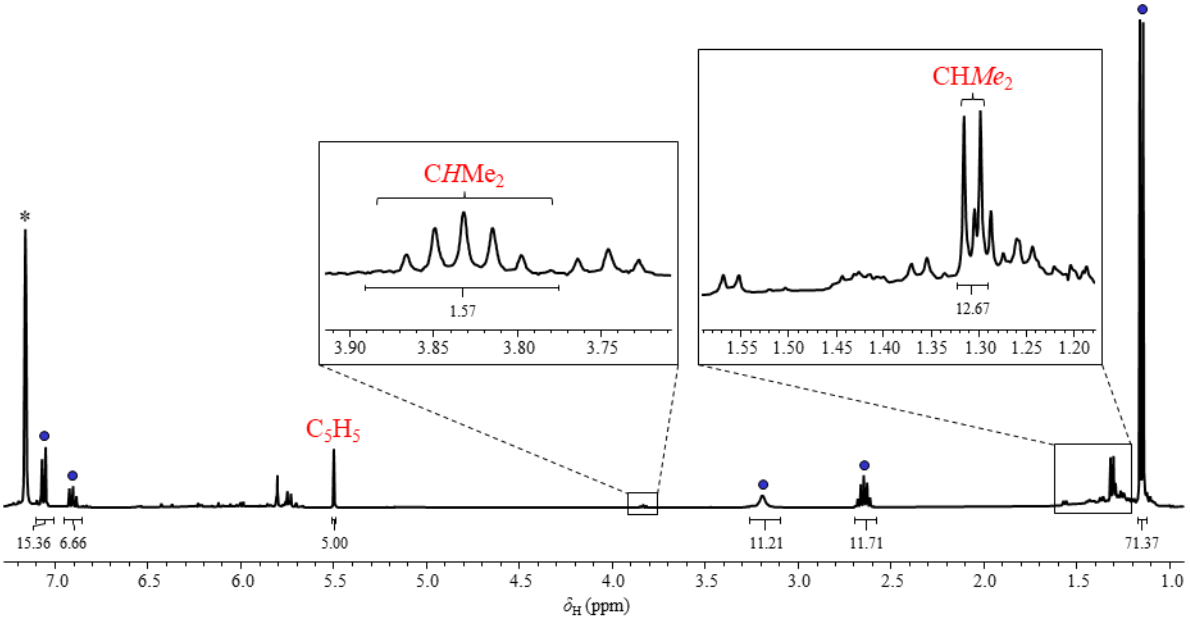

FIGURE 2.5: ^{1}H NMR (400 MHz, C_6D_6) spectrum of the hexanes-soluble product mixture following the reaction between **2** and KC_8. Signals attributed to $DippNH_2$ (•), a new Cp- and Dipp-containing species (red assignments) and residual *protio* NMR solvent (*) were identifiable.

Unfortunately, no further conclusions could be made about the identity of the new Dipp- and Cp-containing product from the KC_8 reduction of complex **2**. The attempted removal of the major component, $DippNH_2$, from the product mixture (through washings with cold petroleum ether) were unsuccessful, as were attempts at crystallising the new species. Isolation of the unidentified product may be aided by scaling up the reaction between complex **2** and KC_8 in THF, however this was not attempted due to the considerable degradation of the reactant complex (to form $DippNH_2$; ~88 mol%) involved with using such a harsh reducing agent.

2.3.2. Reduction of $CpNbCl_2(NDipp)$ using magnesium

Following the near-stoichiometric degradation of complex **2** using alkali metal-based reducing agents (SECTION 2.3.1), the reduction of the complex was attempted using magnesium. The two-electron reduction of complex **2** has already been successfully demonstrated using this reductant, albeit only in the presence of σ-donor species such as THF and PMe_3 (SCHEME 2.6).[101] In order to encourage the subsequent coordination of weakly σ-donating dinitrogen to any transiently formed niobium(III) species, the reduction of complex **2** using activated * magnesium (~3 equivalents) was initially performed in hexanes under an atmosphere of N_2 in the absence of any Lewis basic species. Despite the magnesium being used in excess, neither a colour-change nor the precipitation of $MgCl_2$ was observed over the course of ~1 week at room temperature, indicating that no reaction with complex **2** had occurred in hexanes. However, the subsequent addition of a small volume of THF (~7 equivalents *cf.* **2**) to the

* Magnesium turnings were activated by stirring under dynamic vacuum for ~15 h immediately before use.

suspension in hexanes was sufficient to stimulate a reaction between complex **2** and Mg, as observed from the darkening of the reaction mixture. Instead of affording the desired dinitrogen complex **4**, the previously unreported niobium(IV) chloride-bridging species $\{CpNb(\mu\text{-}Cl)(NDipp)\}_2$ (**5**) was isolated in 5% yield (SCHEME 2.9), in addition to other unidentifiable products.

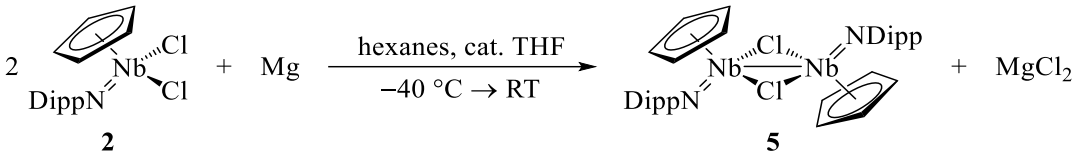

2 **5**

SCHEME 2.9: Synthesis of the niobium(IV) species **5** from the reduction of complex **2** using magnesium (3 equivalents).

Inert ASAP+ (*i*ASAP+) mass spectrometric analysis of complex **5** was consistent with a molecular formula of $Cp_2Nb_2Cl_2(NDipp)_2$ due to the detection of a molecular ion signal at m/z = 736 Da. Furthermore, an XRD study of single crystals of **5** (afforded from a concentrated solution in hexanes stored at –20 °C) confirmed the connectivity of the complex as the chloride-bridging dimer, although crystallographic disorder (34% occupancy) was present in the structure about one imido ligand. The experimentally-determined molecular structure of complex **5** is shown in FIGURE 2.6.

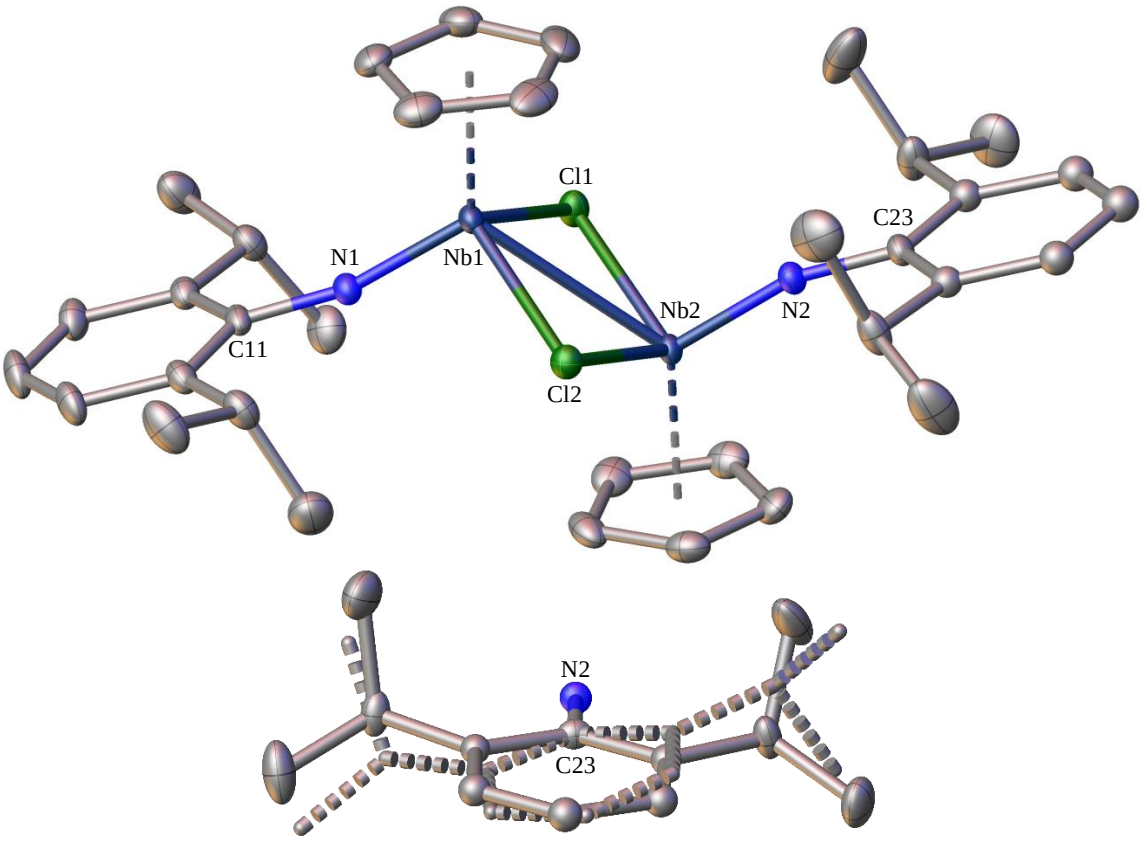

FIGURE 2.6: TOP: Molecular structure of $\{CpNb(\mu\text{-}Cl)(NDipp)\}_2$ (**5**), with crystallographic disorder omitted for clarity. BOTTOM: Crystallographic disorder of one $DippN^{2-}$ ligand in **5**, where the minor component (34% occupancy) is shown as dashed wireframe. In both structures, thermal ellipsoids are shown at 50% probability and H-atoms are omitted for clarity.

As shown in TABLE 2.4, the Nb–N bond length is ~0.03 Å longer in dimer **5** compared to its precursor **2**,[89] despite the imido ligands in both complexes being formally considered LX_2-ligands. This may be

attributed to the metal centres in the niobium(IV) dimer **5** being more electron-rich than in the niobium(V) complex **2** (18- and 16-electron centres, respectively), resulting in weaker donation of the nitrogen lone-pair to niobium in the former complex. Additionally, the Nb–Cl bonds in dimer **5** are ~0.1 Å longer than in its precursor **2**, although this is expected due to the different coordination modes adopted by the chloride ligands (bridging and terminal, respectively). While the average $d_{Nb–Cl}$ of dimer **5** is comparable to those of the only two reported niobium(IV) chloride-bridging dimers $\{NbCl_3(\mu\text{-}Cl)(EMe_2)\}_2$ (E = S or Se; TABLE 2.4),[122] complex **5** is unique in that its μ-chloride ligands are approximately equidistant from each metal centre (*i.e.* $d_{Nb1–Cl1} \approx d_{Nb1–Cl2}$).

TABLE 2.4: Selected interatomic distances (Å) in the crystallographically-determined structures of dimer **5**, its precursor **2**,[89] and other niobium(IV) chloride-bridging dimers $\{NbCl_3(\mu\text{-}Cl)(EMe_2)\}_2$ (E = S or Se).[122]

			$\{NbCl_3(\mu\text{-}Cl)(EMe_2)\}_2$	
	$\{CpNb(\mu\text{-}Cl)(NDipp)\}_2$ (5)	**$CpNbCl_2(NDipp)$ (2)**	**E = S**	**E = Se**
$d_{Nb1–N1}$	1.7946(11) [(a)]	1.761(6)	–	–
$d_{Nb1–Cl1}$	2.4443(4) [(a)]	2.338(2)	2.4205(6)	2.4048(14)
$d_{Nb1–Cl2}$	2.4501(4) [(a)]	2.338(2)	2.5107(6)	2.4717(13)
$d_{Nb1–Nb2}$	2.9875(4)	–	3.1095(3)	3.0524(9)

[(a)] Average value for both equivalent bonds in the structure (since no inversion centre present).

The short Nb–Nb interatomic distance of 2.9875(4) Å of complex **5** is similar to those found within the other dimer complexes (TABLE 2.4) and is consistent with the presence of a metal–metal single-bond. Indeed, MO analysis of dimer **5** reveals that the HOMO primarily resembles a niobium–niobium σ-bond (78% localisation across Nb1 and Nb2; FIGURE 2.7), with the presence of a Nb1–Nb2 single-bond also being confirmed by NBO analysis of the dinuclear complex (WBI = 0.832).[*] So, while each niobium(IV) nucleus in complex **5** has a d^1 electronic configuration, pairing of these electrons in forming a metal–metal bond results in a diamagnetic complex readily analysable by NMR spectroscopy. Indeed, the solution-state ^1H and ^{13}C NMR spectra of **5** are consistent with the solid-state structure shown in FIGURE 2.6.

[*] The crystallographically-determined molecular structure of complex **5** was optimised by DFT prior to MO and NBO analyses. The computed gas-phase structure was found to be similar to the experimental solid-state structure (RMS distance = 0.5838 Å and maximum distance = 1.4447 Å).

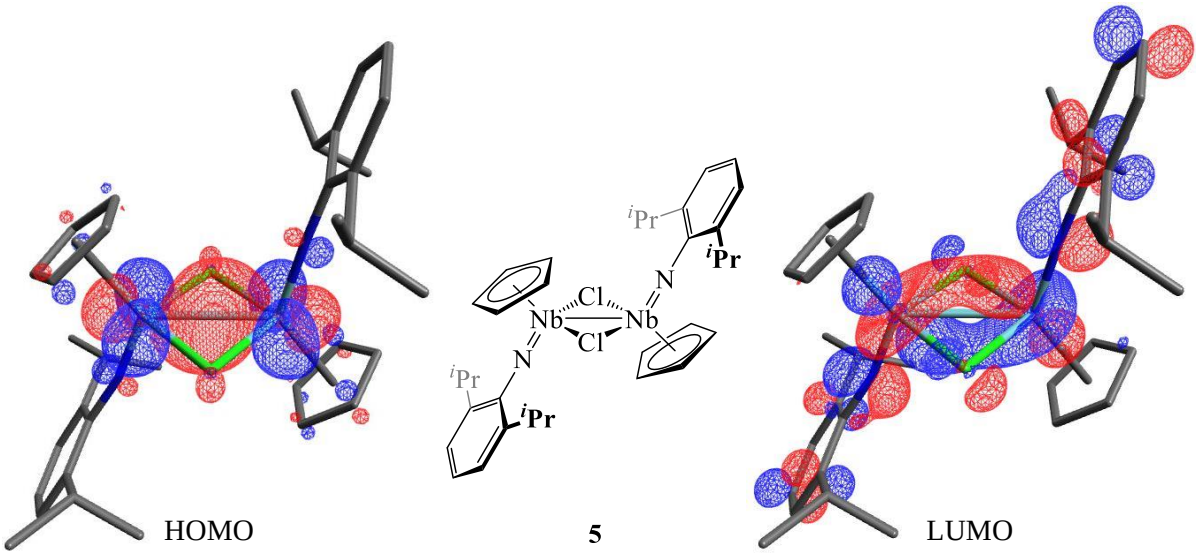

FIGURE 2.7: Computed (B3LYP/3-21G*) FMOs of $\{CpNb(\mu\text{-}Cl)(NDipp)\}_2$ (**5**): HOMO (–5.011 eV; LEFT) and LUMO (–1.717 eV; RIGHT). H-atoms have been omitted for clarity.

Interestingly, dimer **5** presents unusual stability to further reduction as evidenced by the complex being synthesised in the presence of excess reductant (SCHEME 2.9). Furthermore, nucleophilic cleavage of the metal–metal bond within complex **5** is not observed following the introduction of strong σ-donor PMe_3, which enabled the use of the phosphine to aid the purification of the dimer.* While the strength of the Nb–Nb bond (typical bond dissociation energy = 513 kJ mol^{-1})[123] may partially explain the resistance of complex **5** to nucleophilic cleavage, further examination of the FMOs of the dimer indicates another reason for its stability. The computed LUMO of **5** (FIGURE 2.7) resembles a Nb–Nb π-bonding interaction, therefore population of this orbital (by either reduction or a σ-donating nucleophile) would likely strengthen the metal–metal bond rather than cleave it.

Due to the poor reproducibility of the magnesium reduction of complex **2** (SCHEME 2.9), sufficient quantities of complex **5** could not be attained to further explore the reactivity of the dimer. In particular, the synthesis of complex **5** appears to be sensitive to the quality and pre-activation of the magnesium turnings used. However, considering that the niobium(IV) complex **5** was not the target molecule following the reduction of complex **2**, attention turned to finding another $Cp'NbCl_2(NR)$ system capable of forming a dinitrogen complex on reduction.

* It is thought that following removal of the excess magnesium from the reaction mixture, the addition of PMe_3 encourages the precipitation of the $MgCl_2$ by-product from solution. However, this method of purification is unreliable, as satisfactory elemental analysis of complex **5** is still yet to be attained.

2.4. Synthesis of $FluNbCl_2(NDipp)$

As described in SECTION 2.3, reduction of $CpNbCl_2(NDipp)$ (**2**) under an atmosphere of N_2 did not afford the target niobium(III) dinitrogen complex $\{CpNb(NDipp)\}_2(\mu,\eta^2,\eta^2\text{-}N_2)$ (**4**). An explanation for this may be that the transient 14-electron complex $CpNb^{III}(NDipp)$ is simply too electronically and coordinatively unstable in the absence of strong σ-donors (*e.g.* PMe_3),[101] thus rapidly undergoes decomposition. Similar to $CpNb^{III}(NDipp)$, *pseudo*-isolobal 14-electron zirconocene(II) complexes Cp'_2Zr^{II} are not isolable in the absence of σ-donor[81] or π-acceptor[83] ligands (FIGURE 2.8i). However, by replacing the Cp'-motif(s) in Cp'_2Zr^{II} with related indenyl (Ind') derivatives, Chirik and co-workers were able to isolate the base-free, 18-electron zirconocene(II) species (η^5-Cp*)(η^9-Ind')Zr (Ind' = C_9H_5-1,3-^{i}Pr$_2$)[84] and (η^5-Ind')(η^9-Ind')Zr (Ind' = C_9H_5-1-Me-3-^{i}Pr)[124] due to the ability of the indenyl ligand to adopt an η^9-coordination mode (FIGURE 2.8ii). Furthermore, despite its improved electronic and coordinative stability, the mono(indenyl) complex (η^5-Cp*)(η^9-Ind')Zr demonstrated subsequent reactivity with dinitrogen, as outlined in SECTION 1.4.1.

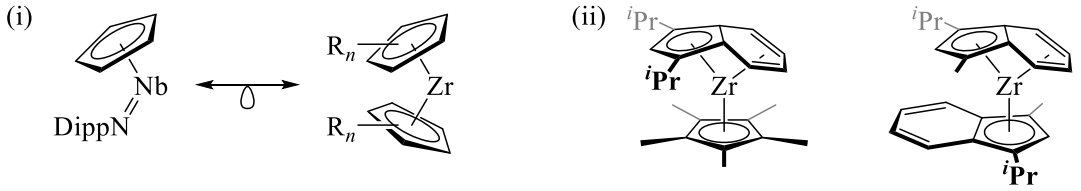

FIGURE 2.8: Differing stabilities of zirconocene(II) derivatives: (i) 14-electron $CpNb^{III}(NDipp)$ and η^5,η^5-zirconocene(II) complexes (not isolable) *vs*. (ii) 18-electron mono(indenyl)[84] and *bis*(indenyl)[124] η^5,η^9-zirconocene(II) complexes (isolable).

With the relative stabilities of cyclopentadienyl and indenyl zirconocene(II) complexes in mind, it was of interest to investigate whether *pseudo*-isolobal $Cp'Nb^{III}(NR)$ complexes could be similarly stabilised using a formally η^9-coordinating indenyl ligand. To date, no precursor niobium(V) half-sandwich indenyl imido complexes, *e.g.* $Ind'NbCl_2(NR)$, have been reported in the literature. Therefore, to facilitate NMR spectroscopic characterisation, attention turned to the synthesis of the symmetrical fluorenyl (Flu^-) derivative of complex **2**, namely $FluNbCl_2(NDipp)$ (**6**). Similar to its indenyl variant, Flu^- has been crystallographically determined to adopt a wide range of coordination modes, depending on the electronic and coordinative requirements of the metal centre (FIGURE 2.9),[125–129] although the η^9-coordination of the ligand has not yet been observed.

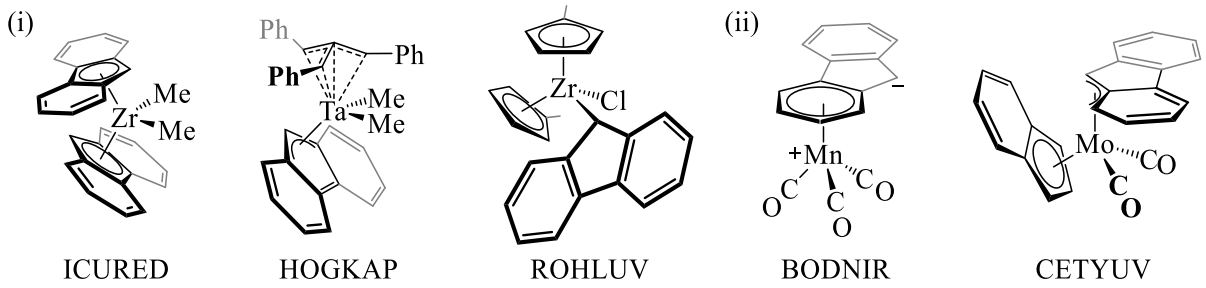

FIGURE 2.9: Examples of the five crystallographically-determined coordination modes of Flu^- within early transition metal complexes deposited in the CSD. (i) Participation of only the central five-membered ring: ICURED[125] (η^5), HOGKAP[126] (η^3) and ROHLUV[127] (η^1). (ii) Additional participation from a six-membered ring: BODNIR[128] (η^3) and CETYUV[129] (η^6).

Prior to the synthesis of complex **6**, it was of interest to investigate whether the fluorenyl ligand could adopt an η^9-coordination mode in order to electronically stabilise the potential reduction product $FluNb^{III}(NDipp)$. Computational analysis* of the hypothetical niobium(III) species indicates that the η^9-fluorenyl complex (η^9-Flu)Nb(NDipp) would indeed be more thermodynamically stable than its counterpart (η^5-Flu)Nb(NDipp) (ΔG = –84 kJ mol^{-1}). The computed gas-phase structures of the two potential reduction products of complex **6** are shown in SCHEME 2.10 and are both located at local energetic minima. Since the DFT study suggests that the η^9-coordination of the fluorenyl ligand is at least thermodynamically accessible herein, this indicates the viability of the precursor complex **6** as a synthetic target.

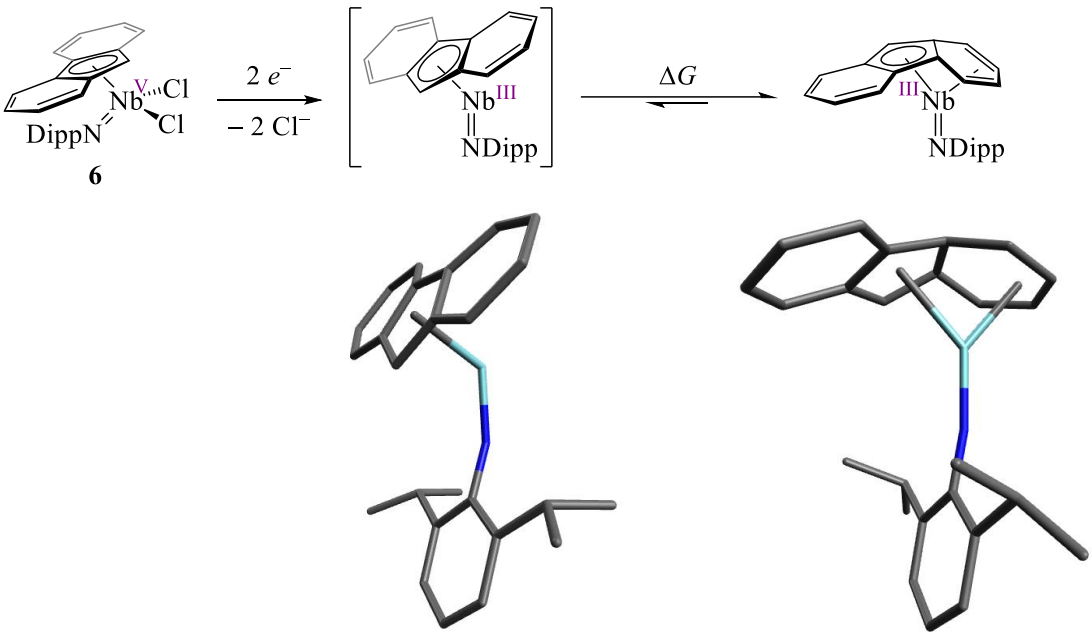

SCHEME 2.10: Envisaged two-electron reduction of complex **6** to form (η^9-Flu)Nb(NDipp) *via* transient (η^5-Flu)Nb(NDipp). The computed (B3LYP/3-21G*) gas-phase structures of the two reduced species are shown.

* The starting geometry for (η^5-Flu)Nb(NDipp) was created by fusing two benzene rings to the Cp-ligand within the experimentally-determined structure of $CpNbCl_2(NDipp)$ (**2**),[89] then removing the two Cl-ligands. Comparatively, that for (η^9-Flu)Nb(NDipp) was formed by superimposing the "(η^9-Ind')" and "Nb(NDipp)" fragments from the solid-state structures of (η^5-Cp*)(η^9-Ind')Zr (Ind' = C_9H_5-1,3-$^iPr_2$)[84] and **2**, respectively, removing the ^{i}Pr-substituents from the indenyl ligand and then fusing a benzene ring to it.

2.4.1. Synthetic routes to $FluNbCl_2(NDipp)$ from $NbCl_3(NDipp)(DME)$

Although the disubstituted complex $Cp_2NbCl(NDipp)$ (**3**) forms undesirably from the reaction between $NbCl_3(NDipp)(DME)$ (**1**) and one equivalent of NaCp·THF (SECTION 2.2.1), the greater degree of steric bulk associated with Flu^- would likely prevent the formation of the *bis*(fluorenyl) complex $Flu_2NbCl(NDipp)$ from the analogous reaction with a reactive fluorenide species.* Accordingly, the synthesis of complex **6** was initially attempted from the reaction of complex **1** with LiFlu (SCHEME 2.11), a fluorenide source which in turn is prepared from fluorene and ^{n}BuLi.[130]

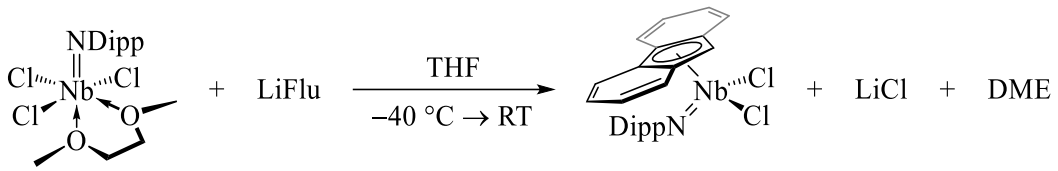

1 **6**

SCHEME 2.11: Attempted synthesis of complex **6** from the reaction between LiFlu and complex **1**.

Analysis of the product resulting from the reaction between complex **1** and LiFlu by ^{1}H NMR spectroscopy was challenging due to the broadness of the signals, despite varying the spectrometer frequency in an attempt to combat effects from complex dynamic behaviour. Aided by ^{1}H–^{1}H correlation spectroscopy (COSY), two sets of ^{1}H NMR signals were identifiable and attributable to the ^{1}H environments of *iso*-propyl groups (assignments in red and blue; FIGURE 2.10). Since these pairs of signals did not match those of either complex **1** or free $DippNH_2$, this suggested that at least two new Dipp-containing species had been produced during the reaction described in SCHEME 2.11. However, repeated attempts to isolate any of these Dipp-containing species *via* crystallisation (in hexanes or toluene) were unsuccessful.

* DFT studies also indicate that $Flu_2NbCl(NDipp)$ is not a viable complex, as no energetic minimum could be located following attempts to optimise its geometry. A starting geometry was formed by fusing two benzene rings to each Cp-ligand within the experimentally-determined molecular structure $Cp_2NbCl(NDipp)$ (**3**).

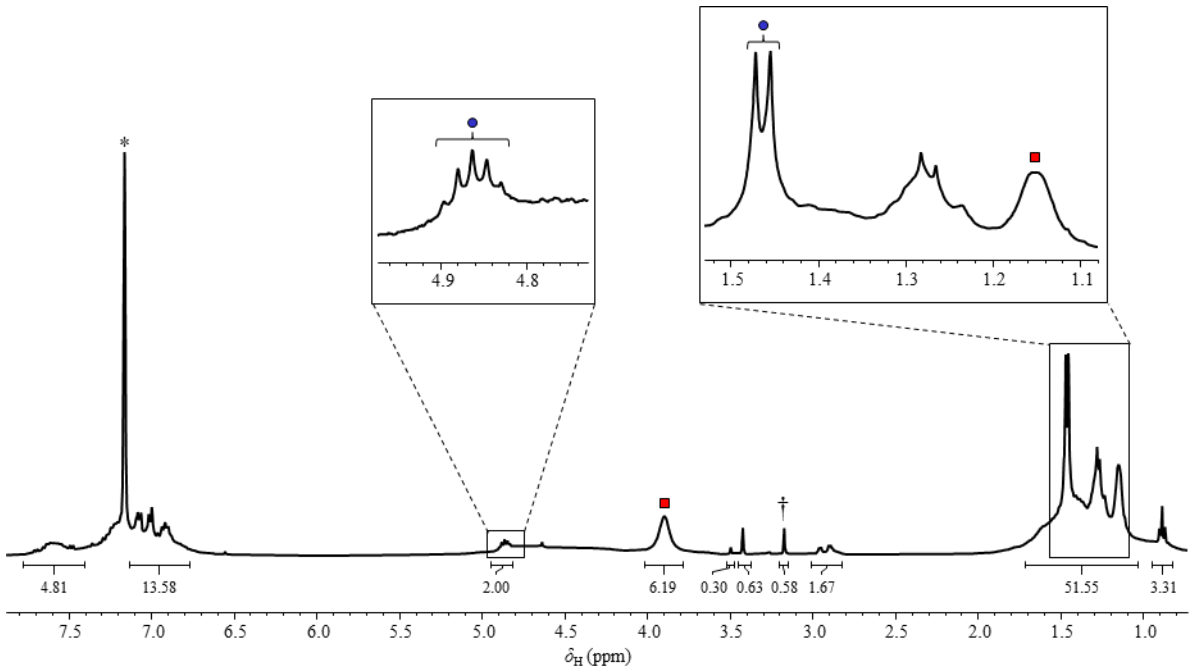

FIGURE 2.10: The ^{1}H NMR (400 MHz, C_6D_6) spectrum of the product mixture from the reaction of LiFlu with $NbCl_3$(NDipp)(DME) (**1**; SCHEME 2.11). Only a few signals attributable to two different Dipp-environments (■ and ●), residual *protio* NMR solvent (*) and fluorene (†) were identifiable.

Mass spectrometric analysis of the product mixture indicated that one of the new Dipp-containing species (FIGURE 2.10) was the desired product **6**, as a signal attributable to its molecular ion (*m*/*z* = 503 Da) was observed in the *i*ASAP+ mass spectrum. Additionally, free fluorene was detected in the spectrum, as determined from a signal at *m*/*z* = 166 Da. While the protonation of a coordinated fluorenyl ligand (*e.g.* in complex **6**) may afford FluH inside the mass spectrometer, there is evidence that fluorene was present prior to mass spectrometric analysis due to the singlet observed at δ_H = 3.42 ppm in the earlier ^{1}H NMR spectrum (designated † in FIGURE 2.10).* The strong basicity of the fluorenide anion (pK_{aH} = 22.6)[131] may account for the competing formation of FluH during the reaction between complex **1** and LiFlu, although the source of the proton remains unclear since rigorous efforts were made to exclude air and moisture.

In an attempt to prevent the competing acid-base reaction during the attempted formation of complex **6** from complex **1**, a less basic (and more covalent) source of the fluorenide moiety was sought. Although thallium(I) fluorenide has been successfully used in transmetallation reactions with $CpMCl_3$ (M = Ti or Zr) to afford $CpFluMCl_2$,[132] the more synthetically-accessible silyl derivative TMSFlu† was selected for reaction with complex **1**. However, despite varying the reaction solvent (between polar DCM and non-polar toluene) and heating at reflux, no reaction occurred between complex **1** and TMSFlu (SCHEME 2.12) since the two reagents were quantitatively recovered from the reaction mixture.

* A singlet at a similar chemical shift (δ_H = 3.47 ppm) was observed in the ^{1}H NMR spectrum of pure FluH, which is attributable to the C*H*$_2$ environment on the five-membered ring.

† TMSFlu is readily synthesised from the reaction between LiFlu and TMSCl.[133]

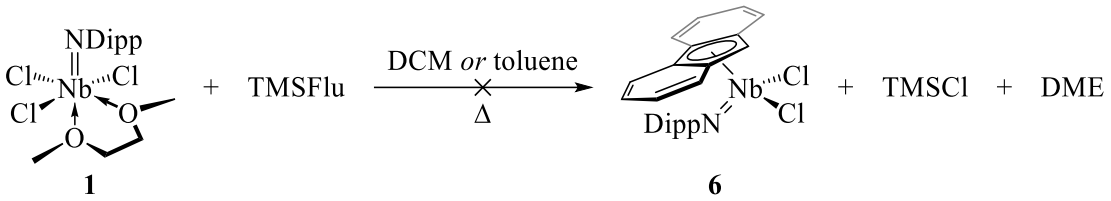

SCHEME 2.12: No reaction occurs between TMSFlu and complex **1** in either DCM or toluene.

The transmetallation reaction between TMSFlu and the imido complex **1** may have been hindered due to the strength of the Si–C bond within the fluorenyl transfer reagent. Furthermore, the considerable steric bulk of the reagents may have also prevented the two species from attaining the close proximity required for transmetallation. In light of this, a different route to complex **6** was sought, proceeding *via* an alternative intermediate to complex **1**.

2.4.2. Synthetic route to $FluNbCl_2(NDipp)$ *via* $FluNbCl_4$

Despite the challenges experienced with preparing cyclopentadienyl complex **2** *via* $CpNbCl_4$ (SECTION 2.1), the synthesis of $FluNbCl_4$ (**7**) was explored as an alternative route to complex **6**. Since Cardoso *et al.* have reported the preparation of $CpNbCl_4$ from $NbCl_5$ and TMSCp,[134] the analogous synthesis of complex **7** was envisaged using the fluorenyl derivative TMSFlu (SCHEME 2.13). Subsequently, the treatment of the fluorenyl complex **7** with DippNH(TMS) in the presence of 2,6-lutidine (2,6-Lut) was proposed to afford the target complex **6**, as achieved by Gibson and co-workers for the synthesis of the cyclopentadienyl analogue **2**.[89]

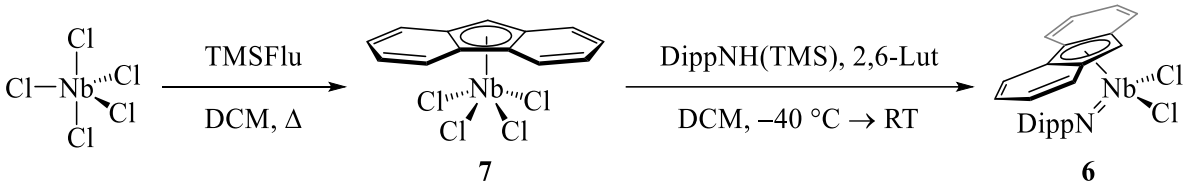

SCHEME 2.13: Proposed route to complex **6** *via* complex **7**, based on the synthesis of $CpNbCl_2(NDipp)$ (**2**)[89] *via* $CpNbCl_4$.[134]

Based on the procedure reported by Cardoso *et al.*,[134] the yellow suspension of $NbCl_5$ and TMSFlu in DCM was heated to reflux. However, no reaction occurred as demonstrated by the near-quantitative recovery of the silyl reagent from the reaction mixture. Since TMSFlu has a larger degree of steric bulk than its cyclopentadienyl derivative, it is possible that the elevated temperatures achievable in a DCM solution were insufficient to overcome the reaction barrier associated with the formation of complex **7** *via* a transmetallation mechanism. Consequently, the reaction between TMSFlu and $NbCl_5$ was repeated in 1,2-dichloroethane (DCE) in order to attain higher reaction temperatures (SCHEME 2.14), where this time, a brown solid was afforded. However, the product proved insoluble in all solvents tested and so could not be analysed by solution-state NMR spectroscopy. Furthermore, no signals were detected in the *i*ASAP+ mass spectrum of the product mixture and elemental analysis was inconclusive (due to

potential contamination from unreacted $NbCl_5$), so no deductions could be drawn regarding the success of the reaction described in SCHEME 2.14.

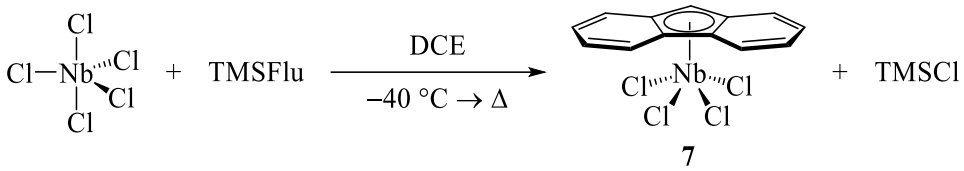

7

SCHEME 2.14: Attempted synthesis of complex **7** from the reaction between $NbCl_5$ and TMSFlu in DCE.

In order to deduce whether complex **7** was present in the brown solid afforded from the reaction in DCE (SCHEME 2.14), this product mixture was treated with DippNH(TMS) and 2,6-Lut according to the literature procedure (SCHEME 2.13) with the intended formation of detectable complex **6**. Following the reaction, extraction into DCM solution and subsequent removal of the solvent *in vacuo* afforded an orange oil. Through ^{1}H NMR spectroscopic analysis, this oil was deduced to contain unreacted DippNH(TMS) along with a new Dipp-containing species (FIGURE 2.11). However, the ^{1}H chemical shifts of the new Dipp-containing species did not coincide with any of those in the earlier impure sample of **6** (synthesised from complex **1** and LiFlu; SECTION 2.4.1). In addition, the molecular ion corresponding to $FluNbCl_2(NDipp)$ (m/z = 503 Da) was not detected in the *i*ASAP+ mass spectrum of the product mixture, further indicating that the half-sandwich imido complex **6** had not been successfully synthesised from $NbCl_5$ *via* the fluorenyl complex **7**.

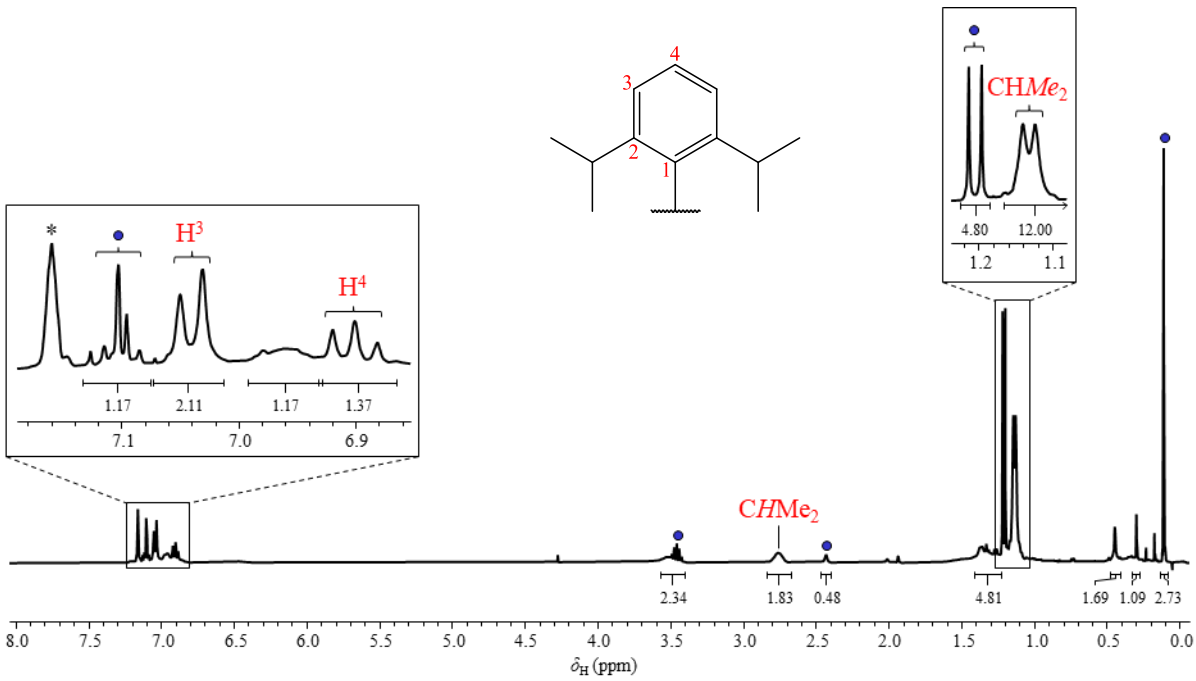

FIGURE 2.11: ^{1}H NMR (400 MHz, C_6D_6) spectrum of the orange oil afforded from the reaction between DippNH(TMS), 2,6-Lut and the solid obtained from the reaction described in SCHEME 2.14. Only signals attributable to unreacted DippNH(TMS) (●), a new Dipp-containing species (red assignments) and residual *protio* NMR solvent (*) were identifiable.

It is possible that the conditions employed during the reaction between $NbCl_5$ and TMSFlu in DCE (SCHEME 2.14) were simply too harsh to result in the successful synthesis of complex **7**. The use of a fluorenyl transfer reagent (MFlu) containing a weaker M–C bond than Si–C (*e.g.* the Sn–C bond in

$^{n}Bu_3SnFlu$) should enable the reaction with $NbCl_5$ to occur at lower temperatures. However, as this would require the additional (and likely non-trivial)* syntheses of new fluorenyl precursors, this route to the half-sandwich fluorenyl imido complex **6** was abandoned.

* For example, the synthesis of $^{n}Bu_3SnFlu$ from LiFlu and $^{n}Bu_3SnCl$ would likely have a challenging purification step if $^{n}Bu_3SnFlu$ proves to be a viscous liquid like its chloride precursor.

2.5. Chapter summary

The work described in this chapter highlights $NbCl_3$(NDipp)(DME) (**1**) as being a useful precursor for the syntheses of various cyclopentadienyl derivatives of the complex, particularly since the mono(imido) complex may be quantitatively synthesised from $NbCl_5$ and $DippNH_2$ in high purity.[102] In addition to providing an alternative route to the half-sandwich imido complex $CpNbCl_2$(NDipp) (**2**) using covalent TlCp, the reaction of complex **1** with ionic NaCp·THF has facilitated the synthesis of the previously unreported niobocene imido complex Cp_2NbCl(NDipp) (**3**). Furthermore, the mono(fluorenyl) derivative $FluNbCl_2$(NDipp) (**6**) may be accessible from the reaction between complex **1** and NaFlu, although this reaction requires further optimisation.

The reduction chemistry of complex **2** has been further explored in an absence of σ-donating and/or π-accepting ligands. However, no niobium(III) species were isolable, not least the target dinitrogen complex $\{CpNb(NDipp)\}_2(\mu,\eta^2,\eta^2\text{-}N_2)$ (**4**). This may be attributed to the instability of the coordinatively and electronically unsaturated intermediate $CpNb^{III}$(NDipp) formed following the two-electron reduction of the niobium(V) complex **2**. Instead, a dinuclear, chloride-bridging niobium(IV) species $\{CpNb(\mu\text{-}Cl)(NDipp)\}_2$ (**5**) was isolable following the reduction of complex **2** using excess magnesium in hexanes (and catalytic THF), although due to the strength of the Nb–Nb bond, the subsequent reactivity of this complex may be limited.

CHAPTER 3:

Exploring chloride abstraction from the sterically-demanding complex $Cp_2NbCl(NDipp)$

3.1. Chapter introduction

With the niobocene imido complex $Cp_2NbCl(NDipp)$ (**3**) in hand (SECTION 2.2.1), it was envisaged that following the removal of the chloride ligand, the resulting cation $[Cp_2Nb(NDipp)]^+$ (**8**$^+$) may exhibit reactivity towards small molecule activation. Indeed, the isoelectronic zirconocene imido counterparts of cation **8**$^+$ have demonstrated the ability of activating the C–H bonds within a range of organic compounds, although the substrate scope for C(sp^3)–H activation remains limited (SECTION 1.3.3).[61,67,68] Since a more electrophilic metal centre has been computed to facilitate C(sp^3)–H activation in early transition metal metallocene imido systems,[42] the niobocenium cation **8**$^+$ may be capable of such reactivity with alkane substrates if the orbital requirements are met. As such, the geometry of the niobocenium imido cation was optimised computationally by density functional theory (DFT) and an MO analysis was performed subsequently;* the resulting computed FMOs for **8**$^+$ are shown in FIGURE 3.1.

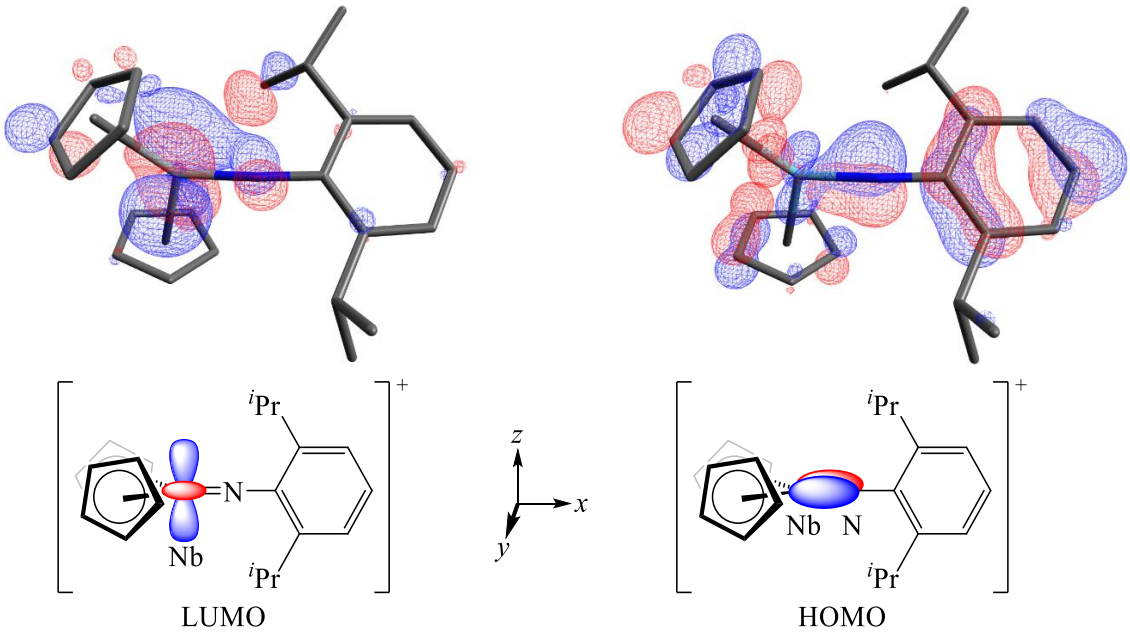

FIGURE 3.1: Computed (B3LYP/3-21G*) FMOs of the hypothetical cation $[Cp_2Nb(NDipp)]^+$ (**8**$^+$), with the significant orbital features shown in the structures below. For clarity, H-atoms are omitted and surfaces are displayed using an isovalue of 0.04.

The computed LUMO of cation **8**$^+$ was found to resemble a metal-based d_{z^2} orbital (67.6% localisation on the Nb-atom), thus fulfilling the orbital requirement for the initial σ-coordination of the alkane R'–H to the cation.[42] However, the HOMO of cation **8**$^+$ has only slight Nb=N π-character (26.9% localisation over the Nb- and N-atoms) and is not fully positioned in the necessitated *xz*-plane. Therefore, the subsequent 1,2-addition of R'–H (and hence overall C–H activation) across the Nb=N

* The input geometry for $[Cp_2Nb(NDipp)]^+$ (**8**$^+$) was generated by removing the Cl-atom from the crystallographically-determined structure of $Cp_2NbCl(NDipp)$ (**3**) and assigning its overall charge as 1+.

bond within the σ-alkane complex $[Cp_2Nb(NDipp)(\eta^2\text{-R'H})]^+$ may be limited by the reorientation of the σ-complex required to achieve the necessary $\pi_{Nb-N}/\sigma^*_{R'-H}$ orbital overlap.

In order to access the niobocenium imido cation $\mathbf{8}^+$ and then assess its reactivity, exchange of the coordinating Cl^- from complex **3** for a weakly-coordinating anion (WCA) is required. There are two main strategies for generating the target cationic complexes [**8**][WCA], as shown in SCHEME 3.1. Firstly, chloride abstraction may be performed using a neutral Lewis acid (LA), where the generated anion $[LA–Cl]^-$ is weakly coordinating. Here, Group III LAs bearing electron-withdrawing groups are typically used, such as EPh^F_3 (E = B or Al and $Ph^F = C_6F_5$)[135] and $Al(OR)_3$ (R = $C\{CF_3\}_3$),[136] with the thermodynamic driving force of the reaction being the formation of a strong covalent E–Cl bond. Alternatively, the WCA (X^-) may be introduced by a salt metathesis reaction using a metal salt (MX), a reaction which is thermodynamically driven by the precipitation of an insoluble by-product MCl, especially for M = alkali metals, thallium(I) or silver(I).[137]

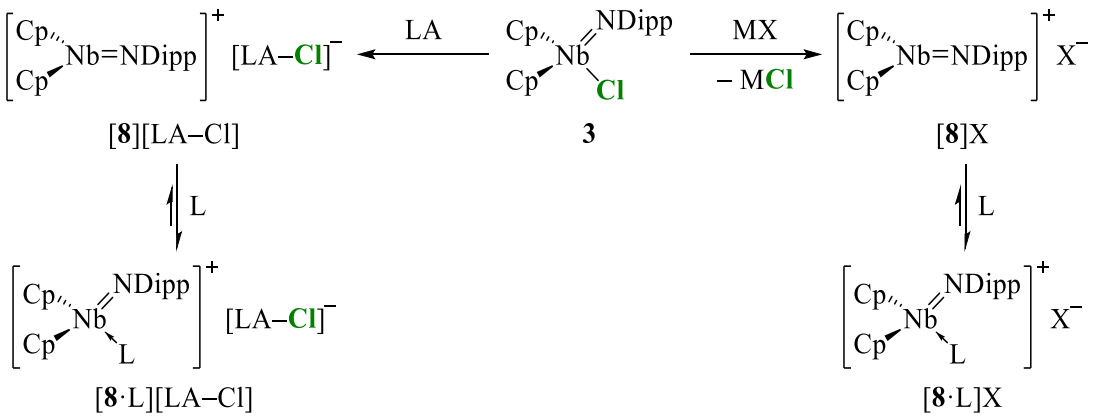

SCHEME 3.1: Proposed routes to cation $[Cp_2Nb(NDipp)]^+$ ($\mathbf{8}^+$) from the chloride complex **3** using either a neutral Lewis acid (LA) or a metal salt (MX); X^- and $[LA–Cl]^-$ are WCAs and L is a Lewis base (*e.g.* MeCN, THF or Et_2O).

As with other metallocene imido complexes, the imido ligand within cation $\mathbf{8}^+$ is only able to act as an X_2-ligand due to the availability of orbitals on the metal centre (SECTION 1.3.1). Consequently, it is likely that the discrete 16-electron niobocenium imido cation $\mathbf{8}^+$ may only exist transiently due to its high reactivity, unless trapped by a Lewis base (L) as the adduct $[Cp_2Nb(NDipp)L]^+$ ($[\mathbf{8}\cdot L]^+$; SCHEME 3.1). Despite being an 18-electron complex, the cation $[\mathbf{8}\cdot L]^+$ may exist in equilibrium with base-free $\mathbf{8}^+$ and hence still present reactivity towards C–H activation. Indeed, dissociation of L is observed with the tantallocenium analogue $[Cp^*_2Ta(N^tBu)(THF)]BPh^F_4$ ($[\mathbf{AK_I}\cdot THF]BPh^F_4$) to facilitate the C–H activation of terminal alkynes (SECTION 1.3.4).[72]

3.2. Electrophilic chloride abstraction from $Cp_2NbCl(NDipp)$

3.2.1. Chloride abstraction from $Cp_2NbCl(NDipp)$ using cations

With a view to synthesising the niobocenium imido species $\mathbf{8}^+$ (or its solvent-adduct $[\mathbf{8}\cdot L]^+$), chloride abstraction from complex **3** was first attempted using $NaBAr^F_4$ (Ar^F = 3,5-*bis*{trifluoromethyl}phenyl). Indeed, this sodium salt has demonstrated capability in removing Cl^- ligands from a variety of transition metal complexes, with the formation of discrete ion-pairs due to $[BAr^F_4]^-$ being an established WCA.[138–140] However, while the equimolar reaction between complex **3** and $NaBAr^F_4$ was attempted herein using multiple solvent systems, in each case no reaction occurred as evidenced by the near-quantitative recovery of the chloride precursor (SCHEME 3.2). Similarly, no reaction took place between $NaSbF_6$ and complex **3**, which indicated that the electrophilicity of the Na^+ cation was insufficient to abstract Cl^- from this niobocene imido system, despite the apparent thermodynamic driving force in forming NaCl.

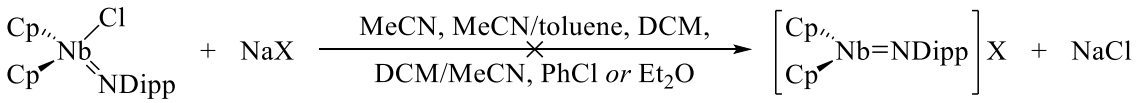

3 [**8**]X

SCHEME 3.2: Attempted chloride abstraction from complex **3** using NaX (X = BAr^F_4 or SbF_6).

As the formation of AgCl has a larger thermodynamic driving force than for the generation of NaCl (with experimental lattice enthalpies of 903 and 786 kJ mol^{-1}, respectively),[141] it was envisaged that silver(I) salts may be more successful at abstracting the chloride ligand from complex **3** than their sodium analogues. Indeed, it has been previously reported that AgOTf is able to abstract the chloride ligand from $Cp_2NbCl(N^tBu)$ (**AK$_{II}$**-Cl), albeit resulting in the covalent triflate complex $Cp_2Nb(N^tBu)(OTf)$ (**AK$_{II}$**-OTf) rather than the discrete ion-pair $[Cp_2Nb(N^tBu)]OTf$ ([**AK$_{II}$**]OTf).[73] Nonetheless, the reactions of complex **3** with silver salts AgX (X = PF_6 or OTf) were attempted herein. However, while the precipitation of an insoluble vivid-blue solid occurred from the starting orange-coloured solution, the target niobocenium cation $\mathbf{8}^+$ was not produced. Instead, it is proposed that a competing reaction occurs between the niobocene imido complex **3** and Ag^+, which will be explored in greater detail in CHAPTER 5.

Phosphenium (R_2P^+) cations have also been reported to abstract chloride anions from transition metal complexes. Use of this class of chloride abstractor has the added benefit that the reactions may be followed by ^{31}P NMR spectroscopy. For example, the chloride abstraction from Cp_2ZrCl_2 by $[(^iPr_2N)_2P]OTf$ results in a marked change in chemical shift from δ_P = +300 ppm (phosphenium) to δ_P = +135 ppm, which is consistent with the formation of the chlorophosphine $(^iPr_2N)_2PCl$ and $Cp_2ZrCl(OTf)$.[142] Consequently, following the success with the zirconocene system, complex **3** was reacted with $[(^iPr_2N)_2P]OTf$ on an NMR-scale in CD_2Cl_2 and the reaction monitored by ^{31}P NMR

spectroscopy. After heating at reflux for ~21 h however, only the signal from the starting phosphenium cation was observed (δ_P = +296.4 ppm), indicating that no reaction had occurred (SCHEME 3.3).

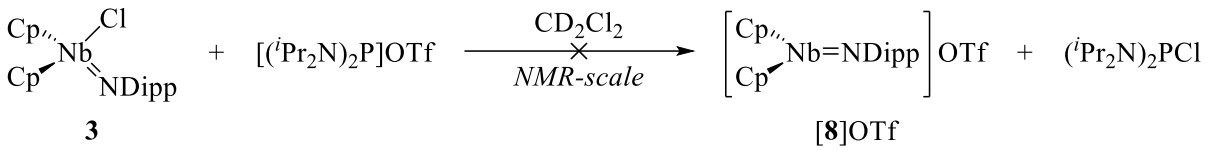

3 [**8**]OTf

SCHEME 3.3: The attempted chloride abstraction from complex **3** using $[(^iPr_2N)_2P]OTf$.

Given that chloride abstraction from the *tert*-butylimido analogue **AK$_{II}$**-Cl was reportedly successful,[73] the lack of reactivity for complex **3** is proposed to result from the greater steric bulk of the Dipp-substituted imido moiety hindering approach of cationic electrophiles to Cl^-. Consequently, the steric bulk of the two $Cp_2NbCl(NR)$ complexes was quantified by the percentage buried volume approach[106] determined at the Cl-atom ($\%V_{bur}^{Cl}$);* the steric maps of the two complexes are shown in FIGURE 3.2. As expected, $Cp_2NbCl(NDipp)$ (**3**) was determined to have a larger $\%V_{bur}^{Cl}$ value than $Cp_2NbCl(N^tBu)$ (**AK$_{II}$**-Cl), with values of 45 and 40%, respectively. While seemingly a small difference in buried volume, a comparable ~2% increase in $\%V_{bur}$ for zirconocene systems has been shown to significantly affect the approach of propene to the metal centre during alkene polymerisation, leading to atactic rather than isotactic polypropylene.[143] Thus, to circumvent the steric constraints imposed by the $DippN^{2-}$ ligand of complex **3**, use of a small electrophile was envisaged as possible route to the chloride abstraction.

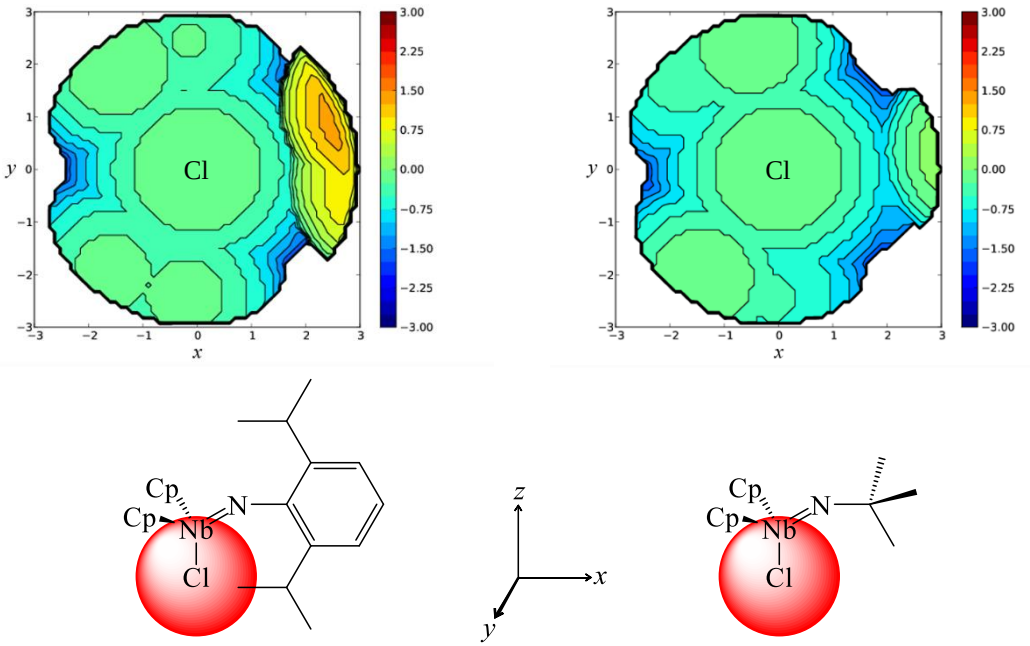

FIGURE 3.2: TOP: Steric maps of $Cp_2NbCl(NDipp)$ (**3**; LEFT) and $Cp_2NbCl(N^tBu)$ (**AK$_{II}$**-Cl; RIGHT) generated using as viewed down the Cl–Nb bond; generated using *SambVca 2.1*.[106] BOTTOM: Illustration of the centring of red spheres (radius = 3 Å) at the Cl-atom of each complex.

* As described in SECTION 2.2.1, *SambVca 2.1* was used to calculate $\%V_{bur}^{Cl}$ by centring a sphere with radius 3 Å at the Cl-atom and determining the percentage volume occupied of that sphere by surrounding atoms.[106] The Cl-atom and all H-atoms were excluded from the calculations.

3.2.2. Chloride abstraction from $Cp_2NbCl(NDipp)$ using $GaCl_3$

Since chloride abstraction from complex **3** was unsuccessful using various cationic Lewis acids (SECTION 3.2.1), attempts to form $[Cp_2Nb(NDipp)]^+$ (**8**$^+$) were instead made using the neutral electrophile gallium trichloride. $GaCl_3$ exists as a dimer (Ga_2Cl_6) in the solid state,[144] making it soluble in most organic solvents (including non-donating solvents), unlike its aluminium counterpart ($\{AlCl_3\}_\infty$) with its principally ionic-lattice structure.[145] The thermodynamic driving force for chloride abstraction by $GaCl_3$ is the formation of a strong Ga–Cl bond (bond dissociation energy = 463 ± 13 kJ mol^{-1})[123] within the tetrachlorogallate ($[GaCl_4]^-$) anion. Generally, $[GaCl_4]^-$ is considered a WCA, as the M···$ClGaCl_3$ interatomic distances in transition metal tetrachlorogallate salts usually exceed the sum of the two atoms' van der Waals' radii ($\sum r_{vdW}$) in crystallographically-determined structures.[24] This reactivity is exemplified by the similar chloride abstraction reported by Trose *et al.* for a dinuclear zirconocene complex as shown in SCHEME 3.4.[146]

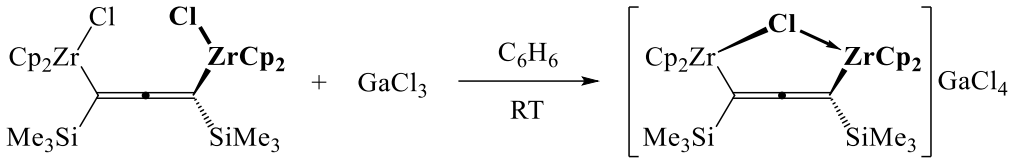

SCHEME 3.4: Chloride abstraction from a dinuclear zirconocene complex using $GaCl_3$ reported by Trose *et al.*[146]

In a method analogous to that used by Trose *et al.*, an NMR-scale reaction between complex **3** and $GaCl_3$ was performed in benzene-d_6 in an attempt to form $[Cp_2Nb(NDipp)]GaCl_4$ ([**8**]$GaCl_4$). Following the addition of equimolar $GaCl_3$ to complex **3**, small single crystals were afforded from solution, indicating that a reaction had occurred between the two soluble reagents. Subsequent X-ray crystallographic analysis indicated the formation of the covalently-bonded tetrachlorogallate complex $Cp_2Nb(ClGaCl_3)(NDipp)$ (**9**; SCHEME 3.5) rather than the discrete ion-pair [**8**]$GaCl_4$. The experimentally-determined molecular structure of **9**, which co-crystallised with a single molecule of C_6D_6, is shown in FIGURE 3.3 and was found to be structurally very similar to its chloride precursor **3**.*

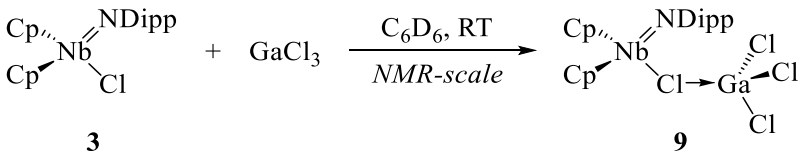

3 **9**

SCHEME 3.5: The reaction between complex **3** and $GaCl_3$ affords the covalent tetrachlorogallate complex $Cp_2Nb(ClGaCl_3)(NDipp)$ (**9**) rather than the ion-pair $[Cp_2Nb(NDipp)]GaCl_4$ ([**8**]$GaCl_4$).

* Calculated structural overlay for the two "$Cp_2NbCl(NDipp)$" fragments of $Cp_2Nb(ClGaCl_3)(NDipp)$ (**9**) and $Cp_2NbCl(NDipp)$ (**3**): RMS distance = 0.2316 Å; maximum distance = 0.4927 Å.

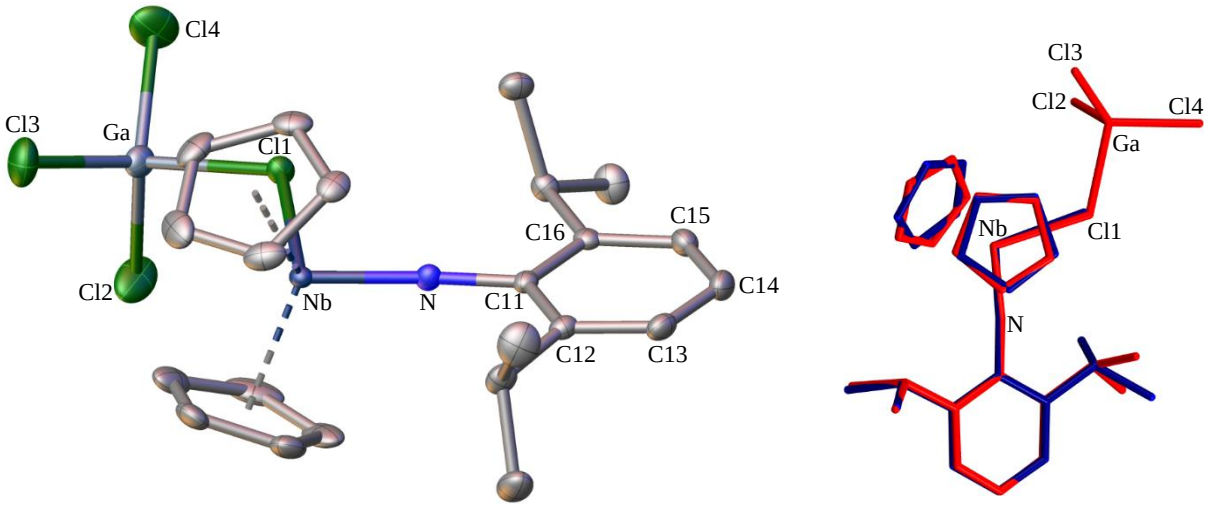

FIGURE 3.3: LEFT: Experimentally-determined molecular structure of $Cp_2Nb(ClGaCl_3)(NDipp)$ (**9**)·C_6D_6; thermal ellipsoids are shown at 50% probability. RIGHT: Molecular overlay between the crystallographically-determined structures of **9** (red) and its precursor $Cp_2NbCl(NDipp)$ (**3**) (blue). H-atoms and the co-crystallised molecule of C_6D_6 are omitted for clarity.

While the Nb–Cl bond of complex **9** is slightly elongated compared to that of its chloride precursor **3** ($\Delta d_{Nb–Cl1} \approx 0.10$ Å; TABLE 3.1), this bond within the tetrachlorogallate complex remains covalent in the solid state as indicated by the interatomic distance of 2.5624(5) Å remaining considerably shorter than the sum of the two atoms' van der Waals' radii ($\sum r_{vdW}$ = 3.95 Å).[147] Although, $[GaCl_4]^-$ anions are typically weakly-coordinating, the reaction between the $GaCl_3$ and L_2CuCl (where L_2 = MeHSi{C_6H_4-*o*-PPh_2}$_2$) also afforded a covalent tetrachlorogallate species, as confirmed crystallographically, where a similar degree of bond elongation was apparent following the binding of $GaCl_3$ ($\Delta d_{Cu–Cl1} \approx 0.13$ Å).[148] Furthermore, the covalency of both complexes **9** and $L_2Cu(ClGaCl_3)$ was evident from the discrepancy between the Ga–Cl1 and Ga–Cl^t (Cl^t = terminal Cl-atom) bonds lengths and the distortion from a tetrahedral geometry about gallium (*i.e.* $\angle_{Cl1–Ga–Cl^t} < 109.5°$; TABLE 3.1).

TABLE 3.1: Selected crystallographically-determined interatomic distances (Å) and angles (°) of complex **9** and literature tetrachlorogallate complex $L_2Cu(ClGaCl_3)$ (L_2 = MeHSi{C_6H_4-*o*-PPh_2}$_2$).[148]

	$Cp_2Nb(ClGaCl_3)(NDipp)$ (9)	**$L_2Cu(ClGaCl_3)$**
$d_{M–Cl1}$ [(a)]	2.5624(5)	2.3587(6)
$\Delta d_{M–Cl1}$ [(a)]	0.1028(6)	0.1300(8)
$d_{Cl1–Ga}$	2.2844(5)	2.2421(5)
$d_{Ga–Cl^t}$ [(b)]	2.1435(4)	2.1544(4)
$\angle_{Cl1–Ga–Cl^t}$ [(c)]	106.00(1)	107.01(1)

[(a)] M = Nb or Cu; $\Delta d_{M–Cl1} = d_{M–Cl1}$(tetrachlorogallate complex) – $d_{M–Cl1}$(chloride complex).
[(b)] Average value of $d_{Cl2–Ga}$, $d_{Cl3–Ga}$ and $d_{Cl4–Ga}$.
[(c)] Average value of $\angle_{Cl1–Ga–Cl2}$, $\angle_{Cl1–Ga–Cl3}$ and $\angle_{Cl1–Ga–Cl4}$.

Although complex **9** has a covalent structure in the solid state, verification of its structure in solution was required to examine whether dissociation may occur to form the target ion-pair [**8**]$GaCl_4$. In order for further solution-state spectroscopic characterisation of the tetrachlorogallate to be performed, the equimolar reaction between complex **3** and $GaCl_3$ was repeated on a larger scale in hexanes, which afforded complex **9** in 43% yield. Subsequent NMR spectroscopic analysis of the tetrachlorogallate complex **9** in CD_2Cl_2 solution revealed that nine separate ^1H environments were attributable to the

$DippN^{2-}$ moiety and two to the Cp-ligands (FIGURE 3.4). This observed magnetic inequivalence was attributed to hindered rotation about the N–C^{ipso} bond in the tetrachlorogallate product, likely resulting from the coordination of the bulky $[ClGaCl_3]^-$ moiety to niobium.* These data are consistent with the integrity of complex **9** as a covalent complex being retained in solution, rather than dissociating to the ion-pair [**8**]$GaCl_4$ (SCHEME 3.6).

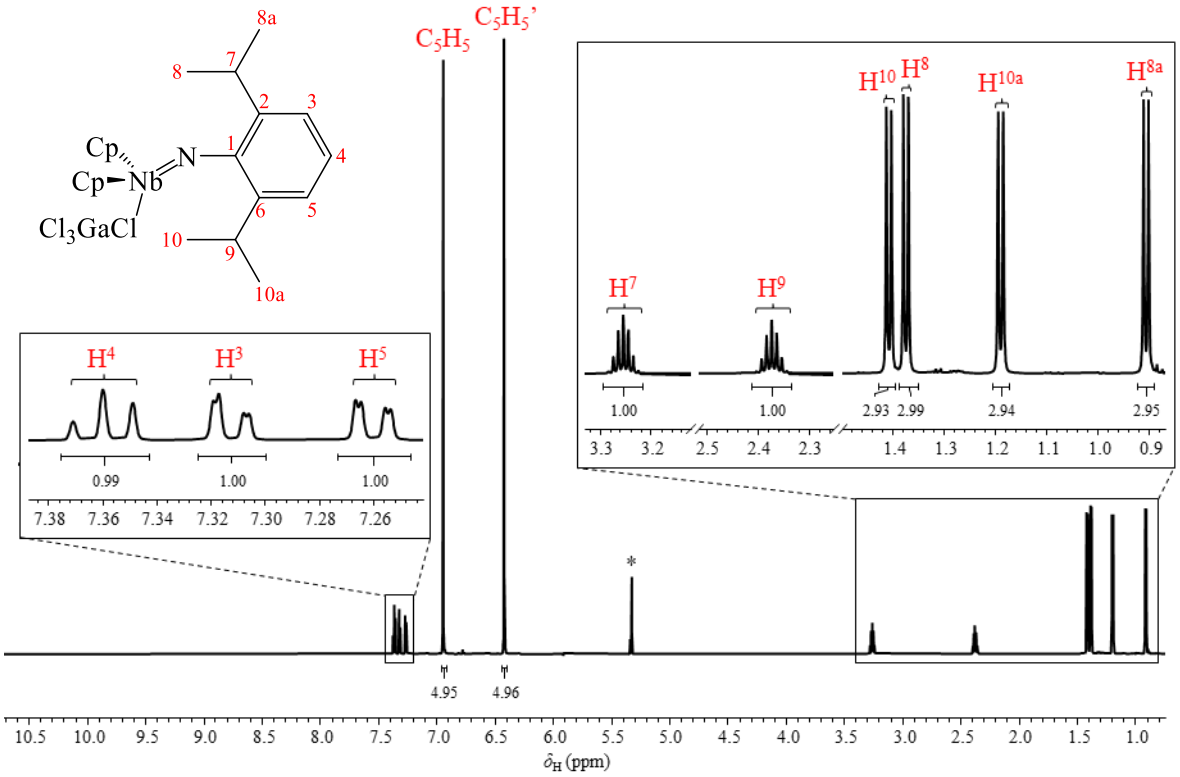

FIGURE 3.4: ^1H NMR (700 MHz, CD_2Cl_2) spectrum of $Cp_2Nb(ClGaCl_3)(NDipp)$ (**9**). Assignments are shown in red and the residual *protio* NMR solvent is designated by an asterisk (*).

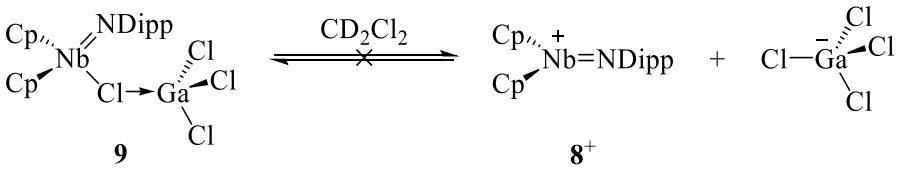

SCHEME 3.6: Dissolution of complex **9** in CD_2Cl_2 unlikely results in its dissociation to $\mathbf{8}^+$ and $[GaCl_4]^-$.

3.2.2.1. Reactivity of $Cp_2Nb(ClGaCl_3)(NDipp)$ with small molecules PMe_3, CO and H_2

While ^1H NMR spectroscopic analysis indicated that complex **9** remained covalent in solution from the magnetic inequivalence about the Dipp- and Cp-ligands, a computational natural bond orbital (NBO)

* For a complex with unhindered rotation, *e.g.* $Cp_2NbCl(NDipp)$ (**3**), only four ^1H NMR signals would be observed for the imido substituent and a lone signal attributable to the two cyclopentadienyl ligands.

analysis* of both complexes **9** and **3** revealed that the Nb–Cl bond was weaker in the tetrachlorogallate species based on Wiberg bond indices (WBIs) of 0.626 and 0.914, respectively. As such, it was envisaged that the introduction of a neutral donor (L) may be sufficient to cleave the Nb–Cl bond in complex **9** and displace the $[GaCl_4]^-$ anion, forming the 18-electron ion-pair $[Cp_2Nb(NDipp)L]GaCl_4$ ($[\mathbf{8}\cdot L]GaCl_4$; SCHEME 3.7i). Indeed, this type of ligand displacement reaction has been demonstrated by Humphries *et al.* for $Cp_2Nb(N^tBu)(OTf)$ ($\mathbf{AK_{II}}$-OTf), where reaction with neutral PMe_3 displaces the weakly-coordinating triflate ligand to afford the ion-pair $[Cp_2Nb(N^tBu)(PMe_3)]OTf$ ($[\mathbf{AK_{II}}\cdot PMe_3]OTf$ in excellent (96%) yield (SCHEME 3.7ii).[73]

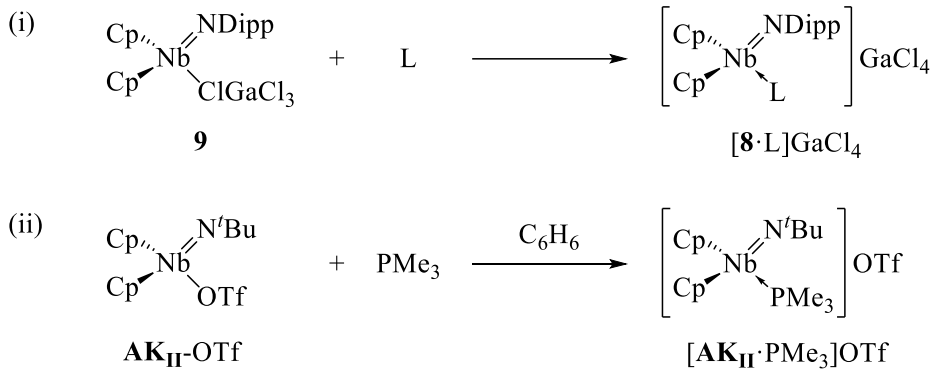

SCHEME 3.7: (i) The envisaged displacement of $[GaCl_4]^-$ from complex **9** by a neutral donor (L) to form ion-pair $[\mathbf{8}\cdot L]GaCl_4$. (ii) Analogous displacement of TfO^- by PMe_3 reported for $Cp_2Nb(N^tBu)(OTf)$ ($\mathbf{AK_{II}}$-OTf).[73]

Based on the success of the reaction described by Humphries *et al.*,[73] PMe_3 was selected as an appropriate neutral nucleophile for the displacement of $[GaCl_4]^-$ from complex **9**. To explore this reactivity, a sample of complex **9** was formed *in situ* from an equimolar reaction between complex **3** and $GaCl_3$ on an NMR-scale in CD_2Cl_2 (the success of which being confirmed by NMR spectroscopic analysis). Subsequently, ~1.5 equivalents of PMe_3 were added by vacuum transfer directly into the Young's NMR tube containing the solution of complex **9** (at –196 °C), whereupon warming to room temperature the rapid precipitation of a white solid occurred. Analysis of the **9**/PMe_3 reaction mixture by solution-state ^1H NMR spectroscopy revealed that the chloride complex **3** had been generated as the only soluble niobium-containing species. This is consistent with the neutral $GaCl_3$ moiety being displaced from complex **9** (SCHEME 3.8) instead of the desired $[GaCl_4]^-$ ligand.

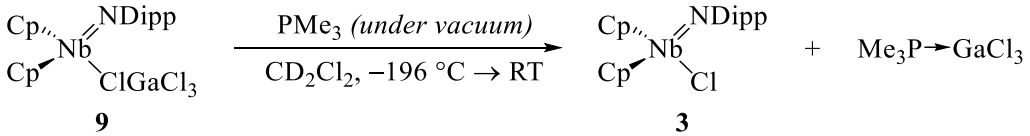

SCHEME 3.8: Reacting complex **9** with PMe_3 produces complex **3** and $GaCl_3\cdot PMe_3$ instead of $[Cp_2Nb(NDipp)(PMe_3)]GaCl_4$ ($[\mathbf{8}\cdot PMe_3]GaCl_4$).

* NBO analyses of $Cp_2Nb(ClGaCl_3)(NDipp)$ (**9**) and $Cp_2NbCl(NDipp)$ (**3**) were performed on the DFT-optimised gas-phase structures of the complexes, where the experimentally-determined molecular structures were used as the input geometries for the calculations.

The formation of the Lewis adduct $GaCl_3{\cdot}PMe_3$ alongside complex **3** was supported by the presence of a symmetrical multiplet in the $^{31}P\{^1H\}$ NMR spectrum (centred at δ_P = –29.0 ppm; FIGURE 3.5). This multiplet arises from two overlapping 1:1:1:1 quartets from the one-bond coupling between the ^{31}P nucleus and the two quadrupolar (both I = 1½) isotopes of gallium, ^{69}Ga ($^1J_{^{69}Ga–P}$ = 783 Hz) and ^{71}Ga ($^1J_{^{71}Ga–P}$ = 999 Hz).* The adduct $GaCl_3{\cdot}PMe_3$ has been synthesised previously from the direct reaction between $GaCl_3$ and PMe_3, although never characterised by NMR spectroscopy;[149,150] however, the related adduct $GaCl_3{\cdot}PPh_3$ was reported to have a similar chemical shift (δ_P = –5.5 ppm) and a coupling constant within the same order of magnitude ($^1J_{^{71}Ga–P}$ = 721 Hz) as those of $GaCl_3{\cdot}PMe_3$ described herein.[151] In addition the multiplet attributable to $GaCl_3{\cdot}PMe_3$, a minor signal was detected in the $^{31}P\{^1H\}$ NMR spectrum of the **3**/$GaCl_3{\cdot}PMe_3$ product mixture (singlet at δ_P = +24.2 ppm; FIGURE 3.5). This is consistent with a signal reported for an unnamed side-product afforded from the reaction between PMe_3 and CD_2Cl_2 (presumably a phosphenium substitution product, *e.g.* $[Me_3P(CD_2Cl)]Cl$).[152]

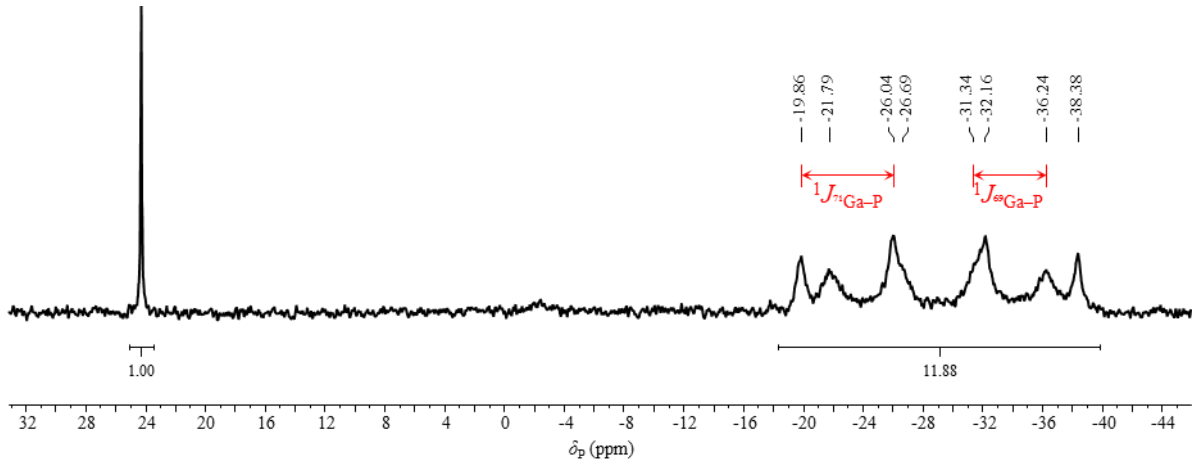

FIGURE 3.5: $^{31}P\{^1H\}$ NMR (162 MHz, CD_2Cl_2) spectrum following the reaction between $Cp_2Nb(ClGaCl_3)(NDipp)$ (**9**) and PMe_3. The multiplet is attributed to $GaCl_3{\cdot}PMe_3$ and the singlet to a side-product from reaction between PMe_3 and CD_2Cl_2.

The preferential attack of complex **9** at the gallium centre rather than niobium by PMe_3 may be explained using simple hard-soft acid-base arguments: the "soft" Lewis base PMe_3 forms a stronger bond with the "soft" Lewis acid $GaCl_3$[153] than with the "harder" monocationic niobium centre,[154] hence forming $GaCl_3{\cdot}PMe_3$ in preference to $[Cp_2Nb(NDipp)(PMe_3)]^+$. Thus, in order to promote reaction at the niobium centre of **9**, reaction with a "harder" Lewis base, namely carbon monoxide,† was attempted in order to displace $[GaCl_4]^-$. To this end, CO (~1 atm) was admitted to a Young's NMR tube containing a degassed solution of **9** in CD_2Cl_2 and the reaction was monitored by NMR spectroscopy. However, no changes in either the ^1H or ^{13}C NMR spectrum of the reaction mixture were observed, even after heating the **9**/CO solution for several hours at 50 °C, indicating that no reaction had occurred (SCHEME

* The relative natural abundances of ^{69}Ga and ^{71}Ga are 60.1% and 39.9%, respectively.

† The hardnesses of CO and PMe_3 have been determined as 7.9 and 4.0 eV, respectively.[154]

3.9).* This is consistent with a relatively strong Nb–Cl bond within the tetrachlorogallate complex **9**, as indicated by the aforementioned NBO analysis.

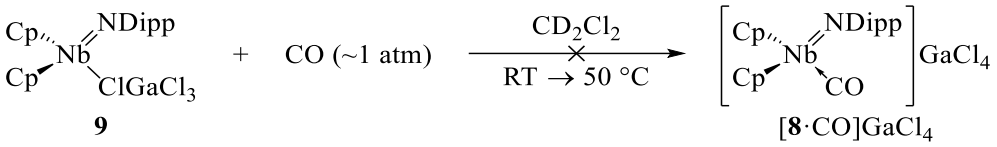

SCHEME 3.9: Attempted reaction of complex **9** with carbon monoxide (~1 atm).

In a similar context, it was of interest to explore whether the reaction between H_2 and complex **9** would result in the 1,2-addition across the Nb=N bond with the synthesis of $[Cp_2NbH(NHDipp)]GaCl_4$. A similar reactivity has been demonstrated by Blake *et al.* with hydrogenation of $[Cp^*_2Ta(N^tBu)(THF)]BPh^F_4$ ($[\mathbf{AK_I}\cdot THF]BPh^F_4$) affording $[Cp^*_2TaH(NH^tBu)]BPh^F_4$ ($[\mathbf{AL}\text{-}H]BPh^F_4$; SECTION 1.3.4),[72] albeit following the dissociation of a neutral THF ligand rather than a coordinating $[GaCl_4]^-$ anion. Thus, a CD_2Cl_2 solution of tetrachlorogallate **9** was charged with H_2 (~1 atm). However, again, neither the ^1H nor ^{13}C NMR spectrum changed following the addition of H_2 to complex **9**, indicating that no reaction had taken place.†

Although $[GaCl_4]^-$ is often described as weakly-coordinating, the Nb–Cl bonding interaction in complex **9** is sufficiently strong that the anionic ligand is not readily displaced by neutral donor ligands or dihydrogen. Therefore, it seemed unlikely that the desirable C–H activation or [2 + 2] cycloaddition reactions of the Group V metallocenium imido complexes (described in SECTION 1.3.4) could be replicated with this tetrachlorogallate complex. As the nucleophilic displacement of the $[GaCl_4]^-$ anion from complex **9** described herein was unsuccessful, attention instead turned to the electrophilic abstraction of this ligand from this complex as a route to the niobocenium cation $\mathbf{8}^+$.

3.2.2.2. Reactivity of $Cp_2Nb(ClGaCl_3)(NDipp)$ with further $GaCl_3$

Since the tetrachlorogallate ligand of complex **9** was not displaceable by nucleophilic substitution, it was envisaged that introduction of a further equivalent of the $GaCl_3$ may result in the electrophilic abstraction of $[GaCl_4]^-$ with the formation of the known heptachlorodigallate ($[Ga_2Cl_7]^-$) anion. Crystallographic comparison of the pnictogenium chlorogallate species $As(ClGa_nCl_{3n})(N\{TMS\}_2)_2$[155] and $P(ClGa_nCl_{3n})(=NMes^*)(\eta^6\text{-}C_6H_5R)$ ($Mes^* = C_6H_2\text{-}2,4,6\text{-}^tBu_3$ and R = H or Me)[156,157] revealed that the pnictogen (E)–chlorine bond is 0.24–0.35 Å longer in the digallate (n = 2) complexes compared with their monogallate (n = 1) counterparts (TABLE 3.2). The elongation of E–Cl in turn suggests that $[Ga_2Cl_7]^-$ is more weakly-coordinating than $[GaCl_4]^-$; therefore, if the heptachlorodigallate anion can

* A signal attributable to unbound, dissolved CO (δ_C = 184.2 ppm) was present throughout the reaction.

† A singlet (at δ_H = 4.60 ppm) corresponding to dissolved H_2 was present throughout the attempted reaction.

be generated from the tetrachlorogallate complex **9** (or its chloride precursor **3**) by the addition of further $GaCl_3$, it was envisaged that the ion-pair $[Cp_2Nb(NDipp)]Ga_2Cl_7$ ([**8**]Ga_2Cl_7) may form (SCHEME 3.10).

TABLE 3.2: Crystallographically-determined pnictogen (E)–chlorine interatomic distances ($d_{E–Cl}$; Å) within the molecular structures of arsenium[155] and phosphenium[156,157] species featuring each of $[ClGaCl_3]^-$ and $[ClGa_2Cl_6]^-$ ligands.

		P(=NMes*)X(η^6-C_6H_5R)	
	As(N{TMS}$_2$)$_2$X	**R = H**	**R = Me**
X = $ClGaCl_3$	3.4696(6)	3.083(4)	3.139(9)
X = $ClGa_2Cl_6$	3.708(1)	3.395(3)	3.487(4)

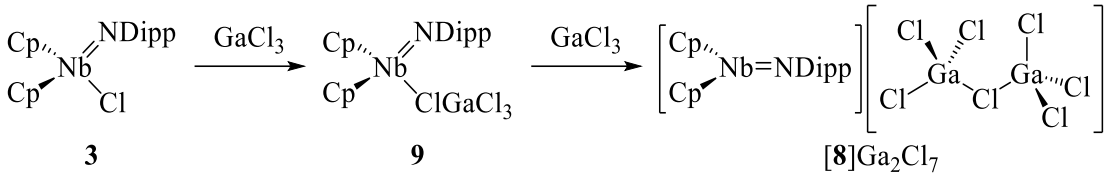

3 **9** [**8**]Ga_2Cl_7

SCHEME 3.10: The envisaged synthesis of the ion-pair [**8**]Ga_2Cl_7 from complex **3** *via* complex **9**.

The envisaged synthesis of the ion-pair [**8**]Ga_2Cl_7 was first attempted on an NMR scale, whereby excess $GaCl_3$ (~2.3 equivalents) was added to a CD_2Cl_2 solution of complex **3**. On standing at room temperature, single crystals formed (over ~18 h) from the CD_2Cl_2 solution, indicating that a new species had been produced.* The XRD analysis of the recovered single crystals revealed that the product was an unusual *para*-aryl Ga_2Cl_6-adduct of **9**, namely $Cp_2Nb(ClGaCl_3)(N\{Dipp{\cdot}Ga_2Cl_6\})$ (**10**), rather than desired ion-pair [**8**]Ga_2Cl_7; the molecular structure of complex **10** is shown in FIGURE 3.6.

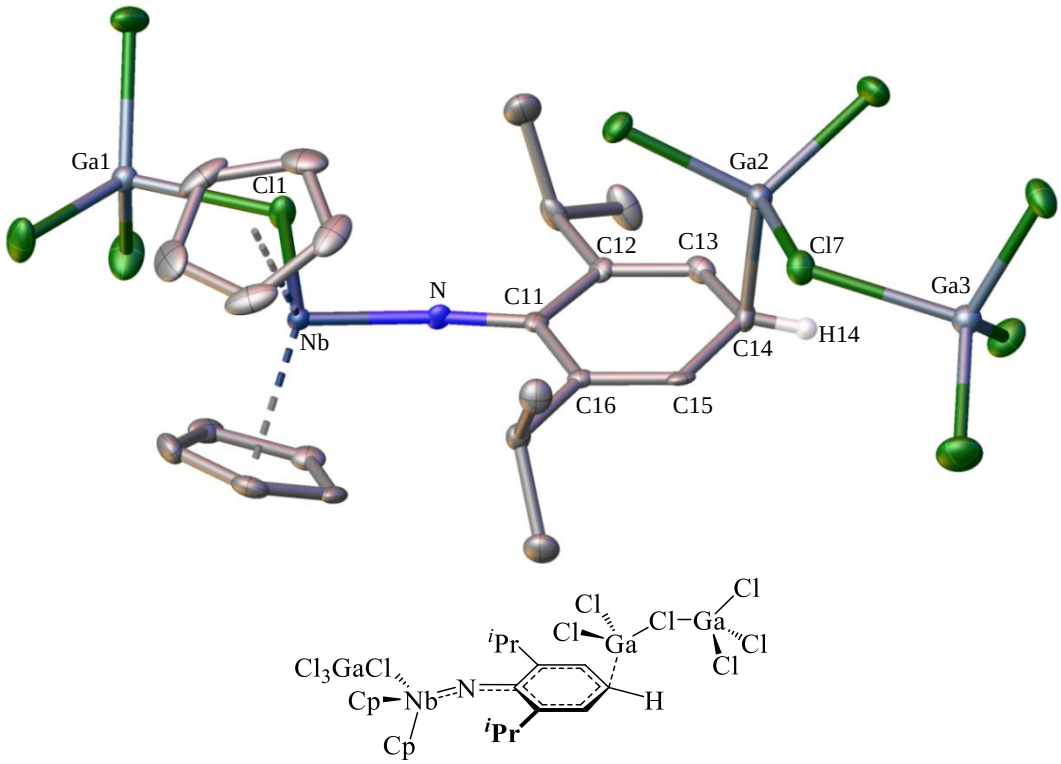

FIGURE 3.6: Crystallographically-determined molecular structure of $Cp_2Nb(ClGaCl_3)(N\{Dipp{\cdot}Ga_2Cl_6\})$ (**10**); thermal ellipsoids are shown at 50% probability and H-atoms (except for H14, computed) are omitted for clarity.

* $GaCl_3$, the chloride complex **3** and the tetrachlorogallate complex **9** are all soluble in DCM.

As shown in TABLE 3.3, the C14–Ga2 interatomic distance of 2.059(5) Å within the molecular structure of **10** is consistent with a formal C···Ga π-bonding interaction between the aryl carbon atom and the gallium centre (since $\sum r_{vdW}$ = 3.9 Å),[147] rather than the simple co-crystallisation of Ga_2Cl_6 with complex **9**. Indeed, computational NBO analysis of complex **10** determined the presence of a weak bond (WBI = 0.328) between C^{para} and the gallium centre. In the context of transition metal arylimido complexes, complex **10** is the only example to date of a crystallographically-determined structure featuring bonding (of any hapticity) between the aryl substituent and a Group XIII element. The only comparable structure in the literature is the main group aluminium imido derivative KOHLID (FIGURE 3.7),[158] which features a similar bonding interaction (WBI = 0.431; TABLE 3.3) between the C^{para}-atom and another Al-atom.

TABLE 3.3: Crystallographically-determined interatomic distances (Å) of $Cp_2Nb(ClGaCl_3)(N\{Dipp{\cdot}Ga_2Cl_6\})$ (**10**), $Cp_2Nb(ClGaCl_3)(NDipp)$ (**9**), KOHLID and MABHAB (FIGURE 3.7). The computed WBIs are displayed in red.*

	Complex 10		**Complex 9**		**KOHLID**		**MABHAB**	
$d_{C14–E}$ [(a)]	2.059(5)	0.328	–	–	2.004(4)	0.431	1.585(2)	0.931
$d_{M–N}$ [(b)]	1.870(2)	1.826	1.7940(15)	2.079	1.734(4)	0.715	1.678(2)	0.755
$d_{N–C11}$	1.315(3)	1.281	1.383(2)	1.121	1.270(5)	1.709	1.267(3)	1.717
$d_{C11–C12}$ [(c)]	1.458(3)	1.220	1.417(1)	1.305	1.487(4)	1.046	1.504(2)	1.039
$d_{C12–C13}$ [(c)]	1.350(3)	1.514	1.392(2)	1.421	1.354(5)	1.729	1.327(2)	1.794
$d_{C13–C14}$ [(c)]	1.436(3)	1.227	1.383(1)	1.417	1.465(4)	1.082	1.490(2)	1.012

[(a)] Where E = Ga (for **10**), Al (for KOHLID) or C (for MABHAB); $d_{C14–E} = ½(d_{C14–C17} + d_{C14–C18})$ for MABHAB.
[(b)] Where M = Nb (for **10** and **9**), Al (for KOHLID) or Si (for MABHAB).
[(c)] Average values for chemically equivalent bonds (*e.g.* C11–C12 ≡ C11–C16).

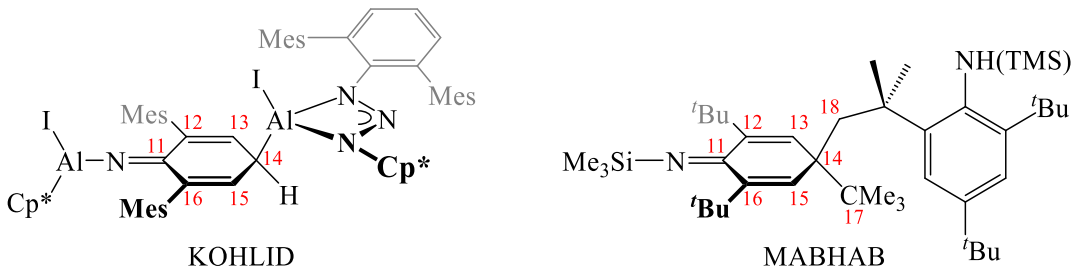

FIGURE 3.7: Crystallographically-determined structures of KOHLID[158] and MABHAB.[159]

Associated with the C^{para}···Ga π-bonding interaction within complex **10** is the elongation of Nb–N, C11–C12 and C13–C14 bonds relative to those in its precursor **9**, along with the shortening of N–C11 and C12–C13 bonds (TABLE 3.3). As also reflected in the computed WBIs of the Ga_2Cl_6-adduct, complex **10** features a slightly quinoidal ring system with alternating bonds of single- and double-bond character, which are similar to those of the aluminium complex KOHLID. In contrast, the conjugated silylimine MABHAB (FIGURE 3.7)[159] has true bond alternation across the ring system due to the presence of two singly-bonded *para*-substituents (average WBI = 0.931).

* The solid-state structures of $Cp_2Nb(ClGaCl_3)(N\{Dipp{\cdot}Ga_2Cl_6\})$ (**10**), $Cp_2Nb(ClGaCl_3)(NDipp)$ (**9**), KOHLID[158] and MABHAB[159] were geometrically optimised by DFT prior to NBO analysis.

The formation of the unusual $C^{para}\cdots Ga$ π-bonding interaction in the Ga_2Cl_6-adduct may be rationalised by examination of the computed FMOs of complex **10** and those of its precursors **9** and Ga_2Cl_6.* As shown in FIGURE 3.8, adduct **10** is formed from the donation of the HOMO of complex **9** into the LUMO of Ga_2Cl_6, leading to the electronic stabilisation of the HOMO (ΔE_{HOMO} = –1.11 eV). While the HOMO of complex **9** is principally localised at the imido N-atom (19.8%; TABLE 3.4), electrophilic attack of this position is likely inhibited by the steric constraints imposed by the Cp-ligands and ^{i}Pr-groups. Consequently, electrophilic attack of complex **9** by Ga_2Cl_6 at the more accessible *para*-position (11.9% localisation of HOMO) occurs to result in the formation of the adduct **10**. Comparatively, there is a negligible contribution to the HOMO from the terminal chlorine (Cl^t) atoms of the tetrachlorogallate ligand, which goes some way to explaining why the desired electrophilic attack of complex **9** at Cl^t by Ga_2Cl_6 does not take place and hence the target ion-pair [**8**]Ga_2Cl_7 is not formed.

TABLE 3.4: Calculated[161] percentage contributions of selected atoms in $Cp_2Nb(ClGaCl_3)(NDipp)$ (**9**) towards its computed LUMO and HOMO.

		Individual atomic contribution to MO (%)								
MO	**Energy / eV**	**Nb**	**μ-Cl**	**N**	**C^{ipso}**	**C^{ortho}** *(a)*	**C^{meta}** *(a)*	**C^{para}**	**Ga**	**Cl^t** *(a,b)*
LUMO	–2.62	61.0	7.4	6.2	0.4	0.3	0.1	0.0	2.8	0.9
HOMO	–5.74	5.3	0.0	19.8	7.5	7.7	1.0	11.9	0.0	0.0

(a) Average values of both C^{ortho}, both C^{meta} and all three Cl^t atoms.
(b) Terminal Cl-atoms of the tetrachlorogallate ligand (Cl2–4 in FIGURE 3.3).

* The crystallographically-determined molecular structures of Ga_2Cl_6,[160] complex **9** and complex **10** were geometrically optimised by DFT prior to MO analysis.

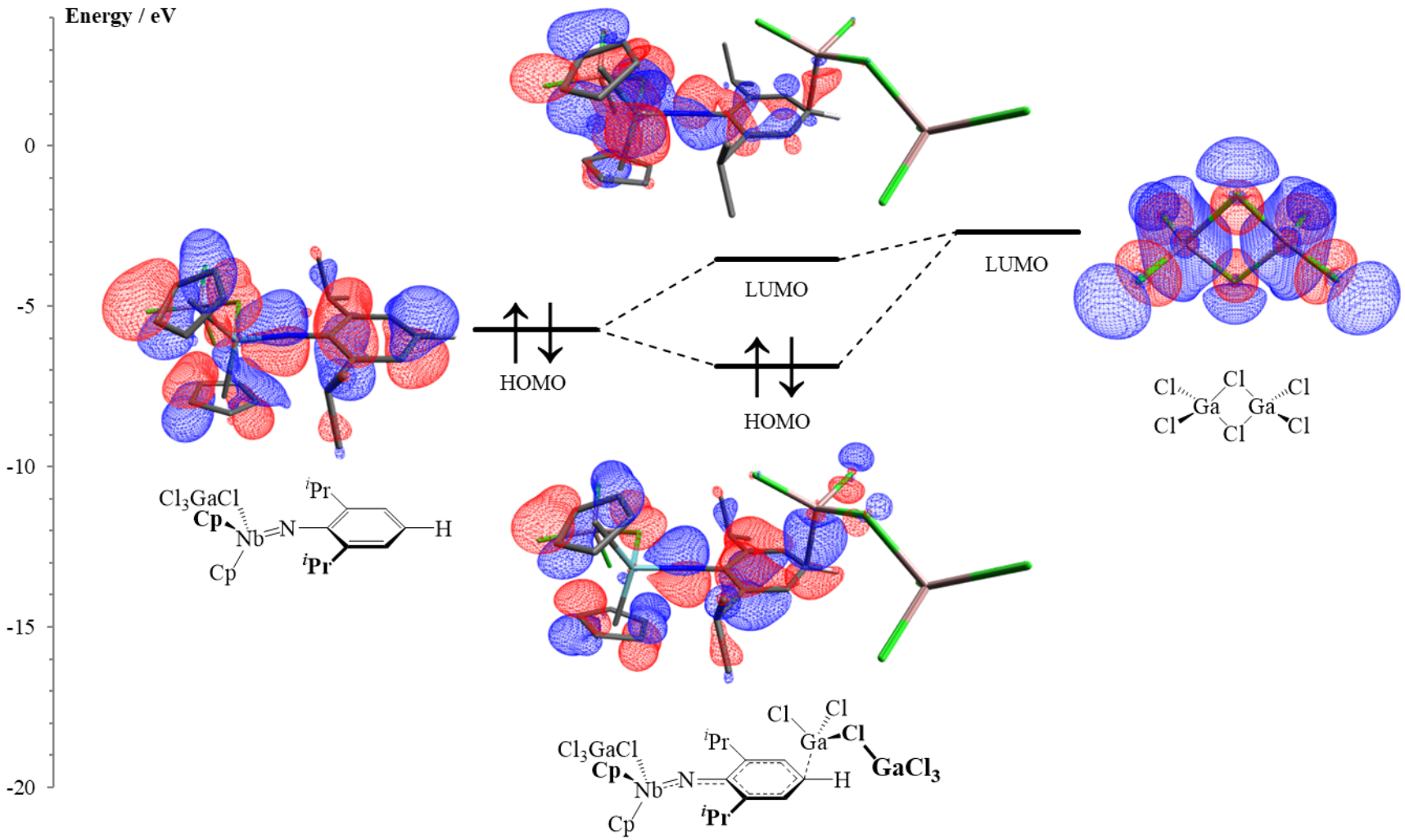

FIGURE 3.8: Computed (B3LYP/3-21G*) MO diagram of $Cp_2Nb(ClGaCl_3)(N\{Dipp{\cdot}Ga_2Cl_6\})$ (**10**), formed from the overlap between the HOMO of $Cp_2Nb(ClGaCl_3)(NDipp)$ (**9**) and the LUMO of Ga_2Cl_6. For clarity, H-atoms are omitted and surfaces are displayed using an isovalue of 0.025.

In order to further characterise the Ga_2Cl_6-adduct **10**, the reaction between complex **3** and $GaCl_3$ was repeated in DCM using three equivalents of gallium trichloride (SCHEME 3.11). As observed during its NMR-scale synthesis, complex **10** precipitated from the DCM solution and was isolated in 45% yield following cannula filtration and drying under a stream of nitrogen (to prevent the sublimation of π-bonded Ga_2Cl_6). Elemental analysis of **10** was consistent with the crystallographically-determined structure of the complex. However, only the $[M - Ga_2Cl_6]^+$ ion (*m/z* = 609 Da) was observed in the *i*ASAP+ mass spectrum of the complex, presumably as the weak $C^{para}\cdots Ga_2Cl_6$ π-bonding interaction is susceptible to fragmentation inside the spectrometer. Furthermore, complex **10** could not be characterised by solution-state NMR spectroscopy due to its insolubility in all solvents trialled; Lewis basic NMR solvents (*e.g.* MeCN-d_3 and THF-d_8) were avoided due to the inevitable disruption of the $C^{para}\cdots Ga$ π-interaction through coordination of the solvent to the electrophilic gallium centres.

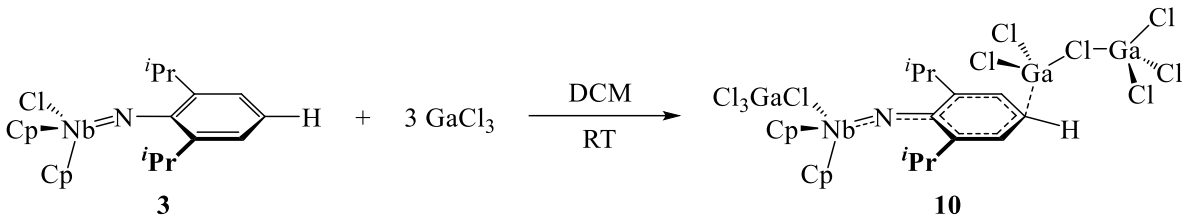

SCHEME 3.11: Formation of $Cp_2Nb(ClGaCl_3)(N\{Dipp{\cdot}Ga_2Cl_6\})$ (**10**) from complex **3** and three equivalents of $GaCl_3$.

3.3. Nucleophilic chloride displacement of $Cp_2NbCl(NDipp)$

Following the unsuccessful attempts to directly abstract the chloride ligand from complex **3** (SECTION 3.2), it was envisaged that the nucleophilic displacement of the Cl^- ligand for another anionic ligand (Nuc^-) to form $Cp_2Nb(NDipp)(Nuc)$, followed by electrophilic abstraction of Nuc^-, may lead to the target cation $\mathbf{8}^+$ (SCHEME 3.12). Due to the previously established strength of the Nb–Cl bond within complex **3**, it is unlikely that nucleophilic displacement of Cl^- by Nuc^- will proceed *via* a dissociative ("S_N1-style") mechanism. However, the introduction of the Nuc^- anion into the coordination sphere of complex **3** may be sufficient to weaken the Nb–Cl bond, either *via* the formation of an anionic intermediate $[Cp_2NbCl(NDipp)(Nuc)]^-$ by an associative mechanism or *via* a concerted process according to an interchange ("S_N2-type") mechanism.

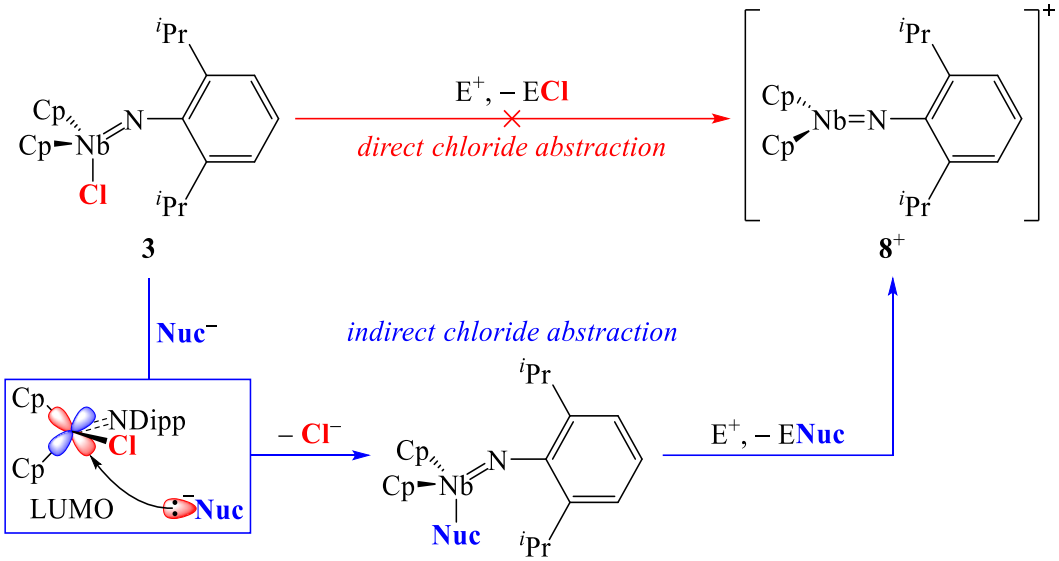

SCHEME 3.12: Proposed alternative route from chloride **3** to cation $\mathbf{8}^+$, *via* the nucleophilic displacement of Cl^- to form $Cp_2Nb(NDipp)(Nuc)$ (Nuc^- = an anionic nucleophile), followed by abstraction of the Nuc^- ligand.

As shown in SCHEME 3.12, the computed LUMO of complex **3** is metal-centred and located within the "Cp_2Nb" plane of the sterically bulky complex,* therefore a small nucleophile must be used in order to achieve attack at this position. Suitable nucleophiles for reaction with complex **3** may include rod-like *pseudo*-halides (*e.g.* N_3^-) or small alkyl anions (*e.g.* Me^-), particularly as subsequent abstraction of these anionic ligands to form cationic species has previously been demonstrated using trialkyloxonium[162] and trityl (Tr^+)[163] salts, respectively (SCHEME 3.13). Notably, methyl abstraction from the *tert*-butylimido analogue of complex **3**, namely $Cp_2NbMe(N^tBu)$ (**AK$_{II}$**-Me), was achieved in good yield (89%) using a trityl salt (SECTION 1.3.4).[73] Therefore, the synthesis and subsequent abstraction of Me^- from $Cp_2NbMe(NDipp)$ seemed a plausible route to cation $\mathbf{8}^+$.

* The MO analysis of complex **3** is discussed in further detail in SECTION 4.1.

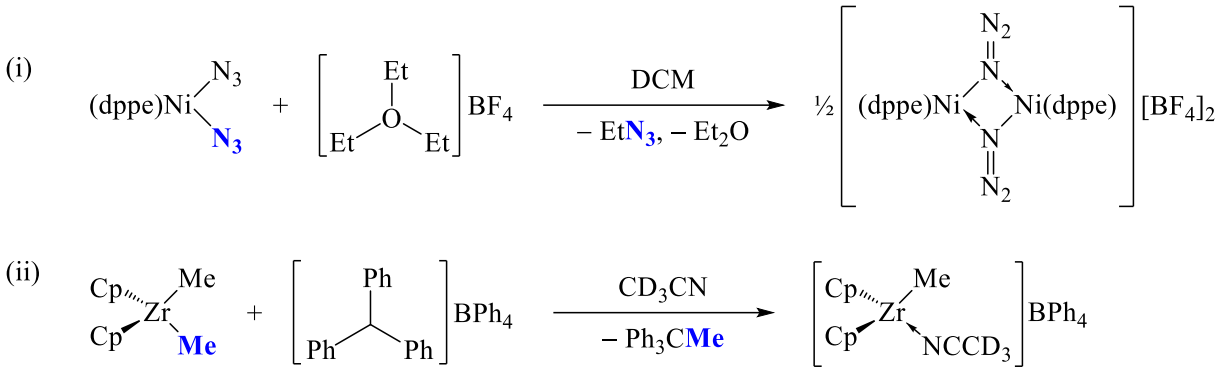

SCHEME 3.13: Reported examples of the formation of cationic complexes *via* abstraction of an anionic ligand (blue): (i) azide abstraction using an trialkyloxonium salt;[162] (ii) methyl abstraction using a trityl salt.[163]

3.3.1. Nucleophilic displacement of Cl^- from $Cp_2NbCl(NDipp)$ using Me^-

Following the reported successful synthesis of $Cp_2NbMe(N^tBu)$ (**AK$_{II}$**-Me) from its chloride precursor in reasonable yield (53%),[109] the analogous synthesis of $Cp_2NbMe(NDipp)$ (**11**) from the reaction between MeMgBr and complex **3** was envisaged. Despite treating the niobocene imido complex **3** with three equivalents MeMgBr, however, no reaction occurred as evident from the quantitative recovery of the starting chloride complex from the reaction mixture (SCHEME 3.14).

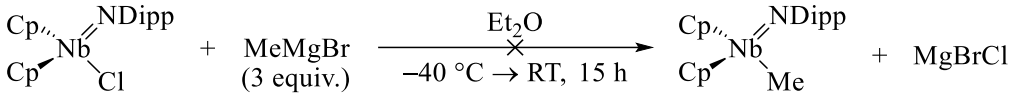

SCHEME 3.14: Attempted methylation of complex **3** using MeMgBr.

Organomagnesium reagents are relatively covalent sources of carbanions, so the lack of reactivity between complex **3** and the Grignard reagent may be attributed to the unfavourable steric interactions between the large "MgBr" moiety and the "$Cp_2Nb(NDipp)$" system. In order to reduce the steric constraints of nucleophilic methylation, the synthesis of complex **11** was reattempted using a more ionic species, namely methyllithium, and the reaction was monitored by ^{1}H NMR spectroscopy. Initially, 1.5 equivalents of MeLi were added to a cold ethereal solution of complex **3**, which resulted in the partial conversion to a new species (~24% by ^{1}H NMR spectroscopy) as evident by the presence of a new singlet (δ_H = 1.02 ppm) in the ^{1}H NMR spectrum. This new signal was attributable to the methyl ligand of complex **11**, given that a signal of similar chemical shift (δ_H = 0.95 ppm) was reported for the analogous Nb–Me moiety in **AK$_{II}$**-Me.[109]

The partially methylated sample of complex **3** was treated with a large excess of MeLi (15 equivalents) to drive the synthesis of complex **11** to completion (SCHEME 3.15). The residual MeLi in the reaction mixture was quenched using TMSCl and the volatile components and LiCl by-product were removed (*in vacuo* and by cannula filtration, respectively) to afford a yellow paste. ^{1}H NMR spectroscopic

analysis of this paste indicated the presence of complex **11**, alongside $DippNH_2$ and other unidentifiable species; the formation of the free amine being indicative that decomposition of the sample had occurred. Subsequent redissolution of the yellow paste in hexanes, followed by concentration and storage of the solution at –20 °C resulted in a trace quantity of orange single crystals (~6% yield). Subsequent X-ray crystallographic analysis of the obtained single crystals revealed the presence of four independent molecules of $Cp_2NbMe(NDipp)$ (**11**) per unit cell, with three of the molecules subject to rotational disorder (FIGURE 3.9).

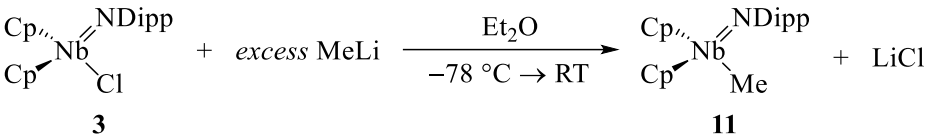

SCHEME 3.15: Formation of complex **11** from reaction of complex **3** with excess MeLi.

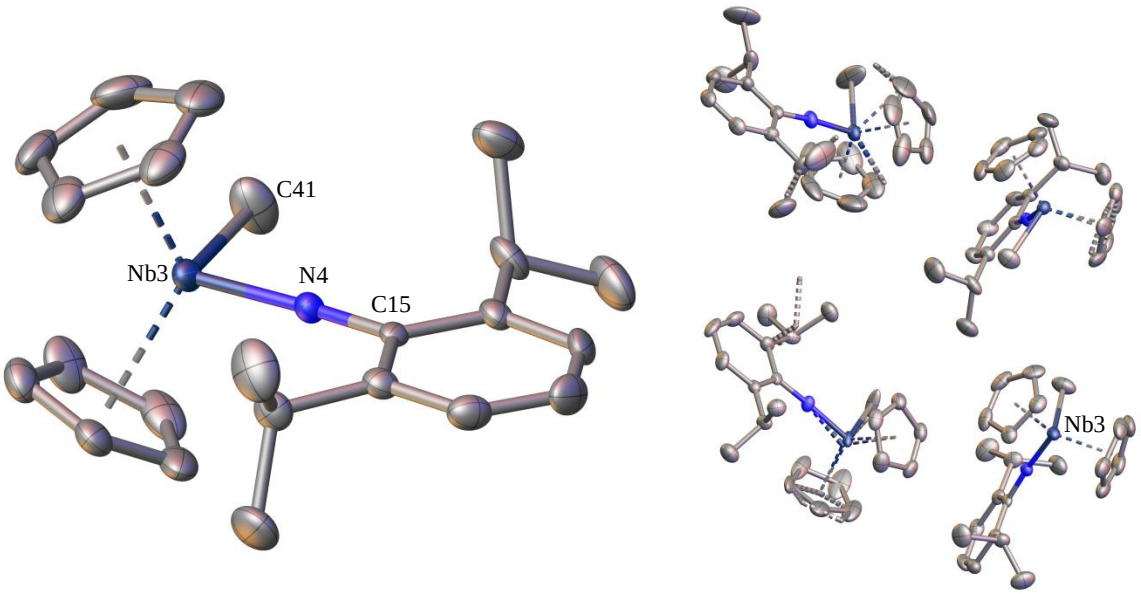

FIGURE 3.9: LEFT: Molecular structure of the non-disordered molecule of $Cp_2NbMe(NDipp)$ (**11**). RIGHT: The four independent molecules of **11** found within the unit cell, with crystallographic disorder of the three molecules shown as dashed bonds. Thermal ellipsoids are shown at 50% probability and H-atoms are omitted for clarity.

As shown in TABLE 3.5, the structural parameters of complex **11** bear close similarity to those of its chloride precursor **3** with regards to the metal–imido moiety; indeed, only a slight elongation of the Nb–N bond ($\Delta d_{Nb–N} \approx 0.006$ Å), a marginal contraction of the N–C^{Ar} bond ($\Delta d_{N–C^{Ar}} \approx 0.003$ Å), and an otherwise identical imido bond angle ($\angle_{Nb–N–C^{Ar}} \approx 171°$) were observed. The molecular structure of the *tert*-butylimido analogue $\mathbf{AK_{II}}$-Me has not been reported, so comparisons cannot be drawn with complex **11**; in fact, no other Group V metallocene alkyl imido complexes of the type $Cp'_2M(NR)R'$ have been crystallographically determined to date. However, the structure of the mono(cyclopentadienyl) derivative CpNbCl(Me)(N^tBu) has been determined elsewhere, and exhibits a similar Nb–C^{Me} bond distance to that observed in the niobocene imido complex **11** ($\Delta d_{Nb–C^{Me}} \approx 0.054$ Å; TABLE 3.5).[164]

TABLE 3.5: Selected interatomic distances (Å) and angles (°) of the crystallographically-determined structures of complex **11**, its chloride precursor **3** and the half-sandwich imido complex CpNbCl(Me)(N^{t}Bu).[164]

	$Cp_2NbMe(NDipp)$ (11) [(a)]	**$Cp_2NbCl(NDipp)$ (3)**	**CpNbCl(Me)(N^{t}Bu)**
$d_{Nb–C^{Me}}$	2.247(3)	–	2.193(5)
$d_{Nb–N}$	1.799(3)	1.7932(9)	1.739(3)
$d_{N–C^{Ar}}$	1.376(4)	1.3794(14)	1.456(5)
$\angle_{Nb–N–C^{Ar}}$	171.20(19)	170.99(8)	169.2(3)

[(a)] Only the parameters for the non-disordered molecule of **11** (FIGURE 3.9; LEFT) are recorded, where Nb, C^{Me}, N and C^{Ar} denote atoms Nb3, C41, N4 and C15, respectively.

While characterisation of the crystals of **11** by *i*ASAP+ mass spectrometry was successful, satisfactory elemental analysis could not be attained due to the partial decomposition of the sample. Unfortunately, repeated attempts at synthesising further complex **11** were unsuccessful, despite using a more direct method of synthesis from complex **3** and different batches of MeLi. Consequently, there was insufficient complex **11** to explore methyl abstraction using Tr^+ or H^+, so an alternative route from complex **3** to the niobocenium cation $\mathbf{8}^+$ was sought.

3.3.2. Nucleophilic displacement of $Cl^–$ from $Cp_2NbCl(NDipp)$ using $[OCP]^–$

In recent years, the rod-like *pseudo*-halide anion $[OCP]^–$ has been of interest as a potent nucleophile, particularly as its sodium salts $Na(OCP)(DME)_2$ (DME = 1,2-dimethoxyethane) and $Na(OCP)\cdot2½(diox)$ (diox = 1,4-dioxane) are relatively air- and thermally-stable compounds.[165] There are two major resonance forms of the $[OCP]^–$ anion in solution, namely the phosphaethynolate ($^–O–C{\equiv}P$) and phosphaketene ($O{=}C{=}P^–$) forms, enabling the possibility of ambidentate nucleophilicity from either the O- or P-atom, respectively.[166] This ambidentate reactivity of $[OCP]^–$ has been demonstrated by Heift *et al.* for the reaction between ^{i}Pr$_3$SiOTf and $Na(OCP)\cdot2½(diox)$, where either an O-bound phosphaethynolate or a P-bound phosphaketene species could be selectively formed by varying the reaction temperature (SCHEME 3.16).[167]

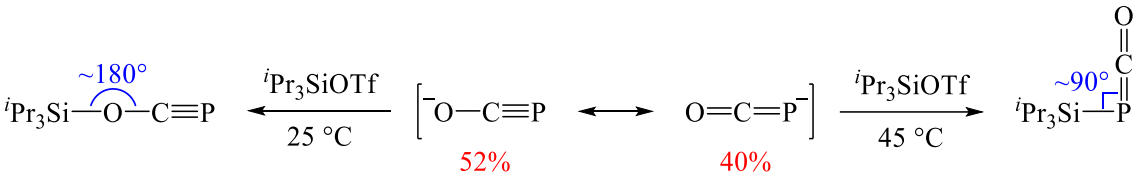

SCHEME 3.16: The two major* resonance forms of the $[OCP]^–$ anion and their reactions with ^{i}Pr$_3$SiOTf at different temperatures, producing either an O-bound phosphaethynolate (LEFT) or a P-bound phosphaketene (RIGHT) species.[167] Calculated percentage weightings of the resonance forms are shown (in red) alongside the typical bond angles of the products (in blue).[166]

NMR spectroscopic analysis of ^{i}Pr$_3$Si–O–C≡P and ^{i}Pr$_3$Si–P=C=O products revealed that relative to the phosphaethynolate species, the phosphaketene isomer is characterised by a lower δ_P and a higher δ_C

* Other minor resonance forms of $[OCP]^–$ have been calculated[166] (*e.g.* O=C:→P$^–$) but these are omitted for clarity.

value, along with a larger $^1J_{P–C}$ coupling constant (TABLE 3.6). Furthermore, the phosphaketene variant shows an infra-red (IR) absorption band at a higher frequency than its phosphaethynolate counterpart, corresponding to a more carbonyl-like CO stretch in the former. These differences in spectroscopic parameters are typical across the range of phosphaketene and phosphaethynolate complexes reported in the literature,[166] aiding the characterisation of products following reaction with the $[OCP]^-$ anion.

TABLE 3.6: Reported spectroscopic parameters of the ^{i}Pr$_3$Si-substituted phosphaethynolate and phosphaketene species.[167]

	phosphaethynolate (^{i}Pr$_3$Si–O–C≡P)	**phosphaketene (^{i}Pr$_3$Si–P=C=O)**
δ_P (ppm)	–307.2	–370.1
δ_C (ppm)	145.5	183.4
$^1J_{P–C}$ / Hz	10	92
ν(C–O) / cm^{-1}	1656	1947

Typically, the reactions of transition metal complexes with $[OCP]^-$ lead to the exclusive formation of P-bound phosphaketene complexes,[166] although a few O-bound phosphaethynolate complexes of rare-earth metals have also been reported.[168,169] For the phosphaketene variants, the electrophilic abstraction of the PCO-ligand may be achievable as demonstrated for its lighter pnictogen analogue, the cyanate ($O=C=N^-$) anion, namely upon reaction with a trialkyloxonium salt (SCHEME 3.17).[170] Consequently, if such electrophilic abstraction of the phosphaketene ligand is possible, synthesis of the complex $Cp_2Nb(NDipp)(PCO)$ from complex **3** may provide a route to the target niobocenium imido cation **8**$^+$.

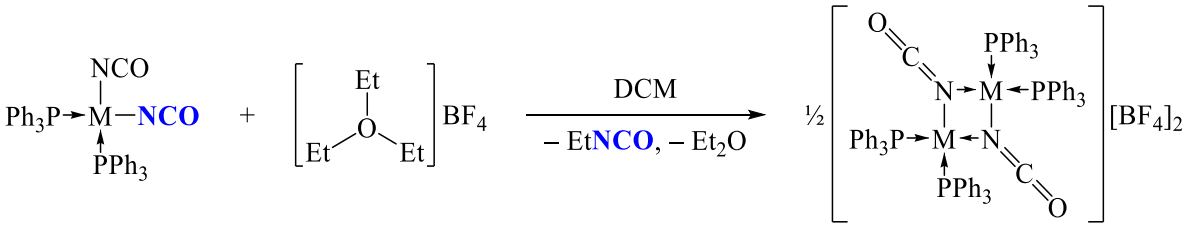

SCHEME 3.17: The reported cyanate abstraction from $M(NCO)_2(PPh_3)_2$ (M = Pd or Pt) using a trialkyloxonium salt.[170]

With the envisaged formation of the phosphaketene complex $Cp_2Nb(NDipp)(PCO)$ (**12**), one equivalent of Na(OCP)·2½(diox) was added to complex **3** at –78 °C in THF, and the resulting solution was allowed to warm gradually to room temperature. ^{31}P NMR spectroscopic analysis of the reaction mixture* after ~5 days showed the depletion of the signal corresponding to the starting $[OCP]^-$ anion (δ_P = –393.0 ppm) and formation of a new signal (δ_P = –344.0 ppm), a chemical shift indicative of the formation of a new phosphaketene species. The subsequent extraction of the reaction mixture with hexanes, followed by concentration and storage of the filtrate at –20 °C, led to the formation of a small quantity of orange single crystals suitable for XRD analysis. The resulting molecular structure was consistent with the NMR spectroscopic data and indeed confirmed the synthesis of the phosphaketene complex **12** (FIGURE 3.10). However, the phosphaketene complex shares identical unit cell parameters

* NMR spectroscopic analysis was performed in the reaction solvent of *protio* THF, referenced against a lock-tube containing C_6D_6.

with its chloride precursor and, as a result, complex **12** was found to have co-crystallised with complex **3** as only the minor component of the single crystals (~17 mol%; FIGURE 3.10).

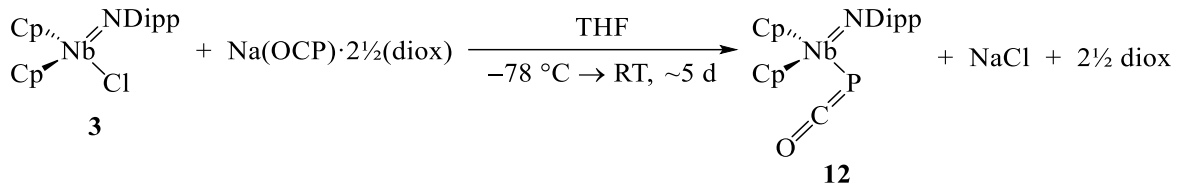

SCHEME 3.18: Formation of complex **12** from reacting complex **3** with Na(OCP)·2½(diox).

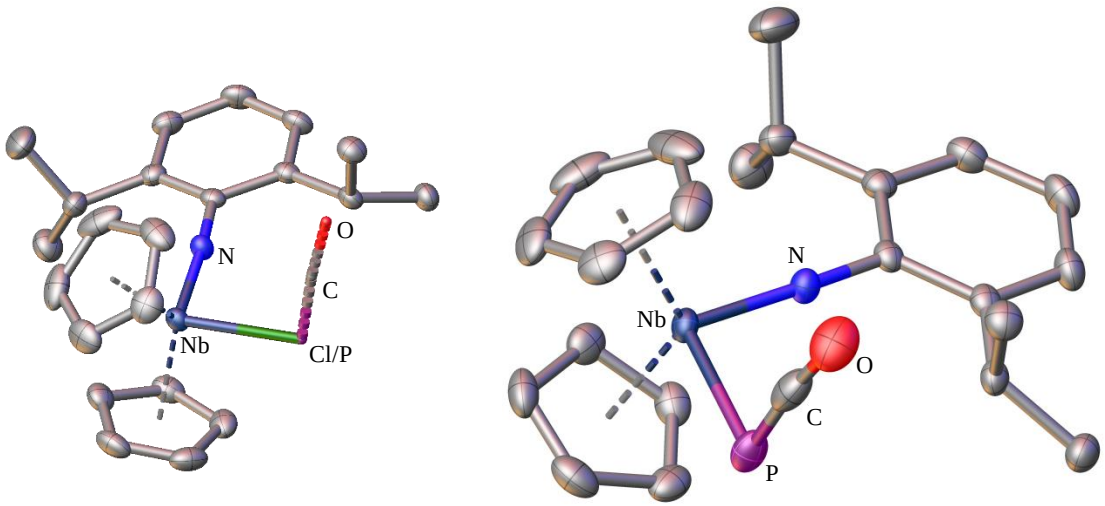

FIGURE 3.10: LEFT: Experimentally-determined molecular structure of $Cp_2Nb(NDipp)(PCO)$ (**12**; dashed wireframe) co-crystallised with $Cp_2NbCl(NDipp)$ (**3**; Cl-ellipsoid omitted for clarity) in a 1:5 molar ratio. RIGHT: A more detailed view of the phosphaketene complex **12**. Thermal ellipsoids are shown at 50% probability and H-atoms are omitted for clarity.

As may be seen from the data in TABLE 3.7, the "M–PCO" component of complex **12** is comparable with those of the other early transition metal phosphaketene complexes reported in the literature (FIGURE 3.11), namely of tungsten (YUQJEB)[171] and rhenium (EDOKIT),[172] along with phosphaketene complexes of the late transition metals cobalt (XACWAC) and gold (XACSUS).[173] Similar to the other phosphaketene complexes, in complex **12** the Nb–P–C angle is ~90° and the "P=C=O" moiety is approximately linear. The short P–C and C–O interatomic distances within the phosphaketene complex **12** are consistent with the presence of P=C and C=O double-bonds, which is supported by the computed WBIs of the complex (1.712 and 1.924, respectively) determined through NBO analysis.*

TABLE 3.7: Selected crystallographically-determined interatomic distances (Å) and angles (°) of $Cp_2Nb(NDipp)(PCO)$ (**12**) and the phosphaketene complexes reported in the literature (FIGURE 3.11).[171–173]

	12	**YUQJEB**	**EDOKIT**	**XACWAC**	**XACSUS**
$\angle_{M–P–C}$	104.5(5)	94.66(10)	93.7(7)	116.23(16)	86.21(12)
$\angle_{P–C–O}$	174.5(12)	176.9(3)	174.8(17)	169.9(4)	176.5(3)
$d_{P–C}$	1.434(14)	1.616(4)	1.62(2)	1.633(4)	1.640(4)
$d_{C–O}$	1.218(17)	1.176(6)	1.22(3)	1.172(5)	1.176(4)

* NBO analysis of $Cp_2Nb(NDipp)(PCO)$ (**12**) was undertaken following geometric optimisation of the experimentally-determined molecular structure (FIGURE 3.10; RIGHT).

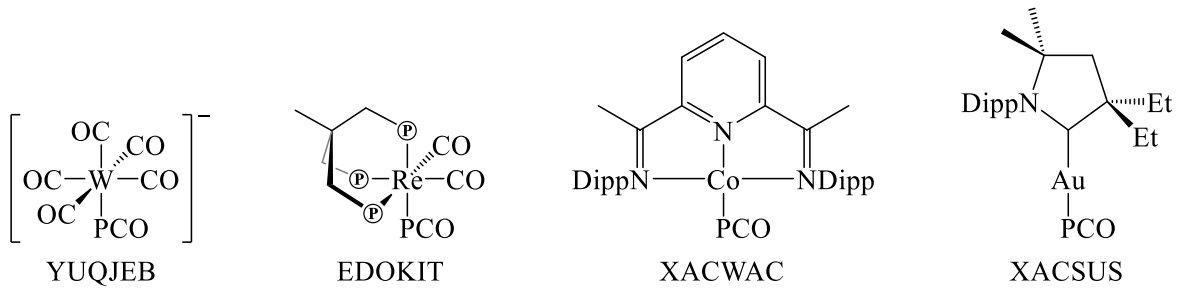

FIGURE 3.11: Experimentally-determined phosphaketene complexes of tungsten,[171] rhenium,[172] cobalt[173] and gold[173] deposited in the CSD. For clarity, the cationic component of YUQJEB is omitted and PPh_2 is abbreviated to Ⓟ.

A sample of complex **12** of greater purity was required for further spectroscopic analysis of the product, however it was found impossible to separate the phosphaketene complex from its chloride precursor **3** by recrystallisation (despite repeated efforts). So instead, in an attempt to drive the synthesis of **12** to completion, complex **3** was reacted with excess $[OCP]^-$ (3 equivalents) at a higher temperature (60 °C) on an NMR-scale and the reaction was monitored by $^{31}P\{^1H\}$ NMR spectroscopy. After 1 h of heating, the ^{31}P NMR signal attributable to the phosphaketene complex **12** (δ_P = –344.0 ppm) was indeed detected, along with those of at least three other species (δ_P = +239.4, +137.0 and +134.4 ppm); however, all four of these signals had disappeared following 16.5 h of heating (FIGURE 3.12), something accompanied by the precipitation of a solid material.

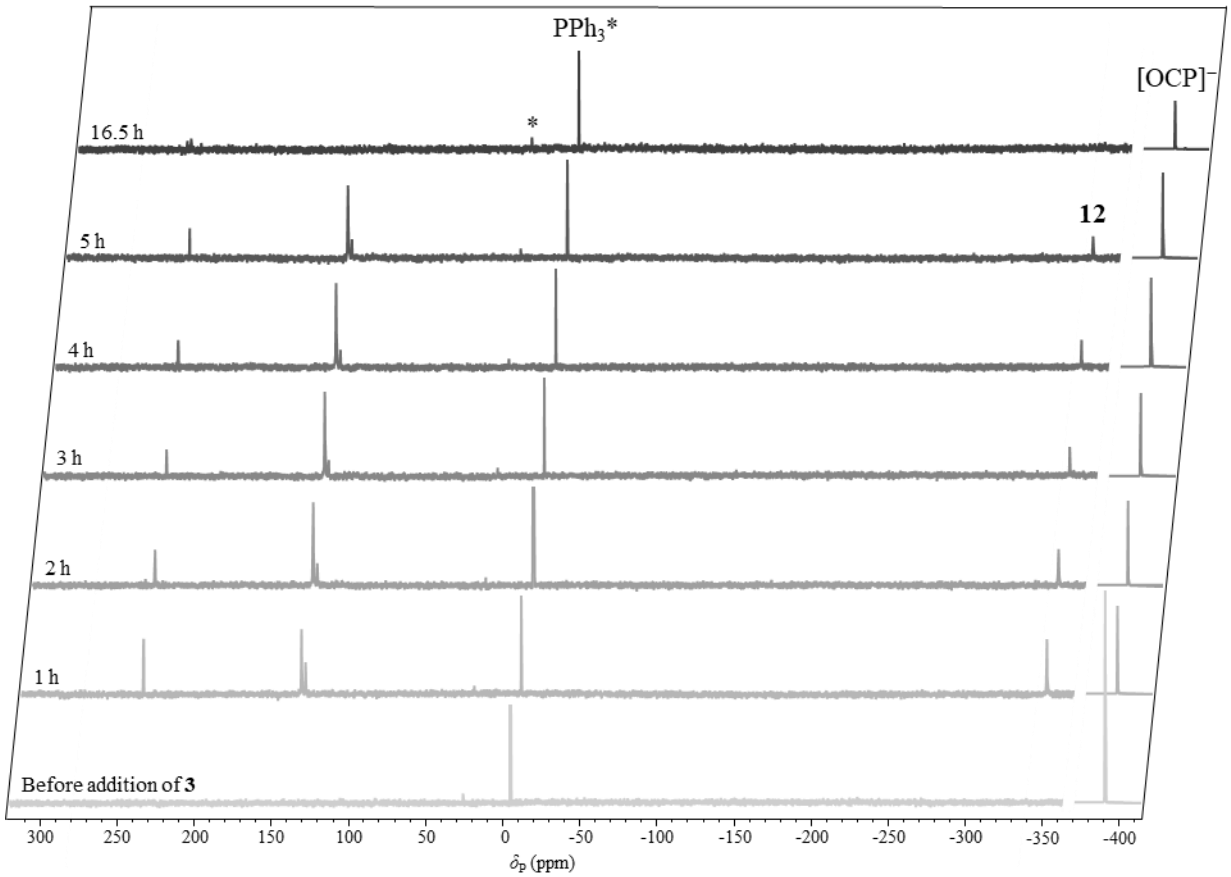

FIGURE 3.12: $^{31}P\{^1H\}$ NMR (162 MHz, THF, C_6D_6/PPh_3 in sealed lock-tube) spectroscopic monitoring of the reaction between $Cp_2NbCl(NDipp)$ (**3**) and $Na(OCP)\cdot2½(diox)$ (3 equiv.) at 60 °C, showing the transient formation of $Cp_2Nb(NDipp)(PCO)$ (**12**). Species found within the reference lock-tube are denoted by an asterisk (*). For clarity, the intensity scale of the $\delta_P < -370$ ppm region is decreased relative to the rest of the spectrum.

As the intensity of the signal corresponding to $[OCP]^-$ also decreased over the course of the NMR-scale reaction (FIGURE 3.12), this may suggest that the surplus anion reacted with the phosphaketene complex **12** (and the other intermediates) to produce insoluble phosphorus-containing species unobservable in the solution-state ^{31}P NMR spectrum. Indeed, further NBO analysis of complex **12** supports its susceptibility to nucleophilic attack, due to a slight positive charge (+0.170) determined at the phosphorus atom. Furthermore, there is literature precedence for the nucleophilic attack at the P-atom of phosphaketene species, with a variety of phosphorus-containing heterocycles being produced from the reaction between $R_3Sn(PCO)$ (R = Cy or Ph) and $[OCP]^-$ (SCHEME 3.19).[174]

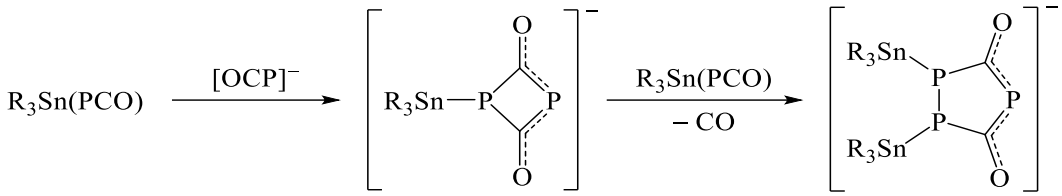

SCHEME 3.19: Two of the heterocyclic products reported for the reaction between $[OCP]^-$ and $R_3Sn(PCO)$ (R = Cy or Ph).[174]

With the nucleophilic susceptibility of complex **12** in mind, the reaction between complex **3** and Na(OCP)·2½(diox) was repeated at 60 °C, but for a shorter time period (~15 h) and using only one equivalent of $[OCP]^-$. Once again, this approach led to the isolation of a mixture of the phosphaketene and chloride complexes. However, this time complex **12** was afforded in higher purity (~47 mol%) in a yield of 11%. This relative concentration of the phosphaketene complex **12** was sufficient for the complete ^{13}C NMR spectroscopic analysis of the product; this showed a triplet (δ_C = 175.6 ppm; $^1J_{P-C}$ = 99 Hz) attributable to the PCO-motif, a chemical shift and coupling constant similar to those of other reported phosphaketene complexes (TABLE 3.8). Furthermore, IR spectroscopic and mass spectrometric analyses of the product mixture were also successful, with the observation of a characteristic band corresponding to the asymmetric PCO stretch (ν = 1892 cm^{-1}) in the IR spectrum and a signal attributable to the molecular ion (m/z = 457 Da) in the *i*ASAP+ mass spectrum.

TABLE 3.8: Selected NMR and IR spectroscopic parameters associated with the "PCO" moieties in complex $Cp_2Nb(NDipp)(PCO)$ (**12**) and the literature complexes (FIGURE 3.11); δ_P and δ_C values are reported in ppm, $^1J_{P-C}$ in Hz and $\nu_{asymm}(PCO)$ in cm^{-1}.

	12	**YUQJEB**	**EDOKIT**	**XACWAC**	**XACSUS**
δ_P [a]	–344.0	–441.0$^\tau$	–225.8	–397.5$^\tau$	–359.5
δ_C [a]	175.4	173.0$^\tau$	181.2	175.4$^\tau$	183
$^1J_{P-C}$ [a]	99	95$^\tau$	99	91$^\tau$	100
$\nu_{asymm}(PCO)$ [b]	1892	1841	1851$^\alpha$	1846$^\alpha$	1887$^\beta$

[a] Solution-state NMR spectroscopy was performed in C_6D_6, unless otherwise specified: $^\tau$ = THF-d_8.
[b] IR spectroscopy was performed using Nujol mull/KBr, unless otherwise specified: $^\alpha$ = ATR; $^\beta$ = C_6H_6 solution.

While the ~47 mol% purity of complex **12** was sufficient for its characterisation, this was unsuitable for subsequent attempts at electrophilic abstraction of the PCO-ligand, particularly as only the abstraction of the cyanate analogue has been reported previously (SCHEME 3.17). As such, there remains a drive to synthesise an alternative $Cp_2Nb(NDipp)(Nuc)$ complex as a route to the formation of cation $\mathbf{8}^+$ following the electrophilic abstraction of Nuc^-.

3.4. Chapter summary

Work in this chapter has demonstrated that for the complex $Cp_2NbCl(NDipp)$ (**3**) the Nb–Cl bond is significantly less reactive than that of the related *tert*-butylimido complex $Cp_2NbCl(N^tBu)$ (**AK$_{II}$**-Cl), both with regard to electrophilic abstraction and nucleophilic displacement of the chloride ligand. The major factor behind this difference is proposed to be the steric bulk of the 2,6-di-*iso*-propylphenylimido ligand (TABLE 3.9), which limits the attack of the Cl- and Nb-atoms to small electrophiles and nucleophiles, respectively.

TABLE 3.9: Summary of the percentage buried volumes determined[106] at the Cl- and Nb-atoms (%V_{bur}^{Cl} and %V_{bur}^{Nb}, respectively) of the experimental structures of complexes **3** and **AK$_{II}$**-Cl.[109]

	$Cp_2NbCl(NDipp)$ (3)	**$Cp_2NbCl(N^tBu)$ (AK$_{II}$-Cl)**
%V_{bur}^{Cl}	45	40
%V_{bur}^{Nb}	96	94

In the case of electrophiles, only neutral $GaCl_3$ was observed to react at the chloride ligand of complex **3**, although this Lewis acid was not strong enough to completely abstract the halide: the covalent adduct $Cp_2Nb(ClGaCl_3)(NDipp)$ (**9**) was formed instead of the ion-pair $[Cp_2Nb(NDipp)]GaCl_4$ ([**8**]$GaCl_4$). The tetrachlorogallate complex **9** did demonstrate interesting reactivity with further electrophiles though, where the Ga_2Cl_6-adduct $Cp_2Nb(ClGaCl_3)(N\{Dipp{\cdot}Ga_2Cl_6\})$ (**10**) was formed due to significant localisation of the HOMO of complex **9** at the C^{para}-position.

In contrast, it was found that small nucleophiles Me^- and $[OCP]^-$ were capable of displacing the chloride ligand from complex **3**, although the isolation of the respective products $Cp_2NbMe(NDipp)$ (**11**) and $Cp_2Nb(NDipp)(PCO)$ (**12**) proved challenging. This was due to the occurrence of competing side reactions (including decomposition to $DippNH_2$), resulting from the required use of such strong nucleophiles to cleave the Nb–Cl bond of **3**.

CHAPTER 4:

Investigating electrophilic addition to the arylimido ligand of $Cp_2NbCl(NDipp)$

4.1. Chapter introduction

In the previous chapter, it was observed that an unusual Lewis adduct $Cp_2Nb(ClGaCl_3)(N\{Dipp{\cdot}Ga_2Cl_6\})$ (**10**) is formed from a $C^{para}\cdots Ga$ π-bonding interaction between the tetrachlorogallate complex $Cp_2Nb(ClGaCl_3)(NDipp)$ (**9**) and Ga_2Cl_6 (SECTION 3.2.2.2). Given the structural similarities between complex **9** and its chloride precursor $Cp_2NbCl(NDipp)$ (**3**), it was of interest to explore whether complex **3** could also demonstrate reactivity with electrophiles at the *para*-position of the aryl imido substituent. Indeed, compared to the tetrachlorogallate derivative **9**, complex **3** might be expected to be more susceptible to electrophilic attack due to the absence of the electron-withdrawing $GaCl_3$ moiety.

If strong, covalent σ-bonds can be formed between an electrophile and the *para*-aryl position of complex **3**, this reactivity would open up new reaction pathways for terminal arylimido complexes. Indeed, electrophilic addition to the *para*-position of ArN^{2-} ligands has only been reported for the electronically quite different bridging arylimido moieties within the electron-rich dirhodium(I) complexes $Rh_2(\mu\text{-NAr})(CO)_2(\mu\text{-dppm})_2$ {Ar = Tol (**U_I**) or Ph (**U_{II}**)} as outlined in SECTION 1.2.4.[50] The rareness of this reactivity may be attributed to few complexes satisfying both the steric requirements to prevent usual electrophilic attack of the imido N-atom (SECTION 1.2.1) and also the electronic requirements to promote reactivity at the *para*-position of the aryl substituent.

In order to determine whether complex **3** meets the electronic requirements for electrophilic addition to the C^{para}-atom, computational analysis of the complex was undertaken prior to experimental investigation. This DFT study revealed that the HOMO and LUMO of the geometrically optimised complex **3** closely resemble those of the tetrachlorogallate complex **9**, both visually (FIGURE 4.1) and in terms of the calculated atomic contributions towards these FMOs (TABLE 4.1). Furthermore, as expected, the steric constraints of the complex **3** are very similar to its $GaCl_3$-adduct **9**, as indicated by the percentage buried volumes ($\%V_{bur}^X$) determined at various atomic positions (X) of the complex (TABLE 4.1).*

* As in SECTION 3.2.1, $\%V_{bur}^X$ values for complex **3** were determined using *SambVca 2.1*,[106] where the crystallographically-determined molecular structure of complex was used as the input. A sphere of radius 3 Å was centred at various atoms (X) of complex **3** and the percentage volume occupied by the surrounding atoms was determined.

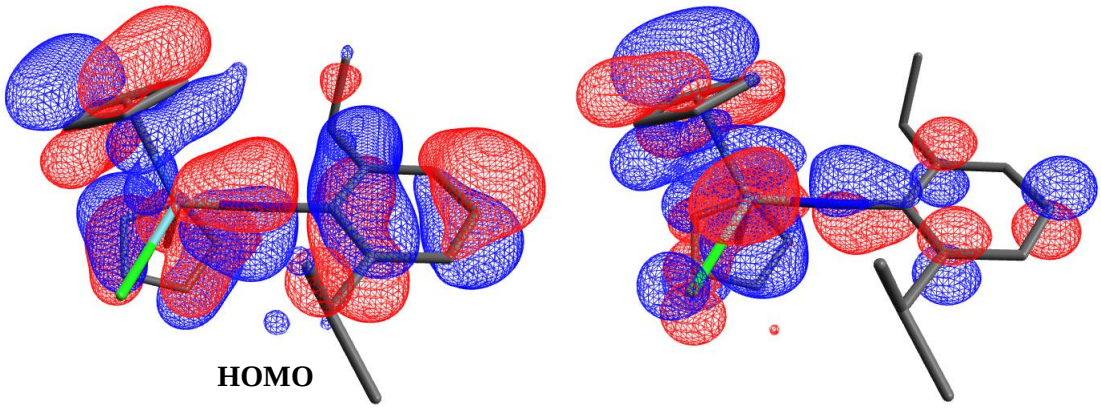

FIGURE 4.1: Computed (B3LYP/3-21G*) HOMO (–5.20 eV) and LUMO (–1.53 eV) of $Cp_2NbCl(NDipp)$ (**3**). For clarity, H-atoms are omitted and surfaces are displayed using an isovalue of 0.02.

TABLE 4.1: Selected atomic parameters calculated for $Cp_2NbCl(NDipp)$ (**3**): percentage atomic contributions[161] towards the LUMO and HOMO, and percentage buried volumes[106] ($\%V_{bur}^{X}$) determined at each atom (X).

	Nb	**Cl**	**N**	**C^{ipso}**	**C^{ortho}** *(a)*	**C^{meta}** *(a)*	**C^{para}**
LUMO contribution (%) *(b)*	61.7	1.2	2.6	0.8	1.6	0.1	2.2
HOMO contribution (%) *(b)*	5.9	0.0	20.4	6.5	7.8	0.8	11.4
$\%V_{bur}^{X}$ *(c)*	97	45	91	84	83	63	54

(a) Average values for both C^{ortho}-atoms and both C^{meta}-atoms.
(b) Computationally-determined for atoms within the optimised structure of **3**.
(c) Determined using the crystallographically-determined molecular structure of **3**.

These structural and computational analyses shows that as with the tetrachlorogallate complex **9**, the imido nitrogen atom of complex **3** is located within a sterically congested environment ($\%V_{bur}^{N}$ = 91%). Consequently, even though the HOMO of complex **3** is principally localised about the imido nitrogen (~20%), electrophilic attack at this heteroatom is likely to be inhibited for all but small electrophiles. In contrast, the C^{para}-atom of complex **3** is more sterically accessible than the imido N-atom ($\%V_{bur}^{C^{para}}$ = 54%), and still provides a significant contribution towards the HOMO of the chloride complex (~11%). Thus, since *N*-addition to complex **3** is likely hindered for more bulky electrophiles, it may be possible for *para*-addition to the complex to occur if the thermodynamic penalty associated with dearomatisation of the imido substituent can be overcome (SCHEME 4.1). Therefore, by employing bulky carbocationic electrophiles, it may be possible to form new C–C bonds at the *para*-position of complex **3**.

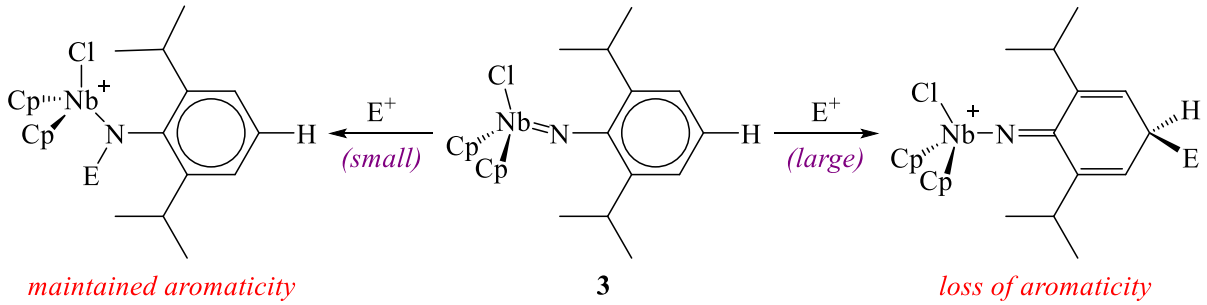

SCHEME 4.1: Generalised electrophilic addition to complex **3** by an electrophile (E^+) at either the imido nitrogen or the C^{para}-atom (depending on the size of E^+).

4.2. Protonation of $Cp_2NbCl(NDipp)$

In order to probe the behaviour of $Cp_2NbCl(NDipp)$ (**3**) towards electrophilic addition, reactions with the simplest electrophile, *i.e.* H^+, were explored initially. Even when solvated, H^+ should be sufficiently small to attack any atom of complex **3** without steric hindrance; consequently, it was expected that electrophilic addition to the atom with the highest contribution to the HOMO would occur, namely at the imido N-atom (see TABLE 4.1), to form the amido cation $[Cp_2NbCl(NHDipp)]^+$ (**13**$^+$). Indeed, computational analysis revealed that the gas-phase structure of the cation **13**$^+$ is more thermodynamically stable (ΔG = –26 kJ mol^{-1}) than its arenium isomer $[Cp_2NbCl(N\{Dipp\text{-}4\text{-}H\})]^+$, where the latter is formed following the protonation of C^{para} and dearomatisation of the aryl ring;[*] the DFT-optimised structures of the two cations are shown in FIGURE 4.2.[†]

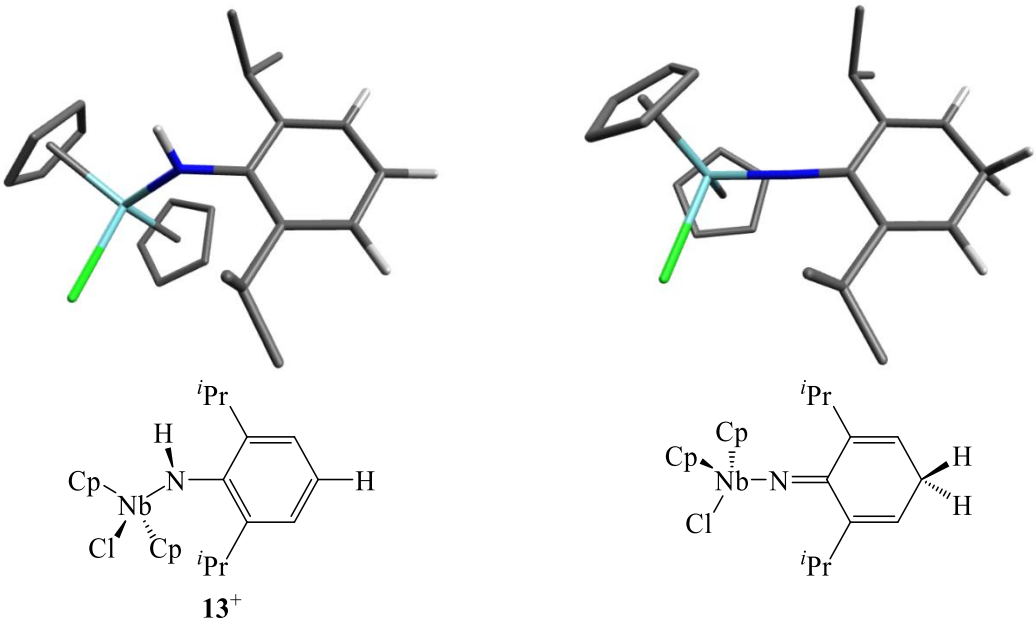

FIGURE 4.2: Computed (B3LYP/3-21G*) gas-phase structures of cations $[Cp_2NbCl(NHDipp)]^+$ (**13**$^+$; LEFT) and $[Cp_2NbCl(N\{Dipp\text{-}4\text{-}H\})]^+$ (RIGHT). H-atoms on the Cp-ligands and ^{i}Pr-groups are omitted for clarity.

Experimentally, the treatment of imido complexes with Brønsted acids typically leads to *N*-protonation (SECTION 1.2.1), even for the sterically bulky dirhodium systems **U$_I$** and **U$_{II}$**.[175] Furthermore, in the context of niobocene imido complexes, the *N*-protonation of $Cp^{TMS}{}_2NbCl(NPh)$ to the amido salt $[Cp^{TMS}{}_2NbCl(NHPh)]BF_4$ has been demonstrated on reaction with the Brønsted acid $HBF_4{\cdot}OEt_2$.[176] Together, these reactivities indicate that the amido cation **13**$^+$ is a plausible synthetic target.

[*] Throughout this work, "{Dipp-4-E}" will be used to denote the arenium derivative of the 2,6-di-*iso*-propylphenyl substituent formed from the addition of E^+ to the *para*-position (*i.e.* "{2,6-^{i}Pr$_2$C$_6$H$_3$-4-E}").

[†] Starting geometries for $[Cp_2NbCl(NHDipp)]^+$ (**13**$^+$) and $[Cp_2NbCl(N\{Dipp\text{-}4\text{-}H\})]^+$ were created by addition of an H-atom to the solid-state molecular structure of $Cp_2NbCl(NDipp)$ (**3**) at either the N- or C^{para}-atom, respectively. In line with the structures of other amido complexes deposited in the CSD, $\angle_{Nb\text{–}N\text{–}C}$ and $d_{Nb\text{–}N}$ parameters were altered to 145° and 2 Å, respectively, for the input geometry of **13**$^+$. Both structures then underwent geometric optimisation by DFT, to afford structures located at energetic minima (FIGURE 4.2).

4.2.1. Treatment of $Cp_2NbCl(NDipp)$ with triflic acid

Since it has been previously shown that the dirhodium imido complexes $\mathbf{U_I}$ and $\mathbf{U_{II}}$ undergo clean protonation at the imido nitrogen with the strong acid[177] TfOH (pK_a = –14.7),[175] an analogous reaction with complex **3** was undertaken. Reaction of complex **3** with TfOH (1 equiv.) was performed in Et_2O, which led to the rapid precipitation of a yellow solid. Following its isolation, ^{1}H NMR spectroscopic analysis of this yellow solid in CD_2Cl_2 revealed the presence of a broad ($\nu_{½}$ = 9 Hz), highly-deshielded (δ_H = 12.78 ppm) singlet resonance characteristic of an NH moiety. This is consistent with the formation of [$Cp_2NbCl(NHDipp)$]OTf ([**13**]OTf) following protonation of complex **3** (75% yield; SCHEME 4.2); indeed, the empirical formula of [**13**]OTf was supported by elemental analysis. The *N*-protonation of complex **3** by TfOH was confirmed by ^{1}H–^{1}H NOESY of the product, with cross-peaks being detected between the amido and cyclopentadienyl proton resonances, but not with the aromatic C*H* moieties of the imido ligand (FIGURE 4.3). Despite repeated attempts however, a characteristic signal attributable to an NH group could not be detected in the solid-state IR spectrum (Nujol mull) of [**13**]OTf.

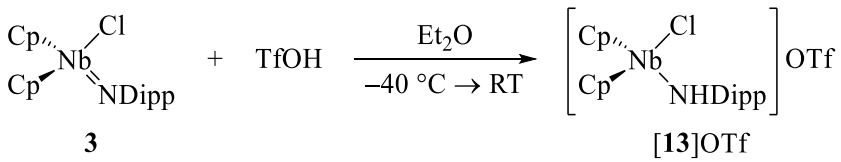

3 [**13**]OTf

SCHEME 4.2: Synthesis of [**13**]OTf from the protonation of the imido complex **3** using triflic acid.

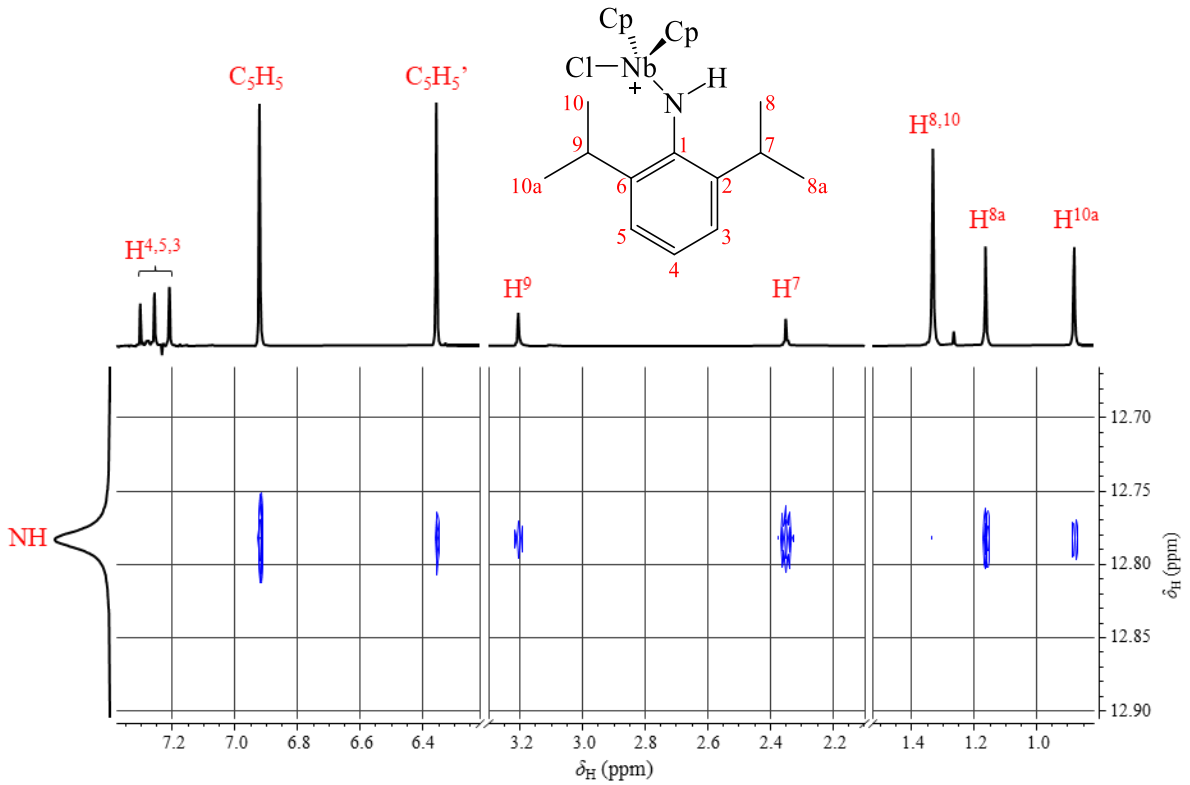

FIGURE 4.3: Partial ^{1}H–^{1}H NOESY (599 MHz; CD_2Cl_2) of [**13**]OTf, displaying the cross-peaks between the NH signal (δ_H = 12.78 ppm) and other H-environments. For clarity, the PSYCHE ^{1}H NMR trace is displayed along the horizontal axis.

Single crystals of [**13**]OTf suitable for XRD analysis were isolated by layering a DCM solution of the complex with hexanes. The resulting crystal structure was found to comprise the dichloromethane-solvate [**13**]OTf·DCM; the molecular structure of the complex is shown in FIGURE 4.4, with selected interatomic distances and angles shown in TABLE 4.2. Compared to its chloride precursor **3**, [**13**]OTf features a longer Nb–N bond ($\Delta d_{Nb–N} \approx 0.19$ Å) and a more acute Nb–N–C11 angle ($\Delta \angle_{Nb–N–C11} \approx 33°$), parameters consistent with the presence of an amido (rather than imido) ligand. The measured N–O1 interatomic distance of 2.959(3) Å is consistent with strong H-bonding between the NH moiety of the cation and the triflate anion (comparable donor-acceptor distances of 2.5–3.2 Å are typical).[178] Indeed, a similar H-bonding arrangement was found for $[Re_2(NH^tBu)(N^tBu)_3(\mu\text{-}N^tBu)_2]OTf$, with $d_{N–O1}$ = 3.05(3) Å.[28] The lack of an NH band in the IR spectrum of complex [**13**]OTf, therefore, is tentatively attributed to the presence of this strong cation–anion H-bonding interaction in the solid-state.

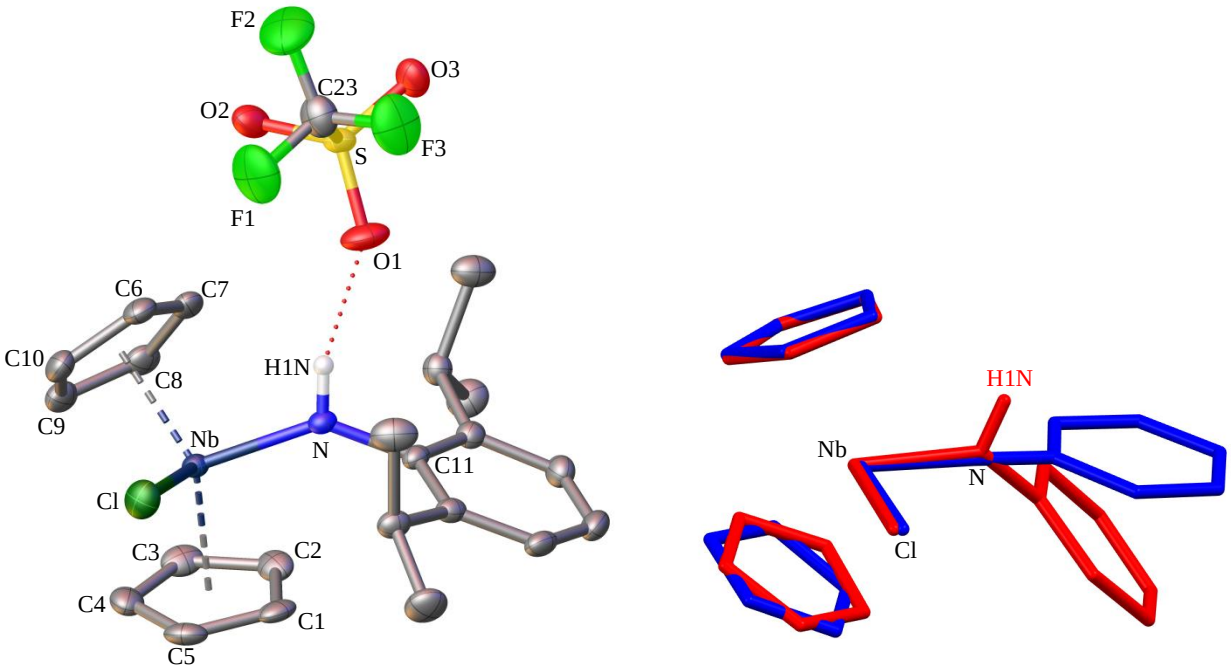

FIGURE 4.4: LEFT: Experimentally-determined molecular structure of [$Cp_2NbCl(NHDipp)$]OTf ([**13**]OTf); thermal ellipsoids are shown at 50% probability and H-atoms (except H1N, computed) and the DCM solvate are omitted for clarity. RIGHT: Molecular overlay of cation $\mathbf{13}^+$ with neutral $Cp_2NbCl(NDipp)$ (**3**); H-atoms (except H1N in [**13**]OTf) and the ^{i}Pr-groups from both structures have been omitted for clarity.

TABLE 4.2: Selected interatomic distances (Å) and angles (°) of [**13**]OTf compared to those of its precursor **3**.

	[$Cp_2NbCl(NHDipp)$]OTf ([13]OTf)	**$Cp_2NbCl(NDipp)$ (3)**
$d_{Nb–N}$	1.983(2)	1.7932(9)
$\angle_{Nb–N–C11}$	138.11(17)	170.99(8)
$d_{N–O1}$	2.959(3)	–

4.2.2. Treatment of $Cp_2NbCl(NDipp)$ with Brookhart's acid, $[H(OEt_2)_2]BAr^F_4$

For structural and spectroscopic comparison with [**13**]OTf, synthesis of the amido cation **13**$^+$ with a more weakly-coordinating counteranion was envisaged. To this end, reaction of complex **3** with an equimolar quantity of Brookhart's acid,[179] $[H(OEt_2)_2]BAr^F_4$, was performed in DCM (SCHEME 4.3). Following the reaction, the DCM solvent was removed and the resulting solid washed with hexanes to afford $[Cp_2NbCl(NHDipp)]BAr^F_4$ ([**13**]BAr^F_4) in 68% yield (purity confirmed by elemental analysis).

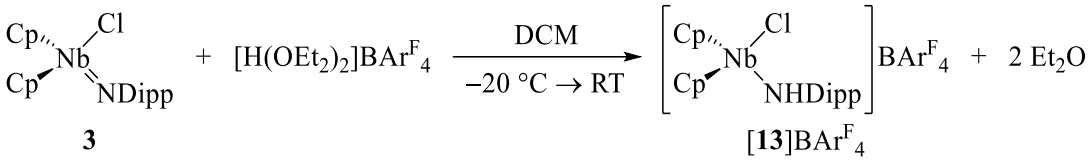

SCHEME 4.3: Synthesis of $[Cp_2NbCl(NHDipp)]BAr^F_4$ ([**13**]BAr^F_4) from the protonation of complex **3** with Brookhart's acid, $[H(OEt_2)_2]BAr^F_4$.

As found for [**13**]OTf, the ^{1}H NMR spectrum of [**13**]BAr^F_4 reveals a broad ($\nu_{½}$ = 18 Hz), highly-deshielded (δ_H = 11.63 ppm) singlet attributable to the NH group, which is identified to have cross-peaks with the cyclopentadienyl ^{1}H environment in the ^{1}H–^{1}H NOESY (as observed for [**13**]OTf; FIGURE 4.3). Compared to its triflate counterpart, the amido ^{1}H NMR signal for [**13**]BAr^F_4 is at a marginally lower frequency (TABLE 4.3), which is taken as being indicative of the absence of H-bonding in the complex. This is something that is supported by a peak characteristic of an N–H stretch being readily observed in the solid-state IR spectrum (Nujol mull) of [**13**]BAr^F_4.

TABLE 4.3: Spectroscopically- and crystallographically-determined parameters of the amido complexes $[Cp_2NbCl(NHDipp)]BAr^F_4$ ([**13**]BAr^F_4) and $[Cp_2NbCl(NHDipp)]OTf$ ([**13**]OTf).

	[13]BAr^F_4	**[13]OTf**
δ_H ($\nu_{½}$) [(a)]	11.63 ppm (18 Hz)	12.78 ppm (9 Hz)
ν(N–H) / cm^{-1} [(b)]	3332	–
$d_{Nb–N}$ / Å	1.978(3), 1.989(3) [(c)]	1.983(2)
$\angle_{Nb–N–C11}$ / °	137.3(2), 135.9(2) [(c)]	138.11(17)

[(a)] NMR spectroscopic analysis performed in CD_2Cl_2 solution.
[(b)] IR spectroscopic analysis performed using Nujol mull.
[(c)] Interatomic parameters for cations 1 and 2 in FIGURE 4.5, respectively.

The discrete ionic structure of the complex was confirmed by X-ray crystallographic analysis of [**13**]BAr^F_4, following growth of single crystals from cooling a concentrated toluene solution of the salt. The crystal structure of [**13**]BAr^F_4 was found to contain two crystallographically-unique geometries for the amido cation (FIGURE 4.5), where disorder was present within the molecular structure of one cation of **13**$^+$ (cation 1; LEFT) and both $[BAr^F_4]^-$ anions (not displayed).* Despite the structural disorder of [**13**]BAr^F_4, the geometries of the "Nb–NHDipp" moieties are identical to that of [**13**]OTf (TABLE 4.3),

* Rotational disorder within trifluoromethyl groups is commonly observed in crystallographically-determined molecular structures,[180] including salts featuring the $[BAr^F_4]^-$ anion.[181]

which implies that H-bonding (and the corresponding cation–anion association) has minimal effect on the structure.

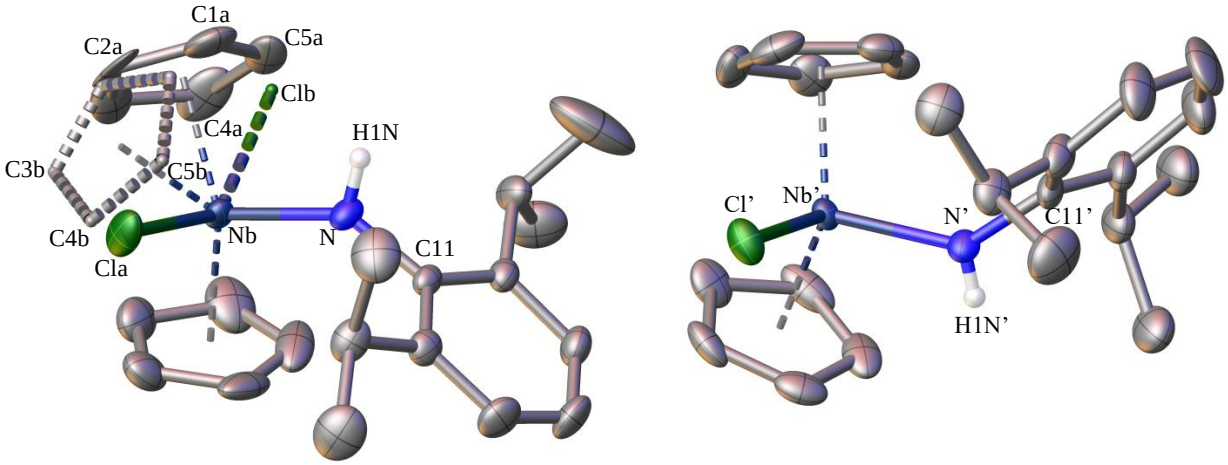

FIGURE 4.5: Experimentally-determined structures of the two independent cations, cation 1 (LEFT) and cation 2 (RIGHT), within the unit cell of $[Cp_2NbCl(NHDipp)]BAr^F_4$ ([**13**]BAr^F_4). Thermal ellipsoids are shown at 50% probability and, for clarity, H-atoms (except H1N and H1N') and $[BAr^F_4]^-$ counteranions are omitted. The minor crystallographic component (~39% occupancy) of the disordered cation 1 is depicted as a dashed wireframe structure.

Since the protonation of complex **3** using either TfOH or Brookhart's acid occurs at the N-atom as predicted by the computational studies, attention was turned to whether electrophilic addition to the *para*-position of the arylimido ligand of complex **3** could be achieved. To this end, reaction with a larger electrophile than H^+ was required, in order to provide sufficient steric bulk to kinetically inhibit electrophilic addition to the heteroatom.

4.3. Methylation of $Cp_2NbCl(NDipp)$

Electrophilic methylation was initially chosen as the simplest example of C–C bond formation at the *para*-position of complex **3**, where the incorporation of a small methyl moiety was envisaged to facilitate the spectroscopic characterisation of the potential *N*- or *para*-methylated products, $[Cp_2NbCl(N\{Me\}Dipp)]^+$ (**14a**$^+$) or $[Cp_2NbCl(N\{Dipp\text{-}4\text{-}Me\})]^+$ (**14b**$^+$), respectively. Furthermore, the *para*-addition of Me^+ to arylimido complexes has literature precedence with the methylation of the dirhodium complexes $Rh_2(\mu\text{-}NAr)(CO)_2(\mu\text{-}dppm)_2$ {Ar = Tol (**U$_I$**) or Ph (**U$_{II}$**); SECTION 1.2.4}, albeit with these complexes possessing bridging rather than a terminal imido moieties.[175] In contrast to the computational analyses undertaken for the protonation of complex **3** (SECTION 4.2), it was found that the *para*-methylated isomer **14b**$^+$ was more thermodynamically stable than its *N*-alkylated counterpart **14a**$^+$ (ΔG = –20 kJ mol^{-1}); the optimised structures of both cations are shown in FIGURE 4.6.* This thermodynamic preference, combined with the lower steric shielding of C^{para} *vs*. the heteroatom in complex **3**, suggests that *para*-methylation of aryl ring in complex **3** should occur and that cation **14b**$^+$ was indeed a realistic synthetic target.

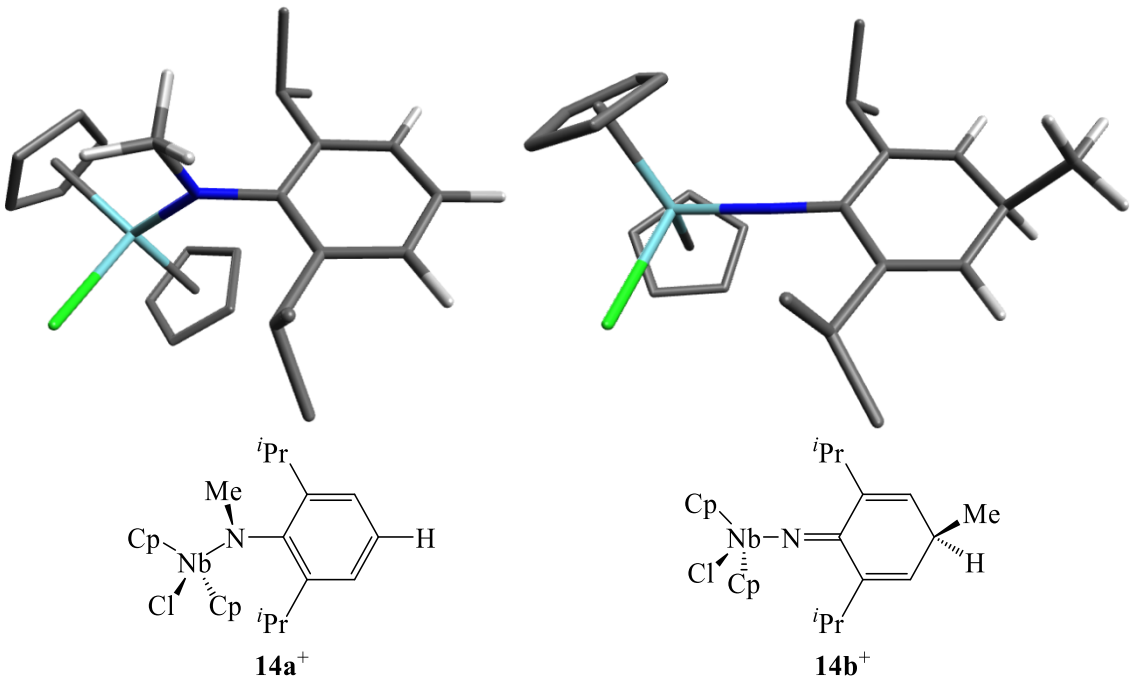

FIGURE 4.6: Computed (B3LYP/3-21G*) gas-phase structures of cations $[Cp_2NbCl(N\{Me\}Dipp)]^+$ (**14a**$^+$) and $[Cp_2NbCl(N\{Dipp\text{-}4\text{-}Me\})]^+$ (**14b**$^+$). H-atoms on the Cp-ligands and ^{i}Pr-groups are omitted for clarity.

A cooled (–40 °C) ethereal solution of complex **3** was treated with an equimolar amount of neat MeOTf, and the reaction mixture was allowed to warm to room temperature. Upon standing, a trace amount

* The optimised structures of $[Cp_2NbCl(NHDipp)]^+$ (**13**$^+$) and $[Cp_2NbCl(N\{Dipp\text{-}4\text{-}H\})]^+$ (FIGURE 4.2) were used as starting geometries for $[Cp_2NbCl(N\{Me\}Dipp)]^+$ (**14a**$^+$) and $[Cp_2NbCl(N\{Dipp\text{-}4\text{-}Me\})]^+$ (**14b**$^+$), following the substitution of H-atoms (at the *N*- and *para*-positions, respectively) for Me-groups. Subsequent geometric optimisation led to the structures of **14a**$^+$ and **14b**$^+$ presented in FIGURE 4.6.

(~5 mg; ~4% yield) of orange single crystals formed in the reaction vessel. However, XRD analysis identified the crystalline material as the amido salt $[Cp_2NbCl(NHDipp)]OTf$ ([**13**]OTf; SECTION 4.2.1), presumably formed as a result of complex **3** reacting with a small amount of TfOH present in the MeOTf (as a result of inherent partial hydrolysis). No reaction otherwise occurred between complex **2** and MeOTf (SCHEME 4.4), as the niobocene imido precursor was almost quantitatively recovered following removal of the volatile components *in vacuo*.

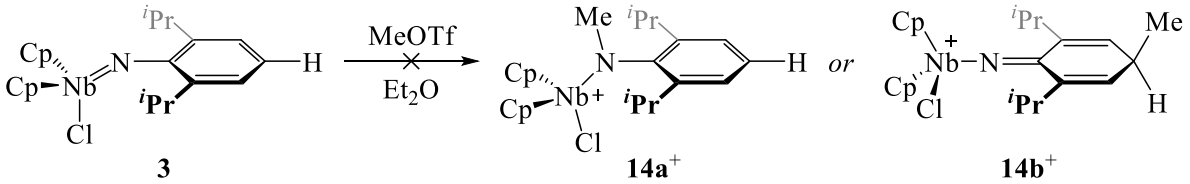

SCHEME 4.4: Attempted electrophilic methylation of the niobocene imido complex **3** using MeOTf.

Since the methylation of complex **3** has been computed to be thermodynamically favourable, the lack of reactivity between the imido complex and MeOTf is thus attributed to kinetic factors. With regard to the differing reactivities with MeOTf observed for complex **3** and previously reported $Rh_2(\mu\text{-NTol})(CO)_2(\mu\text{-dppm})_2$ (**U_I**), complications arise from making direct comparisons as the arylimido motif in each complex adopts different coordination modes (terminal and bridging, respectively). However, with the imido complex **U_I** containing d^8 rhodium(I) metal centres, the aryl substituent is anticipated to be more electron-rich than that of the d^0 niobium(V) complex **3**, potentially making the former complex more reactive. Additionally, it should be noted that natural bond orbital (NBO) analysis of MeOTf reveals that in Et_2O solution the C–O bond is moderately covalent (WBI = 0.696), with only a partial positive charge on the methyl C-atom (+0.644),* and hence the electrophile is less reactive than anticipated.

* NBO analysis was performed following the geometric optimisation of MeOTf, where both DFT calculations employed the SMD solvent model.

4.4. Tritylation of $Cp_2NbCl(NDipp)$

Following the unsuccessful electrophilic addition using the covalent, neutral electrophile MeOTf, it was envisaged that reaction of complex **3** with an ionic, carbocationic electrophile may result in the desired C–C bond formation at the *para*-position of the aryl imido substituent. The triphenylmethyl (or trityl, Tr^+) cation was chosen as the electrophile, as many of its salts are stable and have been crystallographically-determined to have discrete ionic structures.[182–184] While the carbocation is stabilised by the extensive π-resonance across the three conjugated phenyl rings, Tr^+ remains a potent electrophile even capable of abstracting hydride and methyl anions from transition metal complexes (for examples, see SCHEME 4.5).[163,185] Indeed, computational MO analysis herein* supports Tr^+ being more reactive than MeOTf with complex **3**, as the HOMO of the arylimido complex (–5.20 eV) is computed to be more similar in energy to the LUMO of the carbocation (–7.14 eV) than that of MeOTf (+0.46 eV), thus indicating that Tr^+ will have more effective orbital overlap with complex **3**.

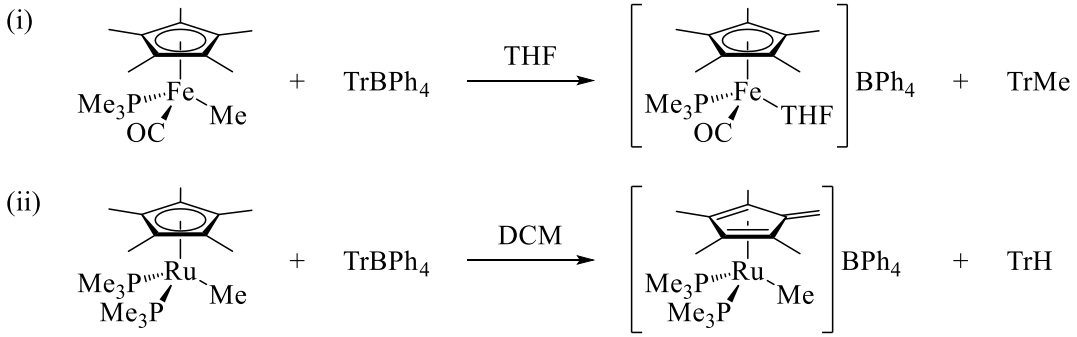

SCHEME 4.5: Example reactivity of the trityl salt $TrBPh_4$ with transition metal complexes, resulting in either (i) methyl abstraction[185] or (ii) hydride abstraction.[163]

Due to the sterically-demanding phenyl groups within the Tr^+ cation, the facilitation of *para*- rather than *N*-addition of the electrophile to the arylimido ligand of complex **3** is expected. Indeed, computational analyses of the potential tritylated products $[Cp_2NbCl(N\{Tr\}Dipp)]^+$ and $[Cp_2NbCl(N\{Dipp\text{-}4\text{-}Tr\})]^+$ revealed that only the latter, *para*-addition product was located at an energetic minimum (FIGURE 4.7).† Furthermore, the tritylation at the *para*-aryl position of complex **3** is expected to be thermodynamically favourable, due to the computed electronic stabilisation of the HOMO induced through the formation of $[Cp_2NbCl(N\{Dipp\text{-}4\text{-}Tr\})]^+$ (ΔE_{HOMO} = –3.31 eV). As a consequence, these computational studies indicated that the cation $[Cp_2NbCl(N\{Dipp\text{-}4\text{-}Tr\})]^+$ was a suitable synthetic target.

* Prior to MO analysis, the gas-phase geometries of MeOTf and Tr^+ were optimised by DFT (B3LYP/3-21G*).

† The optimised structures of $Cp_2NbCl(N\{Me\}Dipp)]^+$ (**14a**$^+$) and $[Cp_2NbCl(N\{Dipp\text{-}4\text{-}Me\})]^+$ (**14b**$^+$) in FIGURE 4.6 were used as a basis for the structures of $[Cp_2NbCl(N\{Tr\}Dipp)]^+$ and $[Cp_2NbCl(N\{Dipp\text{-}4\text{-}Tr\})]^+$, respectively. The three methyl H-atoms in each structure were substituted with predefined[221] phenyl groups and the geometries were reoptimised; however, the optimisation calculation for $[Cp_2NbCl(N\{Tr\}Dipp)]^+$ failed.

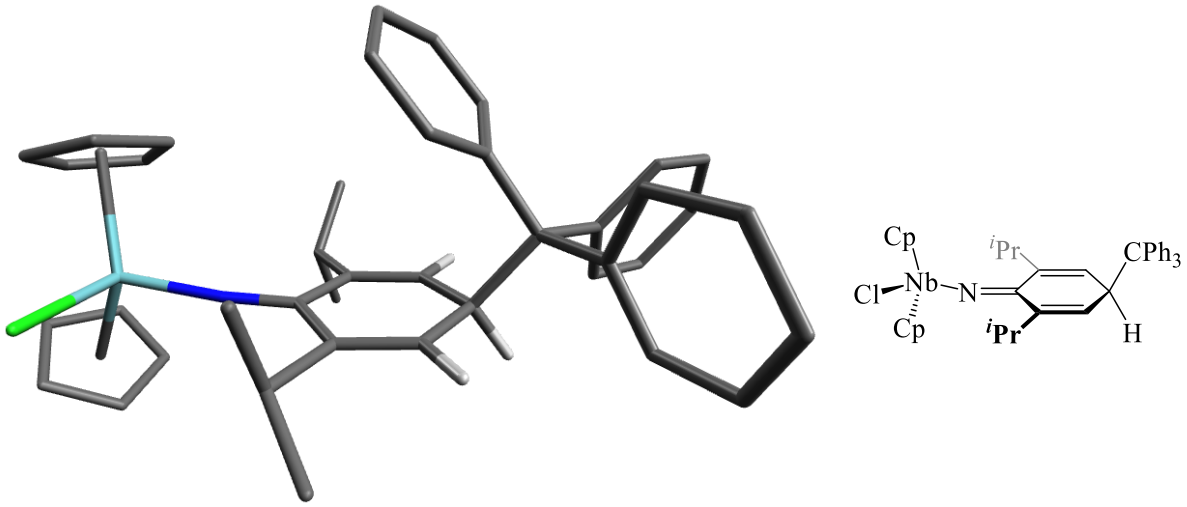

FIGURE 4.7: Computed (B3LYP/3-21G*) structure of $[Cp_2NbCl(N\{Dipp\text{-}4\text{-}Tr\})]^+$. H-atoms on the Cp-, ^{i}Pr- and Tr-moieties are omitted for clarity.

4.4.1. Synthesis of the tritylating agent $TrBAr^F_4$

An array of ionic trityl salts have been reported in the literature, including those with chlorate,[182] tetracyanoborate,[183] hexafluorophosphate,[184] tetrachlorogallate[184] and triflate[184] counteranions. However, the $[BAr^F_4]^-$ (Ar^F = C_6H_3-3,5-$\{CF_3\}_2$) salt, *i.e.* $TrBAr^F_4$ (**15**), was selected for use in the tritylation of complex **3**, since the solubilising nature of the counteranion was envisaged to aid the isolation of the target cationic addition product, namely $[Cp_2NbCl(N\{Dipp\text{-}4\text{-}Tr\})]BAr^F_4$ ([**16**]BAr^F_4). Consequently, using a procedure adapted from that used for $TrBPh^F_4$ (Ph^F = C_6F_5),* the trityl salt **15** was prepared from the reaction between TrCl and $NaBAr^F_4$ in good yield (81%; SCHEME 4.6). ^{1}H NMR (700 MHz, CD_2Cl_2) spectroscopic analysis of **15** was consistent with its anticipated structure.

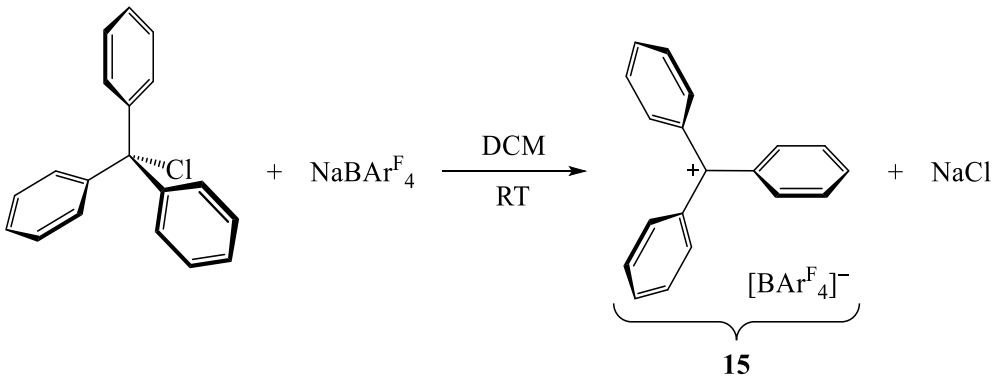

SCHEME 4.6: Synthesis of $TrBAr^F_4$ (**15**) from the reaction between TrCl and $NaBAr^F_4$.

Recrystallisation of the trityl salt **15** was attempted using multiple different solvent systems, however the use of ethereal solutions was found to result in the gradual decomposition of the compound, as signified by the blackening of bright-yellow solutions in Et_2O or THF. Ultimately, recrystallisation of

* $TrBPh^F_4$ is reportedly synthesised from reaction between $KBPh^F_4$ and TrCl.[186]

compound **15** from a warm, concentrated toluene solution proved successful, with single crystals suitable for XRD analysis being obtained. The molecular structure is shown in FIGURE 4.8 and features typical rotational disorder of the CF_3 groups within the anion. As determined by the large $C^+\cdots B^-$ interatomic distance of 7.323(9) Å, $TrBAr^F_4$ (**15**) is comprised of discrete ions (since $\sum r_{vdW}$ = 3.5 Å),[147] with the trityl cation being almost structurally identical to that reported[187] for the analogue $TrBPh^F_4$.*

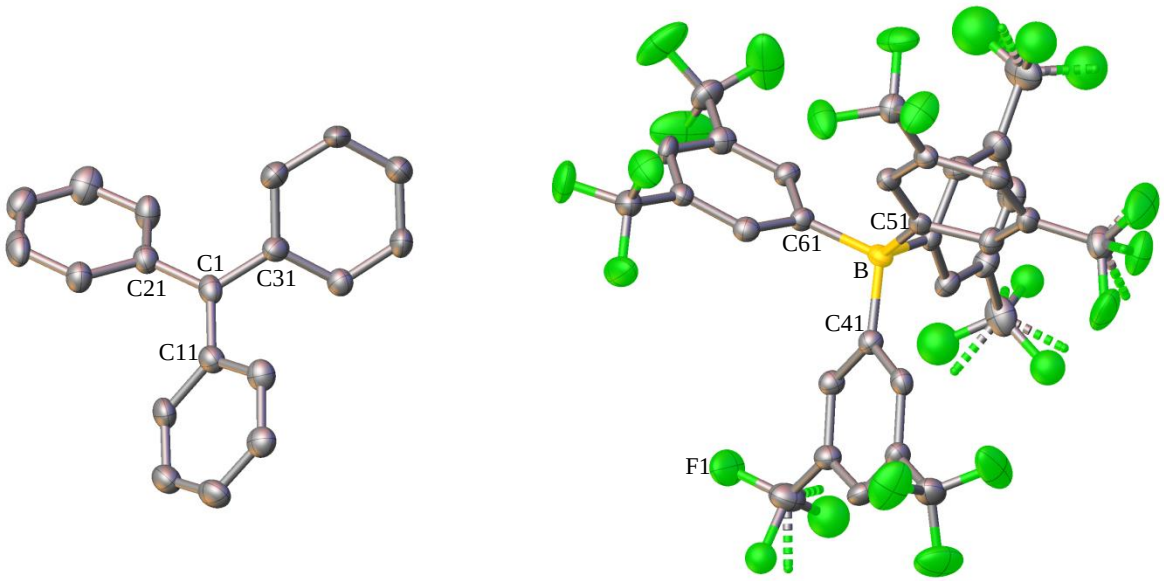

FIGURE 4.8: Experimentally-determined molecular structure of $TrBAr^F_4$ (**15**); thermal ellipsoids are shown at 50% probability and H-atoms are omitted for clarity. Rotational disorder (50% crystallographic occupancy) of the CF_3-groups within the $[BAr^F_4]^-$ anion is displayed as dashed wireframe. Selected parameters: $d_{C1–C11}$ 1.433(7) Å, $d_{C1–C21}$ 1.438(7) Å, $d_{C1–C31}$ 1.452(8) Å, $\angle_{C11–C1–C21}$ 121.6(5)°, $\angle_{C21–C1–C31}$ 119.2(5)°, $\angle_{C31–C1–C11}$ 119.2(5)°, $d_{C1–B}$† 7.323(9) Å.

4.4.2. Reaction between $Cp_2NbCl(NDipp)$ and $TrBAr^F_4$

With the intended formation of $[Cp_2NbCl(N\{Dipp\text{-}4\text{-}Tr\})]BAr^F_4$ ([**16**]BAr^F_4), complex **3** was reacted with an equimolar quantity of the trityl salt **15** in DCM at –40 °C (SCHEME 4.7). Subsequent removal of the solvent *in vacuo* and washing of the resulting residue with hexanes (to remove any unreacted **3**) yielded a deep-red solid. NMR spectroscopic analysis of this hexanes-insoluble solid indicated the presence of the amido salt $[Cp_2NbCl(NHDipp)]BAr^F_4$ ([**13**]BAr^F_4; ~50 mol%) along with other unidentified species (FIGURE 4.9). As the integrals of the ^{1}H NMR signals attributable to the $[BAr^F_4]^-$ anion (H^{12} and H^{14}) were greater than anticipated for pure [**13**]BAr^F_4,‡ this indicated that the product mixture comprised at least one other cation/$[BAr^F_4]^-$ ion-pair. From the characteristically broad

* Calculated structural overlay of trityl cations of crystallographically-determined $TrBAr^F_4$ (**15**) and literature[187] $TrBPh^F_4$: RMS distance = 0.0476 Å; maximum distance = 0.0744 Å.

† Where $d_{C1–B}$ = distance between the two closest Tr^+ and $[BAr^F_4]^-$ ions in the packed structure of **15**.

‡ For pure [**13**]BAr^F_4 (deliberately synthesised in SECTION 4.2.2), the ^{1}H NMR signals attributable to H^{12}, H^{14} and H^{10} had relative intensities of 8:4:3, respectively, rather than ~19:9:3 observed in FIGURE 4.9.

($\nu_{½}$ = 7 Hz) singlet at δ_H = 11.58 ppm, it is plausible that the other cationic component of the product mixture is another amido species; however, recrystallisation attempts from [**13**]BAr^F_4 were unsuccessful and so the species' identity could not be verified.

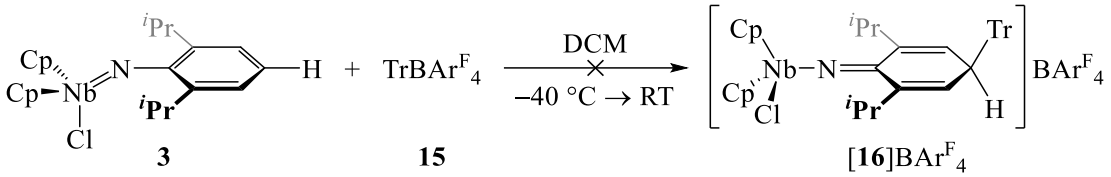

3 **15** [**16**]BAr^F_4

SCHEME 4.7: Attempted synthesis of [$Cp_2NbCl(N\{Dipp\text{-}4\text{-}Tr\})$]$BAr^F_4$ ([**16**]BAr^F_4) from the equimolar reaction between complex **3** and the trityl salt **15**.

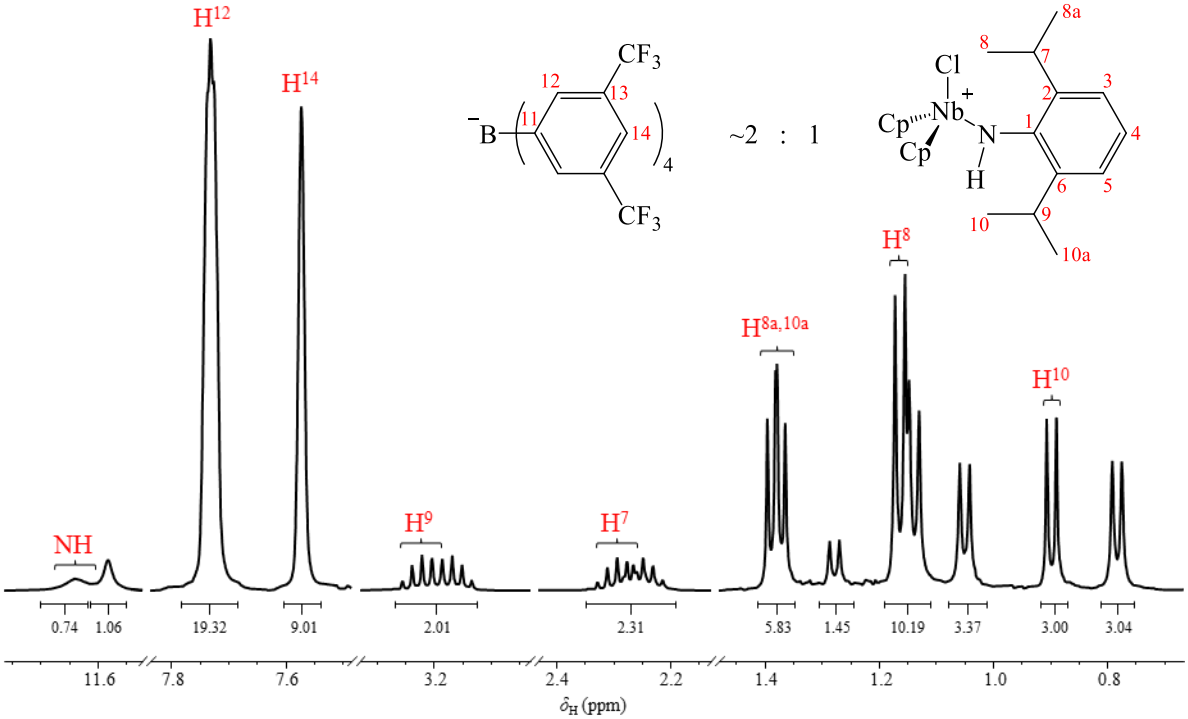

FIGURE 4.9: ^{1}H NMR (400 MHz, CD_2Cl_2) spectrum of the hexanes-insoluble products from reaction between $Cp_2NbCl(NDipp)$ (**3**) and $TrBAr^F_4$ (**15**). Assignments correspond to $[BAr^F_4]^-$ and $[Cp_2NbCl(NHDipp)]^+$ (**13**$^+$).

The formation of the amido salt [**13**]BAr^F_4 is consistent with a competing acid-base reaction occurring during the attempted *para*-tritylation of complex **3** described in SCHEME 4.7. In turn, this may suggest that the reaction between complex **3** and Tr^+ instead occurred *via* an electrophilic aromatic substitution (S_EAr) mechanism (SCHEME 4.8), with residual complex **3** acting as a base for the *para*-deprotonation of the arenium derivative **16**$^+$. While the other substitution product $Cp_2NbCl(NDipp^{Tr})$ (**17**; $Dipp^{Tr}$ = 2,6-$^iPr_2C_6H_2$-4-Tr) was not detected in the ^{1}H NMR spectrum of the product mixture (FIGURE 4.9), it is plausible that the aforementioned N*H* signal (δ_H = 11.58 ppm) may be attributable to the *N*-protonated complex **17**, *i.e.* [$Cp_2NbCl(NHDipp^{Tr})$]BAr^F_4.*

* The generated neutral imido complex $Cp_2NbCl(NDipp^{Tr})$ (**17**) may also deprotonate the arenium derivative $[Cp_2NbCl(N\{Dipp\text{-}Tr\})]^+$ (**16**$^+$; SCHEME 4.8ii).

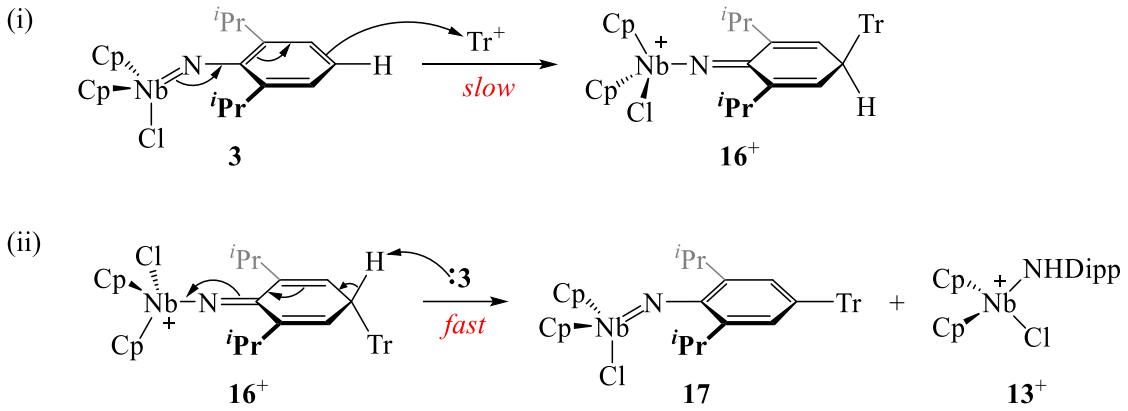

SCHEME 4.8: The proposed electrophilic aromatic substitution (S_EAr) mechanism for the reaction between complex **3** and $TrBAr^F_4$ (**15**; 1 equiv.): (i) slow electrophilic addition of Tr^+ to **3** to form cation **16**$^+$, followed by (ii) rapid deprotonation of **16**$^+$ by complex **3** to form the neutral imido complex **17** and cation **13**$^+$. $[BAr^F_4]^-$ counteranions are omitted for clarity.

In order to prevent the undesirable *N*-protonation of complex **3** during the attempted *para*-tritylation of the complex, the reaction between the imido complex **3** and the trityl salt **15** was repeated in the presence of a strong Brønsted base. Therefore, this meant that the neutral tritylated imido complex $Cp_2NbCl(NDipp^{Tr})$ (**17**) presented itself as a more realistic product of the *para*-tritylation of complex **3**, since the addition product **16**$^+$ would inevitably undergo deprotonation in this basic environment. However, a number of Brønsted bases are known to form stable Lewis adducts with Tr^+, which would likely hinder the desired tritylation of complex **3**. Consequently, 1,4-diazabicyclo[2.2.2]octane (DABCO) was employed as the base due to its steric bulk reportedly preventing its covalent interaction with the Tr^+ cation.[188]

Using a similar procedure to that described in SCHEME 4.7, the reaction between complex **3**, the trityl salt **15** and DABCO (in a 1:1:1 molar ratio) was performed in DCM. Following the removal of the reaction solvent *in vacuo*, extraction into hexanes and subsequent concentration of the filtrate, an orange crystalline material was isolated. NMR spectroscopic, mass spectrometric and elemental analyses of this orange product were consistent with the target complex **17**, which was isolated in 29% yield from the tritylation reaction (SCHEME 4.9).

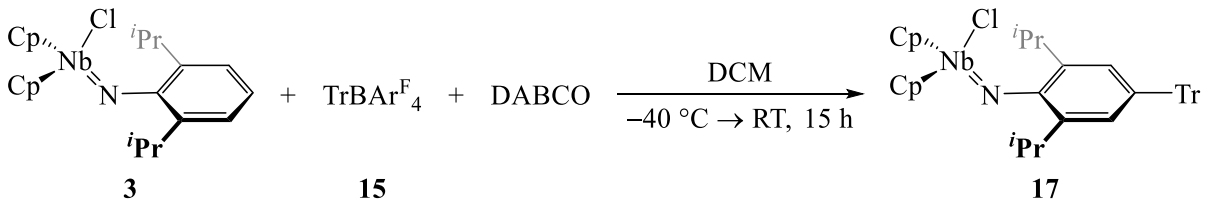

SCHEME 4.9: Formation of $Cp_2NbCl(NDipp^{Tr})$ (**17**) from the tritylation of complex **3** using the trityl salt **15** in the presence of one equivalent of DABCO.

Following the slow cooling of a hot, concentrated solution of complex **17** in hexanes, orange single crystals suitable for XRD analysis were obtained; the experimentally-determined molecular structure of **17** is shown in FIGURE 4.10. As may be seen from the data in TABLE 4.4, the interatomic distance $d_{C14–C23}$ within complex **17** is typical of a single-bond, which confirms the formation of a covalent bond

between the C^{para}-atom of complex **3** and the trityl cation. As determined from the sum of the angles about C14, $\sum(\angle_{X–C14–Y}) \approx 360°$, the C^{para}-atom of complex **17** is sp^2-hybridised. This is consistent with the ring being rearomatised during the tritylation of complex **3** following the deprotonation at the *para*-position of the cationic intermediate $\mathbf{16}^+$ (SCHEME 4.8ii). Additionally, the C–C bond lengths within ring C11–C16 of complex **17**, along with the metric parameters associated with the imido bond (*i.e.* $d_{Nb–N}$, $d_{N–C11}$ and $\angle_{Nb–N–C11}$), are very similar to those of the precursor **3**, which further validates that complex **17** contains an arylimido ligand.

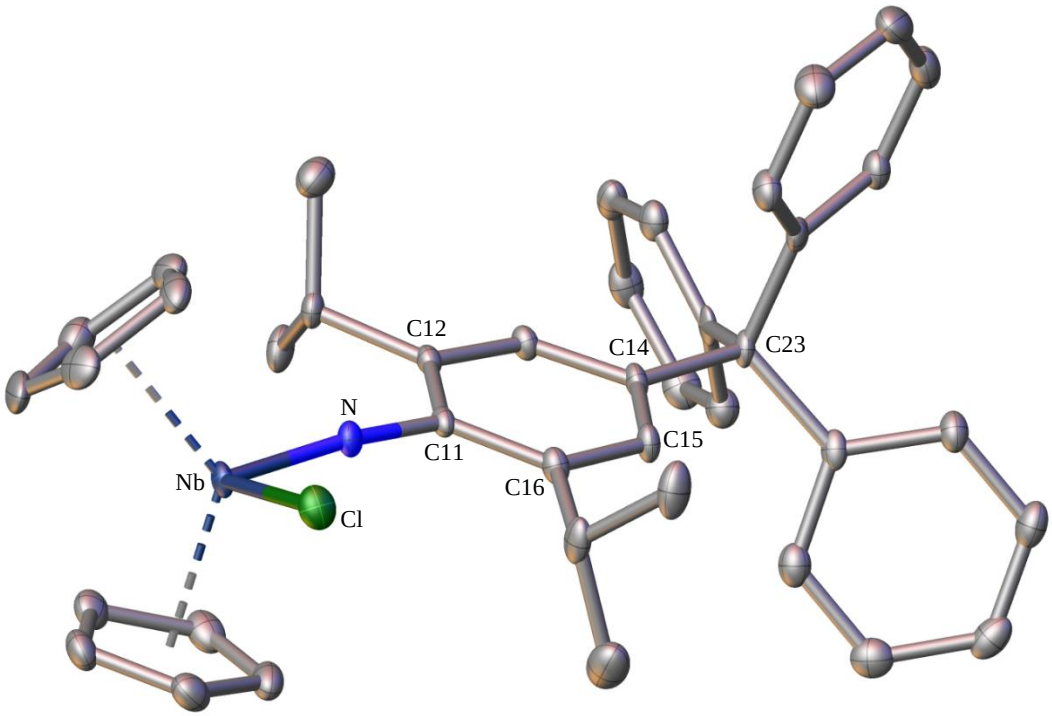

FIGURE 4.10: Crystallographically-determined molecular structure of $Cp_2NbCl(NDipp^{Tr})$ (**17**); thermal ellipsoids are shown at 50% probability and H-atoms are omitted for clarity.

TABLE 4.4: Crystallographically-determined interatomic distances (Å) and angles (°) of complex **17** and its precursor **3**.

	$Cp_2NbCl(NDipp^{Tr})$ (17)	**$Cp_2NbCl(NDipp)$ (3)**
$d_{C14–C23}$	1.542(3)	–
$\sum(\angle_{X–C14–Y})$ [(a)]	359.8(3)	–
$d_{C11–C12}$ [(b)]	1.417(3)	1.4195(10)
$d_{C12–C13}$ [(b)]	1.392(3)	1.3933(11)
$d_{C13–C14}$ [(b)]	1.391(3)	1.3850(12)
$d_{Nb–N}$	1.794(2)	1.7932(9)
$d_{N–C11}$	1.381(3)	1.3794(14)
$\angle_{Nb–N–C11}$	170.7(2)	170.99(8)

[(a)] $\sum(\angle_{X–C14–Y}) = \angle_{C13–C14–C23} + \angle_{C23–C14–C15} + \angle_{C14–C14–C13}$ (*i.e.* the sum of the angles about C14).
[(b)] Average values for chemically equivalent bonds on the aryl ring.

Attempts to improve the ~29% yield of complex **17** were unsuccessful, as further concentration of the mother liquor (hexanes) following the reaction in SCHEME 4.9 instead afforded colourless single crystals

of TrOH,* indicating that the S_EAr reaction between complex **3** and the trityl salt **15** had not gone to completion. Furthermore, extraction of the residual hexanes-insoluble reaction mixture with DCM did not yield further **17**; instead, an intense blue solution was afforded following filtration, which gave a trace amount of vivid-blue solid after the removal of the DCM *in vacuo*. The latter observation suggests that a competing reaction was taking place between complex **3** and the trityl salt **15**, potentially affording a similar blue side-product to that formed from the reaction between the imido complex and Ag^+ salts (SECTION 3.2.1); this reactivity will be explored further in CHAPTER 5.

Despite the low yield of complex **17** achieved overall, its synthesis from the *para*-tritylation of the niobocene imido complex **3** represents a first in the chemistry of imido complexes; previously, only the *para*-tritylation of free amines has been achieved (SCHEME 4.10).[190,191] Furthermore, the tritylation of complex **3** is a unique demonstration of the S_EAr reactivity of d^0 transition metal arylimido complexes, given that the coordination of the N-atom to an electropositive metal centre might be expected to deactivate the aryl ring towards electrophilic attack.

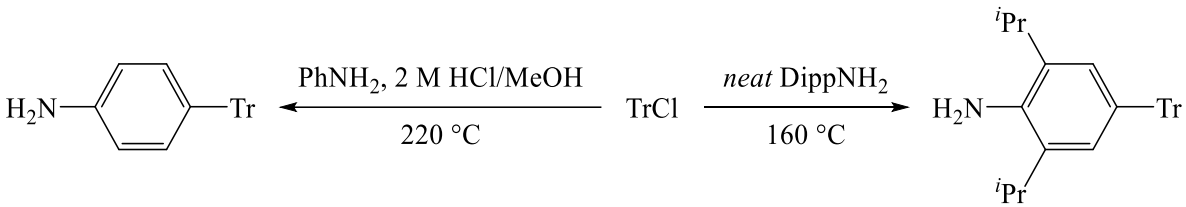

SCHEME 4.10: Reported *para*-tritylation of free amines $PhNH_2$ (95% yield)[190] and $DippNH_2$ (84% yield)[191] using trityl chloride under harsh reaction conditions.

* The molecular structure of TrOH was obtained following X-ray crystallographic analysis of the colourless crystals, which was found to be identical to a previously reported structure deposited in the CSD (KOYNOB).[189]

4.5. Chapter summary

In this chapter, the susceptibility of the niobocene(V) imido complex $Cp_2NbCl(NDipp)$ (**3**) to electrophilic attack has been demonstrated, with steric and electronic factors being shown to have an impact on the site of the reaction. For the small cationic electrophile H^+, electrophilic addition occurs at the imido N-atom of complex **3**, since within the complex this atom is (i) the most electronegative and (ii) the largest contributor to the HOMO. While the formation of the amido cation $[Cp_2NbCl(NHDipp)]^+$ (**13**$^+$) is somewhat unsurprising, it is important in establishing that the heteroatom lone-pair in complex **3** is not involved in bonding to the niobium metal centre and instead the $DippN^{2-}$ ligand adopts an X_2-coordination mode (as anticipated by the "18-electron rule").

Due to the steric constraints imposed by the bulky Cp^- ancillary ligands and *iso*-propyl groups in complex **3**, addition to the N-atom by the large cationic electrophile Tr^+ is prevented and, as such, electrophilic addition instead occurs at the second-largest contributor to the HOMO, *i.e.* at the C^{para}-atom. While the *para*-addition product $[Cp_2NbCl(N\{Dipp\text{-}4\text{-}Tr\})]^+$ (**16**$^+$) is unstable to deprotonation, the neutral elimination product $Cp_2NbCl(NDipp^{Tr})$ (**17**) is isolable when the tritylation of complex **3** is performed in the presence of a Brønsted base.

Since complex **3** is formally a d^0 niobocene(V) arylimido complex, the ability of the complex to undergo tritylation at the *para*-aryl position is wholly attributed to the availability of imido nitrogen lone-pair for donation onto the aryl ring of the imido substituent. Perhaps understandably, the substrate scope for electrophilic attack at the *para*-position of complex **3** is more limited than for the bridging arylimido moieties within some dirhodium(I) systems,[50] as metal–aryl donation of electron-density is not possible in the niobium(V) complex. However, the *para*-tritylation achieved herein with complex **3** does begin to demonstrate the unique properties and reactivities of this unusually electron-rich niobocene imido system.

CHAPTER 5:

Probing oxidative coupling of the d^0 niobium(V) complex $Cp_2NbCl(NDipp)$

5.1. Chapter introduction

Following the successful electrophilic addition to the *para*-position of the aryl imido substituent of $Cp_2NbCl(NDipp)$ (**3**) demonstrated in the previous chapter, it was postulated that this unusually electron-rich niobium(V) arylimido complex may also be susceptible to oxidative coupling at the same position on the aryl ring. Indeed, these two related reactivities have been demonstrated at the *para*-position of the phenyl imido substituent of $Rh_2(\mu\text{-NPh})(CO)_2(\mu\text{-dppm})_2$ ($\mathbf{U_{II}}$; dppm = 1,2-*bis*{diphenylphosphino}methane), with electrophilic addition of MeOTf (Tf = SO_2CF_3)[50] and oxidative coupling using $FcPF_6$ (Fc^+ = ferrocenium)[51] being reported for this arylimido complex (SECTIONS 1.2.4 AND 1.2.5, respectively).

As indicated earlier in this thesis, the susceptibility of complex **3** to oxidation may have been demonstrated during its reactions with cations Ag^+ (SECTION 3.2.1) and Tr^+ (trityl; SECTION 4.4.2), both of which are known oxidants.[137] Following each of these reactions, a distinctive vivid-blue solid was isolated, although efforts to identify the product were unsuccessful. However, in-line with the reported oxidative coupling reactions of arylimido complexes (SECTION 1.2.5), it is plausible that the blue species is a dicationic diketimido complex, featuring either a fully-conjugated diphenoquinoidal (DPQ) or a less-conjugated 4,4'-dihydrodiphenoquinoidal ($DPQH_2$) backbone (FIGURE 5.1).

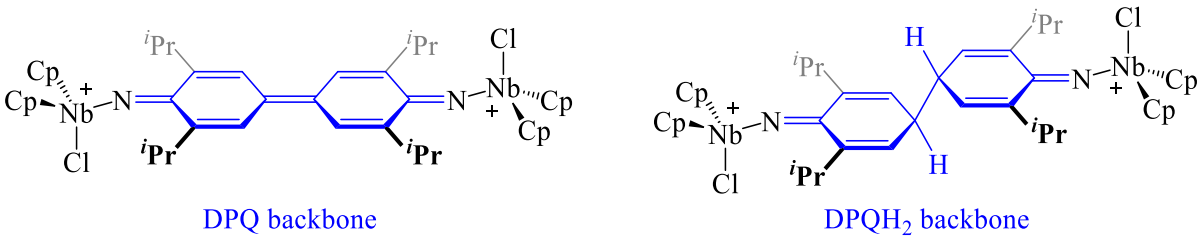

FIGURE 5.1: Potential dicationic diketimido products resulting from the oxidative coupling of $Cp_2NbCl(NDipp)$ (**3**), containing either a diphenoquinoidal (DPQ) or a 4,4'-dihydrodiphenoquinoidal ($DPQH_2$) backbone.

Despite the isolation of a solid as the major product from the reactions between complex **3** and AgX (X = PF_6 or OTf), this material proved too insoluble for spectroscopic analysis to confirm its identity. This insolubility may be attributable to the choice of counteranion, since the blue species recovered from the reaction of the arylimido complex with $TrBAr^F_4$ (Ar^F = 3,5-*bis*{trifluoromethyl}phenyl) proved more soluble, although this was only isolated in trace quantities. Therefore, by combining the higher-yielding Ag^+ oxidant with the solubilising $[BAr^F_4]^-$ counteranion, it was envisaged that the blue material afforded from the reaction between the arylimido complex **3** and $AgBAr^F_4$ may be more easily characterised.

5.2. Oxidative coupling of $Cp_2NbCl(NDipp)$ using $AgBAr^F_4$

To enable comparison with the results from the reactions between $Cp_2NbCl(NDipp)$ (**3**) and silver(I) salts described in SECTION 3.2.1, the arylimido complex **3** was treated with an equimolar quantity of $AgBAr^F_4$ in DCM solution with the exclusion of light. As anticipated, this led to an instantaneous orange-to-blue colour change of the solution. However, in contrast to the reactions of complex **3** with AgX (X = PF_6 or OTf), the formation of a grey precipitate was also observed for the reaction with $AgBAr^F_4$. Following separation *via* cannula filtration, this grey solid was identified as elemental silver by powder XRD analysis, confirming that a redox reaction had indeed taken place between Ag^+ and the arylimido complex **3**. Meanwhile, the volatile components were removed *in vacuo* from the blue mother liquor (DCM) of the reaction mixture; this afforded a deep-blue solid, which was subsequently washed with hexanes. Solution-state ^{1}H NMR spectroscopic analysis of the resulting solid indicated the presence of the amido cation $[Cp_2NbCl(NHDipp)]^+$ (**13**$^+$) alongside the $[BAr^F_4]^-$ anion in a 1:2 molar ratio, respectively (FIGURE 5.2). However, a broad resonance (δ_H = 1.36–1.18 ppm)* was also detected in the ^{1}H NMR spectrum, indicating the presence of another species in the product mixture, potentially responsible for its blue colouration.

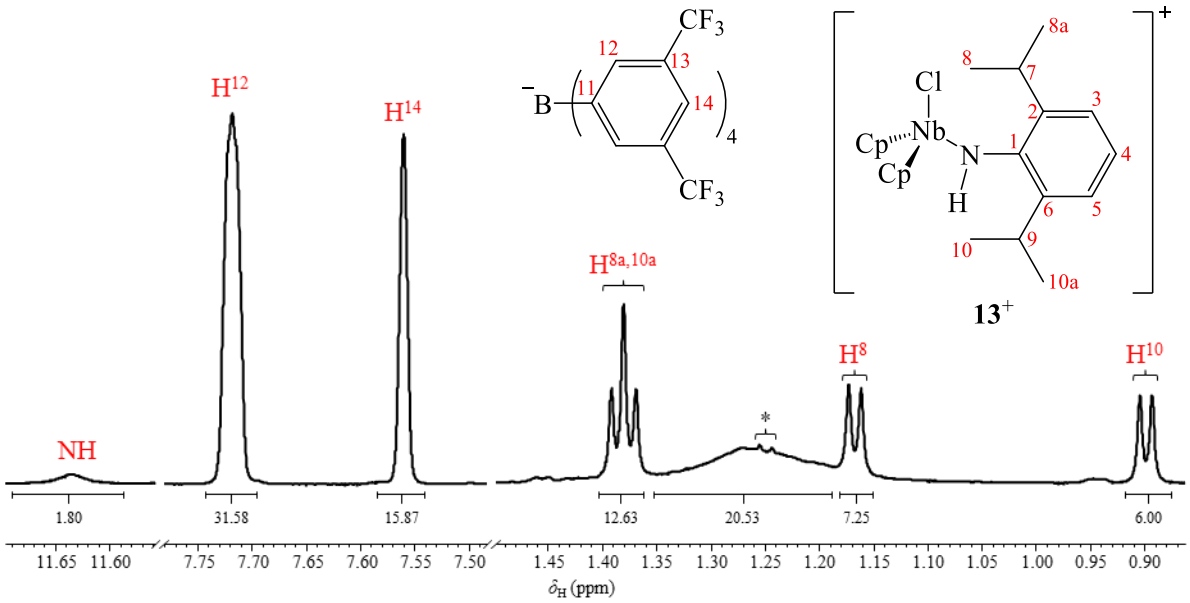

FIGURE 5.2: ^{1}H NMR spectrum (599 MHz, CD_2Cl_2) of the blue product mixture afforded from the reaction between complex **3** and $AgBAr^F_4$. Peak assignments correspond to $[BAr^F_4]^-$, $[Cp_2NbCl(NHDipp)]^+$ (**13**$^+$) and a possible *n*-hexane impurity (*).

The majority of attempts to remove [**13**]BAr^F_4 from the blue product mixture *via* recrystallisation were unsuccessful, since both the amido complex and the other species were found to have very similar solubilities in all solvent systems trialled.† However, after numerous attempts, a very small quantity of

* This broadness may be indicative of the presence of a paramagnetic species in solution (see SECTION 5.3).

† Both salts [**18**][BAr^F_4]$_2$ and [**13**]BAr^F_4 are soluble in DCM, Et_2O, THF, DME and toluene, but insoluble in hexanes and 40/60 petroleum ether.

blue single crystals were grown from layering a DCM solution of the product mixture with hexanes at room temperature. While there were insufficient crystals for spectroscopic characterisation, XRD analysis was successful and confirmed the identity of the blue product as the diphenoquinoidal (DPQ) diketimido complex $[\{Cp_2NbCl\}_2(N\{2,6\text{-}^iPr_2C_6H_2\}_2N)][BAr^F{}_4]_2$ ([**18**][$BAr^F{}_4$]$_2$). The centrosymmetric, experimentally-determined molecular structure of [**18**][$BAr^F{}_4$]$_2$ is shown in FIGURE 5.3.

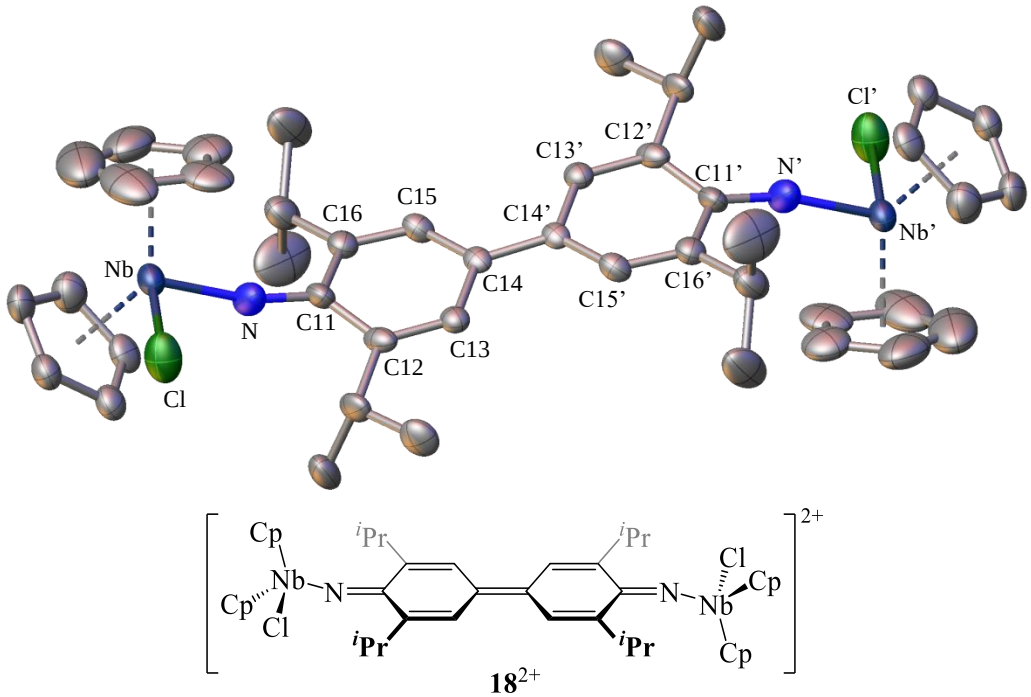

FIGURE 5.3: Crystallographically-determined molecular structure of $[\{Cp_2NbCl\}_2(N\{2,6\text{-}^iPr_2C_6H_2\}_2N)][BAr^F{}_4]_2$ ([**18**][$BAr^F{}_4$]$_2$); thermal ellipsoids are shown at 50% probability. H-atoms, $[BAr^F{}_4]^-$ counteranions and the crystallographic disorder (~16.7% occupancy) about the "Cp_2NbCl" subunits are omitted for clarity.

As indicated by the data in TABLE 5.1, the planar diketimido ligand within complex [**18**][$BAr^F{}_4$]$_2$ bears close structural similarity to those of the rhodium(I) complex $[\{Rh_2(CO)_2(\mu\text{-dppm})_2\}_2(\mu,\mu\text{-}N\{C_6H_4\}_2N)]^{2+}$ (**V**$^{2+}$) and the nickel(II) complex $[\{L_2Ni\}_2(N\{2,6\text{-}Dipp_2C_6H_2\}_2N)]^{2+}$ (**Z**$^{2+}$; L_2 = a *bis*{NHC}) reported in the literature (FIGURE 5.4).[51,54] The interatomic distances within the diketimido moiety of complex **18**$^{2+}$ are consistent with the ligand adopting a diphenoquinoidal (DPQ) structure, namely with alternating double- and single-bonds from N to N', leading to a highly conjugated backbone. Additionally, compared to its imido precursor **3**, the Nb–N bond of complex **18**$^{2+}$ is ~0.08 Å longer, which is associated with a reduction in the niobium–nitrogen bond order following oxidation.

TABLE 5.1: Crystallographically-determined interatomic distances (Å) and angles (°) of the dicationic complex $[\{Cp_2NbCl\}_2(N\{2,6\text{-}^iPr_2C_6H_2\}_2N)]^{2+}$ (**18**$^{2+}$) and its neutral precursor $Cp_2NbCl(NDipp)$ (**3**), along with the DPQ diketimido complexes **V**$^{2+}$ and **Z**$^{2+}$ reported in the literature.[51,54]

	18^{2+}	**3**	**V**$^{2+}$ *(a)*	**Z**$^{2+}$ *(a)*
$d_{Nb–N}$	1.876(8)	1.7932(9)	–	–
$d_{N–C11}$	1.31(1)	1.3794(14)	1.30(1)	1.30(1)
$d_{C11–C12}$ *(b)*	1.46(2)	1.4195(10)	1.44(2)	1.44(4)
$d_{C12–C13}$ *(b)*	1.35(2)	1.3933(11)	1.35(2)	1.35(3)
$d_{C13–C14}$ *(b)*	1.43(2)	1.3850(12)	1.43(2)	1.42(3)
$d_{C14–C14'}$	1.417(9)	–	1.40(1)	1.38(1)

(a) Structures of complexes **V**$^{2+}$ and **Z**$^{2+}$ are shown in FIGURE 5.4; atomic numbering follows that of **18**$^{2+}$ (FIGURE 5.3).
(b) Average values for chemically equivalent bonds in the structure, e.g. C11–C16 ≡ C11–C12.

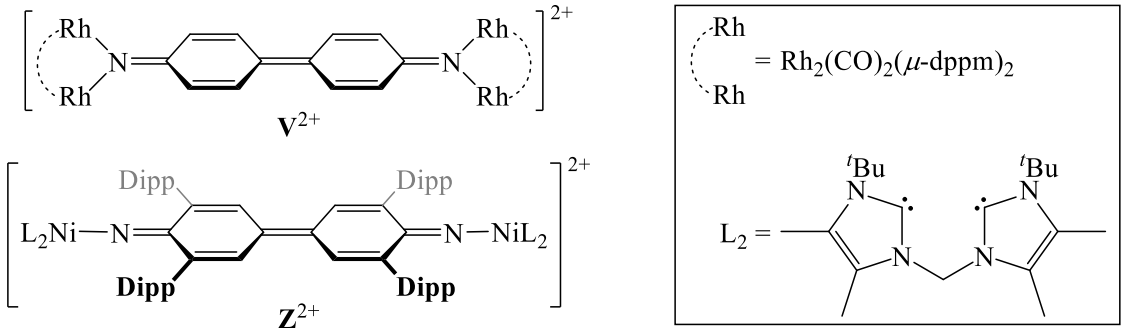

FIGURE 5.4: Crystallographically-determined dicationic DPQ diketimido complexes **V**$^{2+}$ and **Z**$^{2+}$ from the literature.[51,54]

As occurred with the reaction between $AgBAr^F_4$ and **3** herein, the addition of $FcPF_6$ to $Rh_2(\mu\text{-NPh})(CO)_2(\mu\text{-dppm})_2$ (**U$_{II}$**) resulted in the formation of both amido and diketimido salts, namely $Rh_2(\mu\text{-NHPh})(CO)_2(\mu\text{-dppm})_2$ ([**U$_{II}$**·H]PF_6) and [**V**][PF_6]$_2$, respectively.[51] Therefore, it is plausible that the oxidative coupling of the arylimido complex **3** proceeds according to a similar overall reaction, namely that described in SCHEME 5.1, with two (of the four) equivalents of complex **3** serving as a base to facilitate the formation of the 4,4'-deprotonated DPQ diketimido complex **18**$^{2+}$.* Indeed, the 1:2 ratio of signals attributable to **13**$^+$ and [BAr^F_4]$^-$ in the ^{1}H NMR spectrum of the blue product mixture (FIGURE 5.2) is consistent with the expected 1:2 molar ratio of complexes [**18**][BAr^F_4]$_2$ and [**13**]BAr^F_4. Furthermore, elemental analysis of the blue solid was consistent with this ratio of products, albeit with a marginally higher percentage of carbon (+0.71%), which is likely due to the presence of residual hexanes within the product mixture (as evidenced in the NMR spectrum of this material; FIGURE 5.2, denoted *). Together, these data indicate that [**18**][BAr^F_4]$_2$ was produced in an overall yield of 91%.

* The mechanism for the oxidative coupling of complex **3** will be explored in SECTION 5.4.

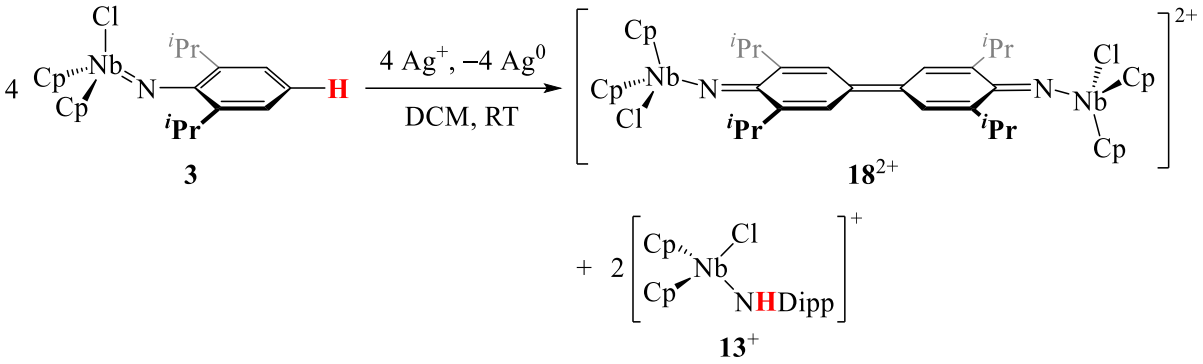

SCHEME 5.1: Formation of the diketimido complex [**18**][BAr^F_4]$_2$ and the amido complex [**13**]BAr^F_4 (in a 1:2 molar ratio, respectively) from the equimolar reaction between complex **3** and $AgBAr^F_4$. For clarity, [BAr^F_4]$^-$ anions are omitted.

Given the problems encountered with separating salts [**18**][BAr^F_4]$_2$ and [**13**]BAr^F_4 by recrystallisation, the addition of a stronger Brønsted base to the reaction between complex **3** and $AgBAr^F_4$ was envisaged as a strategy to prevent the formation of the amido salt. Due to the inevitable formation of [base·H]BAr^F_4 during the oxidative coupling of complex **3**, 1,4-diazabicyclo[2.2.2]octane (DABCO) was selected as the base since its protonated salts are normally highly insoluble (thus easily removed by filtration), which in turn should facilitate the purification of the target complex [**18**][BAr^F_4]$_2$.

In order to ensure the complete oxidation of complex **3** to [**18**][BAr^F_4]$_2$, the arylimido complex was treated with two equivalents of $AgBAr^F_4$ in the presence of DABCO (two equivalents) in DME solution. Once again, a deep-blue solution and a precipitate of elemental silver were afforded, indicating the formation of [**18**][BAr^F_4]$_2$ and Ag^0, respectively (SCHEME 5.2). In an attempt to purify [**18**][BAr^F_4]$_2$, the reaction mixture was filtered and the filtrate was concentrated *in vacuo*. The resulting blue solid was washed with hexanes and 40/60 petroleum ether. However, despite the repeated washings, ^{1}H NMR spectroscopic analysis of the blue solid indicated the presence of unreacted DABCO alongside its protonated salt, thus indicating that [DABCO·H]BAr^F_4 and the target [**18**][BAr^F_4]$_2$ have undesirably similar solubilities. As a consequence of this product mixture comprising at least three components, the quantification of the diketimido complex [**18**][BAr^F_4]$_2$ within the blue material was hindered. Therefore, this product mixture of [**18**][BAr^F_4]$_2$, [DABCO·H]BAr^F_4 and DABCO was not used in subsequent investigations of the diketimido complex.

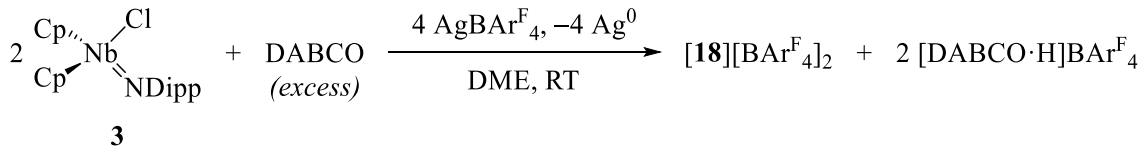

SCHEME 5.2: Alternative synthesis of the diketimido complex [{Cp_2NbCl}$_2$(N{2,6-^{i}Pr$_2$C$_6$H$_2$}$_2$N)][BAr^F_4]$_2$ ([**18**][BAr^F_4]$_2$), producing [DABCO·H]BAr^F_4 as the by-product instead of the amido complex [Cp_2NbCl(NHDipp)]BAr^F_4 ([**13**]BAr^F_4).

5.3. Investigating the diradical character of the dicationic diketimido complex $[\{Cp_2NbCl\}_2(N\{2,6\text{-}^iPr_2C_6H_2\}_2N)]^{2+}$

As outlined in SECTION 5.2, the solution-state ^{1}H NMR spectrum of the [**18**][BAr^F_4]$_2$/[**13**]BAr^F_4 mixture presented a broad feature (δ_H = 1.36–1.18 ppm; FIGURE 5.2) that was notably absent in the spectrum of the pure amido salt [**13**]BAr^F_4. This broadness may be indicative of the dicationic complex **18**$^{2+}$ being a paramagnetic species,[192] although such behaviour has not been reported for the other diketimido complexes **V**$^{2+}$ and **Z**$^{2+}$ (see FIGURE 5.4).[51,54] However, a few metal-free, diphenoquinoidal (DPQ) analogues of **18**$^{2+}$ have been reported to possess some diradical character, namely the dicationic salt $[Ar_2N\{C_6H_4\}_2NAr_2][Al(OR)_4]_2$ (Ar = C_6H_4-4-OMe and R = $C\{CF_3\}_3$; NISHUU)[193] and its neutral homologue $Ph_2C\{C_6H_4\}_2CPh_2$ ("Chichibabin's hydrocarbon"; DUPROV)[194,195] shown in FIGURE 5.5. Furthermore, since such highly-conjugated radical species are often intensely coloured,[196,197] this may explain the unusual, vivid-blue colouration of the diketimido complex **18**$^{2+}$ synthesised herein.

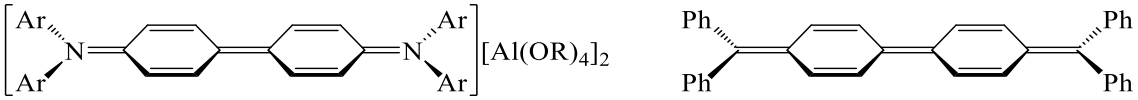

NISHUU DUPROV

FIGURE 5.5: Crystallographically-determined organic DPQ compounds NISHUU (Ar = C_6H_4-4-OMe and R = $C\{CF_3\}_3$)[193] and DUPROV ("Chichibabin's hydrocarbon")[195] that exhibit partial diradical character.

An attempt to probe any paramagnetic character of the diketimido complex **18**$^{2+}$ was made using Evans' method:[198] a CD_2Cl_2 solution of the **18**$^{2+}$/**13**$^+$ mixture (1:2 molar ratio)* was analysed by ^{1}H NMR spectroscopy in the presence of a lock-tube containing pure CD_2Cl_2. A difference in frequency ($\Delta\nu$) was observed between the signals corresponding to the residual *protio* NMR solvent inside the lock-tube and within the product solution (FIGURE 5.6). In turn, this indicated that a paramagnetic species was present in the **18**$^{2+}$/**13**$^+$ product mixture. After correcting for the presence of the diamagnetic species $[BAr^F_4]^-$ and **13**$^+$ within the [**18**][BAr^F_4]$_2$/[**13**]BAr^F_4 mixture (see APPENDIX 2), quantitative analysis determined an effective magnetic moment (μ_{eff}) of 1.88 ± 0.09 μ_B for the dicationic diketimido complex **18**$^{2+}$ (TABLE 5.2).

* Due to the aforementioned challenges with obtaining a pure sample of [**18**][BAr^F_4]$_2$ (SECTION 5.2), the reasonably well-characterised mixture of [**18**][BAr^F_4]$_2$ and [**13**]BAr^F_4 (2:1 molar ratio) was used herein.

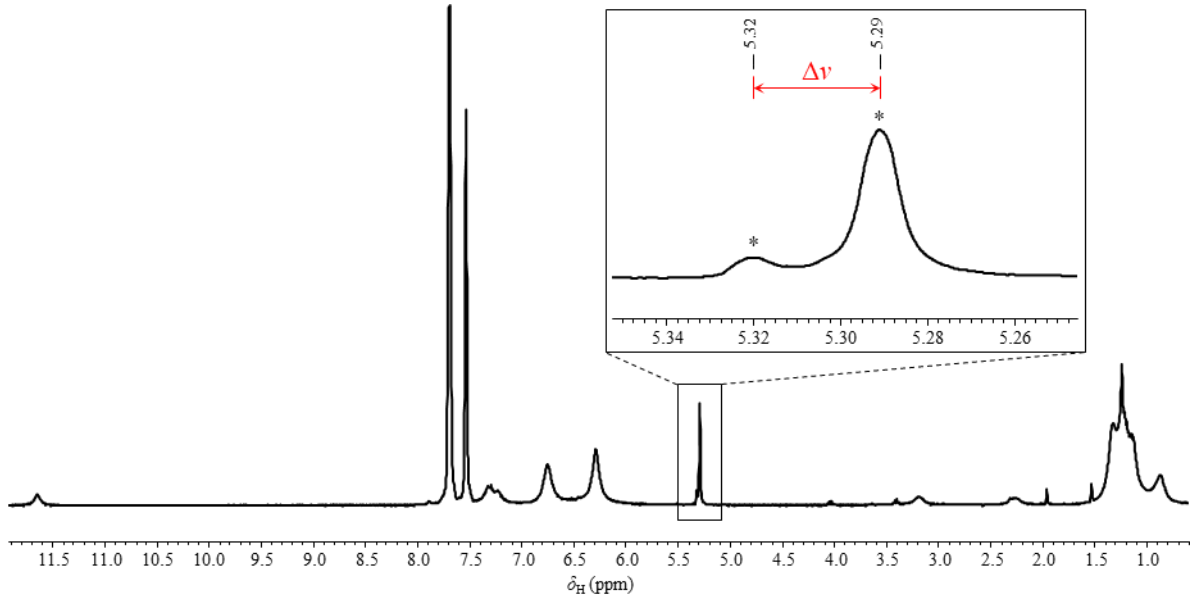

FIGURE 5.6: A typical ^{1}H NMR (400 MHz, CD_2Cl_2, CD_2Cl_2 in sealed lock-tube) spectrum of the 1:2 [**18**][BAr^F_4]$_2$/[**13**]BAr^F_4 product mixture, highlighting two signals corresponding to the residual *protio* NMR solvent (*) separated by $\Delta\nu$.

TABLE 5.2: Experimental parameters used to calculate the effective magnetic moment (μ_{eff}) of dication **18**$^{2+}$. m = mass of product mixture; m_{solv} = mass of solvent (CD_2Cl_2); $\Delta\nu$ = difference in frequency between the two residual *protio* solvent signals (FIGURE 5.6); T = temperature; μ_B = the unit of the Bohr magneton.*

Run	m / g	m_{solv} / g	$\Delta\nu$ / Hz	T / K	μ_{eff} / μ_B
1	0.035	0.913	11.53	293.3	2.05
2	0.021	1.100	8.73	295.7	1.84
3	0.019	0.989	9.81	296.1	1.76
				Average:	**1.88 ± 0.09**

The determined μ_{eff} value is most consistent with a spin-only magnetic moment ($\mu_{s.o}$; see APPENDIX 2) corresponding to a single unpaired electron (S = 0.5; $\mu_{s.o.}$ = 1.73 μ_B). However, this doublet multiplicity is not possible for **18**$^{2+}$ since the diketimido complex contains an even number of electrons. Therefore, a possible explanation for the observed μ_{eff} value is that both the singlet (S = 0; $\mu_{s.o.}$ = 0 μ_B) and triplet (S = 1; $\mu_{s.o.}$ = 2.83 μ_B) states of the diketimido complex **18**$^{2+}$ exist in equilibrium in solution, which would result in an intermediate magnetic moment.†

In order to determine the thermodynamic stability of the theoretical singlet and triplet states of the diketimido dication **18**$^{2+}$ (**18**$_S^{2+}$ and **18**$_T^{2+}$, respectively), a DFT study was undertaken.‡ The two resulting optimised gas-phase structures of **18**$_S^{2+}$ and **18**$_T^{2+}$ are displayed in FIGURE 5.7 and both located at energetic minima. As summarised in TABLE 5.3, these computed structures of **18**$_S^{2+}$ and **18**$_T^{2+}$ differ substantially in geometry, particularly regarding the C12–C13 and C14–C14' bond lengths, along with

* The calculation details and formulae associated with Evans' method are presented in APPENDIX 2.

† While it is possible that orbital angular momentum also contributes towards the observed magnetic moment, the delocalisation of the two unpaired electrons in the triplet state of **18**$^{2+}$ (see FIGURE 5.7) makes the determination of its contribution non-trivial.[192]

‡ The crystallographically-determined structure of **18**$^{2+}$ (FIGURE 5.3) was used as the starting geometry for both **18**$_S^{2+}$ and **18**$_T^{2+}$, where the spin multiplicities were assigned as 1 and 3, respectively, prior to optimisation.

the coplanarity of the two six-membered rings (quantified by the dihedral angle $\phi_{C13–C14–C14'–C13'}$). As indicated by the root-mean-square (RMS) and maximum distances in the table, the crystallographically-determined structure of $\mathbf{18}^{2+}$ bears greater similarity with the computed structure of $\mathbf{18_S}^{2+}$ than $\mathbf{18_T}^{2+}$. In turn, this suggests that the diketimido complex $\mathbf{18}^{2+}$ has a singlet configuration in the solid-state; indeed, this is consistent with the computed gas-phase structure of $\mathbf{18_S}^{2+}$ being more thermodynamically stable than $\mathbf{18_T}^{2+}$ (ΔG = –26.9 kJ mol^{-1}).

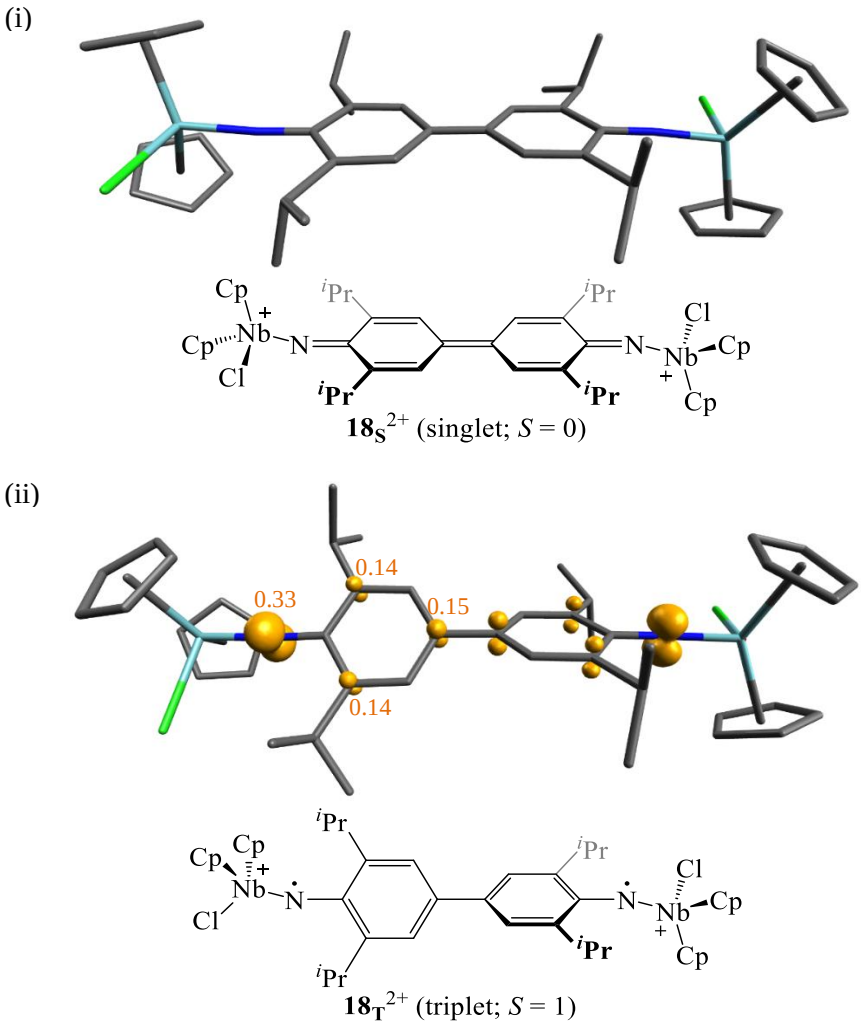

FIGURE 5.7: Computed (B3LYP/3-21G*) gas-phase structures of the (i) singlet ($\mathbf{18_S}^{2+}$) and (ii) triplet ($\mathbf{18_T}^{2+}$) states of the diketimido dication $[\{Cp_2NbCl\}_2(N\{2,6\text{-}^iPr_2C_6H_2\}_2N)]^{2+}$ ($\mathbf{18}^{2+}$). H-atoms are omitted for clarity and the calculated atomic spin densities of $\mathbf{18_T}^{2+}$ are shown in orange.

TABLE 5.3: Selected interatomic distances (Å) and angles (°) of the crystallographically-determined structure of $[\{Cp_2NbCl\}_2(N\{2,6\text{-}^iPr_2C_6H_2\}_2N)]^{2+}$ ($\mathbf{18}^{2+}$; FIGURE 5.3), compared with those of the computed (B3LYP/3-21G*) gas-phase singlet- and triplet-state structures $\mathbf{18_S}^{2+}$ and $\mathbf{18_T}^{2+}$, respectively (FIGURE 5.7).

	$\mathbf{18}^{2+}$ **(XRD)**	$\mathbf{18_S}^{2+}$ **(DFT)**	$\mathbf{18_T}^{2+}$ **(DFT)**
$d_{C12–C13}$ [(a)]	1.35(2)	1.362	1.385
$d_{C14–C14'}$ [(a)]	1.417(9)	1.419	1.486
$\lvert\phi_{C13–C14–C14'–C13'}\rvert$ [(a)]	180.0(4)	175.6	134.8
RMS (max.) [(b)]	–	0.6688 (1.4589)	1.1750 (2.9625)

[(a)] Average parameters for chemically equivalent atoms or bonds (*e.g.* C12 ≡ C16 and C12–C13 ≡ C12'–C13').
[(b)] Distances (Å) calculated from the overlay of the computed structures with the experimental structure (FIGURE 5.3).

Within the diradical complex $\mathbf{18}_T^{2+}$, computational studies reveal that each unpaired electron is primarily localised at the N-atoms of the diketimido complex (33%; FIGURE 5.7ii), although the radicals are partially delocalised onto the *ortho*- and *para*-positions of each six-membered ring through resonance. This delocalisation of the radicals across the diketimido ligand backbone may explain the observed broadening of all signals attributable to the diketimido complex $\mathbf{18}^{2+}$ in the ^{1}H NMR spectrum (FIGURE 5.2), particularly if the intersystem crossing between $\mathbf{18}_S^{2+}$ and $\mathbf{18}_T^{2+}$ is rapid in solution.

Similar to the gas-phase computational results, $\mathbf{18}_S^{2+}$ was computed to be more thermodynamically stable than $\mathbf{18}_T^{2+}$ in DCM solution (ΔG = –28.0 kJ mol^{-1}).* However, the triplet state may be sufficiently electronically stabilised in solution relative to the singlet state, since the two singly-occupied MOs (SOMOs) of $\mathbf{18}_T^{2+}$ are at a lower combined energy than the filled HOMO of $\mathbf{18}_S^{2+}$ (FIGURE 5.8). This in turn may facilitate intersystem crossing between $\mathbf{18}_S^{2+}$ and $\mathbf{18}_T^{2+}$ in DCM solution, although the process by which this occurs remains unknown.

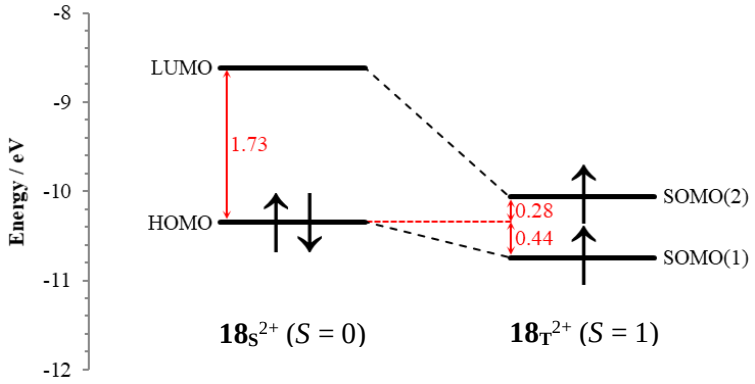

FIGURE 5.8: Computed (B3LYP/3-21G*; SMD solvent model) MO diagram of the singlet ($\mathbf{18}_S^{2+}$) and triplet ($\mathbf{18}_T^{2+}$) states of $[\{Cp_2NbCl\}_2(N\{2,6\text{-}^iPr_2C_6H_2\}_2N)]^{2+}$ ($\mathbf{18}^{2+}$) in DCM solution. Energy differences (in eV) are shown in red.

By way of comparison, the observed paramagnetism of the organic diphenoquinoidal (DPQ) compounds NISHUU and DUPROV (FIGURE 5.8) has been proposed to arise from an "open-shell" singlet (*i.e.* two unpaired electrons of opposite spin) rather than a triplet-state configuration.[193,199] However, an analogous "open-shell" singlet-state structure could not be computed for the diketimido complex $\mathbf{18}^{2+}$, despite using the same unrestricted DFT method as employed in the literature.[199,†] Experimentally, triplet and "open-shell" singlet states would be distinguishable by electron paramagnetic resonance (EPR) spectroscopy. However, considering the lack of purity of the diketimido complex within the product mixture containing [**18**][BAr^F_4]$_2$ and [**13**]BAr^F_4 (in a 1:2 molar ratio), EPR spectroscopic analysis was not undertaken on this sample.

* Analogous geometric optimisation in DCM (using the SMD solvent model) resulted in structures of $\mathbf{18}_S^{2+}$ and $\mathbf{18}_T^{2+}$ that were similar to the gas-phase structures in FIGURE 5.7.

† There are limitations for the use of the unrestricted DFT (UB3LYP) method for more complicated "open-shell" singlet systems.[199] In such cases, the significantly more advanced "multiconfigurational self-consistent field" method is typically used.[200]

5.4. Exploring the oxidative coupling mechanism of $Cp_2NbCl(NDipp)$

In light of the problems encountered with isolating a pure sample of $[\{Cp_2NbCl\}_2(N\{2,6\text{-}^iPr_2C_6H_2\}_2N)][BAr^F{}_4]_2$ ([**18**][$BAr^F{}_4$]$_2$) following reaction of complex $Cp_2NbCl(NDipp)$ (**3**) with $AgBAr^F{}_4$ (SECTION 5.2), an alternative synthetic route to the diphenoquinoidal (DPQ) diketimido complex was desirable. Instead of a one-step synthesis from complex **3**, it was envisaged that [**18**][$BAr^F{}_4$]$_2$ could be synthesised in a stepwise fashion with the isolation of any intermediate species, thereby ensuring that each step during the overall oxidative coupling mechanism attains completion. Such an approach was adopted by Sharp and co-workers for the oxidative coupling of $Rh_2(\mu\text{-NPh})(CO)_2(\mu\text{-dppm})_2$ (**U_{II}**) to the DPQ diketimido complex $[\{Rh_2(CO)_2(\mu\text{-dppm})_2\}_2(\mu,\mu\text{-N}\{C_6H_4\}_2N)][PF_6]_2$ ([**V**][PF_6]$_2$), where the intermediates $[\{Rh_2(CO)_2(\mu\text{-dppm})_2\}_2(\mu,\mu\text{-N}\{4,4'\text{-Ph}_2\}N)][PF_6]_2$ ([**W**][PF_6]$_2$) and $\{Rh_2(CO)_2(\mu\text{-dppm})_2\}_2(\mu,\mu\text{-N}\{C_6H_4\}_2N)$ (**X**) were isolated (SECTION 1.2.5).[51]

As outlined earlier, the rhodium(I) system of Sharp and co-workers bears similarity with the niobocene(V) system herein. This is considering that for both systems, a 2:1 mixture of the amido and DPQ diketimido salts are afforded following the addition of the arylimido complex to an equimolar quantity of the oxidant.[51] Consequently, it is plausible that the mechanism for the oxidative coupling of the imido complex **3** may be similar to that of complex **U_{II}**. Therefore, the formation of the DPQ diketimido dication **18**$^{2+}$ from the imido complex **3** would proceed according to the mechanism described in SCHEME 5.3, namely *via* the radical cation $[Cp_2NbCl(NDipp)]^{\bullet+}$ (**3**$^{\bullet+}$), the dicationic 4,4'-dihydrodiphenoquinoidal ($DPQH_2$) diketimido complex $[\{Cp_2NbCl\}_2(N\{4,4'\text{-Dipp}_2\}N)]^{2+}$ (**19**$^{2+}$) and the neutral biphenyl diimido complex $\{Cp_2NbCl\}_2(N\{2,6\text{-}^iPr_2C_6H_2\}_2N)$ (**20**).

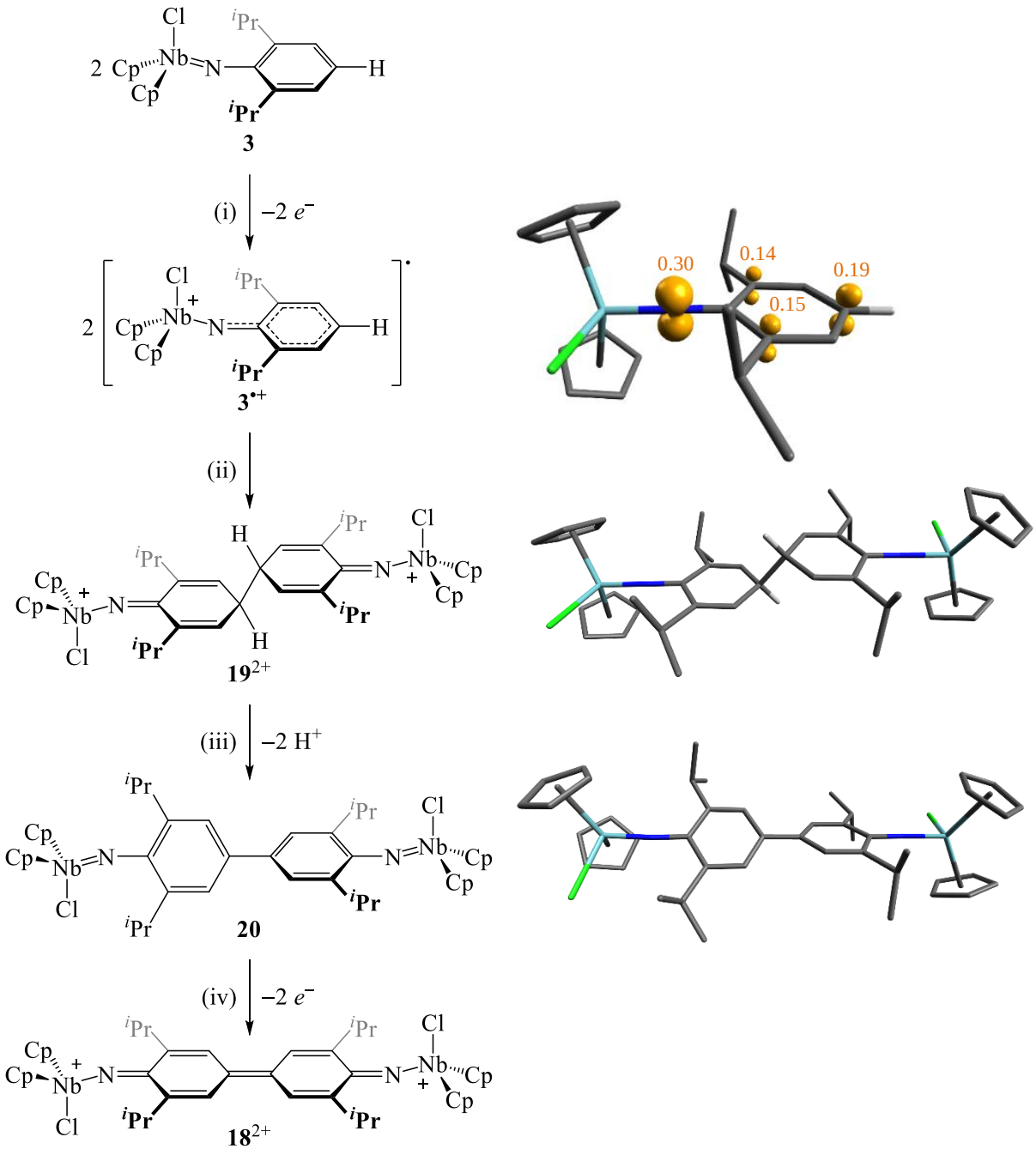

SCHEME 5.3: Proposed mechanism for the oxidation coupling of the arylimido complex **3**: (i) oxidation to the radical cation **3**$^{\bullet+}$, (ii) dimerisation to the DPQH$_2$ diketimido dication **19**$^{2+}$, (iii) deprotonation to the diimido complex **20** and (iv) oxidation to DPQ diketimido dication **18**$^{2+}$. The computed (B3LYP/3-21G*) gas-phase structures of the intermediates **3**$^{\bullet+}$, **19**$^{2+}$ and **20** are shown, with H-atoms (except at the *para*-position, where applicable) omitted for clarity. Calculated atomic spin-densities on **3**$^{\bullet+}$ are displayed in orange.

To support this proposed mechanism for the oxidative coupling of complex **3**, a DFT study was performed on the proposed intermediates **3**$^{\bullet+}$, **19**$^{2+}$ and **20**, which following geometric optimisation resulted in all three structures being located at energetic minima (SCHEME 5.3).[*] NBO analysis was also

[*] The crystallographically-determined molecular structure of $Cp_2NbCl(NDipp)$ (**3**) was used as the starting geometry for the radical cation **3**$^{\bullet+}$ (setting the charge to 1+ and spin-multiplicity to 2), whereas that of $[\{Cp_2NbCl\}_2(N\{2,6\text{-}^iPr_2C_6H_2\}_2N)]^{2+}$ (**18**$^{2+}$) was used for both the DPQH$_2$ diketimido complex **19**$^{2+}$ (with the addition of an H-atom to each of the 4- and 4'-positions) and the diimido complex **20** (setting the charge to 0).

performed on the radical cation $\mathbf{3}^{\bullet+}$, which revealed that the unpaired electron is partially (19%) localised at the C^{para}-atom, away from the bulk positive charge at niobium (NBO charge = +0.504).* Consequently, there should be minimal coulombic repulsion between the C^{para}-positions of two molecules of $\mathbf{3}^{\bullet+}$ and hence their coupling to the $DPQH_2$ diketimido complex $\mathbf{19}^{2+}$ (SCHEME 5.3ii) is likely to be rapid. Therefore, the radical cation $\mathbf{3}^{\bullet+}$ is unlikely to be isolable during the oxidative coupling of complex **3**. Indeed, the radical cation $[L_2Ni(N\{2,6\text{-}Dipp_2C_6H_3\})]^{\bullet+}$ ($\mathbf{Y}^{\bullet+}$; L_2 = *bis*{3-*tert*-butyl-4,5-dimethylimidazol-2-yliden-1-yl}methane), which had similar computed spin- and charge-density distributions to that of $\mathbf{3}^{\bullet+}$ (SECTION 1.2.5), was reportedly never isolated during the oxidative coupling of the arylimido complex **Y** to $[\{L_2Ni\}_2(N\{2,6\text{-}Dipp_2C_6H_2\}_2N)]^{2+}$ ($\mathbf{Z}^{2+}$).[54]

On the other hand, the dicationic $DPQH_2$ diketimido complex $\mathbf{19}^{2+}$ may be more stable than the radical cation $\mathbf{3}^{\bullet+}$, particularly given that Sharp and co-workers successfully demonstrated the isolation of the analogous complex [**W**][PF_6]$_2$.[51] In this reported rhodium(I) system, the order of addition of the reagents proved crucial, since the $DPQH_2$ diketimido complex [**W**][PF_6]$_2$ was only afforded following the slow addition of the arylimido complex $\mathbf{U_{II}}$ to $FcPF_6$ (rather than *vice versa*), a methodology that maintains the oxidant in excess at all times. Adopting the strategy of Sharp and co-workers herein, the synthesis of the $DPQH_2$ diketimido complex [**19**][$BAr^F{}_4$]$_2$ was attempted *via* the slow addition of a CD_2Cl_2 solution of complex **3** to an equimolar amount of $AgBAr^F{}_4$ (SCHEME 5.4). However, the resulting vivid-blue colouration indicated the formation of the fully-conjugated DPQ diketimido species $\mathbf{18}^{2+}$ instead of the desired $DPQH_2$ diketimido complex $\mathbf{19}^{2+}$. The synthesis herein of $\mathbf{18}^{2+}$ was further confirmed by the detection of the amido salt [**13**]$BAr^F{}_4$ in the ^{1}H NMR spectrum of the reaction mixture, indicating that the residual imido complex **3** in the reaction had deprotonated any transient $DPQH_2$ diketimido complex $\mathbf{19}^{2+}$ at the 4- and 4'-positions (SCHEME 5.3iii).

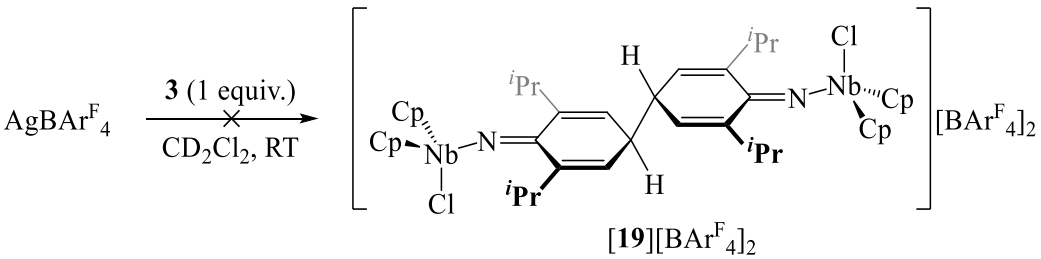

[**19**][$BAr^F{}_4$]$_2$

SCHEME 5.4: Attempted formation of the $DPQH_2$ diketimido complex [**19**][$BAr^F{}_4$]$_2$ from the slow addition of Cp_2NbCl(NDipp) (**3**) to $AgBAr^F{}_4$.

As the deprotonation of the $DPQH_2$ diketimido complex $\mathbf{19}^{2+}$ appeared to be unavoidable during the oxidative coupling of **3**, attention instead turned to the isolation of the product formed directly after the deprotonation step, namely the neutral biphenyl diimido complex **20**. In an attempt to prevent the second oxidation step (SCHEME 5.3iv) from occurring, the milder oxidant† $FcPF_6$ was substituted for $AgBAr^F{}_4$

* Comparatively, NBO analysis determined a smaller charge of –0.147 on the C^{para}-atom of radical cation $\mathbf{3}^{\bullet+}$.

† The standard reduction potentials (E_{red}°) of Ag^+ and Fc^+ are +0.800 and +0.400 V, respectively, *vs.* SHE.[115]

prior to the addition of complex **3**. However, no reaction occurred between complex **3** and $FcPF_6$ (SCHEME 5.5), as evidenced by the quantitative recovery of the monomeric imido reagent following extraction of the reaction mixture into hexanes.

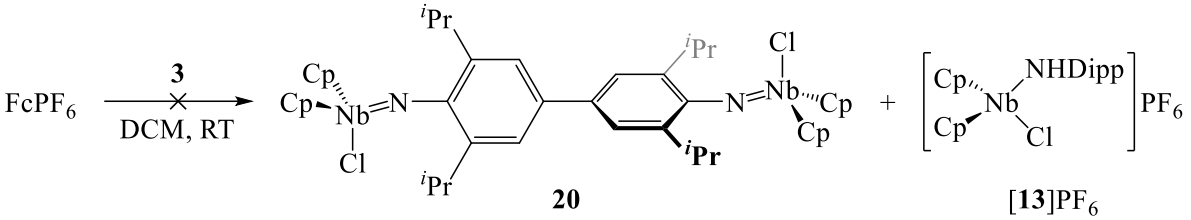

SCHEME 5.5: Attempted formation of the diimido complex **20** by gradual addition of $Cp_2NbCl(NDipp)$ (**3**) to $FcPF_6$.

In order to meet the requirements for the isolation of complex **20**, an oxidant must be selected with a reduction potential greater than $E_{red}(\mathbf{3}^{\bullet+}/\mathbf{3})$ (to enable the first oxidation step; SCHEME 5.3i), but also less than $E_{red}(\mathbf{18}^{2+}/\mathbf{20})$ (to prevent the subsequent oxidation of **20**; SCHEME 5.3iv). While oxidants of various reduction potentials are available,[115] without an electrochemical investigation into this niobocene imido system, there is no guarantee that the further requirement of $E_{red}(\mathbf{3}^{\bullet+}/\mathbf{3}) < E_{red}(\mathbf{18}^{2+}/\mathbf{20})$ is met; hence, it may never be possible to isolate complex **20** *via* this methodology.

With a view to exploring the final oxidation step during the oxidative coupling of complex **3** (SCHEME 5.3iv), the reverse of this reaction (*i.e.* the reduction of the DPQ diketimido complex [**18**]BAr^F_4) was attempted. As a pure sample of the diketimido complex was unobtainable (SECTION 5.2), the mixture of salts [**18**][BAr^F_4]$_2$/[**13**]BAr^F_4 (in a 1:2 molar ratio)* was reacted with excess Na sand in THF solution, with the envisaged formation of the diimido complex **20** and complex **3**, respectively (SCHEME 5.6). Over the course of heating this reaction mixture at reflux for ~5 days, the vivid-blue solution reddened in colour, indicative of the consumption of the DPQ diketimido species $\mathbf{18}^{2+}$. The surplus sodium was separated from reaction mixture *via* filtration, following which the volatile components of the filtrate were removed *in vacuo*. The resultant red paste was extracted in hexanes and the filtrate was concentrated to afford a deep-red solid (~10% of the original mass).†

* This diketimido/amido salt mixture was afforded from the reaction described in SCHEME 5.1.

† ^{1}H NMR spectroscopic analysis of the remaining mother liquor (hexanes) indicated only the presence of the imido complex **3** by-product, and so this solution was discarded.

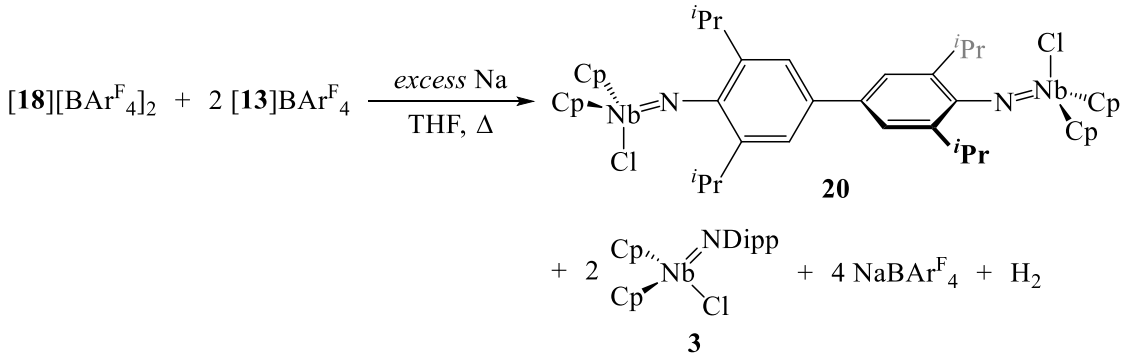

SCHEME 5.6: Reduction of the 1:2 $[\{Cp_2NbCl\}_2(N\{2,6\text{-}^iPr_2C_6H_2\}_2N)][BAr^F{}_4]_2$ ([**18**][$BAr^F{}_4$]$_2$) and $[Cp_2NbCl(NHDipp)]BAr^F{}_4$ ([**13**]$BAr^F{}_4$) mixture using Na sand to produce the neutral imido complexes **20** and **3**, respectively.

Due to the small amount of red solid isolated from the reduction reaction, subsequent solution-state ^{1}H NMR spectroscopic analysis was unable to verify the formation of the diimido complex **20**, as only signals attributable to the imido complex **3** by-product were identifiable. However, recrystallisation of the red solid from a hot, concentrated toluene solution afforded red single crystals, which following successful XRD analysis were determined to be of the target complex **20** (~30% yield). The experimentally-determined molecular structure of the biphenyl diimido complex **20** is shown in FIGURE 5.9.

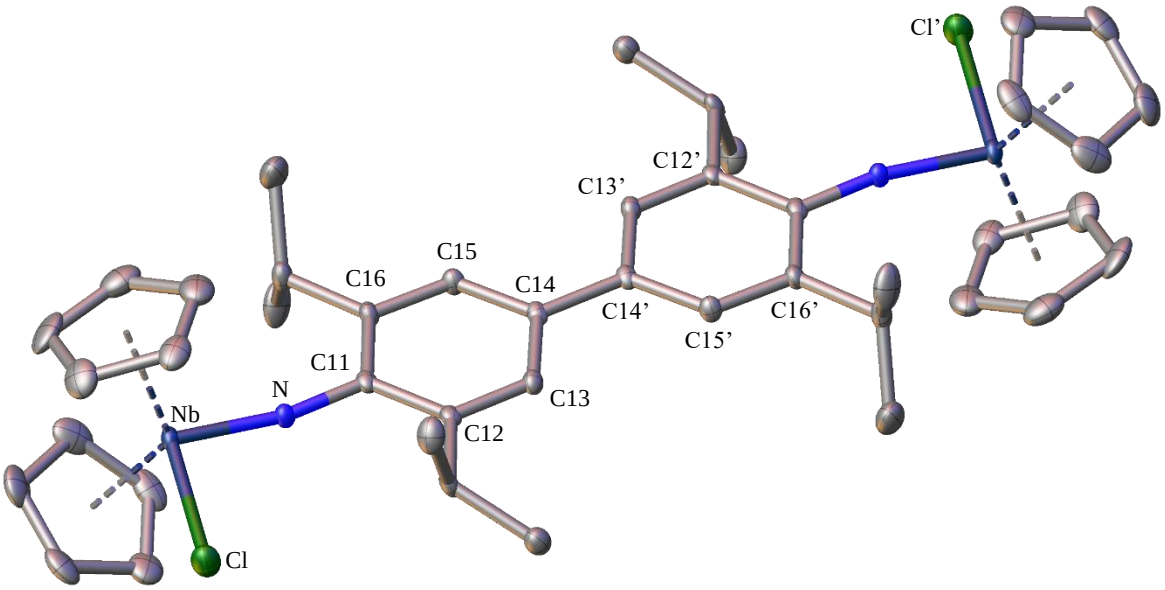

FIGURE 5.9: Experimentally-determined molecular structure of $\{Cp_2NbCl\}_2(N\{2,6\text{-}^iPr_2C_6H_2\}_2N)$ (**20**); thermal ellipsoids are shown at 50% probability and H-atoms are omitted for clarity.

As shown by the data in TABLE 5.4, compared to its dicationic precursor **18**$^{2+}$, the neutral complex **20** features shorter Nb–N bonds, along with longer N–C11 and C14–C14' bonds. Furthermore, there is less variation between the aryl C–C bond lengths ($d_{C11–C12}$, $d_{C12–C13}$ and $d_{C13–C14}$) of complex **20** than determined for the dication **18**$^{2+}$. Together, these crystallographically-determined interatomic distances are consistent with the complex **20** adopting a diaromatic biphenyl diimido structure, rather than maintaining the fully-conjugated DPQ diketimido ligand backbone of **18**$^{2+}$.

TABLE 5.4: Selected experimentally-determined interatomic distances (Å) and angles (°) of structures of neutral $\{Cp_2NbCl\}_2(N\{2,6\text{-}^iPr_2C_6H_2\}_2N)$ (**20**; FIGURE 5.9), its dication $[\{Cp_2NbCl\}_2(N\{2,6\text{-}^iPr_2C_6H_2\}_2N)]^{2+}$ (**18**$^{2+}$; FIGURE 5.3) and reported tungsten diimido complex OHIWEJ (FIGURE 5.10).[201]

	Neutral complex 20 [(a)]		**Dication 18^{2+}**	**OHIWEJ**
$d_{Nb–N}$	1.7993(19)	1.793	1.876(8)	–
$d_{N–C11}$	1.378(3)	1.381	1.31(1)	1.377(4)
$d_{C11–C12}$ [(b)]	1.417(2)	1.426	1.46(2)	1.395(4)
$d_{C12–C13}$ [(b)]	1.386(2)	1.392	1.35(2)	1.388(4)
$d_{C13–C14}$ [(b)]	1.399(2)	1.404	1.43(2)	1.391(4)
$d_{C14–C14'}$	1.488(4)	1.483	1.417(9)	1.491(4)
$\lvert\phi_{C13–C14–C14'–C13'}\rvert$ [(b)]	180.00(8)	143.1	180.0(6)	180.0(3)

[(a)] Computed (B3LYP/3-21G*) parameters for diimido complex **20** (SCHEME 5.3) are shown in red.
[(b)] Average parameters for chemically equivalent bonds in the structures (*e.g.* C11–C12 ≡ C16–C15 ≡ C11'–C12' *etc.*).

The crystallographically- and computationally-determined interatomic distances of complex **20** are identical within error. However, the two aryl rings C11–C16 and C11'–C16' were found to be coplanar in the solid-state structure of complex **20** (quantified by the dihedral angle $|\phi_{C13–C14–C14'–C13'}| = 180°$), which differed substantially to the twist computed in the gas-phase structure. This discrepancy in the coplanarity of the two aryl rings may be attributable to crystal packing effects in the solid-state; indeed, the biphenyl moiety of the tungsten diimido complex OHIWEJ (FIGURE 5.10) was also reported to adopt a coplanar conformation in its solid-state structure.[201]

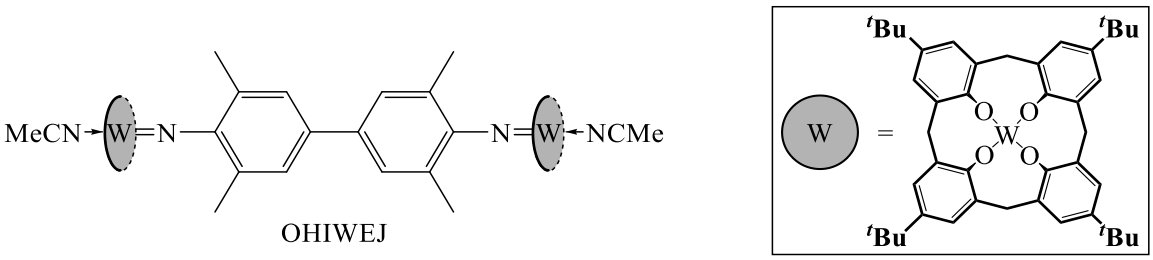

FIGURE 5.10: Reported crystallographically-determined structure of the planar biphenyl diimido complex OHIWEJ.[201]

Unfortunately, elemental analysis of the remaining crystals of complex **20** indicated that decomposition had occurred following selection of the material for the XRD studies. Therefore, further characterisation of the biphenyl diimido complex was not possible. Furthermore, due to time constraints, the synthesis of a further batch of the diimido complex **20** was not undertaken, particularly as a route to the diketimido complex [**18**][BAr^F_4]$_2$ was unoptimised. However, as demonstrated herein, the predicted diimido complex **20** is a thermodynamically accessible species following the two-electron reduction of the DPQ diketimido salt [**18**][BAr^F_4]$_2$. Therefore, together with the evidence of deprotonation occurring during the synthesis of the DPQ diketimido salt [**18**][BAr^F_4]$_2$ (SECTION 5.2), it is likely that the oxidative coupling of complex **3** does indeed proceed as proposed (SCHEME 5.3) *via* an intermediate of the biphenyl diimido complex **20**.

5.5. Chapter summary

The work in this chapter has demonstrated the unusual susceptibility of the d^0 niobocene imido complex $Cp_2NbCl(NDipp)$ (**3**) to oxidation, through exploiting the high electron-density on the aryl imido substituent observed in CHAPTER 4. Analogous to only a limited number of late transition metal arylimido complexes,[51,54] complex **3** undergoes oxidative coupling to form the diketimido salt $[\{Cp_2NbCl\}_2(N\{2,6\text{-}^iPr_2C_6H_2\}_2N)][BAr^F{}_4]_2$ ([**18**][$BAr^F{}_4$]$_2$). The highly-conjugated diphenoquinoidal (DPQ) structure of the diketimido ligand backbone within [**18**][$BAr^F{}_4$]$_2$ has been confirmed X-ray crystallographically.

The diketimido dication $\mathbf{18}^{2+}$ is unique amongst DPQ diketimido complexes due to its partial diradical character in solution, which in turn may be responsible for its intense blue colouration. The paramagnetic behaviour of complex $\mathbf{18}^{2+}$ was confirmed by analysis according to Evans' method with a determined effective magnetic moment (μ_{eff}) of 1.88 ± 0.09 μ_B. In contrast to organic DPQ systems possessing diradical character,[193,195] this *bis*(niobocenyl) diketimido complex displays surprising stability both in solution and under aerobic conditions.

While the oxidative coupling mechanism of the arylimido complex **3** has been explored computationally, the experimental isolation of any proposed intermediates was hindered under the oxidative (and basic) conditions of the reaction. One potential intermediate, the neutral biphenyl diimido complex $\{Cp_2NbCl\}_2(N\{2,6\text{-}^iPr_2C_6H_2\}_2N)$ (**20**), has been accessed from the reduction of the diketimido complex [**18**][$BAr^F{}_4$]$_2$, as also confirmed crystallographically. While not established directly, the formation of complex **20** during the oxidative coupling of complex **3** is consistent with the observed stoichiometry of reagents and products from the reaction, particularly as a deprotonation step has been verified to occur by the formation of the amido salt $[Cp_2NbCl(NHDipp)]BAr^F{}_4$ ([**13**]$BAr^F{}_4$).

CHAPTER 6:

Conclusions and future work

6.1. Overall conclusions

The work in this thesis has identified a new synthetic route to both half-sandwich and *bis*(cyclopentadienyl) derivatives of niobium arylimido complexes bearing the 2,6-di-*iso*-propylphenyl (Dipp) imido ligand from a single precursor, namely $NbCl_3$(NDipp)(DME) (**1**; DME = 1,2-dimethoxyethane). Compared to the cyclopentadienyl-containing precursor Cp'$NbCl_4$ typically employed in literature,[89,96] the synthesis of complex **1** is more straightforward and higher yielding, and has fewer problems associated with its purification.[102] As demonstrated in SECTIONS 2.2 & 2.4.1, both $CpNbCl_2$(NDipp) (**2**; 39% yield) and Cp_2NbCl(NDipp) (**3**; 71% yield), along with the mono(fluorenyl) derivative $FluNbCl_2$(NDipp) (**6**; unoptimised), can be synthesised from complex **1** through careful tuning of the covalency (and hence nucleophilicity) of the Cp'-source.

The reduction chemistry of complex **2** was explored under an atmosphere of N_2 in the absence of strong σ-donating and π-accepting species, with a view to the potential formation of the dinitrogen complex {CpNb(NDipp)}$_2$(μ,η^2,η^2-N_2) (**4**; SECTION 2.3). However, the reduced species $CpNb^{III}$(NDipp) and/or its adduct with dinitrogen were neither observed nor isolated. Instead, attempts to reduce **2** resulted in either decomposition (SECTION 2.3.1) or dimerisation to the chloride-bridged niobium(IV) complex {CpNb(μ-Cl)(NDipp)}$_2$ (**5**; SECTION 2.3.2).

In contrast to the half-sandwich imido complex **2**, the *bis*(cyclopentadienyl) derivative **3** was found to be relatively inert to subsequent transformations, most notable of which being the removal of the chloride ligand by either electrophilic abstraction (SECTION 3.2) or nucleophilic displacement (SECTION 3.3). This lack of reactivity of complex **3** has been attributed to the presence of the sterically demanding *iso*-propyl and cyclopentadienyl moieties hindering access to the niobium–chloride unit. As such, reaction of the Nb–Cl moiety of complex **3** is limited to attack by small electrophiles ($GaCl_3$) or nucleophiles (Me^- or OCP^-), with the formation of covalent products Cp_2Nb(NDipp)X {X = $ClGaCl_3$ (**9**), Me (**11**) or PCO (**12**)} rather than ion-pairs of the type $[Cp_2Nb(NDipp)]^+X^-$ ([**8**]X).

In combination with the steric bulk of the system, the significant localisation of the highest-occupied molecular orbital (HOMO) of complex **3** on the C^{para}-atom of the arylimido ligand (as deduced computationally; SECTION 4.1) enables reactions of electron-deficient species at this position. Firstly, electrophilic aromatic substitution (S_EAr) can be induced at the *para*-aryl position of complex **3**. For example, reaction of complex **3** with the large trityl (Tr^+) cation affords the modified imido complex Cp_2NbCl(N{2,6-^{i}Pr$_2$C$_6$H$_2$-4-Tr}) (**17**; SECTION 4.4.2). Alternatively, complex **3** is susceptible to oxidative coupling at the same aryl position using silver(I) as the oxidant, which leads to the formation of the vivid-blue diphenoquinoidal (DPQ) diketimido complex [{Cp_2NbCl}$_2$(N{2,6-^{i}Pr$_2$C$_6$H$_2$}$_2$N)]$^{2+}$ (**18**$^{2+}$; SECTION 5.2) that has been determined to possess some paramagnetic character (SECTION 5.3).

Overall, as demonstrated in this thesis, the incorporation of an additional cyclopentadienyl moiety can result in marked differences in reactivities observed for the niobium 2,6-di-*iso*-propylphenylimido complexes **2** and **3**. As a consequence of both steric and electronic effects, new reaction pathways have been enabled for the niobocene derivative **3** that have otherwise not been observed for d^0 arylimido complexes.

6.2. Future work

6.2.1. Synthesis and reduction of FluNbCl$_2$(NDipp)

Considering that coordination of dinitrogen does not appear to be possible upon reduction of the half-sandwich imido complex CpNbCl$_2$(NDipp) (**2**; SECTION 2.3), attention should turn to other cyclopentadienyl derivatives capable of adopting a more stable niobium(III) species. As deduced computationally in SECTION 2.4, the two-electron reduction of the mono(fluorenyl) derivative FluNbCl$_2$(NDipp) (**6**) may lead to a more stable, 18-electron complex (η^9-Flu)Nb^{III}(NDipp), since the fluorenyl ligand has been computed to be capable of adopting an η^9-coordination mode. It would therefore be of interest to explore the reduction of FluNbCl$_2$(NR) complexes in order to establish whether coordination of dinitrogen can occur (SCHEME 6.1i). Subsequently, hydrogenation of the dinitrogen complex may be able to afford ammonia along with a dihydride complex (SCHEME 6.1ii), as reported for the *pseudo*-isolobal zirconocene(II) dinitrogen complex of Chirik, namely {Cp$^{\dagger}_2$Zr}$_2$(μ,η^2,η^2-N$_2$) (**AQ**; Cp† = C$_5$HMe$_4$).[80] However, in contrast to this zirconium system, it is envisaged that (η^9-Flu)Nb^{III}(NR) may be sufficiently stable to be regenerated following the reductive elimination of dihydrogen from (η^5-Flu)NbH$_2$(NR) (SCHEME 6.1iii), thereby forming a desirable catalytic cycle for the reduction of dinitrogen to ammonia.

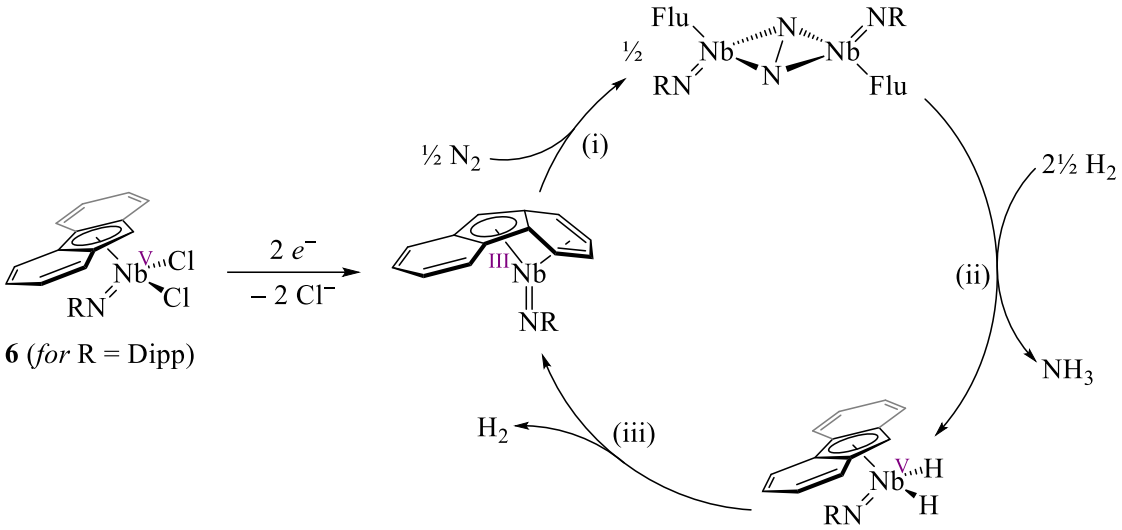

6 (*for* R = Dipp)

SCHEME 6.1: Proposed possible catalytic dinitrogen reduction using reduced niobium fluorenyl half-sandwich imido systems.

Prior to attempting the reduction of the Dipp-derivative **6**, it is desirable to find a synthetic route to the complex from NbCl$_3$(NDipp)(DME) (**1**) using an alternative source of the fluorenyl moiety to LiFlu and TMSFlu attempted in SECTION 2.4.1. Since TlCp was found to incorporate a single Cp-moiety in its reaction with complex **1** (SECTION 2.2.2), it is plausible that the use of thallium(I) fluorenide would be an appropriate route to access the mono(fluorenyl) derivative **6** (SCHEME 6.2). Indeed, the use of TlFlu has been reported for the synthesis of CpFluMCl$_2$ (M = Ti or Zr) from CpMCl$_3$ in the literature.[132] However, due to the high toxicity of thallium(I) species, there remains a drive to find other covalent

fluorenyl sources for the synthesis of **6** at larger scales from complex **1**. It would therefore be of interest to explore the use of the non-toxic fluorenyl reagents, such as the zinc[202] and magnesium[203] derivatives $Flu_2Zn(THF)_2$ and $Flu_2Mg(OEt_2)_2$, as a route to complex **6** from complex **1** (SCHEME 6.2).

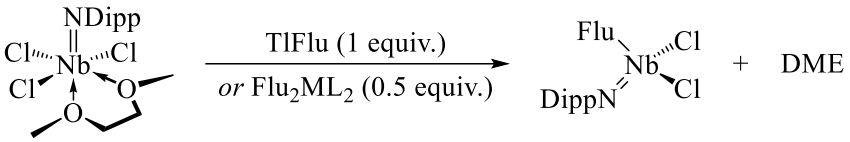

1 **6**

SCHEME 6.2: Possible routes to the mono(fluorenyl) complex **6** from the imido complex **1**; $ML_2 = Zn(THF)_2$ or $Mg(OEt_2)_2$.

6.2.2. Synthesis and reactivity of niobocenium arylimido cations

As $Cp_2NbCl(NDipp)$ (**3**) proved resistant to direct electrophilic abstraction of the chloride ligand (SECTION 3.2), there remains a drive to find an alternative route to cationic niobocenium arylimido derivatives. Substitution of the Cl^- ligand of complex **3** by a small, nucleophilic anion (X^-), followed by electrophilic abstraction of X^-, may be a plausible route to $[Cp_2Nb(NDipp)]^+$ (**8**$^+$). However, due to problems with purification, the samples of $Cp_2NbMe(NDipp)$ (**11**) and $Cp_2Nb(NDipp)(PCO)$ (**12**) produced herein (SECTION 3.3) were unsuitable for subsequent anion abstraction.

The derivatives $Cp_2Nb(NCO)(NDipp)$ and $Cp_2Nb(NDipp)(NH_2)$ may prove more suitable precursors to the niobocenium cation **8**$^+$, particularly as abstraction of isocyanate and amido anions have previously been reported in the literature using trialkyloxonium salts[170] and weak acids,[105] respectively. Indeed, the weak acid $[HNMe_3]BPh_4$ has been shown to selectively protonate the amido (rather than the imido) ligand in the niobocene complex $\{ansa\text{-}Me_2C(C_5H_4)_2\}Nb(NDipp)(NEt_2)$, resulting in the formation of the ion-pair $[\{ansa\text{-}Me_2C(C_5H_4)_2\}Nb(NDipp)(NHEt_2)]BPh_4$.[105] The proposed synthetic strategies to $Cp_2Nb(NDipp)X$ (X = NCO or NH_2) from complex **3** and NaX, along with the possible electrophilic abstraction routes to the niobocenium cation **8**$^+$, are outlined in SCHEME 6.3.

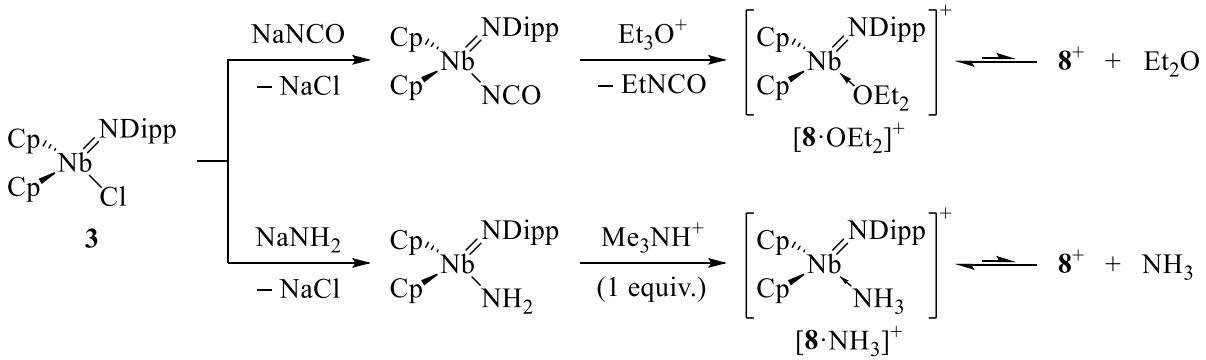

SCHEME 6.3: Proposed routes to the niobocenium imido cation **8**$^+$ *via* $Cp_2Nb(NDipp)X$ (X = NCO or NH_2).

If the routes to complex **8**$^+$ *via* $Cp_2Nb(NDipp)X$ (X = NCO or NH_2) prove unsuccessful, an alternative strategy to cationic niobocenium imido derivatives may be to attempt the electrophilic chloride

abstraction from *para*-aryl substituted complexes such as $Cp_2NbCl(NDipp^{Tr})$ (**17**; $Dipp^{Tr}$ = 2,6-$^{i}Pr_2C_6H_2$-4-Tr). By hindering the dimerisation at the *para*-position, the presence of a bulky trityl group in complex **17** is envisaged to make this niobocene arylimido complex more resistant to oxidative coupling than complex **3**. In turn, the reduced reactivity of complex **17** towards oxidation should enable the Ag^+ cation to act as an electrophilic chloride abstracting agent rather than as an oxidant, and hence form the niobocenium arylimido species $[Cp_2Nb(NDipp^{Tr})]^+$ (SCHEME 6.4).

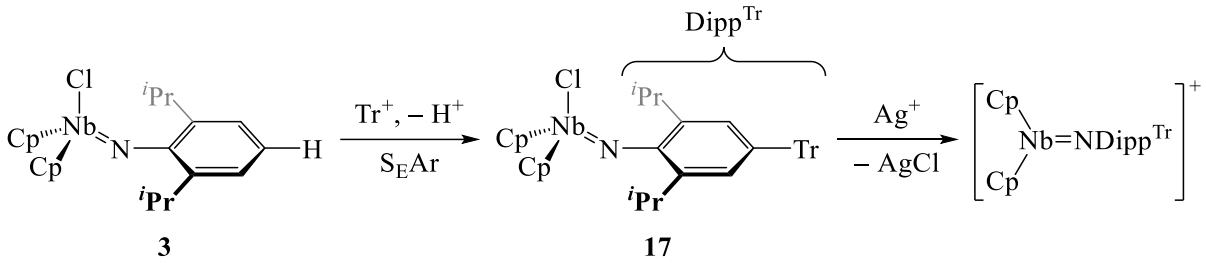

SCHEME 6.4: Synthesis of complex **17** (established in SECTION 4.4.2) and its proposed chloride abstraction using Ag^+.

Following the successful synthesis of the niobocenium arylimido cation $[Cp_2Nb(NAr)]^+$ (Ar = Dipp or $Dipp^{Tr}$), it would be of interest to explore the subsequent reactivity of the complex towards the [2 + 2] cycloaddition and C–H activation of saturated and unsaturated small molecules, respectively (SECTION 1.3.4). Proposed applications of $[Cp_2Nb(NAr)]^+$ could include carbon dioxide fixation or catalytic alkane carbonylation (SCHEME 6.5), transformations which may produce useful commodity chemicals such as isocyanates and aldehydes, respectively.

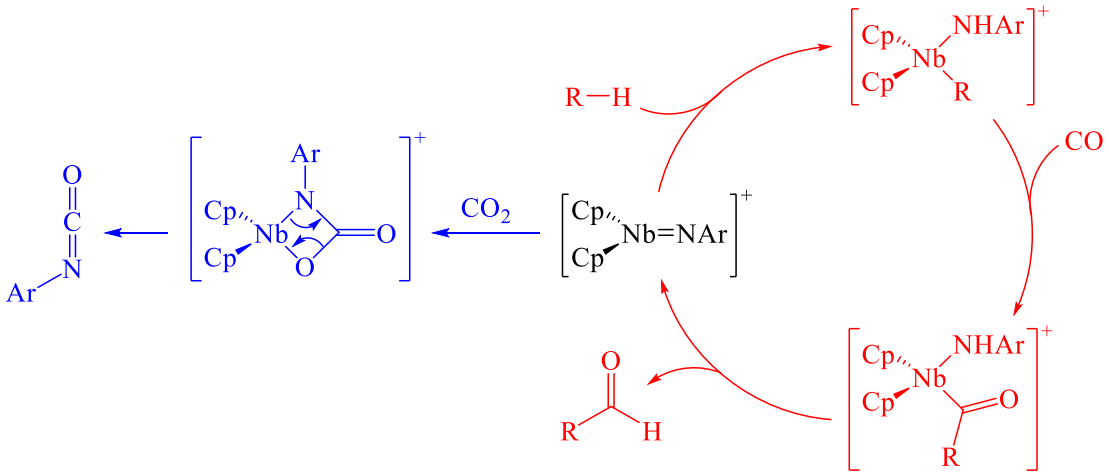

SCHEME 6.5: Proposed reactivity of the niobocenium imido cation $[Cp_2Nb(NAr)]^+$ (Ar = Dipp or $Dipp^{Tr}$) towards the [2 + 2] cycloaddition of CO_2 (blue) or catalytic alkane (R–H) carbonylation (red).

6.2.3. Investigating the paramagnetic properties of dicationic *bis*(niobocenyl) DPQ diketimido complexes

As investigated by Evans' method in SECTION 5.3, the vivid-blue, dicationic diketimido complex $[\{Cp_2NbCl\}_2(N\{2,6\text{-}^iPr_2C_6H_2\}_2N)]^{2+}$ (**18**$^{2+}$) was determined to have paramagnetic character in solution. While this phenomenon has been attributed to thermodynamically accessible diradical species for complex **18**$^{2+}$, the exact nature of the diradical (triplet *vs.* "open-shelled" singlet), and how it is generated from the diphenoquinoidal (DPQ) singlet-state, are unclear. Consequently, there remains a drive to synthesise complex **18**$^{2+}$ in higher purity than afforded from the oxidative coupling of the arylimido complex **3**, in order to further investigate the paramagnetic properties of the DPQ diketimido complex.

Oxidation of the biphenyl diimido complex $\{Cp_2NbCl\}_2(N\{2,6\text{-}^iPr_2C_6H_2\}_2N)$ (**20**) using $AgBAr^F{}_4$ should afford the DPQ diketimido complex [**18**][$BAr^F{}_4$]$_2$ in high yield and purity, therefore the synthesis of this neutral dimeric species should be the focus of future study. As established for the monoimido complex **3**, synthesis of the diimido complex **20** may be possible from its amine precursor (*i.e.* the tetrasubstituted benzidine) and $NbCl_5$, with the cyclopentadienyl moieties being subsequently incorporated using NaCp (SCHEME 6.6). Additionally, by varying the substituents on the benzidine precursors, this approach could be used to synthesise a variety of diketimido complexes in order to explore the effect of substituents on the electronic (and hence paramagnetic) properties of these unusual dicationic complexes.

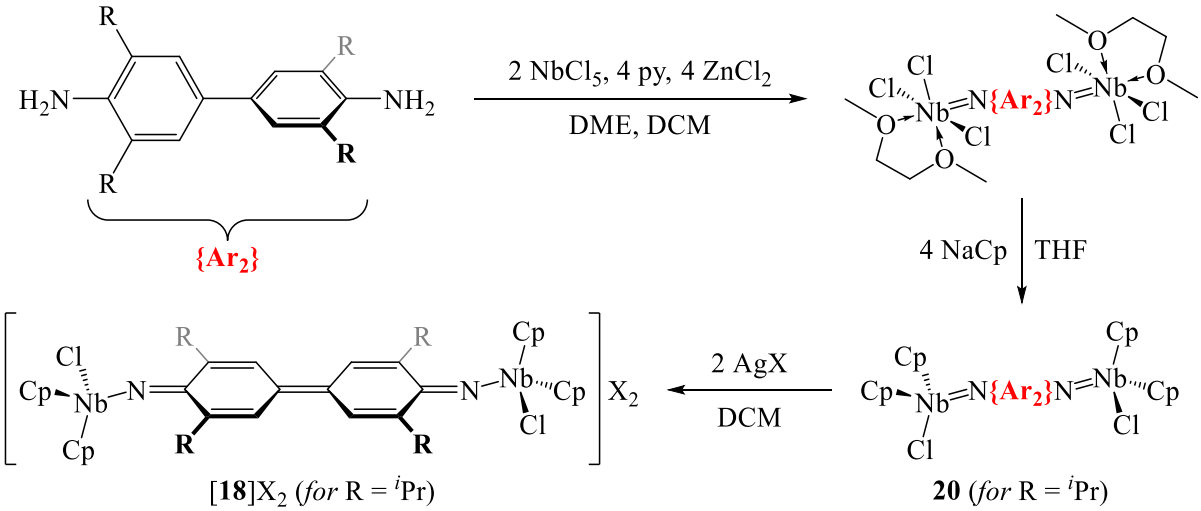

SCHEME 6.6: Potential route to dicationic *bis*(niobocenyl) DPQ diketimido complexes (*e.g.* [**18**][$BAr^F{}_4$]$_2$ for X = $BAr^F{}_4$) from their benzidine (1,1'-diamino-4,4'-biphenyl) derivatives.

CHAPTER 7:

Experimental

7.1. General considerations

Unless otherwise stated, all manipulations were carried under an atmosphere of dry dinitrogen using standard Schlenk line techniques or in a *Saffron Scientific* dinitrogen-filled glovebox. All glassware was oven dried prior to use. All solvents and liquid reagents were degassed using freeze-pump-thaw cycles and stored under an atmosphere of dinitrogen.

7.1.1. Solvents and reagents

Reaction solvents were purchased from *Fisher Scientific* and deuterated solvents were purchased from either *Goss Scientific* or *Apollo Scientific*. Acetonitrile, dichloromethane (DCM), diethyl ether, hexanes and 40/60 petroleum ether were dried using an *Innovative Technologies Solvent Purification System* (SPS). Chlorobenzene was distilled from calcium hydride, 1,2-dichloroethane (DCE) was distilled from phosphorus pentoxide and tetrahydrofuran (THF) was distilled from sodium wire/benzophenone prior to use. Benzene-d_6 and dichloromethane-d_2 were dried over calcium hydride and vacuum transferred prior to use.

Chemical reagents were purchased from either *Sigma Aldrich* or *Fisher Scientific*, with the exception of dinitrogen, dihydrogen and carbon monoxide which were purchased from *BOC*. All reagents were used as received, with the following exceptions: gallium trichloride was purified by vacuum sublimation before use; magnesium turnings were activated by stirring under dynamic vacuum (room temperature, ~15 h) before use; triflic acid (TfOH) and methyl triflate (MeOTf) were purified by distillation before use; trimethylsilyl chloride (TMSCl) was dried over calcium hydride and purified by distillation before use. The following reagents were prepared according to established literature procedures: $AgBAr^F{}_4$,[204] DippNH(TMS),[205] $[H(OEt_2)_2]BAr^F{}_4$,[179] KC_8,[206] LiFlu,[130] $NaBAr^F{}_4$,[207] NaCp·THF,[208] Na(OCP)·2½(diox),[209] $NbCl_3$(NDipp)(DME) (**1**),[102] PMe_3,[210] $[(^iPr_2N)_2P]OTf$,[211] $TaCl_3$(NDipp)(DME),[102] and TMSFlu.[133] Sodium sand was prepared from the melt by agitation in hot toluene and sodium-mercury amalgam was prepared by the cautious addition of the sodium sand to distilled mercury inside a dinitrogen-filled glovebox.

7.1.2. Spectroscopic and spectrometric characterisation

Solution-state ^1H, $^{13}C\{^1H\}$, ^{11}B, $^{19}F\{^1H\}$ and ^{31}P (or $^{31}P\{^1H\}$) nuclear magnetic resonance (NMR) spectroscopies were performed using a *Bruker Avance* spectrometer (400 MHz). High-field (^1H and ^{13}C) and two-dimensional (^1H–^1H and ^1H–^{13}C) solution-state NMR spectroscopies were performed using a *Varian VNMRS* spectrometer (600 or 700 MHz) by Dr Alan Kenwright, Dr Juan Aguilar Malavia or Mrs Catherine Heffernan (Department of Chemistry, Durham University). All sample

solutions were prepared under inert atmosphere in NMR tubes fitted with J. Young tap valves and all analyses were carried out at 22 °C. Chemical shifts (δ) are reported in parts per million (ppm), referenced to residual *protio* impurities in the deuterated solvent (^{1}H), the solvent itself (^{13}C), external 15% $BF_3{\cdot}OEt_2$ (^{11}B), external $CFCl_3$ (^{19}F) or external 85% H_3PO_4 aqueous solution (^{31}P); reference δ_H and δ_C values employed: C_6D_6 (δ_H = 7.16 ppm; δ_C = 128.1 ppm) and CD_2Cl_2 (δ_H = 5.32 ppm; δ_C = 53.8 ppm).[212] Coupling constants ($^{n}J_{A–B}$ or, when nuclei A and B are not known, J) are reported in hertz (Hz), with the following multiplicity abbreviations used: singlet (s), doublet (d), triplet (t), quartet (q), pentet (p), septet (sept) and multiplet (m). For broad singlets (br s), full width at half maximum ($\nu_{½}$) values are reported in Hz.

Mass spectrometry (MS) was performed by Mr Peter Stokes and Dr Dave Parker (Department of Chemistry, Durham University). Positive-ion atmospheric solids analysis probe (ASAP+) mass spectra were acquired using either a *Waters LCT Premier XE* or a *Waters Xevo QToF* mass spectrometer equipped with an ASAP ionisation source. Inert ASAP+ (*i*ASAP+) mass spectrometry was performed by transferring the sample into the spectrometer under dinitrogen. Accurate mass ASAP+ measurements were made using a lock-mass correction (to provide <5 mDa accuracy) and were processed using *Elemental Composition 4.0* embedded within *MassLynx 4.1* software. Mass-to-charge ratios (*m/z*) for detected signals in the mass spectrum are reported in daltons (Da).

Infra-red (IR) spectroscopy was performed using a *Perkin Elmer Frontier FT-IR* spectrometer, with solid samples prepared as a suspension in Nujol mull between two KBr discs (unless otherwise stated). IR spectroscopic frequencies (ν_{max}) are reported in cm^{-1}, with the following suffixes: w (weak), br (broad) and sh (shoulder).

Elemental analyses were performed by either Dr Emily Unsworth (Department of Chemistry, Durham University) or Stephen Boyer (Service Technical Support Unit, London Metropolitan University) under inert atmosphere, unless otherwise specified.

Magnetic susceptibility measurements of solutions were determined according to Evans' method[198] using a *Bruker Avance* spectrometer (400 MHz). Calculated effective magnetic moments (μ_{eff}) are reported in Bohr magnetons (μ_B). Further experimental and calculation details may be found in APPENDIX 2.

7.1.3. Crystallographic and computational structural analyses

Acquisition, solving and refinement of X-ray crystallographic data were performed by Dr Andrei Batsanov or Dr Dmitry Yufit (Department of Chemistry, Durham University). Single crystals were selected and mounted under dinitrogen on a *Brucker D8 Venture* diffractometer and kept at 120 or

273.15 K during data collection. Using the *Olex2* software package,[213] the structures were solved with the *ShelXS* structure solution program[214] using the Patterson Method and refined with the *ShelXL* refinement package[215] using Least Squares minimisation. Images of experimental structures were generated using *Olex2 1.3.0* software,[213] with thermal ellipsoids set at the 50% level. Additional crystallographic data are tabulated in APPENDIX 1 and CIF files may be found in the ELECTRONIC SUPPLEMENTARY INFORMATION.

Computational studies were performed by density functional theory (DFT) using *Gaussian 09 (Revision A.02)* software,[216] with the Becke three-parameter Lee–Yang–Parr (B3LYP) functional[217,218] and the 3-21G* basis set.[219,220] Input geometries and files for geometric optimisation were created using *GaussView 4.1* software[221] prior to geometric optimisation, with crystallographically-determined molecular structures being used as starting geometries wherever possible. Gas-phase calculations were performed unless otherwise specified; else, solution-state calculations were performed using the polarizable continuum model (PCM)[222] to correct for solvent effects. Wiberg bond indices (WBIs) and atomic charges were calculated using natural bond orbital (NBO) analysis by the *NBO 3.1* program.[223] Percentage atomic contributions towards molecular orbitals (MOs) were calculated using *GaussSum* software.[161] Images of computed geometries and MOs were generated using *Avogadro* software;[224] H-atoms were included in calculations, but omitted from images for clarity (unless otherwise indicated). MOL2 files for computed structures may be found in the ELECTRONIC SUPPLEMENTARY INFORMATION.

The following abbreviations are used to describe interatomic distances (in ångströms, Å) and angles (in degrees, °): $d_{A–B}$ (distance between atoms A and B), $\angle_{A–B–C}$ (angle A–B–C), $\phi_{A–B–C–D}$ (dihedral angle; angle made by bonds A–B and C–D) and θ (fold angle; angle between two defined planes). Searches of the *Cambridge Structural Database* (CSD)[225] were performed using *ConQuest 2020.1* software.[226] Molecular overlays between experimental and/or computed structures are calculated and visualised using *Mercury 3.10* software.[227]

Percentage buried volumes measured at atom X ($\%V_{bur}^{X}$), along with associated steric maps, for experimental or computed molecular structures were determined using the *SambVca 2.1* web application.[106] Within the application, atom X was selected as the central atom, then deleted, and the following parameters/constraints were assigned: sphere radius (3.0 Å), atomic radius scale factor (1.17), distance of coordination point from sphere centre (0.0 Å), mesh spacing (0.10 Å) and exclusion of H-atoms.

7.2. Syntheses and reduction of niobium cyclopentadienyl imido complexes

7.2.1. Synthesis of $CpNbCl_2(NDipp)$ (2)

$$NbCl_3(NDipp)(DME) + TlCp \xrightarrow[\Delta,\ 18\ h]{DCM} CpNbCl_2(NDipp) + TlCl + DME$$

DCM (~100 ml) was added to a mixture of solid $NbCl_3(NDipp)(DME)$ (**1**; 0.50 g, 1.08 mmol) and solid TlCp (0.29 g, 1.08 mmol). The resulting suspension was heated to reflux, and this temperature maintained for ~18 h. The subsequent deep-red suspension was allowed to cool, and then volatile components were removed *in vacuo*. Extraction of the red residue with hexanes (~160 + {2 × ~30} ml), followed by concentration of the extracts resulted in the precipitation of a red solid. This solid was extracted with DCM (~20 ml) and removal of the solvent from the extract afforded complex **2** as a red solid (0.17 g, 39%).[*]

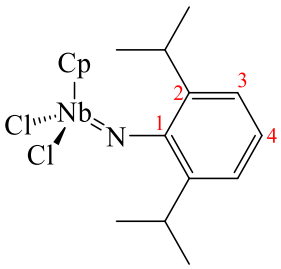

^{1}H NMR (400 MHz, C_6D_6): δ 7.01–6.98 (2 H, m, H^3), 6.89 (1 H, dd, $^3J_{H–H}$ = 8.3 and 7.0 Hz, H^4), 5.83 (5 H, s, C_5H_5), 3.73 (2 H, sept, $^3J_{H–H}$ = 6.9 Hz, C*H*Me$_2$), 1.26 (12 H, d, $^3J_{H–H}$ = 6.9 Hz, CH*Me*$_2$).[†]

[*] SR074, page 80(1).

[†] ^{1}H NMR spectroscopic data in agreement with those of **2** previously synthesised in the literature.[89]

7.2.2. Synthesis of $Cp_2NbCl(NDipp)$ (3)

$$NbCl_3(NDipp)(DME) + 2\ NaCp{\cdot}THF \xrightarrow[-40\ °C \rightarrow RT]{THF} Cp_2NbCl(NDipp) + 2\ NaCl + 2\ THF + DME$$

With the exclusion of light, a solution of NaCp·THF (2.46 g, 15.4 mmol) in THF (~50 ml) was added dropwise to a cooled (–40 °C) solution of $NbCl_3$(NDipp)(DME) (**1**; 3.41 g, 7.33 mmol) in THF (~60 ml). The reaction mixture was then allowed to warm to room temperature, whereupon it was subsequently stirred for a further ~65 h. Volatile components were then removed from the red/orange solution under vacuum, and the resulting orange residue was extracted with Et_2O (~150 + {3 × ~20} ml). Concentration of the subsequent ethereal extracts and then storage at –20 °C led to the precipitation of **3** as an orange solid (2.26 g, 71%).*

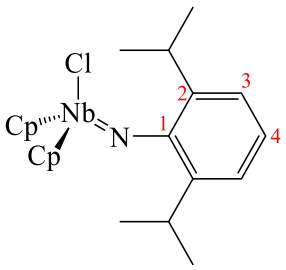

^{1}H NMR (400 MHz, C_6D_6): δ 7.05 (2 H, d, $^3J_{H–H}$ = 7.7 Hz, H^3), 6.84 (1 H, t, $^3J_{H–H}$ = 7.7 Hz, H^4), 5.81 (10 H, s, C_5H_5), 3.52 (2 H, sept, $^3J_{H–H}$ = 6.9 Hz, C*H*Me$_2$), 1.30 (12 H, d, $^3J_{H–H}$ = 6.9 Hz, CH*Me*$_2$).

^{13}C{^{1}H} NMR (151 MHz, C_6D_6): δ 154.9 (C^1), 139.2 (C^2), 122.9 (C^3), 122.7 (C^4), 112.8 (C_5H_5), 27.7 (*C*HMe$_2$), 24.7 (CH*Me*$_2$).†

^{1}H NMR (400 MHz, CD_2Cl_2): δ 6.96 (2 H, d, $^3J_{H–H}$ = 7.7 Hz, H^3), 6.72 (1 H, t, $^3J_{H–H}$ = 7.7 Hz, H^4), 6.23 (10 H, s, C_5H_5), 3.32 (2 H, sept, $^3J_{H–H}$ = 6.9 Hz, C*H*Me$_2$), 1.20 (12 H, d, $^3J_{H–H}$ = 6.9 Hz, CH*Me*$_2$).‡

^{13}C{^{1}H} NMR (101 MHz, CD_2Cl_2): δ 154.8 (C^1), 139.3 (C^2), 122.9 (C^3), 122.3 (C^4), 113.3 (C_5H_5), 27.8 (*C*HMe$_2$), 24.6 (CH*Me*$_2$).‡

Elemental analysis: C, 61.03; H, 6.03; N, 3.15% ($C_{22}H_{27}ClNNb$ requires: C, 60.91; H, 6.47; N, 3.23%).

MS (ASAP+, 450 °C): *m*/*z* 434 (100%, M^+), 258 (3, [M – NDipp]$^+$), 161 (2, [Dipp]$^+$).

Accurate mass (ASAP+, 450 °C): *m*/*z* 434.0982 ($C_{22}H_{27}ClNNb$ requires: 434.0974).

The analogous reaction between $NbCl_3$(NDipp)(DME) (0.45 g, 0.97 mmol) and NaCp·THF (0.15 g, 0.94 mmol) also formed complex **3** (0.06 g, 29% based on NaCp·THF). Single crystals suitable for XRD analysis were obtained by recrystallisation of **3** from hot hexanes.†

* SR140, page 146(1).

† SR021, page 26(1).

‡ SR119, page 125(1).

7.2.3. Synthesis of $Cp_2TaCl(NDipp)$ ($\mathbf{3_{Ta}}$)

$$TaCl_3(NDipp)(DME) + 2\ NaCp{\cdot}THF \xrightarrow[-50\ °C \rightarrow RT]{THF} Cp_2TaCl(NDipp) + 2\ NaCl + 2\ THF + DME$$

With the exclusion of light, a solution of NaCp·THF (0.072 g, 0.45 mmol) in THF (~10 ml) was added dropwise to a cooled (–50 °C) solution of $TaCl_3(NDipp)(DME)$ (0.25 g, 0.45 mmol) in THF (~40 ml). The reaction mixture was allowed to warm to room temperature, whereupon it was stirred for a further ~17 h. Volatile components were then removed from the subsequent red/orange solution under vacuum, and the resulting orange residue was extracted with hexanes (~50 ml). Removal of the hexanes *in vacuo* produced a yellow paste (~50 mg), consisting of $Cp_2TaCl(NDipp)$ ($\mathbf{3_{Ta}}$) and $DippNH_2$, in a ~2:1 molar ratio. Due to the small amount of paste produced, purification of $\mathbf{3_{Ta}}$ was not pursued.*

^{1}H NMR (400 MHz, C_6D_6): δ 7.17 (2 H, d, $^3J_{H–H}$ = 7.5 Hz, H^3), 6.80 (1 H, t, $^3J_{H–H}$ = 7.5 Hz, H^4), 5.76 (10 H, s, C_5H_5), 3.46 (2 H, sept, $^3J_{H–H}$ = 6.9 Hz, C*H*Me$_2$), 1.33 (12 H, d, $^3J_{H–H}$ = 6.9 Hz, CH*Me*$_2$).†

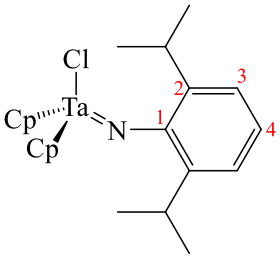

* SR158, page 14(2).

† Signals corresponding to $DippNH_2$ have been omitted for clarity; no signals corresponding to monosubstituted $CpTaCl_2(NDipp)$ were observed, which has been prepared in the literature[101] from $CpTaCl_4$ and DippNH(TMS).

7.2.4. Reduction chemistry of $CpNbCl_2(NDipp)$ (2)

7.2.4.1. Reduction of 2 using sodium amalgam

$$2\ CpNbCl_2(NDipp) + 4\ Na(Hg) + N_2 \xrightarrow[-78\ ^\circ C \rightarrow RT]{THF} \{CpNb(NDipp)\}_2(\mu\text{-}N_2) + 4\ NaCl + 4\ Hg$$

At –78 °C, a solution of $CpNbCl_2(NDipp)$ (**2**; 0.25 g, 0.62 mmol) in THF (~30 ml) was added dropwise *via* cannula Na(Hg) (3.03 g, 0.99 wt% Na, 1.3 mmol Na). The resulting suspension was allowed to warm to room temperature, at which point the Schlenk tube was sealed and stirred at this temperature for ~72 h. After allowing the suspension to settle, the solution was removed by filtration leaving the residual mercury; volatile components were then removed from the filtrate *in vacuo*. The resulting solid was extracted with DCM (3 × ~50 ml) and the solvent was removed from the combined extracts under vacuum to leave a yellow oily residue. ^{1}H NMR spectroscopic analysis showed this residue to contain $DippNH_2$ as the major component, along with other unidentified impurities.[*]

7.2.4.2. Reduction of 2 using sodium naphthalenide

$$2\ CpNbCl_2(NDipp) + 4\ NaNaphth + N_2 \xrightarrow[-60\ ^\circ C \rightarrow RT]{THF} \{CpNb(NDipp)\}_2(\mu\text{-}N_2) + 4\ NaCl + 4\ Naphth$$

THF (~10 ml) was added to a mixture of sodium sand (0.13 g, 5.43 mmol) and naphthalene (0.07 g, 0.54 mmol), and the resulting suspension was stirred at room temperature for ~1.5 h. After allowing the residual sodium to settle, the deep-green solution was transferred *via* cannula to a cold (–60 °C) solution of $CpNbCl_2(NDipp)$ (**2**; 0.10 g, 0.25 mmol) in THF (~60 ml). The reaction mixture was allowed to warm gradually to room temperature (over ~2 h), at which temperature it was stirred for a further ~18 h. Volatile components from the resulting brown solution were removed *in vacuo*, and the ensuing brown residue extracted with hexanes (~100 + {2 × 30} ml). Removal of the solvent from the combined extracts resulted in a yellow oily residue, consisting of $DippNH_2$ and naphthalene by ^{1}H NMR spectroscopic analysis.[†]

[*] SR054, page 60(1).

[†] SR188, page 44(2).

7.2.4.3. Reduction of 2 using potassium graphite

$$2\ CpNbCl_2(NDipp) + 4\ KC_8 + N_2 \xrightarrow[-78\ ^\circ C \rightarrow RT]{THF} \{CpNb(NDipp)\}_2(\mu\text{-}N_2) + 4\ KCl + 32\ C$$

To a cold (–78 °C), stirred suspension of KC_8 (0.14 g, 1.0 mol) in THF (~20 ml) was added dropwise *via* cannula a solution of $CpNbCl_2(NDipp)$ (**2**; 0.20 g, 0.50 mmol) in THF (~20 ml). The resulting suspension was allowed to warm gradually to room temperature (over ~ 2 h), at which temperature it was stirred for a further ~36 h. The suspension was allowed to settle and the THF solution was separated from the graphite *via* cannula filtration. Following the removal of the volatile components *in vacuo* from the filtrate, the residue was extracted into hexanes (~100 + {2 × 50} ml). The solvent was removed under vacuum from the combined extracts, producing a brown oily residue. NMR spectroscopic analysis showed this residue to contain ~88 mol% $DippNH_2$ along with at least one other component.[*]

^{1}H NMR (400 MHz, C_6D_6): δ 5.50 (5 H, s), 3.83 (2 H, sept, $^3J_{H–H}$ = 7.0 Hz), 1.31 (~12 H,[†] d, $^3J_{H–H}$ = 7.0 Hz).[‡]

The reduction reaction of **2** with KC_8 was repeated in hexanes, but unreacted **2** was isolated in quantitative yield isolated, following removal of the volatile components and subsequent extraction into hexanes.[§]

[*] SR171, page 27(2).

[†] Due to the presence of overlapping impurities, this integral has been approximated.

[‡] Signals corresponding to $DippNH_2$ have been omitted for clarity.

[§] SR184, page 40(2).

7.2.4.4. Reduction of 2 using magnesium: Synthesis of {CpNb(*μ*-Cl)(NDipp)}$_2$ (5)

$$2\ CpNbCl_2(NDipp) + Mg \xrightarrow[-40\ °C \rightarrow RT]{\text{hexanes, cat. THF}} \{CpNb(\mu\text{-}Cl)(NDipp)\}_2 + MgCl_2$$

Hexanes (~15 ml) and THF (0.7 ml, 8.63 mmol) were added to activated magnesium (0.09 g, 3.72 mmol) and the suspension was cooled to –40 °C. A solution of $CpNbCl_2(NDipp)$ (**2**; 0.50 g, 1.24 mmol) in hexanes (~120 ml) was added dropwise *via* cannula to the suspension, following which the reaction mixture was allowed to warm to room temperature and stirred for a further 93 h. The resulting suspension was allowed to settle, and the deep red filtrate was separated from the solid by cannula filtration. Volatile components were removed from the filtrate under vacuum and the residue was extracted with hexanes (~150 + {3 × ~20} ml). Concentration of extracts and storage at –20 °C produced a purple/grey solid of impure **5** (0.06 g, <40 wt% purity, <5% yield).*

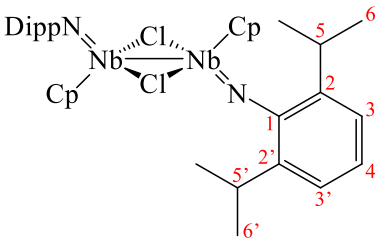

^{1}H NMR (400 MHz, C_6D_6): δ 7.24 (2 H, dd, $^3J_{H–H}$ = 7.5 Hz, $^4J_{H–H}$ = 1.9 Hz, H^3), 7.14 (2 H, t, $^3J_{H–H}$ = 7.5 Hz, H^4), 7.10 (2 H, dd, $^3J_{H–H}$ = 7.5 Hz, $^4J_{H–H}$ = 1.9 Hz, H$^{3'}$), 5.79 (10 H, s, C_5H_5), 2.85 (2 H, sept, $^3J_{H–H}$ = 6.7 Hz, H^5), 2.39 (2 H, sept, $^3J_{H–H}$ = 6.6 Hz, H$^{5'}$), 1.27 (12 H, d, $^3J_{H–H}$ = 6.7 Hz, H^6), 1.12 (12 H, d, $^3J_{H–H}$ = 6.6 Hz, H$^{6'}$).†

Elemental analysis: C, 35.56; H, 0.00; N, 1.05% ($C_{34}H_{44}Cl_2N_2Nb_2$ requires: C, 55.38; H, 6.01; N, 3.80%).

* SR160, page 16(2).

† Other unassignable signals observed: δ 7.06 (1 H, d, *J* = 7.6 Hz), 6.95 (1 H, dd, *J* = 8.3 and 7.0 Hz), 5.87 (0 H, s), 5.84 (0 H, s), 5.68 (0 H, s), 4.30 (0 H, s), 1.40 (1 H, d, *J* = 6.5 Hz), 1.23–1.17 (8 H, m), 0.28–0.24 (0 H, m).

Purification of 5:

To an ampule containing a frozen (–195 °C) solution of impure **5** (0.043 g) in toluene (~10 ml) was added PMe_3 (0.466 mmol) *via* a vacuum-transfer. Following which, the ampule was sealed and gradually warmed to room temperature, whereupon it was stirred for 1 h. Volatile components were removed under dynamic vacuum, more toluene (~60 ml) was added to the subsequent solid, and the resulting suspension was subjected to cannula filtration. Removal of the solvent *in vacuo* of the filtrate yielded a dark purple solid of **5** (0.017 g).*

^{1}H NMR (600 MHz, C_6D_6): δ 7.20 (2 H, dd, $^3J_{H–H}$ = 7.6 Hz, $^4J_{H–H}$ = 1.7 Hz, H^3), 7.10 (2 H, t, $^3J_{H–H}$ = 7.6 Hz, H^4), 7.07 (2 H, dd, $^3J_{H–H}$ = 7.6 Hz, $^4J_{H–H}$ = 1.7 Hz, $H^{3'}$), 5.76 (10 H, s, C_5H_5), 2.81 (2 H, sept, $^3J_{H–H}$ = 6.8 Hz, H^5), 2.35 (2 H, sept, $^3J_{H–H}$ = 6.7 Hz, $H^{5'}$), 1.22 (12 H, d, $^3J_{H–H}$ = 6.8 Hz, H^6), 1.09 (12 H, d, $^3J_{H–H}$ = 6.7 Hz, $H^{6'}$).†

^{13}C{^{1}H} NMR (151 MHz, C_6D_6): δ 167.7 (C^1), 140.6 (C^2), 134.5 ($C^{2'}$), 125.5 (C^4), 125.1 (C^3), 123.5 ($C^{3'}$), 110.3 (C_5H_5), 27.7 ($C^{5'}$), 26.7 (C^5), 26.5 ($C^{6'}$), 24.9 (C^6).†

Elemental analysis: C, 46.85; H, 6.03; N, 2.88% ($C_{34}H_{44}Cl_2N_2Nb_2$ requires: C, 55.38; H, 6.01; N, 3.80%).‡

MS (*i*ASAP+, 450 °C): *m*/*z* 736 (100%, M^+), 178 (21, $[DippNH_3]^+$), 177 (47, $[DippNH_2]^+$).

Crystallisation of 5:

Single crystals suitable for XRD analysis were produced by concentration of a solution of **5** in hexanes and storage at –20 °C.§ Due to exposure to air and the oil used to coat the crystals during their retrieval, further analyses of these crystals could not be performed satisfactorily.

* SR175, page 31(2).

† SR045, page 51(1).

‡ Despite multiple attempts, satisfactory elemental analyses could not be achieved for **5** due to possible contamination with residual solvents and salts.

§ SR031, page 37(1).

7.2.5. Attempted synthesis of $FluNbCl_2(NDipp)$ (6)

7.2.5.1. Reaction between $NbCl_3(NDipp)(DME)$ (1) and LiFlu

$$NbCl_3(NDipp)(DME) + LiFlu \xrightarrow[-40\ °C \rightarrow RT]{THF} FluNbCl_2(NDipp) + LiCl + DME$$

With the exclusion of light, a solution of LiFlu (0.093 g, 0.54 mmol) in THF (~30 ml) was added dropwise *via* cannula to a –40 °C solution of $NbCl_3(NDipp)(DME)$ (**1**; 0.25 g, 0.54 mmol) in THF (~30 ml). The resulting solution darkened in colour and was allowed to warm to room temperature (over ~15 h) to produce a deep red solution. Volatile components were removed *in vacuo* and the residue afforded was extracted with hexanes (3 × ~50 ml). Following cannula filtration, the combined extracts were concentrated and stored at –20 °C to produce an impure red-orange solid (0.046 g). Attempts to crystallise **6** from solutions of the product mixture, in either hexanes or toluene, were unsuccessful.*

^{1}H NMR (400 MHz, C_6D_6): δ 7.77–7.40 (m), 7.07 (dd, J = 7.9, 3.2 Hz), 7.03–6.96 (m), 6.96–6.83 (m), 4.86 (p, J = 6.7 Hz), 4.64 (s), 3.90 (s), 3.50 (s), 3.42 (s), 3.17 (s), 2.95 (dd, J = 5.5, 2.9 Hz), 2.89 (dd, J = 6.1, 3.5 Hz), 1.46 (d, J = 6.7 Hz), 1.33–1.21 (m), 1.19–1.09 (m), 0.93–0.85 (m).†
MS (*i*ASAP+, 450 °C): *m*/*z* 503 (18%, M^+), 373 (98, $[M - Flu + HCl]^+$), 341 (16), 256 (15), 234 (23), 220 (17), 178 (57, $[DippNH_3]^+$), 166 (11, $[FluH]^+$), 162 (73).

7.2.5.2. Reaction between $NbCl_3(NDipp)(DME)$ (1) and TMSFlu

$$NbCl_3(NDipp)(DME) + TMSFlu \xrightarrow[various\ conditions]{DCM\ or\ toluene} FluNbCl_2(NDipp) + TMSCl + DME$$

Either DCM or toluene (~40 ml) was added to a mixture of $NbCl_3(NDipp)(DME)$ (**1**; 0.25 g, 0.54 mmol) and TMSFlu (0.13 g, 0.54 mmol) and the subsequent solution was stirred under various conditions (see table below). Volatile components were then removed *in vacuo* and analysis of the residue by ^{1}H NMR spectroscopy verified that only the starting materials were present.‡

Solvent	Reaction conditions
DCM	0 °C → RT; then RT, 15 h
DCM	Reflux, 18 h
Toluene	Reflux, 60 h

* SR169, page 25(2).

† The ^{1}H NMR signals are very broad, irrespective of spectrometer frequency, so integrals have not been reported. Cross-peaks in the ^{1}H–^{1}H COSY were observed between the following signals: δ 7.07, 7.03–6.96 and 6.96–6.83 ppm (ArH groups); δ 4.86 and 1.46 ppm (^{i}Pr group); δ 3.90 and 1.15 ppm (^{i}Pr group). The signal at δ 3.42 ppm may be attributable to the CH_2 group on fluorene.

‡ SR076, page 82(1).

7.2.5.3. Attempted synthesis of $FluNbCl_4$ (7)

$$NbCl_5 + TMSFlu \xrightarrow[-40\ °C \rightarrow \Delta,\ 18\ h]{DCE} FluNbCl_4 + TMSCl$$

A solution of TMSFlu (0.25 g, 1.05 mmol) in DCE (~30 ml) was added dropwise to a stirred, cooled (–40 °C) suspension of $NbCl_5$ (0.28 g, 1.05 mmol) in DCE (~10 ml). The resulting suspension was allowed to warm to room temperature (over ~1 h) and heated to reflux; the temperature was maintained for ~18 h. After cooling and allowing the suspension to settle, the pale brown solution was removed *via* cannula filtration and the solid was washed with DCM (3 × ~10 ml). Volatile components were removed *in vacuo* to leave an impure, brown solid (0.15 g). Due to the insolubility of the solid, solution-state NMR spectroscopic analysis was not possible on the sample.[*]

Elemental analysis: C, 5.85; H, 0.90% ($C_{13}H_9Cl_4Nb$ requires: C, 39.04; H, 2.24%).
MS (*i*ASAP+, 450 °C): No signals were observed.

[*] SR204, page 60(2).

7.2.5.4. Attempted synthesis of $FluNbCl_2(NDipp)$ (6) from $FluNbCl_4$ (7)

$$FluNbCl_4 + DippNH(TMS) + 2,6\text{-Lut} \xrightarrow[-40\ °C \rightarrow RT]{DCM} FluNbCl_2(NDipp) + TMSCl + 2,6\text{-Lut}\cdot HCl$$

A solution of DippNH(TMS) (0.062 g, 0.25 mmol) and 2,6-lutidine (0.03 ml, 0.25 mmol) in DCM (~10 ml) was added dropwise *via* cannula to a stirred, cooled (–40 °C) suspension of impure $FluNbCl_4$* (**7**; 0.10 g, <0.25 mmol) in DCM (~10 ml). The mixture was allowed to warm to room temperature, following which it was stirred at this temperature for ~15 h. The resulting suspension was allowed to settle, and the solution was removed and combined with DCM extracts (3 × ~10 ml) of the residual solid. Volatile components were removed *in vacuo* to produce an orange oil, which through ^{1}H NMR spectroscopic analysis was found to contain DippNH(TMS) and a new Dipp-containing species in a ~2:5 molar ratio.†

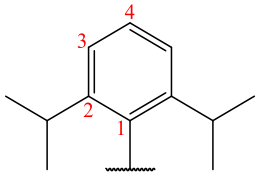

^{1}H NMR (400 MHz, C_6D_6): δ 7.04 (2 H, d, $^3J_{H–H}$ = 7.7 Hz, H^3), 6.90 (1 H, t, $^3J_{H–H}$ = 7.7 Hz, H^4), 2.76 (2 H, br s, $\nu_{½}$ = 24 Hz, C*H*Me$_2$), 1.13 (12 H, d, $^3J_{H–H}$ = 6.8 Hz, CH*Me*$_2$).‡

MS (*i*ASAP+, 450 °C): *m*/*z* 629 (10%), 609 (14), 555 (37), 535 (37), 481 (100), 449 (10), 249 (24, [DippNH(TMS)]$^+$), 218 (24), 178 (9, [DippNH$_3$]$^+$), 162 (31).

* Impure solid from reaction in SECTION 7.2.5.3.

† SR212, page 68(2). Based on the reported synthesis of $CpNbCl_2(NDipp)$ (**2**) from $CpNbCl_4$ and DippNH(TMS).[89]

‡ ^{1}H NMR signals corresponding to unreacted DippNH(TMS) have been omitted for clarity. Other unassignable signals were also observed: δ 8.15 (s), 7.14–7.07 (1 H, m), 6.52–6.31 (m), 5.61 (s), 5.41 (d, *J* = 12.4 Hz), 4.68–4.47 (m), 4.27 (s), 4.20 (t, *J* = 5.6 Hz), 3.90 (t, *J* = 6.7 Hz), 3.68–3.38 (1 H, m), 2.96–2.87 (m), 2.64–2.56 (m), 2.43 (1 H, s), 2.01 (s), 1.93 (s), 1.63–1.44 (m), 1.46–1.23 (7 H, m), 1.13 0.44 (1 H, s), 0.29 (1 H, d, *J* = 1.3 Hz), 0.24–0.21 (m), 0.17 (d, *J* = 2.5 Hz), 0.11 (3 H, s).

7.3. Electrophilic abstraction and nucleophilic displacement of the chloride ligand from $Cp_2NbCl(NDipp)$ (3)

7.3.1. Attempted synthesis of $[Cp_2Nb(NDipp)]BAr^F{}_4$ ($[8]BAr^F{}_4$)

$$Cp_2NbCl(NDipp) + NaBAr^F{}_4 \xrightarrow[\text{\& conditions}]{\text{various solvents}} [Cp_2Nb(NDipp)]BAr^F{}_4 + NaCl$$

The reaction between $NaBAr^F{}_4$ (1 equiv.) and $Cp_2NbCl(NDipp)$ (**3**; 1 equiv.) was attempted using various solvent systems (tabulated below). Following each reaction, the volatile components were removed *in vacuo* and the resultant residue was extracted into hexanes. Subsequent removal of the hexanes afforded unreacted **3** in quantitative amounts, as identified by ^1H NMR spectroscopy.

Solvent(s)	Reaction conditions
MeCN	RT, ~72 h
MeCN/toluene	70 °C, ~96 h
DCM	RT, ~96 h
DCM/MeCN (4.1 equiv.)	RT, ~96 h
PhCl	RT, ~108 h; *then* 60°C, ~5 h
Et_2O	RT, ~168 h

7.3.2. Attempted synthesis of $[Cp_2Nb(NDipp)]SbF_6$ ($[8]SbF_6$)

$$Cp_2NbCl(NDipp) + NaSbF_6 \xrightarrow[\text{RT, ~60 h}]{\text{MeCN}} [Cp_2Nb(NDipp)]SbF_6 + NaCl$$

As described in SECTION 7.3.1, but reacting $NaSbF_6$ (0.06 g, 0.23 mmol) with $Cp_2NbCl(NDipp)$ (**3**; 0.10 g, 0.23 mmol) in MeCN at room temperature for ~60 h.*

* SR108, page 114(1).

7.3.3. Attempted synthesis of [Cp$_2$Nb(NDipp)]OTf ([8]OTf)

$$Cp_2NbCl(NDipp) + [(^iPr_2N)_2P]OTf \xrightarrow[50\ °C,\ 21\ h]{CD_2Cl_2} [Cp_2Nb(NDipp)]OTf + (^iPr_2N)_2PCl$$

Inside a glovebox, a solution of [(^{i}Pr$_2$N)$_2$P]OTf (0.02 g, 0.053 mmol) in CD_2Cl_2 (~0.7 ml) was added to a sample vial containing Cp$_2$NbCl(NDipp) (**3**; 0.023 g, 0.053 mmol) and mixed *via* pipette and transferred to a Young's NMR tube. In an oil bath (50 °C), the NMR tube was heated for 21 h, however monitoring of the reaction by ^{1}H, ^{19}F and ^{31}P NMR spectroscopy showed no changes in chemical shifts.[*]

^{1}H NMR (400 MHz, CD_2Cl_2): δ 4.16 (4 H, dsept, $^3J_{P–H}$ = 9.8 Hz, $^3J_{H–H}$ = 6.8 Hz, [({Me$_2$C*H*}$_2$N)$_2$P]OTf), 1.49 (24 H, d, $^3J_{H–H}$ = 6.8 Hz, [({*Me*$_2$CH}$_2$N)$_2$P]OTf).[†]

^{31}P NMR (162 MHz, CD_2Cl_2): δ 296.4 (s, [(^{i}Pr$_2$N)$_2$P]OTf).

^{19}F{^{1}H} NMR (376 MHz, CD_2Cl_2): δ –78.8 (s, [(^{i}Pr$_2$N)$_2$P]OSO$_3$C*F*$_3$).

[*] SR163, page 19(2).

[†] ^{1}H NMR resonances corresponding to unreacted **3** have been omitted for clarity.

7.3.4. Synthesis of $Cp_2Nb(ClGaCl_3)(NDipp)$ (9)

$$Cp_2NbCl(NDipp) + GaCl_3 \xrightarrow[RT,\ \sim 20\ h]{hexanes} Cp_2Nb(ClGaCl_3)(NDipp)$$

A solution of $GaCl_3$ (0.04 g, 0.23 mmol) in hexanes (~40 ml) was added dropwise *via* cannula to a stirred solution of $Cp_2NbCl(NDipp)$ (**3**; 0.10 g, 0.23 mmol) in hexanes (~80 ml) at room temperature. Precipitation of a yellow solid resulted over the course of addition. The subsequent suspension was stirred at room temperature for ~20 h, following which the solid was allowed to settle and the solution removed by cannula filtration. After washing with more hexanes (2 × ~10 ml), the solid was dried under a flow of nitrogen gas and subjected briefly to vacuum for transfer into the glovebox, where **9** was isolated as a yellow solid (0.06 g, 43%).*

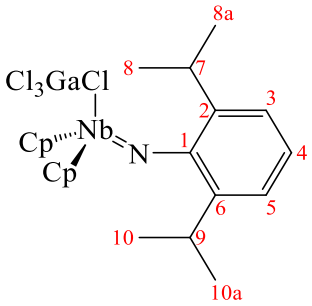

^{1}H NMR (700 MHz, CD_2Cl_2): δ 7.36 (1 H, t, $^3J_{H–H}$ = 7.7 Hz, H^4), 7.31 (1 H, dd, $^3J_{H–H}$ = 7.7 Hz, $^4J_{H–H}$ = 1.5 Hz, H^3), 7.26 (1 H, dd, $^3J_{H–H}$ = 7.7 Hz, $^4J_{H–H}$ = 1.5 Hz, H^5), 6.94 (5 H, s, C_5H_5), 6.42 (5 H, s, C_5H_5'), 3.25 (1 H, sept, $^3J_{H–H}$ = 6.8 Hz, H^7), 2.37 (1 H, sept, $^3J_{H–H}$ = 6.8 Hz, H^9), 1.41 (3 H, d, $^3J_{H–H}$ = 6.8 Hz, H^{10}), 1.37 (3 H, d, $^3J_{H–H}$ = 6.8 Hz, H^8), 1.19 (3 H, d, $^3J_{H–H}$ = 6.8 Hz, H^{10a}), 0.90 (3 H, d, $^3J_{H–H}$ = 6.8 Hz, H^{8a}).†

^{13}C{^{1}H} NMR (176 MHz, CD_2Cl_2): δ 153.8 (C^1), 144.5 (C^2), 138.5 (C^6), 129.9 (C^4), 125.6 (C^3), 124.0 (C^5), 117.4 (C_5H_5'), 116.5 (C_5H_5), 29.8 (C^9), 28.4 (C^7), 25.6 (C^{8a}), 24.9 (C^{10a}), 22.4 (C^8), 22.1 (C^{10}).†

Elemental analysis: C, 36.65; H, 3.82; N, 1.83% ($C_{22}H_{27}Cl_4GaNNb$ requires: C, 43.33; H, 4.46; N, 2.30%).‡

IR (Nujol mull, KBr): ν_{max}/cm^{-1} 3117w, 1604w.

MS (*i*ASAP+, 450 °C): *m/z* 495 (40%), 433 (100, $[M – GaCl_3]^+$), 404 (73), 258 (19, $[Cp_2NbCl]^+$), 177 (62, $[DippNH_2]^+$).

Single crystals of **9**·C_6D_6 suitable for XRD analysis were afforded following the reaction between **3** (0.03 g, 0.069 mmol) and $GaCl_3$ (0.012 g, 0.069 mmol) in C_6D_6 (~0.7 ml) inside a Young's NMR tube, which was allowed to stand at room temperature.§

* SR152, page 8(2).

† SR142, page 148(1).

‡ Satisfactory elemental analysis could not be performed, despite repeated attempts, due to possible contamination of **9** with trace $Cp_2Nb(ClGaCl_3)(N\{Dipp{\cdot}Ga_2Cl_6\})$ (**10**) formed. The closest elemental analysis (C, 42.52; H, 4.38; N, 1.67%) was achieved with another sample of **10**: SR128, page 134(1).

§ SR123, page 129(1).

7.3.4.1. Reaction between 9 and PMe_3

$$Cp_2Nb(ClGaCl_3)(NDipp) + PMe_3 \xrightarrow[-196\ °C \rightarrow RT]{CD_2Cl_2} Cp_2NbCl(NDipp) + Me_3P{\rightarrow}GaCl_3$$

Inside the glovebox, a solution of $Cp_2NbCl(NDipp)$ (**3**; 0.03 g, 0.069 mmol) in CD_2Cl_2 (~0.7 ml) was added *via* pipette to a sample vial containing $GaCl_3$ (0.012 g, 0.069 mmol). Following mixing with a pipette, the resulting solution was added to a Young's NMR tube, and the tube was then sealed and removed from the glovebox. The contents of the NMR tube were frozen (–196 °C) and degassed *in vacuo*, following which PMe_3 (0.104 mmol) was added *via* vacuum transfer to the tube. The NMR tube was gradually warmed to room temperature and, following agitation, precipitation occurred. The white precipitate was allowed to settle; NMR spectroscopic analysis of the red/orange solution indicated the presence of **3** and $Me_3P{\rightarrow}GaCl_3$ in ~1:1 molar ratio.[*]

^{1}H NMR (400 MHz, CD_2Cl_2): δ 11.79 (s), 7.39–7.34 (m), 7.29 (ddd, J = 20.2, 7.6, 1.8 Hz), 6.42 (1 H, s), 1.85 (d, J = 13.5 Hz), 1.67 (12 H, d, $^2J_{P–H}$ = 11.8 Hz, $GaCl_3{\cdot}PMe_3$), 1.40 (1 H, dd, J = 13.8, 6.9 Hz), 0.92 (1 H, d, J = 6.8 Hz).[†]

^{31}P{^{1}H} NMR (162 MHz, CD_2Cl_2): δ 24.2 (1 P, s),[‡] –29.0 (12 P, m,[§] $Cl_3Ga{\cdot}PMe_3$).

7.3.4.2. Reaction between 9 and either CO or H_2

A solution of $Cp_2Nb(ClGaCl_3)(NDipp)$ (**9**; 0.02 g, 0.03 mmol) in CD_2Cl_2 (~0.7 ml) was prepared inside the glovebox and transferred into a Young's NMR tube. Following removal from the glovebox, the contents of the NMR tube were degassed *via* the freeze-pump-thaw method (×3) and left sealed under vacuum once at room temperature. The contents of the NMR tube were then exposed to ~1 atmosphere of either CO or H_2, under which they were sealed, shaken and heated in an oil bath set at 50 °C for ~3 h. The progress of the reaction was monitored *via* ^{1}H and ^{13}C NMR spectroscopies. Aside from the additional signal corresponding to the dissolved, unbound gas (δ_H = 4.60 ppm for H_2; δ_C = 184.2 ppm for CO), the ^{1}H and ^{13}C NMR spectra were identical to that of unreacted **9**.[**]

[*] SR126–127, pages 132–133(1).

[†] Signals corresponding to $Cp_2NbCl(NDipp)$ (**3**) formed have been omitted for clarity.

[‡] This chemical shift (δ_P = 24.2 ppm) closely matches one observed by Tay *et al.*, assigned to the an unnamed product from the reaction between PMe_3 and DCM.[152]

[§] Overlap between two 1:1:1:1 quartets: $^1J_{^{69}Ga–P}$ = 783 Hz (~60% of integral) and $^1J_{^{71}Ga–P}$ = 999 Hz (~40% of integral). A similar signal was observed in the literature for $GaCl_3{\cdot}PPh_3$ (δ_P = –5.5 ppm and $^1J_{^{71}Ga–P}$ = 721 Hz).[151]

[**] Reaction with CO: SR155, page 11(2); reaction with H_2: SR156, page 12(2).

7.3.5. Synthesis of $Cp_2Nb(ClGaCl_3)(N\{Dipp{\cdot}Ga_2Cl_6\})$ (10)

$$Cp_2NbCl(NDipp) + 3\ GaCl_3 \xrightarrow[RT]{DCM} Cp_2Nb(ClGaCl_3)(NDipp{\cdot}Ga_2Cl_6)$$

A solution of $Cp_2NbCl(NDipp)$ (**3**; 0.10 g, 0.23 mmol) in DCM (~10 ml) was added dropwise to a stirred solution of $GaCl_3$ (0.122 g, 0.69 mmol) in DCM (~10 ml) at room temperature and then left for 18 h. The resulting solid was separated from the dark brown solution *via* cannula filtration and dried by slow evaporation under a stream of N_2, leading to the isolation of **10** as a yellow solid (0.10 g, 45%).*

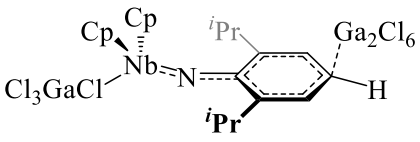

Elemental analysis: C, 27.32; H, 2.43; N, 1.44% ($C_{22}H_{27}Cl_{10}Ga_3NNb$ requires: C, 27.47; H, 2.83; N, 1.46%).
MS (*i*ASAP+, 400 °C): *m*/*z* 609 (2%, $[M - Ga_2Cl_6]^+$), 567 (5), 535 (2), 495 (8), 457 (4), 293 (6), 220 (35), 178 (100, $[DippNH_3]^+$), 162 (17).
IR (Nujol mull, KBr): ν_{max}/cm^{-1} 3117w, 1603w.

Single crystals suitable for XRD analysis were grown at room temperature in a Young's NMR tube, following the addition of a solution of $GaCl_3$ (0.028 g, 0.16 mmol) in CD_2Cl_2 (~0.7 ml) to **3** (0.03 g, 0.069 mmol) inside a glovebox.†

* SR143, page 149(1).

† SR138, page 144(1).

7.3.6. Synthesis of $Cp_2NbMe(NDipp)$ (11)

$$Cp_2NbCl(NDipp) + MeLi \xrightarrow[-78\ ^\circ C \rightarrow RT]{Et_2O} Cp_2NbMe(NDipp) + LiCl$$

With the exclusion of light, a solution of MeLi in Et_2O (1.6 M, 0.32 ml, 0.52 mmol) was added dropwise *via* plastic syringe to a cold (–78 °C) solution of $Cp_2NbCl(NDipp)$ (**3**; 0.15 g, 0.35 mmol) in Et_2O (~30 ml). The subsequent solution was allowed to warm to room temperature over ~20 h, forming a white precipitate. The volatile components were removed *in vacuo* and the orange residue extracted into hexanes (~50 ml), which were separated from a white solid *via* cannula filtration. The solvent was removed under vacuum and the resulting residue was redissolved in Et_2O (~30 ml). A further aliquot of MeLi in Et_2O (1.6 M, 3.2 ml, 5.19 mmol) was added dropwise to the cold (–78 °C) ethereal solution, which was allowed to warm to room temperature over ~6 h and stirred for a further ~60 h. Volatile components were removed *in vacuo*, and the orange-brown residue was extracted first into 40/60 petroleum ether (~100 + {2 × ~50} ml), then, following the removal of the solvent under vacuum, into hexanes (~20 + {4 × ~10} ml), in order to remove successive white solids from the product mixture. Removal of the hexanes *in vacuo*, followed by redissolution in Et_2O (~20 ml), cooling to 0 °C, the solution was treated dropwise *via* syringe with TMSCl (0.59 ml, 4.7 mmol). After stirring at 0 °C for ~30 min, then at room temperature for ~2 h, the volatile components were removed *in vacuo* and the product was extracted into hexanes (~80 + ~20 ml) and separated from a white solid *via* cannula filtration. Removal of the hexanes under vacuum afforded a yellow paste containing complex **11**, along with $DippNH_2$, grease and other impurities. Crystallisation of **11** from a solution in hexanes at –20 °C resulted in orange single crystals (~10 mg, ~6%) that were suitable for XRD analysis.*

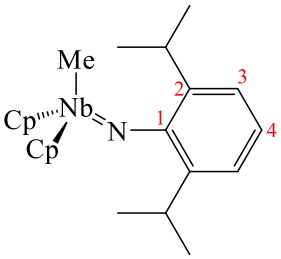

^{1}H NMR (400 MHz, C_6D_6): δ 7.07 (2 H, d, $^3J_{H–H}$ = 7.6 Hz, H^3), 6.85 (1 H, t, $^3J_{H–H}$ = 7.6 Hz, H^4), 5.50 (10 H, s, C_5H_5), 3.54 (2 H, sept, $^3J_{H–H}$ = 6.9 Hz, C*H*Me$_2$), 1.29 (12 H, d, $^3J_{H–H}$ = 6.9 Hz, CH*Me*$_2$), 1.02 (3 H, s, Nb*Me*).†

Elemental analysis: C, 65.05; H, 6.65; N, 3.14% ($C_{23}H_{30}NNb$ requires: C, 66.82; H, 7.31; N, 3.39%).‡

MS (*i*ASAP+, 350 °C): *m/z* 430 (14%), 414 (100, $[M + H]^+$), 413 (55, M^+).

* SR116, page 122(1); unoptimised synthesis.

† Additional ^{1}H NMR signals corresponding to $DippNH_2$, silicone grease and unknown contaminants have been omitted for clarity: δ 3.19 (1 H, s, NH), 2.64 (1 H, sept, $^3J_{H–H}$ = 6.8 Hz, C*H*Me$_2$), 1.36 (2 H, s), 1.21 (1 H, dd, *J* = 6.8, 2.1 Hz), 1.15 (6 H, d, $^3J_{H–H}$ = 6.8 Hz, CH*Me*$_2$), 0.96–0.88 (1 H, m), 0.30 (65 H, s, silicone grease), 0.15 (1 H, s).

‡ Due to exposure of the crystals to air and/or the oil used to mount them for XRD analysis, satisfactory elemental analyses of complex **11** could not be performed.

7.3.7. Synthesis of $Cp_2Nb(NDipp)(PCO)$ (12)

$$Cp_2NbCl(NDipp) + Na(OCP)\cdot 2½(diox) \xrightarrow[60\ °C,\ 16\ h]{THF} Cp_2Nb(NDipp)(PCO) + NaCl + 2½\ diox$$

A solution of Na(OCP)·2½(diox) (0.19 g, 0.63 mmol) in THF (~100 ml) was added dropwise to a stirred solution of $Cp_2NbCl(NDipp)$ (**3**; 0.25 g, 0.58 mmol) in THF (~20 ml) heated at 60 °C. The solution was maintained at this temperature for 16 h, following which time the volatile components were removed *in vacuo*. The residue was extracted with hexanes (~100 + {3 × ~30} ml), the solvent from the combined extracts was removed under vacuum to produce an orange paste. Precipitation from cold (–78 °C) 40/60 petroleum ether (~60 ml) and subsequent isolation *via* cannula filtration yielded an orange solid (0.057 g), containing complex **12** (47 mol%, 11% yield) and unreacted **3** (53 mol%) as determined by NMR spectroscopic analysis.[*]

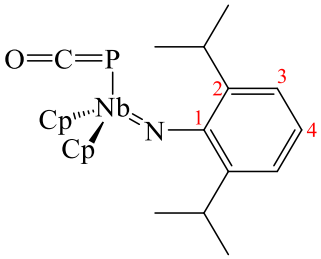

^{1}H NMR (599 MHz, C_6D_6): δ 7.00 (2 H, d, $^3J_{H–H}$ = 7.7 Hz, H^4), 6.81 (1 H, t, $^3J_{H–H}$ = 7.7 Hz, H^3), 5.63 (10 H, s, C_5H_5), 3.42 (2 H, dsept, $^3J_{H–H}$ = 6.9 Hz, J = 2.2 Hz,[†] C*H*Me$_2$), 1.23 (12 H, d, $^3J_{H–H}$ = 6.9 Hz, CH*Me*$_2$).[‡]

^{13}C{^{1}H} NMR (151 MHz, C_6D_6): δ 175.4 (d, $^1J_{P–C}$ = 99 Hz, P*C*O), 154.8 (C^1), 137.6 (C^2), 123.0 (C^3), 122.5 (C^4), 110.5 (d, $^2J_{P–C}$ = 2 Hz, C_5H_5), 27.8 (d, J = 6 Hz,[†] *C*HMe$_2$), 24.6 (CH*Me*$_2$).[‡]

^{31}P{^{1}H} NMR (162 MHz, C_6D_6): δ –344.0 (s).

IR (Nujol mull, KBr): ν_{max}/cm^{-1} 1892w (P=C=O asymm).

MS (*i*ASAP+, 450 °C): *m*/*z* 457 (26%, M^+), 433 (100, $[Cp_2NbCl(NDipp)]^+$), 430 (13, $[M – CO + H]^+$), 177 (8, $[DippNH_2]^+$).

Single crystals (containing **12** co-crystallised with **3** in a 1:5 molar ratio) suitable for XRD analysis were afforded from a concentrated solution of complexes **12** and **3** in hexanes at –20 °C.[§]

Elemental analysis: C, 54.04; H, 5.98; N, 4.72% ($C_{133}H_{162}Cl_5N_6Nb_6OP$[**] requires: C, 60.82; H, 6.22; N, 3.20%).

[*] SR162, page 18(2).

[†] It remains unclear why additional coupling is observed for the ^{1}H and ^{13}C NMR signals corresponding to *CH*Me$_2$, but not elsewhere on the complex.

[‡] NMR signals corresponding to $Cp_2NbCl(NDipp)$ (**3**) have been omitted for clarity.

[§] SR109, page 115(1).

[**] The molecular formula corresponding to $Cp_2Nb(NDipp)(PCO)\cdot 5\{Cp_2NbCl(NDipp)\}$.

7.4. Electrophilic addition to $Cp_2NbCl(NDipp)$ (3)

7.4.1. Protonation of $Cp_2NbCl(NDipp)$ (3)

7.4.1.1. Synthesis of $[Cp_2NbCl(NHDipp)]OTf$ ([13]OTf)

$$Cp_2NbCl(NDipp) + TfOH \xrightarrow[-40\ °C \rightarrow RT]{Et_2O} [Cp_2NbCl(NHDipp)]OTf$$

A solution of TfOH (0.04 ml, 0.45 mmol) in Et_2O (~10 ml) was added dropwise to a stirred, cooled (–40 °C) solution of $Cp_2NbCl(NDipp)$ (**3**; 0.09 g, 0.21 mmol) in Et_2O (~20 ml), resulting in the instantaneous precipitation of a yellow solid. The resulting suspension was allowed to warm gradually to room temperature (over ~1 h), after which time it was stirred for a further ~2 h. After leaving the precipitate to settle, the colourless filtrate was removed *via* cannula filtration and the solid was washed with Et_2O (3 × ~10 ml). Drying of the solid under vacuum yielded [**13**]OTf as a yellow powder (0.09 g, 75%).[*]

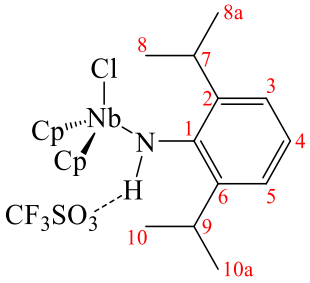

^{1}H NMR (599 MHz, CD_2Cl_2): δ 12.78 (1 H, br s, $\nu_{½}$ = 9 Hz, NH), 7.30 (1 H, t, $^3J_{H–H}$ = 7.6 Hz, H^4), 7.25 (1 H, dd, $^3J_{H–H}$ = 7.6 Hz, $^4J_{H–H}$ = 1.7 Hz, H^5), 7.21 (1 H, dd, $^3J_{H–H}$ = 7.6 Hz, $^4J_{H–H}$ = 1.7 Hz, H^3), 6.92 (5 H, s, C_5H_5), 6.35 (5 H, s, C_5H_5'), 3.20 (1 H, sept, $^3J_{H–H}$ = 6.8 Hz, H^9), 2.35 (1 H, sept, $^3J_{H–H}$ = 6.8 Hz, H^7), 1.33 (6 H, d, $^3J_{H–H}$ = 6.8 Hz, $H^{8,10}$), 1.16 (3 H, d, $^3J_{H–H}$ = 6.8 Hz, H^{8a}), 0.88 (3 H, d, $^3J_{H–H}$ = 6.8 Hz, H^{10a}).

^{13}C{^{1}H} NMR (151 MHz, CD_2Cl_2): δ 154.7 (C^1), 144.0 (C^6), 138.7 (C^2), 129.1 (C^4), 125.1 (C^5), 123.8 (C^3), 117.0 (C_5H_5'), 116.4 (C_5H_5), 29.5 (C^7), 28.4 (C^9), 25.3 (C^{10a}), 24.8 (C^{8a}), 22.6 (C^8), 22.2 (C^{10}).[†]

^{19}F{^{1}H} NMR (376 MHz, CD_2Cl_2): δ –78.7 (s, OSO_2CF_3).

Elemental analysis: C, 47.25; H, 4.92; N, 2.33% ($C_{23}H_{28}ClF_3NNbO_3S$ requires: C, 47.31; H, 4.83; N, 2.40%).

IR (Nujol mull, KBr): ν_{max}/cm^{-1} 3120br (C–H), 3195sh (C–H).

MS (ASAP+, 350 °C): *m/z* 547 (100%, [M – HCl]$^+$), 433 (98, [M – TfOH]$^+$), 407 (77, $[Cp_2NbCl(OTf)]^+$), 352 (87, $[\{DippHN\}_2]^+$).

Single crystals of [**13**]OTf·DCM suitable for XRD analysis were obtained by layering a DCM solution with hexanes at room temperature.[‡]

[*] SR217, page 73(2).

[†] A ^{13}C NMR signal corresponding to OSO_3CF_3 was not observed.

[‡] SR213, page 69(2).

7.4.1.2. Synthesis of [$Cp_2NbCl(NHDipp)$]BAr^F_4 ([13]BAr^F_4)

$$Cp_2NbCl(NDipp) + [H(OEt_2)_2]BAr^F_4 \xrightarrow[-20\ °C \rightarrow RT]{DCM} [Cp_2NbCl(NHDipp)]BAr^F_4 + 2\ Et_2O$$

At –20 °C, a solution of $[H(OEt_2)_2]BAr^F_4$ (0.15 g, 0.15 mmol) in DCM (~10 ml) was added dropwise to a stirred solution of $Cp_2NbCl(NDipp)$ (**3**; 0.08 g, 0.81 mmol) in DCM (~20 ml). The reaction mixture was allowed to warm gradually to room temperature, after which point it was stirred for a further 15 h. Volatile components were removed from the resulting solution *in vacuo* and the residue was washed with hexanes (~100 + {3 × ~10} ml). Drying the solid under vacuum yielded [**13**]BAr^F_4 as a yellow powder (0.13 g, 68%). Single crystals suitable for XRD analysis were obtained by recrystallisation from a concentrated toluene solution at 4 °C.*

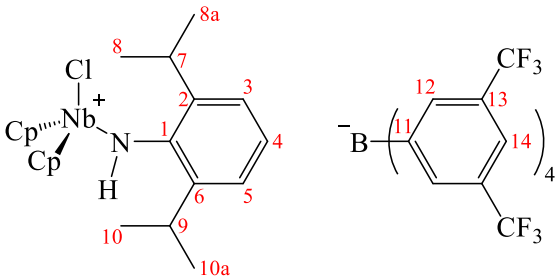

^{1}H NMR (700 MHz, CD_2Cl_2): δ 11.63 (1 H, br s, $\nu_{½}$ = 18 Hz, NH), 7.75–7.70 (8 H, m, H^{12}), 7.57 (4 H, br s, $\nu_{½}$ = 5 Hz, H^{14}), 7.38 (1 H, t, $^3J_{H–H}$ = 7.7 Hz, H^5), 7.36–7.31 (1 H, m, H^3), 7.26 (1 H, dd, $^3J_{H–H}$ = 7.7, 1.6 Hz, H^4), 6.79 (5 H, s, C_5H_5), 6.32 (5 H, s, C_5H_5'), 3.22 (1 H, sept, $^3J_{H–H}$ = 6.8 Hz, H^9), 2.29 (1 H, sept, $^3J_{H–H}$ = 6.9 Hz, H^7), 1.39 (3 H, d, $^3J_{H–H}$ = 6.8 Hz, H^{10a}), 1.37 (3 H, d, $^3J_{H–H}$ = 6.9 Hz, H^{8a}), 1.16 (3 H, d, $^3J_{H–H}$ = 6.9 Hz, H^8), 0.90 (3 H, d, $^3J_{H–H}$ = 6.8 Hz, H^{10}).

^{13}C{^{1}H} NMR (176 MHz, CD_2Cl_2): δ 162.3 (q,† $^1J_{B–C}$ = 50 Hz, C^{11}), 153.8 (C^1), 144.5 (C^6), 137.9 (C^2), 135.4 (C^{12}), 130.4 (C^5), 129.9–129.1 (m, C^{13}), 126.0 (C^3), 125.2 (q, $^1J_{C–F}$ = 272 Hz, CF_3), 124.0 (C^4), 118.6–117.7 (m, C^{14}), 117.2 (C_5H_5'), 116.0 (C_5H_5), 29.9 (C^7), 28.5 (C^9), 25.6 (C^{10}), 24.6 (C^8), 22.1 (C^{8a}), 21.9 (C^{10a}).

^{19}F{^{1}H} NMR (376 MHz, CD_2Cl_2): δ –62.8 (s, CF_3).

^{11}B NMR (128 MHz, CD_2Cl_2): δ –7 (br s, $\nu_{½}$ = 10 Hz, $[BAr^F_4]^-$).

Elemental analysis: C, 50.22; H, 3.20; N, 1.39% ($C_{54}H_{40}BClF_{24}NNb$ requires: C, 49.97; H, 3.11; N, 1.08%).

IR (Nujol mull, KBr): ν_{max}/cm^{-1} 3332 (N–H stretch), 3133, 1609.

MS (*i*ASAP+, 450 °C): *m/z* 434 (100%, M^+), 433 (82, $[M – H]^+$), 178 (12, $[DippNH_3]^+$).‡

---

* SR182, page 38(2).

† 1:1:1:1 quartet.

‡ Where M^+ denotes cation $[Cp_2NbCl(NHDipp)]^+$ (**13**$^+$).

7.4.2. Attempted electrophilic methylation of $Cp_2NbCl(NDipp)$ (3)

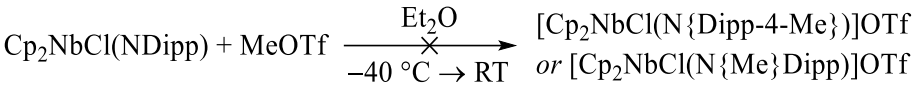

Neat MeOTf (0.03 ml, 0.27 mmol) was added dropwise *via* a syringe to a Schlenk tube containing Et_2O (~50 ml) and the resulting ethereal solution was then added dropwise *via* cannula to a cooled (–40 °C), stirred solution of $Cp_2NbCl(NDipp)$ (**3**; 0.10 g, 0.23 mmol) in Et_2O (~20 ml). The resulting solution was allowed to warm gradually to room temperature (over ~3 h), over the course of which precipitation of an orange solid occurred. After stirring at room temperature for ~15 h, the suspension was allowed to settle and the orange solution was separated from the solid *via* cannula filtration. Washing of the solid with Et_2O (3 × ~10 ml) and concentration of the ethereal washings yielded near-quantitative amounts of unreacted **3**, as identified by ^1H NMR spectroscopy; the Et_2O-insoluble fraction (~5 mg, ~4%) was determined as $[Cp_2NbCl(NHDipp)]OTf$ ([**13**]OTf).*

* SR213, page 69(2).

7.4.3. Tritylation of $Cp_2NbCl(NDipp)$ (3)

7.4.3.1. Synthesis of $TrBAr^F_4$ (15)

$$TrCl + NaBAr^F_4 \xrightarrow[RT]{DCM} TrBAr^F_4 + NaCl$$

To a stirred suspension of $NaBAr^F_4$ (0.96 g, 1.1 mmol) in DCM (~40 ml) at room temperature was added a solution of TrCl (0.30 g, 1.1 mmol) in DCM (~15 ml). The suspension was stirred at room temperature for ~60 h, over the course of which the solution became lime-green and most of the precipitate dissolved. The solution was separated from the white solid by cannula filtration, and the solid extracted with more DCM (2 × ~20 ml) which was combined with the filtrate. Concentration of the DCM solution to ~40 ml, followed by the addition of hexanes (~50 ml), resulted in the precipitation of a yellow/green solid, which was subsequently washed with more hexanes (2 × ~20 ml) and dried under vacuum and isolated (0.97 g, 81%).*

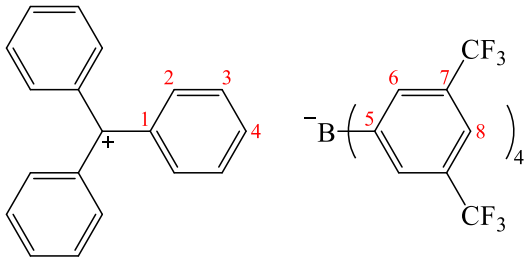

^{1}H NMR (700 MHz, CD_2Cl_2): δ 8.23 (3 H, tt, $^2J_{H–H}$ = 7.5 Hz, $^3J_{H–H}$ = 1.3 Hz, H^4), 7.88–7.83 (6 H, m, H^3), 7.74–7.71 (9 H, m, H^6), 7.66–7.63 (6 H, m, H^2), 7.55 (4 H, br s, $\nu_{½}$ = 5 Hz, H^8).†

^{13}C{^{1}H} NMR (176 MHz, CD_2Cl_2): δ 211.5 (Ph_3C^+), 162.3 (q,‡ $^1J_{^{11}B–C}$ = 50 Hz, C^5), 144.2 (C^4), 143.2 (C^2), 140.5 (C^1), 135.4 (C^6), 131.2 (C^3), 129.8–129.1 (m, C^7), 125.2 (q, $^1J_{C–F}$ = 272 Hz, CF_3), 118.5–116.9 (m, C^8).†

^{19}F{^{1}H} NMR (376 MHz, CD_2Cl_2): δ –62.9 (s, CF_3).

^{11}B NMR (128 MHz, CD_2Cl_2): δ –7 (br s, $\nu_{½}$ = 10 Hz, $[BAr^F_4]^-$).

Elemental analysis: C, 54.92; H, 2.39% ($C_{51}H_{27}BF_{24}$ requires: C, 55.36; H, 2.46%).

MS (*i*ASAP+, 350 °C): *m/z* 456 (9%, $[M + Ar^F]^+$), 379 (9), 259 (14), 243 (100, M^+).§

Recrystallisation of **15** from a warm toluene solution in a sample vial (sealed under N_2) resulted in single crystals suitable for XRD analysis.†

---

* SR145, page 1(2). Adapted from the reported synthesis of $TrBPh^F_4$ from TrCl and $KBPh^F_4$.[186]

† SR113, page 119(1).

‡ A 1:1:1:1 quartet.

§ Where M^+ is the cationic component of **15**, namely Tr^+.

7.4.3.2. Attempted synthesis of [$Cp_2NbCl(N\{Dipp\text{-}4\text{-}Tr\})$]$BAr^F_4$ ([16]BAr^F_4)

$$Cp_2NbCl(NDipp) + TrBAr^F_4 \xrightarrow[-40\ ^\circ C \rightarrow RT]{DCM} [Cp_2NbCl(N\{Dipp\text{-}4\text{-}Tr\})]BAr^F_4$$

To a cooled (–40 °C) solution of $Cp_2NbCl(NDipp)$ (**3**; 0.10 g, 0.23 mmol) in DCM (~20 ml) was added dropwise *via* cannula a solution of $TrBAr^F_4$ (**15**; 0.26 g, 0.23 mmol) in DCM (~35 ml). The resulting yellow solution was allowed to warm to room temperature, at which temperature it was stirred for ~15 h where the solution reddened. The volatile components were then removed *in vacuo* to leave behind an oily residue, which was washed with hexanes (~70 + {3 × ~20} ml, with sonication) to leave behind a red residue following cannula filtration. Removal of the solvent under vacuum produced a deep-red solid (0.19 g), consisting of ~50 mol% $[Cp_2NbCl(NHDipp)]BAr^F_4$ ([**13**]BAr^F_4) and at least one other unidentified component.*

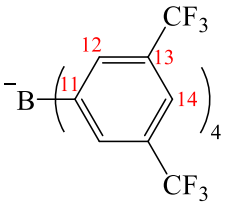

^{1}H NMR (400 MHz, CD_2Cl_2): δ 11.58 (1 H, br s, $\nu_{½}$ = 7 Hz), 7.76–7.70 (~8 H,† m, H^{12}), 7.57 (~4 H,‡ br s, $\nu_{½}$ = 5 Hz, H^{14}), 7.32–7.19 (~20 H,† m), 7.14 (1 H, d, J = 2.2 Hz), 6.76 (5 H, s), 6.55 (2 H, s), 6.32 (~5 H,† s), 3.17 (1 H, sept, J = 6.9 Hz), 1.14 (5 H, d, J = 7.0 Hz), 1.05 (4 H, d, J = 6.8 Hz), 0.78 (4 H, d, J = 6.8 Hz).‡

^{19}F{^{1}H} NMR (376 MHz, CD_2Cl_2): δ –62.7 (s, CF_3).

^{11}B NMR (128 MHz, CD_2Cl_2): δ –7 (br s, $\nu_{½}$ = 9 Hz, [BAr^F_4]$^-$).

* SR209, page 65(2).

† Estimated integral of the ^{1}H resonance, following the deduction of the contribution associated to [**13**]BAr^F_4.

‡ Signals corresponding to [**13**]BAr^F_4 have been omitted for clarity.

7.4.3.3. Synthesis of $Cp_2NbCl(NDipp^{Tr})$ (17)

$$Cp_2NbCl(NDipp) + TrBAr^F{}_4 + DABCO \xrightarrow[-40\ °C \rightarrow RT]{DCM} Cp_2NbCl(NDipp^{Tr}) + [DABCO{\cdot}H]BAr^F{}_4$$

A solution of $TrBAr^F{}_4$ (0.28 g, 0.25 mmol) in DCM (~20 ml) was added dropwise to a cooled (–40 °C), stirred solution of $Cp_2NbCl(NDipp)$ (**3**; 0.10 g, 0.23 mmol) and DABCO (0.026 g, 0.23 mmol) in DCM (~30 ml). The resulting red solution was allowed to warm to room temperature gradually (over ~3 h), following which it was stirred for another 15 h. Volatile components were removed from the subsequent green solution *in vacuo* and the residue was extracted with hexanes (60 + {2 × 20} ml, with sonication) to afford an orange solution. Concentration and subsequent recrystallisation at –20 °C of this solution resulted in orange crystals of **17** (0.047 g, 29%). Single crystals suitable for XRD analysis were obtained by recrystallisation from hot hexanes.*

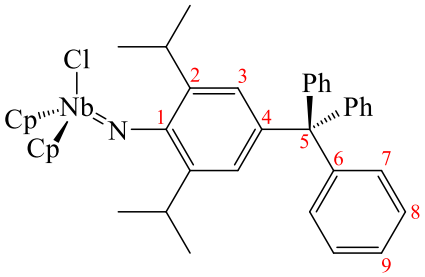

^{1}H NMR (599 MHz, CD_2Cl_2): δ 7.29–7.22 (12 H, m, $H^{7,8}$), 7.20–7.15 (3 H, m, H^9), 6.84 (3 H, s, H^3), 6.24 (10 H, s, C_5H_5), 3.27 (2 H, sept, $^3J_{H–H}$ = 6.9 Hz, C*H*Me$_2$), 1.05 (12 H, d, $^3J_{H–H}$ = 6.9 Hz, CH*Me*$_2$).

^{13}C{^{1}H} NMR (151 MHz, CD_2Cl_2): δ 152.6 (C^1), 148.1 (C^5), 140.2 (C^4), 138.2 (C^2), 131.5 (C^8), 127.9 (C^7), 126.2 (C^9), 125.9 (C^3), 113.4 (C_5H_5), 65.5 (C^6), 27.8 (*C*HMe$_2$), 24.5 (CH*Me*$_2$).

Elemental analysis: C, 72.64; H, 6.10; N, 2.04% ($C_{41}H_{41}NClNb$ requires: C, 72.83; H, 6.11; N, 2.07%).

MS (ASAP+, 350 °C): *m*/*z* 675 (96%, M^+), 660 (8, $[M – Me]^+$), 640 (29, $[M – Cl]^+$), 610 (8, $[M – C_5H_5]^+$), 433 (13, $[M – Tr + H]^+$), 243 (12, $[Tr]^+$).

Accurate mass (ASAP+, 350 °C): *m*/*z* 676.2061 ($C_{41}H_{42}NClNb$† requires: 676.2070).

* SR211, page 67(2).

† Accurate mass determined for the $[M + H]^+$ cation, $[Cp_2NbCl(NHDipp^{Tr})]^+$.

7.5. Oxidative coupling of $Cp_2NbCl(NDipp)$

7.5.1. Synthesis of $[\{Cp_2NbCl\}_2(N\{2,6\text{-}^iPr_2C_6H_2\}_2N)][BAr^F{}_4]_2$ ([18][$BAr^F{}_4$]$_2$)

7.5.1.1. Addition of $AgBAr^F{}_4$ (1 equiv.) to $Cp_2NbCl(NDipp)$ (3)

$$4\ Cp_2NbCl(NDipp) + 4\ AgBAr^F{}_4 \xrightarrow[RT,\ 2.5\ h]{DCM} [\{Cp_2NbCl\}_2(N\{2,6\text{-}^iPr_2C_6H_2\}_2N)][BAr^F{}_4]_2 + 2\ [Cp_2NbCl(NHDipp)]BAr^F{}_4 + 4\ Ag^0$$

To a stirred solution of $Cp_2NbCl(NDipp)$ (**3**; 0.20 g, 0.46 mmol) in DCM (~20 ml) was added dropwise a solution of $AgBAr^F{}_4$ (0.41 g, 0.42 mmol) in DCM (~10 ml) at room temperature, where an intense blue coloration immediately occurred. After stirring for 2.5 h, standing of the reaction mixture resulted in the precipitation of a grey solid, which was removed from the solution *via* cannula filtration. The volatile components were removed from the DCM solution *in vacuo* and the subsequent solid was washed with hexanes (4 × ~10 ml). Drying under vacuum led to the isolation of the deep-blue solid (0.49 g, 91%), consisting of $[\{Cp_2NbCl\}_2(N\{2,6\text{-}^iPr_2C_6H_2\}_2N)][BAr^F{}_4]_2$ ([**18**][$BAr^F{}_4$]$_2$) and $[Cp_2NbCl(NHDipp)]BAr^F{}_4$ ([**13**]$BAr^F{}_4$) in a 1:2 molar ratio, respectively.*

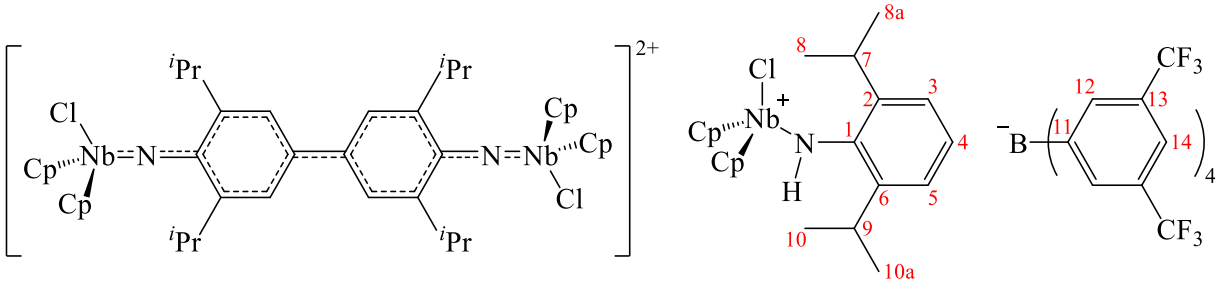

1 : 2 : 4

^{1}H NMR (599 MHz, CD_2Cl_2): δ 11.63 (2 H, br s, $\nu_{½}$ = 18 Hz, NH), 7.73–7.70 (32 H, m, H^{12}), 7.56 (16 H, br s, $\nu_{½}$ = 4 Hz, H^{14}), 7.38 (2 H, t, $^3J_{H–H}$ = 7.7 Hz, H^5), 7.36–7.32 (2 H, m, H^3), 7.26 (2 H, d, $^3J_{H–H}$ = 7.5 Hz, H^4), 6.79 (10 H, s, C_5H_5), 6.32 (10 H, s, C_5H_5'), 3.22 (2 H, sept, $^3J_{H–H}$ = 6.8 Hz, H^9), 2.30 (2 H, sept, $^3J_{H–H}$ = 6.5 Hz, H^7), 1.39 (6 H, d, $^3J_{H–H}$ = 6.8 Hz, H^{10a}), 1.37 (6 H, d, $^3J_{H–H}$ = 6.8 Hz, H^{8a}), 1.36–1.18 (~30 H, m),† 1.17 (6 H, d, $^3J_{H–H}$ = 6.9 Hz, H^8), 0.90 (6 H, d, $^3J_{H–H}$ = 6.8 Hz, H^{10}).

^{19}F{^{1}H} NMR (376 MHz, CD_2Cl_2): δ –62.8 (s, CF_3).

^{11}B NMR (128 MHz, CD_2Cl_2): δ –7 (br s, $\nu_{½}$ = 6 Hz, [$BAr^F{}_4$]$^-$).

Elemental analysis: C, 50.72; H, 3.46; N, 1.13% ($C_{216}H_{156}B_4Cl_4F_{96}N_4Nb_4$‡ requires: C, 50.01; H, 3.03; N, 1.08%).

---

* SR170, page 26(2).

† Very broad region of ^{1}H NMR spectrum overlaid with a sharper multiplet centred at $\delta_H \approx 1.26$ ppm, attributable to *n*-hexane.

‡ Formula calculated for [**18**][$BAr^F{}_4$]$_2$·2[**13**]$BAr^F{}_4$.

IR (Nujol mull, KBr): No signals were observed.

MS (*i*ASAP+, 350 °C): *m*/*z* 650 (68%, $[BAr^{F}_{3}]^{+}$), 434 (46, M^{+}), 433 (100, $[M - H]^{+}$), 214 (25).*

Magnetic susceptibility (CD_2Cl_2): μ_{eff} 1.88 ± 0.09 μ_B.

Single crystals of [**18**]$[BAr^{F}_{4}]_2$ suitable for XRD analysis were afforded following the layering of a DCM solution of [**18**]$[BAr^{F}_{4}]_2$/[**13**]BAr^{F}_{4} with hexanes at room temperature.†

7.5.1.2. Addition of $AgBAr^{F}_{4}$ (2 equiv.) and DABCO (2 equiv.) to $Cp_2NbCl(NDipp)$ (3)

$$\begin{array}{r} 2\ Cp_2NbCl(NDipp) \\ +\ 4\ AgBAr^{F}_{4} + 2\ DABCO \end{array} \xrightarrow[RT,\ 2.5\ h]{DME} \begin{array}{l} [\{Cp_2NbCl\}_2(N\{2,6\text{-}^{i}Pr_2C_6H_2\}_2N)][BAr^{F}_{4}]_2 \\ +\ 4\ Ag^{0} + 2\ [DABCO{\cdot}H]BAr^{F}_{4} \end{array}$$

A solution of $Cp_2NbCl(NDipp)$ (**3**; 0.10 g, 0.23 mmol) in DME (~20 ml) was added dropwise to a stirred solution of DABCO (0.057 g, 0.51 mmol) and $AgBAr^{F}_{4}$ (0.43 g, 0.44 mmol) in DME (~30 ml) at room temperature, resulting in an immediate blue coloration and the precipitation of a grey solid. After continuing to stir for 2.5 h, the grey precipitate was removed *via* cannula filtration, then the volatile components were removed from the blue filtrate *in vacuo*. The resulting blue solid was washed with hexanes (~100 + {3 × ~20} ml) and petroleum ether 40/60 (3 × ~80 ml, with sonication), then dried under vacuum and isolated (0.27 g).‡

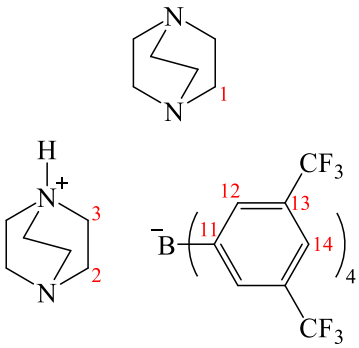

^{1}H NMR (400 MHz, CD_2Cl_2): δ 9.32 (1 H, s, NH), 7.92 (0 H, s), 7.81–7.64 (8 H, m, H^{12}), 7.57 (4 H, s, H^{14}), 7.37 (s), 7.32 (s), 6.93 (s), 6.51 (s), 6.44 (s), 6.35 (s), 6.25 (s), 6.21 (s), 6.18 (s), 4.72 (s), 3.81–3.49 (m), 3.29 (2 H, s, H^{1}), 3.09 (12 H, s, $H^{2,3}$), 2.97–2.88 (m), 2.16 (s), 1.41–0.99 (m).§

^{19}F{^{1}H} NMR (376 MHz, CD_2Cl_2): δ –62.8 (s, CF_3).

^{11}B NMR (128 MHz, CD_2Cl_2): δ –7 (br s, $\nu_{½}$ = 10 Hz, $[BAr^{F}_{4}]^{-}$).

* Where M^{+} denotes cation $[Cp_2NbCl(NHDipp)]^{+}$ (**13**$^{+}$).

† Unfortunately, the simultaneous crystallisation of [**13**]BAr^{F}_{4} prevented the isolation of [**18**]$[BAr^{F}_{4}]_2$ at a scale suitable for characterisation of the pure material.

‡ SR208, page 64(2).

§ Tentative assignments were made for DABCO and $[DABCO{\cdot}H]^{+}$ in the product mixture.

7.5.2. Attempted synthesis of oxidative addition intermediates

7.5.2.1. Addition of $Cp_2NbCl(NDipp)$ (3) to $AgBAr^F_4$ (1 equiv.)

$$2\ Cp_2NbCl(NDipp) + 2\ AgBAr^F_4 \xrightarrow[\text{NMR-scale}]{CD_2Cl_2} [\{Cp_2NbCl\}_2(N\{4,4'\text{-}Dipp_2\}N)][BAr^F_4]_2 + 2\ Ag^0$$

In a glovebox, a solution of $Cp_2NbCl(NDipp)$ (**3**; 0.03 g, 0.067 mmol) in CD_2Cl_2 (~0.35 ml) was added dropwise *via* pipette (over ~10 min) to a sample vial containing a solution of $AgBAr^F_4$ (0.07 g, 0.069 mmol) in CD_2Cl_2 (~0.35 ml). The resulting deep-blue solution was decanted into a Young's NMR tube and was spectroscopically analysed to reveal the presence of $[Cp_2NbCl(NHDipp)]^+$ (**13**$^+$) and $[BAr^F_4]^-$ in a ~2:5 molar ratio, along with other unidentified species.*

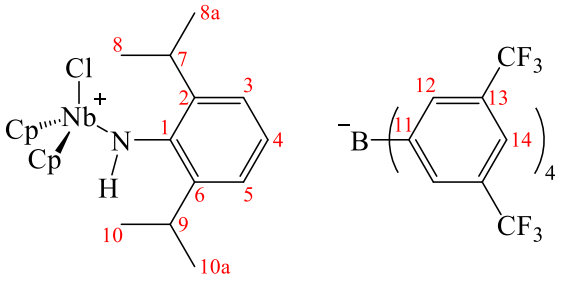

^{1}H NMR (400 MHz, CD_2Cl_2): δ 12.20 (1 H, br s, $\nu_{½}$ = 16 Hz, NH), 7.84–7.64 (18 H, m, H^{12}), 7.57 (9 H, br s, $\nu_{½}$ = 5 Hz, H^{14}), 7.39–7.28 (2 H, m, H^{3,5}), 7.25 (1 H, dd, $^3J_{H–H}$ = 7.1, 2.1 Hz, H^4), 6.79 (5 H, s, C_5H_5), 6.74–6.33 (6 H, m), 6.30 (5 H, s, C_5H_5'), 6.13 (s), 5.87 (s), 3.19 (1 H, sept, $^3J_{H–H}$ = 6.8 Hz, H^9), 2.29 (1 H, sept, $^3J_{H–H}$ = 6.9 Hz, H^7), 1.96 (18 H, s, MeCN),† 1.37 (~5 H, d, $^3J_{H–H}$ = 6.7 Hz, H^{10a}),‡ 1.33 (~8 H, d, $^3J_{H–H}$ = 7.3 Hz, H^{8a}),‡ 1.21 (6 H, d, J = 6.7 Hz), 1.17 (3 H, d, $^3J_{H–H}$ = 6.8 Hz, H^8), 0.90 (3 H, d, J = 6.8 Hz, H^{10}).

^{19}F{^{1}H} NMR (376 MHz, CD_2Cl_2): δ –62.7 (s, CF_3).

^{11}B NMR (128 MHz, CD_2Cl_2): δ –7 (br s, $\nu_{½}$ = 9 Hz, [*B*Ar$^F_4$]$^-$).

* SR205, page 61(2).

† MeCN present within the $AgBAr^F_4$ reagent.

‡ Approximate integrals due to partial overlap of two doublets; integrals larger than expected (3 H in each case) due to the overlap with other signals.

7.5.2.2. Addition of $Cp_2NbCl(NDipp)$ (3) to $FcPF_6$ (1 equiv.)

$$2\ Cp_2NbCl(NDipp) + 2\ FcPF_6 \xrightarrow[RT]{DCM} [\{Cp_2NbCl\}_2(N\{4,4'\text{-}Dipp_2\}N)][PF_6]_2 + 2\ Fc^0$$

A solution of $Cp_2NbCl(NDipp)$ (**3**; 0.03 g, 0.069 mmol) in DCM (~5 ml) was added dropwise *via* syringe to a stirred solution of $FcPF_6$ (0.025 g, 0.076 mmol) in DCM (~5 ml) at room temperature. The reaction mixture was stirred for ~3 h, following which the solution was filtered *via* cannula and volatile components were removed from the filtrate *in vacuo*. The resulting teal solid was extracted into Et_2O (~30 ml) and filtered, where removal of the solvent under vacuum afforded an orange solid (0.03 g). ^1H NMR spectroscopic analysis of the orange solid confirmed the quantitative recovery of unreacted complex **3**.[*]

[*] SR203, page 59(2).

7.5.3. Synthesis of {Cp$_2$NbCl}$_2$(N{2,6-^{i}Pr$_2$C$_6$H$_2$}$_2$N) (20)

$$[\{Cp_2NbCl\}_2(N\{2,6\text{-}^iPr_2C_6H_2\}_2N)][BAr^F{}_4]_2 + 2\ [Cp_2NbCl(NHDipp)]BAr^F{}_4 + 4\ Na \xrightarrow[\Delta,\ \sim 116\ h]{THF} \{Cp_2NbCl\}_2(N\{2,6\text{-}^iPr_2C_6H_2\}_2N) + 2\ Cp_2NbCl(NDipp) + 4\ NaBAr^F{}_4 + H_2$$

The 2:1 mixture* (0.10 g) containing [{Cp$_2$NbCl}$_2$(N{2,6-^{i}Pr$_2$C$_6$H$_2$}$_2$N)][BAr$^F{}_4$]$_2$ ([**18**][BAr$^F{}_4$]$_2$; 0.019 mmol) and [Cp$_2$NbCl(NHDipp)]BAr$^F{}_4$ ([**13**]BAr$^F{}_4$; 0.039 mmol) was dissolved in THF (~15 ml) and added dropwise *via* cannula to a cooled (–78 °C), stirred suspension of Na sand (0.003 g, 0.13 mmol). The resulting suspension was allowed to warm to room temperature gradually (over ~20 h), following which it was heated at reflux for ~116 h. After allowing the suspension to settle and cool, cannula filtration afforded a red solution. The volatile components of this filtrate were removed *in vacuo* and the resulting residue was extracted into hexanes (~80 ml), where the undissolved solids were removed *via* filtration. Subsequent concentration of the hexanes filtrate and storage at –20 °C afforded a deep red solid (~10 mg) which was analysed by ^{1}H NMR spectroscopy.†

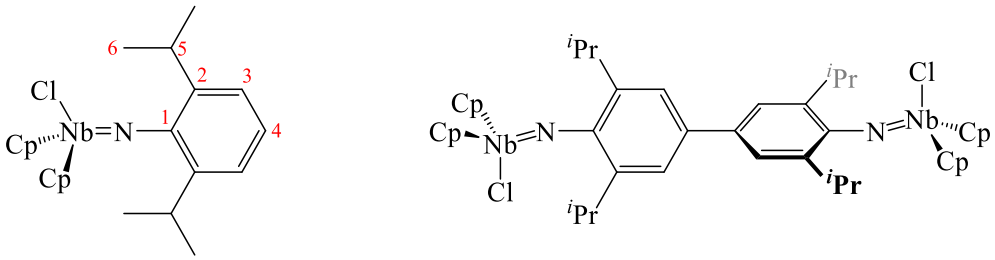

^{1}H NMR (400 MHz, C$_6$D$_6$): δ 8.34 (6 H, br s, $\nu_{½}$ = 10 Hz), 8.14 (1 H, s), 7.65 (4 H, br s, $\nu_{½}$ = 5.0 Hz), 5.81 (~5 H, br s, $\nu_{½}$ = 5 Hz), 5.80 (~5 H, s), 5.29 (4 H, br s, $\nu_{½}$ = 13 Hz), 5.09 (3 H, br s, $\nu_{½}$ = 11 Hz), 4.26 (s), 4.19 (1 H, t, J = 5.7 Hz), 3.57–3.49 (2 H, m, H^5), 1.47 (6 H, s), 1.41–1.32 (124 H, d, J = 4.0 Hz), 1.30 (12 H, d, $^3J_{H–H}$ = 6.9 Hz, H^6), 1.27–1.19 (12 H, m), 0.92–0.77 (10 H, m).‡

Recrystallisation of the solid from a hot, concentrated toluene solution afforded deep-red single crystals of the diimido complex **20** (~5 mg, ~30%) suitable for XRD analysis.

Elemental analysis: C, 52.71; H, 5.60; N, 0% (C$_{44}$H$_{52}$Cl$_2$N$_2$Nb$_2$ requires: C, 61.05; H, 6.06; N, 3.24%).§

* The product mixture formed following the reaction described in SECTION 7.5.1.1.

† SR202, page 58(2).

‡ Integrals reported are relative to the Cp$_2$NbCl(NDipp) (**3**) impurity.

§ Due to exposure of the crystals to air and/or the oil used to mount them for XRD analysis, satisfactory elemental analyses of complex **20** could not be performed.

APPENDICES

APPENDIX 1: Crystallographic data

	3	**5**
Formula	$Cp_2NbCl(NDipp)$	$\{CpNb(\mu\text{-}Cl)(NDipp)\}_2$
Internal identification code	16srv167	16srv289
Empirical formula	$C_{22}H_{27}ClNNb$	$C_{34}H_{44}Cl_2N_2Nb_2$
Formula weight / g mol^{-1}	433.8	737.43
Temperature / K	120	120
Crystal system	monoclinic	monoclinic
Space group	$P2_1/n$	$P2_1/c$
a / Å	10.2986(9)	12.2455(5)
b / Å	17.7623(15)	17.2690(7)
c / Å	11.0892(9)	15.5502(6)
α / °	90	90
β / °	90.451(3)	90.0046(13)
γ / °	90	90
Volume / Å^3	2028.4(3)	3288.4(2)
Z	4	4
ρ_{calc}g / cm^3	1.42	1.49
μ / mm^{-1}	0.729	0.885
F(000)	896	1512
Crystal size / mm^3	0.257 × 0.256 × 0.127	0.22 × 0.185 × 0.171
Radiation	MoKα (λ = 0.71073)	MoKα (λ = 0.71073)
Data collection range / °	$4.33 \leq 2\Theta \leq 64.812$	$4.846 \leq 2\Theta \leq 66.336$
Index ranges	$-15 \leq h \leq 15$, $-26 \leq k \leq 26$, $-16 \leq l \leq 16$	$-18 \leq h \leq 18$, $-26 \leq k \leq 26$, $-23 \leq l \leq 23$
Reflections collected	50753	76024
Independent reflections	7283 [R_{int} = 0.0313, R_{sigma} = 0.0206]	12552 [R_{int} = 0.0471, R_{sigma} = 0.0394]
Data/restraints/parameters	7283/0/274	12552/414/389
Goodness-of-fit on F^2	1.041	1.021
Final R indexes [I ≥ 2σ (I)]	R_1 = 0.0219, wR_2 = 0.0482	R_1 = 0.0339, wR_2 = 0.0705
Final R indexes [all data]	R_1 = 0.0296, wR_2 = 0.0508	R_1 = 0.0574, wR_2 = 0.0781
Largest diff. peak/hole / e Å^{-3}	0.50/–0.56	1.42/–0.71

	9 · C_6D_6	**10**
Formula	$Cp_2Nb(ClGaCl_3)(NDipp)\cdot C_6D_6$	$Cp_2Nb(ClGaCl_3)(N\{Dipp\cdot Ga_2Cl_6\})$
Internal identification code	18srv116	18srv197
Empirical formula	$C_{28}H_{33}Cl_4GaNNb$	$C_{22}H_{27}Cl_{10}Ga_3NNb$
Formula weight / g mol^{-1}	687.98	962.01
Temperature / K	120	120
Crystal system	monoclinic	triclinic
Space group	C2/c	P-1
a / Å	13.2805(5)	10.2526(7)
b / Å	15.7987(6)	13.1165(8)
c / Å	28.3752(11)	13.7201(9)
α / °	90	116.394(2)
β / °	100.5924(15)	92.683(2)
γ / °	90	92.364(2)
Volume / Å^3	5852.1(4)	1646.93(19)
Z	8	2
ρ_{calc}g / cm^3	1.562	1.94
μ / mm^{-1}	1.696	3.594
F(000)	2784	940
Crystal size / mm^3	0.291 × 0.182 × 0.08	0.085 × 0.057 × 0.049
Radiation	MoKα (λ = 0.71073)	MoKα (λ = 0.71073)
Data collection range / °	$4.104 \leq 2\Theta \leq 59.992$	$3.986 \leq 2\Theta \leq 54.968$
Index ranges	$-18 \leq h \leq 18$, $-22 \leq k \leq 22$, $-39 \leq l \leq 39$	$-13 \leq h \leq 13$, $-17 \leq k \leq 17$, $-17 \leq l \leq 17$
Reflections collected	58008	28240
Independent reflections	8550 [R_{int} = 0.0385, R_{sigma} = 0.0285]	7545 [R_{int} = 0.0556, R_{sigma} = 0.0727]
Data/restraints/parameters	8550/0/325	7545/0/347
Goodness-of-fit on F^2	1.026	0.992
Final R indexes [I ≥ 2σ (I)]	R_1 = 0.0263, wR_2 = 0.0528	R_1 = 0.0329, wR_2 = 0.0547
Final R indexes [all data]	R_1 = 0.0386, wR_2 = 0.0555	R_1 = 0.0622, wR_2 = 0.0598
Largest diff. peak/hole / e Å^{-3}	0.59/–0.53	0.58/–0.61

	11	**12** · 5{**3**}*
Formula	$Cp_2NbMe(NDipp)$	$Cp_2Nb(NDipp)(PCO)\cdot 5\{Cp_2NbCl(NDipp)\}$
Internal identification code	18srv112	18srv005
Empirical formula	$C_{23}H_{30}NNb$	$C_{22.16}H_{27}Cl_{0.83}NNbO_{0.17}P_{0.17}$
Formula weight / g mol^{-1}	413.39	437.69
Temperature / K	120	273.15
Crystal system	triclinic	monoclinic
Space group	P-1	$P2_1/n$
a / Å	14.5570(8)	10.3885(4)
b / Å	17.2854(11)	17.6165(6)
c / Å	18.2998(12)	11.1398(4)
α / °	117.868(2)	90
β / °	91.307(3)	90.2980(14)
γ / °	90.070(2)	90
Volume / Å^3	4069.2(4)	2038.66(13)
Z	8	4
ρ_{calc}g / cm^3	1.35	1.426
μ / mm^{-1}	0.596	0.718
F(000)	1728	904
Crystal size / mm^3	0.1 × 0.2 × 0.2	0.312 × 0.178 × 0.052
Radiation	MoKα (λ = 0.71073)	MoKα (λ = 0.71073)
Data collection range / °	$4.442 \le 2\Theta \le 54.97$	$4.326 \le 2\Theta \le 61.012$
Index ranges	$-18 \le h \le 18$, $-22 \le k \le 22$, $-23 \le l \le 23$	$-14 \le h \le 14$, $-25 \le k \le 24$, $-15 \le l \le 15$
Reflections collected	71755	46222
Independent reflections	18633 [R_{int} = 0.0563, R_{sigma} = 0.0805]	6212 [R_{int} = 0.0482, R_{sigma} = 0.0354]
Data/restraints/parameters	18633/1264/997	6212/0/279
Goodness-of-fit on F^2	1.041	1.042
Final R indexes [I ≥ 2σ (I)]	R_1 = 0.0423, wR_2 = 0.0881	R_1 = 0.0309, wR_2 = 0.0641
Final R indexes [all data]	R_1 = 0.0744, wR_2 = 0.0975	R_1 = 0.0521, wR_2 = 0.0690
Largest diff. peak/hole / e Å^{-3}	0.98/–0.65	0.85/–0.75

* Complexes **12** and **3** co-crystallised in a 1:5 molar ratio.

	[**13**]OTf · DCM	[**13**]BAr^F_4
Formula	$[Cp_2NbCl(NHDipp)]OTf{\cdot}DCM$	$[Cp_2NbCl(NHDipp)]BAr^F_4$
Internal identification code	19srv084	18srv502
Empirical formula	$C_{24}H_{30}Cl_3F_3NNbO_3S$	$C_{54}H_{40}BClF_{24}NNb$
Formula weight / g mol^{-1}	668.81	1298.04
Temperature / K	120	120
Crystal system	monoclinic	triclinic
Space group	$P2_1/c$	P-1
a / Å	10.4701(9)	13.823(2)
b / Å	14.0755(12)	14.866(2)
c / Å	18.9388(17)	28.719(4)
α / °	90	91.722(4)
β / °	100.640(3)	92.323(6)
γ / °	90	115.761(5)
Volume / Å^3	2743.1(4)	5302.9(14)
Z	4	4
ρ_{calc}g / cm^3	1.619	1.626
μ / mm^{-1}	0.855	0.401
F(000)	1360	2600
Crystal size / mm^3	0.42 × 0.081 × 0.036	0.332 × 0.3 × 0.283
Radiation	MoKα (λ = 0.71073)	MoKα (λ = 0.71073)
Data collection range / °	$3.958 \leq 2\Theta \leq 59$	$4.208 \leq 2\Theta \leq 52$
Index ranges	$-14 \leq h \leq 14$, $-19 \leq k \leq 19$, $-26 \leq l \leq 26$	$-17 \leq h \leq 17$, $-16 \leq k \leq 18$, $-35 \leq l \leq 35$
Reflections collected	53540	56599
Independent reflections	7651 [R_{int} = 0.0597, R_{sigma} = 0.0408]	20740 [R_{int} = 0.0454, R_{sigma} = 0.0693]
Data/restraints/parameters	7651/0/337	20740/131/1614
Goodness-of-fit on F^2	1.029	1.07
Final R indexes [I ≥ 2σ (I)]	R_1 = 0.0372, wR_2 = 0.0879	R_1 = 0.0446, wR_2 = 0.0984
Final R indexes [all data]	R_1 = 0.0559, wR_2 = 0.0957	R_1 = 0.0773, wR_2 = 0.1067
Largest diff. peak/hole / e Å^{-3}	1.28/–0.82	0.69/–0.54

	15	**17**
Formula	$TrBAr^{F}_{4}$	$Cp_2NbCl(NDipp^{Tr})$
Internal identification code	18srv467	19srv177
Empirical formula	$C_{51}H_{27}BF_{24}$	$C_{41}H_{41}ClNNb$
Formula weight / g mol^{-1}	1106.53	676.11
Temperature / K	120	120
Crystal system	monoclinic	monoclinic
Space group	$P2_1/n$	$P2_1/n$
a / Å	14.3673(5)	10.7932(9)
b / Å	18.7596(6)	9.3584(8)
c / Å	18.1481(6)	32.934(3)
α / °	90	90
β / °	107.5557(19)	98.788(3)
γ / °	90	90
Volume / Å^3	4663.5(3)	3287.5(5)
Z	4	4
ρ_{calc}g / cm^3	1.576	1.366
μ / mm^{-1}	1.423	0.478
F(000)	2216	1408
Crystal size / mm^3	0.41 × 0.06 × 0.03	0.258 × 0.082 × 0.081
Radiation	CuKα (λ = 1.54178)	MoKα (λ = 0.71073)
Data collection range / °	$6.918 \leq 2\Theta \leq 135.994$	$4.196 \leq 2\Theta \leq 54.998$
Index ranges	$-17 \leq h \leq 17$, $-22 \leq k \leq 21$, $-20 \leq l \leq 21$	$-14 \leq h \leq 14$, $-12 \leq k \leq 12$, $-42 \leq l \leq 42$
Reflections collected	59482	49760
Independent reflections	8227 [R_{int} = 0.1238, R_{sigma} = 0.0998]	7544 [R_{int} = 0.0600, R_{sigma} = 0.0570]
Data/restraints/parameters	8227/267/704	7544/0/406
Goodness-of-fit on F^2	1.045	1.223
Final R indexes [I ≥ 2σ (I)]	R_1 = 0.0940, wR_2 = 0.2216	R_1 = 0.0485, wR_2 = 0.1043
Final R indexes [all data]	R_1 = 0.1647, wR_2 = 0.2603	R_1 = 0.0597, wR_2 = 0.1082
Largest diff. peak/hole / e Å^{-3}	0.67/–0.61	0.67/–1.06

	[**18**][$BAr^F{}_4$]$_2$	**20**
Formula	[{Cp_2NbCl}$_2$(N{2,6-^{i}Pr$_2$C$_6$H$_2$}$_2$-N)][$BAr^F{}_4$]$_2$	{Cp_2NbCl}$_2$(N{2,6-^{i}Pr$_2$C$_6$H$_2$}$_2$N)
Internal identification code	18srv406	19srv036
Empirical formula	$C_{108}H_{74}B_2Cl_2F_{48}N_2Nb_2$	$C_{44}H_{52}Cl_2N_2Nb_2$
Formula weight / g mol^{-1}	2590.03	865.59
Temperature / K	120	120
Crystal system	triclinic	orthorhombic
Space group	P-1	Pbca
a / Å	13.3827(15)	12.4216(7)
b / Å	14.0398(17)	15.9886(9)
c / Å	15.6424(18)	19.7990(11)
α / °	78.601(3)	90
β / °	82.165(3)	90
γ / °	70.389(3)	90
Volume / Å^3	2706.2(5)	3932.2(4)
Z	1	4
ρ_{calc}g / cm^3	1.589	1.462
μ / mm^{-1}	0.393	0.752
F(000)	1294	1784
Crystal size / mm^3	0.201 × 0.147 × 0.025	0.539 × 0.077 × 0.035
Radiation	MoKα (λ = 0.71073)	MoKα (λ = 0.71073)
Data collection range / °	4.348 ≤ 2Θ ≤ 50.268	4.114 ≤ 2Θ ≤ 57.998
Index ranges	–15 ≤ h ≤ 15, –16 ≤ k ≤ 16, –18 ≤ l ≤ 18	–16 ≤ h ≤ 16, –21 ≤ k ≤ 21, –24 ≤ l ≤ 27
Reflections collected	42852	45611
Independent reflections	9624 [R_{int} = 0.0870, R_{sigma} = 0.0940]	5230 [R_{int} = 0.0794, R_{sigma} = 0.0568]
Data/restraints/parameters	9624/66/767	5230/0/235
Goodness-of-fit on F^2	1.026	1.053
Final R indexes [I ≥ 2σ (I)]	R_1 = 0.0787, wR_2 = 0.1726	R_1 = 0.0358, wR_2 = 0.0639
Final R indexes [all data]	R_1 = 0.1316, wR_2 = 0.1966	R_1 = 0.0658, wR_2 = 0.0725
Largest diff. peak/hole / e Å^{-3}	1.27/–0.82	0.57/–0.62

APPENDIX 2: Determination of magnetic susceptibility by Evans' method

Experimental and calculation details of Evans' method[198] are outlined below.

For each run: Inside a N_2-filled glovebox, an empty sample vial and lid were placed on a balance and then tared. A portion (~20 mg) of the 1:2 mixture of [**18**][$BAr^F{}_4$]$_2$ and [**13**]$BAr^F{}_4$ was transferred to this sample vial, which was subsequently resealed and returned to the balance for reweighing (to provide *m*) and then re-taring. CD_2Cl_2 (~0.7 ml) was transferred *via* pipette into the solid-containing sample vial, and the vial was resealed, placed on the balance and reweighed (to provide m_{solv}). The sealed sample vial was agitated (for ~5 min) until the solid had completely dissolved. The resulting solution was rapidly transferred *via* pipette to a Young's NMR tube containing a CD_2Cl_2 lock-tube, following which the NMR tube was promptly sealed for removal from the glovebox. ^{1}H NMR spectroscopic analysis was performed on the sample solution, where the temperature (*T*) was recorded and the frequency difference ($\Delta\nu$) measured between the two ^{1}H signals attributable to residual *protio* NMR solvent (at ~5.3 ppm).

A typical ^{1}H NMR spectrum (400 MHz, CD_2Cl_2, CD_2Cl_2 lock-tube) of the paramagnetic sample solution is shown below (LEFT), displaying the two ^{1}H resonances resulting from residual *protio* solvent inside and outside the lock-tube (separated by $\Delta\nu$). The equations below (RIGHT) were used to determine the effective magnetic moment (μ_{eff}) from the experimental parameters.

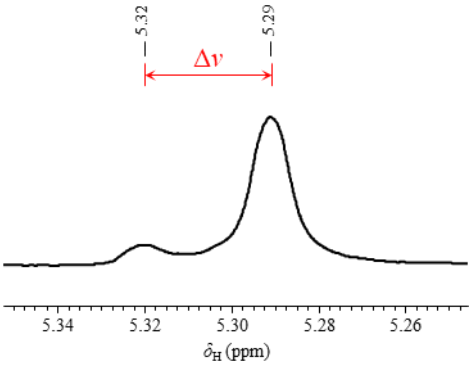

$$\mu_{\text{eff}} = 2.84\sqrt{\chi_{\text{n}}' \cdot T}$$

$$\chi_{\text{n}}' = \chi_{\text{n}} + \chi_{\text{d}}$$

$$\chi_{\text{n}} = M \cdot \chi_{\text{m}}$$

$$\chi_{\text{m}} = \frac{3|\Delta\nu|}{4\pi f c_i} + \chi_{\text{m,solv}}$$

$$c_i = \frac{m_i}{V_{\text{solv}}}$$

$$m_i = m \cdot \frac{M_i}{M}$$

$$V_{\text{solv}} = \frac{m_{\text{solv}}}{\rho_{\text{solv}}}$$

The parameters used in the equations above are defined in the table below and, where constant, the values are also provided.

Parameter		Definition	Value
μ_{eff}	/ μ_{B}	Effective magnetic moment	
c_i	/ g cm^{-3}	Mass concentration of paramagnetic component (**18**$^{2+}$)	
f	/ Hz	NMR spectrometer frequency	400.07 × 10^{6}
m	/ g	Total mass of sample	
m_i	/ g	Mass of paramagnetic component (**18**$^{2+}$) in sample	
m_{solv}	/ g	Mass of NMR solvent (CD_2Cl_2)	
M	/ g mol^{-1}	Total relative molecular weight of sample	5,188.17
M_i	/ g mol^{-1}	Relative molecular mass of paramagnetic component (**18**$^{2+}$)	865.63
ρ_{solv}	/ g cm^{-3}	Density of NMR solvent (CD_2Cl_2)	1.362
T	/ K	Temperature	
V_{solv}	/ cm^3	Volume of NMR solvent (CD_2Cl_2)	
$\Delta\nu$	/ Hz	Observed change in frequency of residual *protio* signal	
$\chi_{\text{m,solv}}$	/ cm^3 g^{-1}	Mass susceptibility of NMR solvent (CD_2Cl_2)	–5.38 × 10^{-7}
χ_{d}	/ cm^3 mol^{-1}	Diamagnetic contribution to molar magnetic susceptibility of all components (1 × **18**$^{2+}$, 2 × **13**$^{+}$ and 4 × [BAr$^{\text{F}}{}_4$]$^{-}$)[228]	–2.93644 × 10^{-3}
χ_{m}	/ cm^3 g^{-1}	Mass magnetic susceptibility	
χ_{n}	/ cm^3 mol^{-1}	Uncorrected molar magnetic susceptibility	
χ_{n}'	/ cm^3 mol^{-1}	Corrected molar magnetic susceptibility	

For comparison with μ_{eff}, the spin-only magnetic moment ($\mu_{\text{s.o.}}$) may be calculated from the total spin quantum number (S) of the complex:

$$\mu_{\text{s.o.}} = \sqrt{4S\,(S+1)}$$

APPENDIX 3: Seminars, symposia and conferences attended

APPENDIX 3.1: Seminars attended

"Sustainability in industrial chemistry"
John Hayler (GlaxoSmithKline)
04 November 2015

"Transition metal catalysis"
Katherine Wheelhouse (GlaxoSmithKline)
04 November 2015

"Biocatalysis"
Keith Mulholland (AstraZeneca)
04 November 2015

"Biorenewable feedstocks and chemicals"
Jeroen ten Dam (Johnson Matthey)
04 November 2015

"Sustainability, green chemistry, solvent guide"
Helen Sneddon (GlaxoSmithKline)
05 November 2015

"Sustainable agrochemical manufacturing"
George Hodges (Syngenta)
05 November 2015

"Sustainability in research and development"
Matt Grist (AstraZeneca)
05 November 2015

"A view-master look at catalyst driven advances in sustainable polymer synthesis"
Michael Shaver (University of Edinburgh, UK)
11 November 2015

"New main-group metal mediated strategies for ring functionalisation"
Eva Hevia (University of Strathclyde, UK)
18 November 2015

"Using organometallics as catalysts: From drug precursors to little black dresses"
Patrick McGowan (University of Leeds, UK)
27 January 2016

"Transition metal catalyzed borylation of C–H and C–X bonds: Synthesis of aryl and alkyl boronates"
Todd Marder (JMU Würzburg, Germany)
01 February 2016

"Solid-state NMR studies of quadrupolar nuclei"
Karen Johnston (Durham University, UK)
16 February 2016

"New and disruptive NMR methods"
Juan Aguilar Malavia (Durham University, UK)
16 February 2016

"Women in science: What has chemistry done for me?"
Lesley Yellowlees (University of Edinburgh, UK)
16 March 2016

"Energy materials: Structural chemistry of fast ion conductors for solid oxide fuel cells"
Ivana Evans (Durham University, UK)
16 March 2016

"Chemistry with binary main group metal aggregates"
Stefanie Dehnen (Philipps-Universität Marburg, Germany)
16 March 2016

"Hydroboration of CO_2: From understanding to complex transformations"
Sébastien Bontemps (LCC Toulouse, France)
03 May 2016

"Alkynes: A chemical Swiss army knife"
Alison Hulme (University of Edinburgh, UK)
10 May 2016

"Challenges and opportunities in natural product synthesis" (Musgrave Lecture)
Steven Ley (University of Cambridge, UK)
18 May 2016

"Substituent effects on TADF molecules for OLED applications"
Jonathan Ward (Durham University, UK)
21 October 2016

"Sodium phosphaethynolate Na(OCP) as a building block"
Dominikus Heift (Durham University, UK)
21 October 2016

"3D graphene foams via soft templated metal monoliths"
David Johnson (Durham University, UK)
04 November 2016

"The magnificent seven: From luminescent cycloheptatrienes to shapeshifting cations"
Paul McGonigal (Durham University, UK)
04 November 2016

"New luminescent platinum and palladium complexes of 1,2,4-triazole and tetrazole ligands"
Melissa Walden (Durham University, UK)
18 November 2016

"The synthesis and analysis of potential histone deacetylase inhibitors from piano-stool complexes"
Jasmine Cross (Durham University, UK)
18 November 2016

"Heterogeneous ethylene trimerisation catalysis: Probing catalytic behaviour and reaction mechanism"
Michael Lamb (Durham University, UK)
18 November 2016

"Diarylhydrazide-bridged cyclometallated diiridium phosphors and their matrix-dependent emission properties"
Daniel Congrave (Durham University, UK)
18 November 2016

"Development of Au- and Pd-catalysed reactions"
Ai-Lan Lee (Heriot-Watt University, UK)
23 November 2016

"HD or not HD? That is the question"
Alan Kenwright (Durham University, UK)
25 November 2016

"Nanoscale structures from supramolecular assembly of molecular magnets"
Richard Winpenny (University of Manchester, UK)
25 January 2017

"A new dimension in metal-organic chemistry"
Jonathan Foster (University of Sheffield, UK)
03 February 2017

"Successive ring expansion: From ball-in-a-cup to macrocycles with medicinal applications"
Will Unsworth (University of York, UK)
03 February 2017

"Ionic liquids: Solvents for sustainable chemistry"
Tom Welton (Imperial College London, UK)
06 February 2017

"Developing heterobimetallic hydrides for catalysis"
Mark Crimmin (Imperial College London, UK)
08 February 2017

"Novel routes to generate molecular and nanoparticle-containing nanomaterials"
Tom Chamberlain (University of Leeds, UK)
10 March 2017

"Catalytic biomass conversions in a lignocellulosic biorefinery"
Bert Sels (KU Leuven, Belgium)
15 March 2017

"Exploiting the 'chemical memory' of materials to create new processes"
Ian Metcalfe (Newcastle University, UK)
10 May 2017

"Charge localisation vs. delocalisation in tetranuclear mixed-valence complexes: A spectroscopic study"
Claude Lapinte (Université de Rennes 1, France)
17 May 2017

"Fluorescent retinoids for cell biology and beyond"
David Chrisholm (Durham University, UK)
17 May 2017

"Fluorenyl-porphyrin dendrimers for optics"
Christine Paul-Roth (Université de Rennes 1, France)
17 May 2017

"Solid-state NMR studies of battery materials"
Karen Johnston (Durham University, UK)
17 May 2017

"Transformations of π-arene Ru complexes"
Jack Pike (Durham University, UK)
17 May 2017

"Boron-substituted helicenes: Synthesis, functionalisation and future prospects in catalysis"
Fabienne Berrée (Université de Rennes 1, France)
17 May 2017

"Generation of skeletal diversity and complexity from boron-substituted 1,3-dienes and nitroso compounds"
Benjamin François (Université de Rennes 1, France)
17 May 2017

"On the move: Molecular rearrangement and macroscopic transport"
Matthew Kitching (Durham University, UK)
17 May 2017

"Theoretical studies of organometallic quantum cellular automata: From charge localization to information transfer"
Thomas Groizard (Université de Rennes 1, France)
17 May 2017

"Alkane activation and functionalisation in zeolites: towards understanding the role of extra-framework metal and zeolite framework type"
Russell Taylor (Durham University, UK)
17 May 2017

"Controlling the deep-red emission in diplatinum complexes"
Véronique Guerchais (Université de Rennes 1, France)
17 May 2017

"The atmosphere's detergent"
Marsha Lester (University of Pennsylvania, USA)
19 June 2017

"Conversion of lignin to functionalised alkylphenols over heterogeneous catalysts"
David Jackson (University of Glasgow, UK)
17 July 2017

"The catalytic production of chemicals from waste bio-oils"
David Cole-Hamilton (University of St Andrews, UK)
17 July 2017

"Modelling, synchrotron radiation and neutron scattering studies of structure, dynamics and reactivity in catalytic systems"
Richard Catlow (University College London, UK)
19 July 2017

"Catalyst characterisation"
Steve Bailey (Johnson-Matthey)
20 July 2017

"Order and disorder in modern materials chemistry"
Andrew Goodwin (University of Oxford, UK)
29 August 2017

"Catalysis on the edge"
Robert Tooze (Sasol)
29 August 2017

"Sustainable manufacturing of functional material"
Claire Carmait (University College London, UK)
30 August 2017

"Wide bite angle phosphine ligands in catalysis: From molecular complexes to nanoparticles"
Piet van Leeuwen (INAS Toulouse, France)
30 August 2017

"Regioselective functionalisation of aromatic and heteroaromatic compounds using organometallic reagents"
Giuliano Cesar Clososki (Universidade de São Paulo, Brazil)
29 September 2017

"Casting iron in softer catalytic roles"
Robin Bedford (University of Bristol, UK)
25 October 2017

"Disorder in inorganic solids: Exploiting multinuclear NMR spectroscopy and DFT calculations"
Sharon Ashbrook (University of St Andrews, UK)
01 November 2017

"In situ EXAFS studies of electrocatalysts for direct alcohol fuel cells"
Andrea Russell (University of Southampton, UK)
17 January 2018

"Catalysis for challenging C–H bond activation"
Uwe Schneider (University of Edinburgh, UK)
20 February 2018

"f-Elements as a playground of magnetic phenomena"
Nicholas Chilton (University of Manchester, UK)
09 April 2018

"What has Eu revealed in 15 years?"
Robert Pal (Durham University, UK)
09 April 2018

"The importance of questioning scientific assumptions: Lessons from the rare-earth and actinide metals" (RSC Centenary Lecture)
William Evans (University of California, USA)
09 April 2018

"Transition-metal catalysed enyne cascade reactions"
Na Wu (Guangxi Normal University, China)
04 May 2018

"Transition metal catalyzed C–H bond functionalization: Applications to the synthesis of life and material molecules"
Jean-Françoise Soulé (Université de Rennes 1, France)
04 May 2018

"From materials to cosmology: Studying the early universe under the microscope"
Nicola Spaldin (ETH Zürich, Switzerland)
05 June 2018

"The fixation with fixation: Chemical transformations of N_2"
Sven Schneider (Georg-August-Universität Göttingen, Germany)
02 July 2018

"The modular synthesis of rare earth-transition metal complexes utilizing a redox-active ligand"
Joy Farnaby (University of Glasgow, UK)
02 July 2018

"Cation-disordered cathodes for Li-ion battery cathodes"
Alex Urban (University of St Andrews, UK)
02 July 2018

"Catalysis for sustainable chemical processes"
Mike Watson (Johnson Matthey)
02 July 2018

"Bi-functional pnictogen cage catalysts: Understanding the reactivity of phosphabismatranes"
Dominikus Heift (Durham University, UK)
02 July 2018

"Catalytic applications of designer ligand-supported iron and aluminium complexes"
Jennifer Gardens (University of Edinburgh, UK)
02 July 2018

"Magnesium aluminate complexes for rechargeable battery electrolytes"
Stuart Robertson (University of Strathclyde, UK)
02 July 2018

"Design of advanced materials?"
Matthew Rosseinsky, FRS (University of Liverpool, UK)
02 July 2018

"Large single crystals for the exploration of structure and function in solid-state energy materials"
Josie Auckett (Durham University, UK)
02 July 2018

"Discrete polymetallic complexes and their application in the ROP of lactide"
Ruaraidh McIntosh (Herriot-Watt University, UK)
02 July 2018

"Be practical! Homogeneous catalysis for a sustainable future"
Matthias Beller (Leibniz-Institut für Katalyse, Germany)
15 July 2018

"Transition-metal-catalyzed asymmetric direct transformations of aromatic compounds"
Shu-Li You (Shanghai Institute of Organic Chemistry, China)
16 July 2018

"The development of organometallic anticancer drugs that operate via epigenetic mechanisms"
Paul Dyson (École polytechnique fédérale de Lausanne, Switzerland)
16 July 2018

"Sustainable catalysis based on metal-ligand cooperation"
David Milstein (Weizmann Institute of Science, Israel)
17 July 2018

"Ru- and Ir-catalyzed hydrogen transfer and amine sp^3 C–H bond functionalization"
Christian Bruneau (Université de Rennes 1, France)
17 July 2018

"Catalytic functionalization with small and large catalysts"
John Hartwig (University of California, USA)
18 July 2018

"Rare-earth and early transition-metal complexes for novel chemical transformations"
Zhaomin Hou (RIKEN Center for Sustainable Resource Science, Japan)
18 July 2018

"Luminescent platinum(II) complexes: Assemblies, sensing and artificial viruses"
Luisa De Cola (Université de Strasbourg, France)
19 July 2018

"Exploring catalytic space with metal-based systems"
Ben Feringa (Rijksuniversiteit Groningen, Netherlands)
19 July 2018

"Challenging hybrid interfaces: Magnetic molecules on surfaces"
Roberta Sessoli (Università degli Studi di Firenze, Italy)
20 July 2018

"Theory meets experiments: The chemistry of P-containing anions"
Zoltán Benkő (Budapest University of Technology and Economics, Hungary)
31 January 2019

"Cooperative catalysis: From frustrated Lewis pairs to advanced biofuels"
Duncan Wass (Cardiff University, UK)
20 February 2019

"Changing the landscape: Prospects for NMR and MRI through SABRE"
Simon Duckett (University of York, UK)
27 February 2019

"Teflon-coated molecules: Electronic structure and reactivity"
Linda Doerrer (Boston University, USA)
20 March 2019

"Exploring computation with chemical reactions"
Lee Cronin (University of Glasgow, UK)
01 May 2019

"Main group metallocenes: Beyond transmetallation"
André Schäfer (Universität des Saarlandes, Germany)
26 May 2020

"The impact of central elements and ligands on structure, Lewis acidity and stability of p-block catecholates"
Lutz Greb (Ruprecht-Karls-Universität Heidelberg, Germany)
26 May 2020

"Carbenes as building blocks for organic electronics"
Dominik Munz (Universität des Saarlandes, Germany)
26 May 2020

"Spectroelectrochemistry: From electrochemical mechanism to reactivity"
Mark Ringenberg (Universität Stuttgart, Germany)
26 May 2020

"Ambiphilic PEP ligands for homogeneous transition metal catalysis"
Michael Tauchert (RWTH Aachen University, Germany)
02 June 2020

"Photocatalytic CO_2 reduction with dinuclear rhenium complexes: Are two metals better than one?"
Matthias Schwalbe (Humboldt-Universität zu Berlin, Germany)
02 June 2020

"Triphosphiranes: Trimers of phosphinidenes"
Christian Hering-Junghans (Leibniz-Institut für Katalyse, Germany)
02 June 2020

"Zirconium in the spotlight: Photochemistry with d^0 metals"
Carsten Milsmann (West Virginia University, USA)
02 June 2020

"The effects of exchange on NMR"
Juan Aguilar Malavia (Durham University, UK)
08 June 2020

"Bismuth compounds in radical reactions: Reactive species and catalytic applications"
Crispin Lichtenberg (JMU Würzburg, Germany)
09 June 2020

"Reductive elimination: Are oxidation state changes in elementary organometallic mechanisms always clear-cut?"
Johannes Klein (Rijksuniversiteit Groningen, Netherlands)
09 June 2020

"The versatile coordination chemistry of 2,2'-diphosphinotolanes"
Joachim Ballmann (Ruprecht-Karls-Universität Heidelberg, Germany)
09 June 2020

"Lanthanides and actinides: Biologically relevant"
Lena Daumann (LMU München, Germany)
09 June 2020

"Macrocyclic NHC ligand platforms in supramolecular organometallics"
Alexander Pöthig (TU München, Germany)
16 June 2020

"Amido-substituted silicon and germanium clusters"
Felicitas Lips (WWU Münster, Germany)
16 June 2020

"Replacing UV photochemistry by novel visible-light driven 2-photon mechanisms"
Christoph Kerzig (Universität Basel, Switzerland)
16 June 2020

"Molecular switches and chemosensors based on valence tautomeric metal complexes"
Marat Khusniyarov (FAU Erlangen-Nürnberg, Germany)
16 June 2020

"C–H bond activation by trigonal imido and amido cobalt complexes"
Gunnar Werncke (Philipps-Universität Marburg, Germany)
23 June 2020

"Turn-on fluorescence sensors based on dynamic intramolecular N→B-coordination
Frank Pammer (Universität Ulm, Germany)
23 June 2020

"Mimicking photosynthesis in phospholipid bilayers"
Andrea Pannwitz (Universität Ulm, Germany)
23 June 2020

"Pyrazinediimine iron complexes: Redox chemistry, unconventional carbenes and reversible C–C bond formation"
Dragoş-Adrian Roşca (Ruprecht-Karls-Universität Heidelberg, Germany)
23 June 2020

APPENDIX 3.2: Symposia and conferences attended

RSC Sustainability in Industrial Chemistry Symposium and Workshop
Durham University, UK
04–05 November 2015

Inorganic Chemistry in Action in British Science Week Symposium
Durham University, UK
16 March 2016

Annual Chemistry Postgraduate Symposium 2016
Durham University, UK
15 June 2016

One-Day Joint Rennes-Durham Symposium
Durham University, UK
17 May 2017

Annual Chemistry Postgraduate Symposium 2017
Durham University, UK
15 June 2017
Poster presentation: *"Synthesis and reduction of niobium cyclopentadienyl imido complexes"*
Prize awarded: Best second-year poster

Catalysis Fundamentals and Practice Summer School
University of Liverpool, UK
17–21 July 2017
Poster presentation: *"Synthesis and reduction of niobium cyclopentadienyl imido complexes"*

Universities of Scotland Inorganic Chemistry (USIC) Conference 2017
University of St Andrews, UK
29–30 August 2017
Poster presentation: *"Synthesis and reduction of niobium cyclopentadienyl imido complexes"*

RSC Centenary Lecture Symposium
Durham University, UK
09 April 2018

Annual Chemistry Postgraduate Symposium 2018
Durham University, UK
21 June 2018
Oral presentation: *"Synthesis and reactivity of cyclopentadienyl imido complexes of niobium"*

RSC Scottish Dalton Meeting 2018
Durham University, UK
02 July 2018

28th International Conference on Organometallic Chemistry (ICOMC) 2018
Florence, Italy
15–20 July 2018
Poster presentation: *"Synthesis and reactivity of niobium bis(cyclopentadienyl) imido complexes"*

REFERENCES

1. W. A. Nugent and J. M. Mayer, *Metal-Ligand Multiple Bonds*, Wiley, New York, 1988.
2. D. E. Wigley, in *Progress in Inorganic Chemistry, Volume 42*, ed. K. D. Karlin, John Wiley & Sons, Inc., Hoboken, NJ, USA, 1994, vol. 42, pp. 239–482.
3. J. D. Burrington, C. T. Kartisek and R. K. Grasselli, *J. Catal.*, 1984, **87**, 363–380.
4. D. M. T. Chan and W. A. Nugent, *Inorg. Chem.*, 1985, **24**, 1422–1424.
5. D. M. T. Chan, W. C. Fultz, W. A. Nugent, D. C. Roe and T. H. Tulip, *J. Am. Chem. Soc.*, 1985, **107**, 251–253.
6. J. Belgacem, J. Kress and J. A. Osborn, *J. Chem. Soc. Chem. Commun.*, 1993, 1125.
7. W. R. H. Wright, A. S. Batsanov, A. M. Messinis, J. A. K. Howard, R. P. Tooze, M. J. Hanton and P. W. Dyer, *Dalton Trans.*, 2012, **41**, 5502–5511.
8. A. M. Messinis, W. R. H. Wright, A. S. Batsanov, J. A. K. Howard, M. J. Hanton and P. W. Dyer, *ACS Catal.*, 2018, **8**, 11235–11248.
9. A. M. Messinis, A. S. Batsanov, W. R. H. Wright, J. A. K. Howard, M. J. Hanton and P. W. Dyer, *ACS Catal.*, 2018, **8**, 11249–11263.
10. A. M. Messinis, A. S. Batsanov, J. A. K. Howard, M. J. Hanton and P. W. Dyer, *ChemCatChem*, 2019, **11**, 1756–1764.
11. J. Chatt, J. R. Dilworth and R. L. Richards, *Chem. Rev.*, 1978, **78**, 589–625.
12. D. Mansuy, P. Battioni and J. P. Mahy, *J. Am. Chem. Soc.*, 1982, **104**, 4487–4489.
13. V. C. Gibson, in *Modern Coordination Chemistry*, eds. N. Winterton and J. Leigh, Royal Society of Chemistry, Cambridge, 2002, pp. 140–153.
14. W. A. Nugent and B. L. Haymore, *Coord. Chem. Rev.*, 1980, **31**, 123–175.
15. A. A. Danopoulos and G. Wilkinson, *Polyhedron*, 1990, **9**, 1009–1010.
16. M. L. H. Green, *J. Organomet. Chem.*, 1995, **500**, 127–148.
17. W. A. Nugent, R. L. Harlow and R. J. McKinney, *J. Am. Chem. Soc.*, 1979, **101**, 7265–7268.

18. B. L. Haymore, E. A. Maatta and R. A. D. Wentworth, *J. Am. Chem. Soc.*, 1979, **101**, 2063–2068.

19. J. T. Anhaus, T. P. Kee, M. H. Schofield and R. R. Schrock, *J. Am. Chem. Soc.*, 1990, **112**, 1642–1643.

20. P. Barrie, T. A. Coffey, G. D. Forster and G. Hogarth, *J. Chem. Soc. Dalton Trans.*, 1999, 4519–4528.

21. K. C. Chew, W. Clegg, M. P. Coles, M. R. J. Elsegood, V. C. Gibson, A. J. P. White and D. J. Williams, *J. Chem. Soc. Dalton Trans.*, 1999, 2633–2640.

22. A. Bell, W. Clegg, P. W. Dyer, M. R. J. Elsegood, V. C. Gibson and E. L. Marshall, *J. Chem. Soc. Chem. Commun.*, 1994, 2247–2248.

23. A. S. Batsanov, A. E. Goeta, J. A. K. Howard, A. K. Hughes, A. L. Johnson and K. Wade, *J. Chem. Soc. Dalton Trans.*, 2001, **2**, 1210–1217.

24. F. H. Allen, *Acta Cryst. B*, 2002, **58**, 380–388.

25. A. A. Danopoulos, G. Wilkinson, T. K. N. Sweet and M. B. Hursthouse, *J. Chem. Soc. - Dalt. Trans.*, 1996, 271–281.

26. H. K. Hall, *J. Am. Chem. Soc.*, 1957, **79**, 5441–5444.

27. D. L. Morrison, P. M. Rodgers, Y.-W. Chao, M. A. Bruck, C. Grittini, T. L. Tajima, S. J. Alexander, A. L. Rheingold and D. E. Wigley, *Organometallics*, 1995, **14**, 2435–2446.

28. A. A. Danopoulos, G. Wilkinson, T. K. N. Sweet and M. B. Hursthouse, *J. Chem. Soc., Dalton Trans.*, 1996, 2995–3000.

29. C. Cárdenas, F. Heidar-Zadeh and P. W. Ayers, *Phys. Chem. Chem. Phys.*, 2016, **18**, 25721–25734.

30. A. A. Danopoulos, G. Wilkinson, T. K. N. Sweet and M. B. Hursthouse, *J. Chem. Soc. Dalton Trans.*, 1995, 937–950.

31. J. Chatt, J. R. Dilworth and G. J. Leigh, *J. Chem. Soc. A Inorganic, Phys. Theor.*, 1970, 2239.

32. J. Chatt, R. J. Dosser, F. King and G. J. Leigh, *J. Chem. Soc. Dalton Trans.*, 1976, 2435.

33. D. S. Glueck, F. J. Hollander and R. G. Bergman, *J. Am. Chem. Soc.*, 1989, **111**, 2719–2721.

34. D. S. Glueck, J. Wu, F. J. Hollander and R. G. Bergman, *J. Am. Chem. Soc.*, 1991, **113**, 2041–

2054.

35. J. de With, A. D. Horton and A. G. Orpen, *Organometallics*, 1993, **12**, 1493–1496.

36. C. C. Cummins, S. M. Baxter and P. T. Wolczanski, *J. Am. Chem. Soc.*, 1988, **110**, 8731–8733.

37. J. L. Bennett and P. T. Wolczanski, *J. Am. Chem. Soc.*, 1994, **116**, 2179–2180.

38. J. L. Bennett and P. T. Wolczanski, *J. Am. Chem. Soc.*, 1997, **119**, 10696–10719.

39. T. R. Cundari, T. R. Klinckman and P. T. Wolczanski, *J. Am. Chem. Soc.*, 2002, **124**, 1481–1487.

40. T. R. Cundari, *J. Am. Chem. Soc.*, 1994, **116**, 340–347.

41. J. Y. Saillard and R. Hoffmann, *J. Am. Chem. Soc.*, 1984, **106**, 2006–2026.

42. P. T. Wolczanski, *Organometallics*, 2018, **37**, 505–516.

43. J. Scott, F. Basuli, A. R. Fout, J. C. Huffman and D. J. Mindiola, *Angew. Chemie - Int. Ed.*, 2008, **47**, 8502–8505.

44. J. Chu, E. Lu, Z. Liu, Y. Chen, X. Leng and H. Song, *Angew. Chemie Int. Ed.*, 2011, **50**, 7677–7680.

45. T. Chu, W. E. Piers, J. L. Dutton and M. Parvez, *Organometallics*, 2013, **32**, 1159–1165.

46. J. Chu, X. Han, C. E. Kefalidis, J. Zhou, L. Maron, X. Leng and Y. Chen, *J. Am. Chem. Soc.*, 2014, **136**, 10894–10897.

47. C. P. Schaller and P. T. Wolczanski, *Inorg. Chem.*, 1993, **32**, 131–144.

48. D. F. Schafer and P. T. Wolczanski, *J. Am. Chem. Soc.*, 1998, **120**, 4881–4882.

49. Y. W. Ge and P. R. Sharp, *J. Am. Chem. Soc.*, 1990, **112**, 3667–3668.

50. Y. W. Ge and P. R. Sharp, *Inorg. Chem.*, 1993, **32**, 94–100.

51. Y.-W. Ge, Y. Ye and P. R. Sharp, *J. Am. Chem. Soc.*, 1994, **116**, 8384–8385.

52. L. Zhai, R. Shukla and R. Rathore, *Org. Lett.*, 2009, **11**, 3474–3477.

53. B. T. King, J. Kroulík, C. R. Robertson, P. Rempala, C. L. Hilton, J. D. Korinek and L. M. Gortari, *J. Org. Chem.*, 2007, **72**, 2279–2288.

54. N. D. Harrold and G. L. Hillhouse, *Chem. Sci.*, 2013, **4**, 4011–4015.

55. V. M. Iluc, A. J. M. Miller, J. S. Anderson, M. J. Monreal, M. P. Mehn and G. L. Hillhouse, *J. Am. Chem. Soc.*, 2011, **133**, 13055–13063.

56. K. E. Aldrich, B. S. Fales, A. K. Singh, R. J. Staples, B. G. Levine, J. McCracken, M. R. Smith and A. L. Odom, *Inorg. Chem.*, 2019, **58**, 11699–11715.

57. J. W. Lauher and R. Hoffmann, *J. Am. Chem. Soc.*, 1976, **98**, 1729–1742.

58. R. L. Zuckerman, S. W. Krska and R. G. Bergman, *J. Am. Chem. Soc.*, 2000, **122**, 751–761.

59. P. J. Walsh, F. J. Hollander and R. G. Bergman, *Organometallics*, 1993, **12**, 3705–3723.

60. A. P. Duncan and R. G. Bergman, *Chem. Rec.*, 2002, **2**, 431–445.

61. P. J. Walsh, F. J. Hollander and R. G. Bergman, *J. Am. Chem. Soc.*, 1988, **110**, 8729–8731.

62. S. A. Blum and R. G. Bergman, *Organometallics*, 2004, **23**, 4003–4005.

63. S. Y. Lee, *Ph.D. Thesis*, University of California, Berkeley, 1995.

64. S. Y. Lee and R. G. Bergman, *J. Am. Chem. Soc.*, 1995, **117**, 5877–5878.

65. P. J. Walsh, A. M. Baranger and R. G. Bergman, *J. Am. Chem. Soc.*, 1992, **114**, 1708–1719.

66. A. M. Baranger, P. J. Walsh and R. G. Bergman, *J. Am. Chem. Soc.*, 1993, **115**, 2753–2763.

67. H. M. Hoyt, F. E. Michael and R. G. Bergman, *J. Am. Chem. Soc.*, 2004, **126**, 1018–1019.

68. H. M. Hoyt and R. G. Bergman, *Angew. Chemie Int. Ed.*, 2007, **46**, 5580–5582.

69. K. J. Cavell, *Coord. Chem. Rev.*, 1996, **155**, 209–243.

70. T. Sakakura and M. Tanaka, *J. Chem. Soc., Chem. Commun.*, 1987, 758–759.

71. T. Zhou, S. Malakar, S. L. Webb, K. Krogh-Jespersen and A. S. Goldman, *Proc. Natl. Acad. Sci.*, 2019, **116**, 3419–3424.

72. R. E. Blake, D. M. Antonelli, L. M. Henling, W. P. Schaefer, K. I. Hardcastle and J. E. Bercaw, *Organometallics*, 1998, **17**, 718–725.

73. M. J. Humphries, R. E. Douthwaite and M. L. H. Green, *J. Chem. Soc. Dalton Trans.*, 2000, **758**, 2952–2959.

74. M. P. Shaver and M. D. Fryzuk, *Adv. Synth. Catal.*, 2003, **345**, 1061–1076.

75. J. M. Manriquez and J. E. Bercaw, *J. Am. Chem. Soc.*, 1974, **96**, 6229–6230.

76. J. M. Manriquez, R. D. Sanner, R. E. Marsh and J. E. Bercaw, *J. Am. Chem. Soc.*, 1976, **98**, 3042–3044.

77. J. E. Bercaw, in *Transition Metal Hydrides*, ed. R. Bau, American Chemical Society, 1978, pp. 136–148.

78. P. T. Wolczanski and J. E. Bercaw, *Acc. Chem. Res.*, 1980, **13**, 121–127.

79. E. A. MacLachlan and M. D. Fryzuk, *Organometallics*, 2006, **25**, 1530–1543.

80. J. A. Pool, E. Lobkovsky and P. J. Chirik, *Nature*, 2004, **427**, 527–530.

81. L. B. Kool, M. D. Rausch, H. G. Alt, M. Herberhold, U. Thewalt and B. Honold, *J. Organomet. Chem.*, 1986, **310**, 27–34.

82. C. A. Bradley, E. Lobkovsky and P. J. Chirik, *J. Am. Chem. Soc.*, 2003, **125**, 8110–8111.

83. C. A. Bradley, I. Keresztes, E. Lobkovsky, V. G. Young and P. J. Chirik, *J. Am. Chem. Soc.*, 2004, **126**, 16937–16950.

84. D. Pun, E. Lobkovsky and P. J. Chirik, *J. Am. Chem. Soc.*, 2008, **130**, 6047–6054.

85. C. A. Bradley, S. Flores-Torres, E. Lobkovsky, H. D. Abruña and P. J. Chirik, *Organometallics*, 2004, **23**, 5332–5346.

86. D. S. Williams, J. T. Anhaus, M. H. Schofield, R. R. Schrock and W. M. Davis, *J. Am. Chem. Soc.*, 1991, **113**, 5480–5481.

87. D. S. Williams, M. H. Schofield, J. T. Anhaus and R. R. Schrock, *J. Am. Chem. Soc.*, 1990, **112**, 6728–6729.

88. V. C. Gibson, *J. Chem. Soc., Dalton Trans.*, 1994, 1607–1618.

89. D. N. Williams, J. P. Mitchell, A. D. Poole, U. Siemeling, W. Clegg, D. C. R. Hockless, P. A. O'Neil and V. C. Gibson, *J. Chem. Soc. Dalton Trans.*, 1992, 739–751.

90. S. L. Buchwald, B. T. Watson and J. C. Huffman, *J. Am. Chem. Soc.*, 1986, **108**, 7411–7413.

91. G. Erker, *J. Organomet. Chem.*, 1977, **134**, 189–202.

92. J. K. Cockcroft, V. C. Gibson, J. A. K. Howard, A. D. Poole, U. Siemeling and C. Wilson, *J. Chem. Soc., Chem. Commun.*, 1992, 1668–1670.

93. D. S. Williams and R. R. Schrock, *Organometallics*, 1993, **12**, 1148–1160.

94. G. I. Nikonov, P. Mountford, L. G. Kuzmina, J. A. K. Howard, D. A. Lemenovskii and D. M. Roitershtein, *J. Organomet. Chem.*, 2001, **628**, 25–29.

95. N. A. McLeod, L. G. Kuzmina, A. V Churakov, P. Mountford and G. I. Nikonov, *Dalton Trans.*, 2014, **43**, 188–195.

96. A. Castro, M. V. Galakhov, M. Gómez and F. Sánchez, *J. Organomet. Chem.*, 1999, **580**, 161–168.

97. V. C. Gibson, D. N. Williams, W. Clegg and D. C. R. Hockless, *Polyhedron*, 1989, **8**, 1819–1820.

98. S. Schmidt and J. Sundermeyer, *J. Organomet. Chem.*, 1994, **472**, 127–138.

99. M. C. Maestre, P. B. Gratal, M. E. G. Mosquera, T. Cuenca and G. Jiménez, *Eur. J. Inorg. Chem.*, 2017, **2017**, 1060–1066.

100. M. C. W. Chan, J. M. Cole, V. C. Gibson, J. A. K. Howard, C. Lehmann, A. D. Poole and U. Siemeling, *J. Chem. Soc. Dalton Trans.*, 1998, 103–111.

101. G. I. Nikonov, P. Mountford, S. K. Ignatov, J. C. Green, M. A. Leech, L. G. Kuzmina, A. G. Razuvaev, N. H. Rees, A. J. Blake, J. A. K. Howard and D. A. Lemenovskii, *J. Chem. Soc. Dalton Trans.*, 2001, 2903–2915.

102. A. V Korolev, A. L. Rheingold and D. S. Williams, *Inorg. Chem.*, 1997, **36**, 2647–2655.

103. A. Antiñolo, M. Fajardo, C. Huertas, A. Otero, S. Prashar and A. M. Rodriguez, *J. Organomet. Chem.*, 1999, **585**, 154–161.

104. C. M. Widdifield, J. A. Tang, C. L. B. Macdonald and R. W. Schurko, *Magn. Reson. Chem.*, 2007, **45**, S116–S128.

105. W. A. Herrmann, W. Baratta and E. Herdtweck, *J. Organomet. Chem.*, 1997, **541**, 445–460.

106. L. Falivene, Z. Cao, A. Petta, L. Serra, A. Poater, R. Oliva, V. Scarano and L. Cavallo, *Nat. Chem.*, 2019, **11**, 872–879.

107. K. S. Heinselman, V. M. Miskowski, S. J. Geib, L. C. Wang and M. D. Hopkins, *Inorg. Chem.*, 1997, **36**, 5530–5538.

108. H.-T. Chiu, J.-C. Lin, S.-H. Chuang, G.-H. Lee and S.-M. Peng, *J. Chinese Chem. Soc.*, 1998, **45**, 355–360.

109. A. N. Chernega, M. L. H. Green and A. G. Suárez, *J. Chem. Soc., Dalton Trans.*, 1993, **2**, 3031–

3034.

110. K. Osakada, in *Current Methods in Inorganic Chemistry*, 2003, vol. 3, pp. 233–291.

111. A. Dashti-Mommertz, B. Neumüller, S. Melle, D. Haase and W. Uhl, *Zeitschrift für Anorg. und Allg. Chemie*, 1999, **625**, 1828–1832.

112. C. Janiak, *Coord. Chem. Rev.*, 1997, **163**, 107–216.

113. W. Leung, M.-C. Wu, K.-Y. Wong and Y. Wang, *J. Chem. Soc. Dalton Trans.*, 1994, 1659–1663.

114. C. D. Wood, S. J. McLain and R. R. Schrock, *J. Am. Chem. Soc.*, 1979, **101**, 3210–3222.

115. P. Vanýsek, in *CRC Handbook of Chemistry and Physics, 96th Edition*, ed. W. M. Haynes, CRC Press/Taylor and Francis, Boca Raton, FL, 2016.

116. N. G. Connelly and W. E. Geiger, *Chem. Rev.*, 1996, **96**, 877–910.

117. R. R. Gagne, C. A. Koval and G. C. Lisensky, *Inorg. Chem.*, 1980, **19**, 2854–2855.

118. S. Hayano and M. Fujihira, *Bull. Chem. Soc. Jpn.*, 1971, **44**, 1496–1503.

119. L. B. Ebert, D. R. Mills and J. C. Scanlon, *Mater. Res. Bull.*, 1982, **17**, 1319–1328.

120. S. A. Hodge, H. H. Tay, D. B. Anthony, R. Menzel, D. J. Buckley, P. L. Cullen, N. T. Skipper, C. A. Howard and M. S. P. Shaffer, *Faraday Discuss.*, 2014, **172**, 311–325.

121. M. D. Fryzuk, C. M. Kozak, M. R. Bowdridge, B. O. Patrick and S. J. Rettig, *J. Am. Chem. Soc.*, 2002, **124**, 8389–8397.

122. Y. P. Chang, W. Levason, M. E. Light and G. Reid, *Dalton Trans.*, 2016, **45**, 16262–16274.

123. Y.-R. Luo, *Comprehensive Handbook of Chemical Bond Energies*, CRC Press, Boca Raton, FL., 2007.

124. D. Pun, C. A. Bradley, E. Lobkovsky, I. Keresztes and P. J. Chirik, *J. Am. Chem. Soc.*, 2008, **130**, 14046–14047.

125. F. Calderazzo, F. Marchetti, M. Moreno, G. Pampaloni and F. Tumminia, *J. Organomet. Chem.*, 2001, **631**, 110–116.

126. G. Rodriguez, J. P. Graham, W. D. Cotter, C. K. Sperry, G. C. Bazan and B. E. Bursten, *J. Am. Chem. Soc.*, 1998, **120**, 12512–12523.

127. M. A. Schmid, H. G. Alt and W. Milius, *J. Organomet. Chem.*, 1997, **541**, 3–7.

128. P. M. Treichel, K. P. Fivizzani and K. J. Haller, *Organometallics*, 1982, **1**, 931–934.

129. M. J. Calhorda, I. S. Gonçalves, E. Herdtweck, C. C. Romão, B. Royo and L. F. Veiros, *Organometallics*, 1999, **18**, 3956–3958.

130. G. Cortial, X.-F. Le Goff, M. Bousquié, C. Boisson, P. Le Floch, F. Nief and J. Thuilliez, *New J. Chem.*, 2010, **34**, 2290–2297.

131. F. G. Bordwell, J. P. Cheng and J. A. Harrelson, *J. Am. Chem. Soc.*, 1988, **110**, 1229–1231.

132. A. K. Sharma and N. K. Kaushik, *Acta Chim. Hungarica*, 1984, **116**, 361–365.

133. K. Cocq, V. Maraval, N. Saffon-Merceron, A. Saquet, C. Poidevin, C. Lepetit and R. Chauvin, *Angew. Chemie Int. Ed.*, 2015, **54**, 2703–2706.

134. A. M. Cardoso, R. J. H. Clark and S. Moorhouse, *J. Chem. Soc. Dalton Trans.*, 1980, **277**, 1156–1160.

135. L. Postigo, L. Bellarosa, J. Sánchez-Nieves, P. Royo, A. Lledós and M. E. G. Mosquera, *Organometallics*, 2010, **29**, 642–655.

136. A. Kraft, J. Beck and I. Krossing, *Chem. - A Eur. J.*, 2011, **17**, 12975–12980.

137. I. M. Riddlestone, A. Kraft, J. Schaefer and I. Krossing, *Angew. Chemie Int. Ed.*, 2018, **57**, 13982–14024.

138. A. C. Cooper, E. Clot, J. C. Huffman, W. E. Streib, F. Maseras, O. Eisenstein and K. G. Caulton, *J. Am. Chem. Soc.*, 1999, **121**, 97–106.

139. T. A. Martin, C. E. Ellul, M. F. Mahon, M. E. Warren, D. Allan and M. K. Whittlesey, *Organometallics*, 2011, **30**, 2200–2211.

140. I. M. Riddlestone, D. McKay, M. J. Gutmann, S. A. Macgregor, M. F. Mahon, H. A. Sparkes and M. K. Whittlesey, *Organometallics*, 2016, **35**, 1301–1312.

141. P. W. Atkins, T. L. Overton, J. P. Rourke, M. T. Weller and F. A. Armstrong, *Shriver & Atkins' Inorganic Chemistry*, Oxford University Press, Oxford, Fifth edit., 2010.

142. F. Boutonnet, M. Zablocka, A. Igau, J.-P. Majoral, J. Jaud and K. M. Pietrusiewicz, *J. Chem. Soc. Chem. Commun.*, 1993, 1487.

143. L. Cavallo, P. Corradini, G. Guerra and M. Vacatello, *Polymer (Guildf).*, 1991, **32**, 1329–1335.

144. S. I. Troyanov, T. Krahl and E. Kemnitz, *Zeitschrift für Krist. - Cryst. Mater.*, 2004, **219**, 88–92.

145. W. E. Laschkarew, *Zeitschrift fur Anorg. und Allg. Chemie*, 1930, **193**, 270–276.

146. M. Trose, M. Reiß, F. Reiß, F. Anke, A. Spannenberg, S. Boye, A. Lederer, P. Arndt and T. Beweries, *Dalton Trans.*, 2018, **47**, 12858–12862.

147. S. S. Batsanov, *Inorg. Mater.*, 2001, **37**, 871–885.

148. M. Joost, S. Mallet-Ladeira, K. Miqueu, A. Amgoune and D. Bourissou, *Organometallics*, 2013, **32**, 898–902.

149. J. R. Durig and K. K. Chatterjee, *J. Mol. Struct.*, 1982, **81**, 167–180.

150. D. L. W. Kwoh and R. C. Taylor, *Spectrochim. Acta Part A Mol. Spectrosc.*, 1991, **47**, 409–417.

151. F. Cheng, H. L. Codgbrook, A. L. Hector, W. Levason, G. Reid, M. Webster and W. Zhang, *Polyhedron*, 2007, **26**, 4147–4155.

152. M. Q. Y. Tay, Y. Lu, R. Ganguly and D. Vidović, *Angew. Chemie Int. Ed.*, 2013, **52**, 3132–3135.

153. A. Ogawa and H. Fujimoto, *Inorg. Chem.*, 2002, **41**, 4888–4894.

154. R. G. Pearson, *J. Am. Chem. Soc.*, 1985, **107**, 6801–6806.

155. C. Hering, J. Rothe, A. Schulz and A. Villinger, *Inorg. Chem.*, 2013, **52**, 7781–7790.

156. N. Burford, J. A. C. Clyburne, P. K. Bakshi and T. S. Cameron, *J. Am. Chem. Soc.*, 1993, **115**, 8829–8830.

157. N. Burford, J. A. C. Clyburne, P. K. Bakshi and T. S. Cameron, *Organometallics*, 1995, **14**, 1578–1585.

158. S. G. Minasian and J. Arnold, *Chem. Commun.*, 2008, 4043–4045.

159. C. Hering-Junghans, A. Schulz, M. Thomas and A. Villinger, *Dalton Trans.*, 2016, **45**, 6053–6059.

160. S. C. Wallwork and I. J. Worrall, *J. Chem. Soc.*, 1965, 1816.

161. N. M. O'Boyle, A. L. Tenderholt and K. M. Langner, *J. Comput. Chem.*, 2008, **29**, 839–845.

162. K. V. Werner and W. Beck, *Chem. Ber.*, 1972, **105**, 3209–3214.

163. D. A. Straus, C. Zhang and T. D. Tilley, *J. Organomet. Chem.*, 1989, **369**, C13–C17.

164. V. C. Gibson, A. D. Poole, U. Siemeling, D. N. Williams, W. Clegg and D. C. R. Hockless, *J. Organomet. Chem.*, 1993, **462**, C12–C14.

165. F. F. Puschmann, D. Stein, D. Heift, C. Hendriksen, Z. A. Gal, H.-F. Grützmacher and H. Grützmacher, *Angew. Chemie Int. Ed.*, 2011, **50**, 8420–8423.

166. J. M. Goicoechea and H. Grützmacher, *Angew. Chemie Int. Ed.*, 2018, **57**, 16968–16994.

167. D. Heift, Z. Benkő and H. Grützmacher, *Dalton Trans.*, 2014, **43**, 5920–5928.

168. L. N. Grant, B. Pinter, B. C. Manor, H. Grützmacher and D. J. Mindiola, *Angew. Chemie*, 2018, **130**, 1061–1064.

169. S. Bestgen, Q. Chen, N. H. Rees and J. M. Goicoechea, *Dalton Trans.*, 2018, **47**, 13016–13024.

170. W. Beck and K. V. Werner, *Chem. Ber.*, 1971, **104**, 2901–2907.

171. A. R. Jupp, M. B. Geeson, J. E. McGrady and J. M. Goicoechea, *Eur. J. Inorg. Chem.*, 2016, **2016**, 639–648.

172. S. Alidori, D. Heift, G. Santiso-Quinones, Z. Benkå, H. Grützmacher, M. Caporali, L. Gonsalvi, A. Rossin and M. Peruzzini, *Chem. - A Eur. J.*, 2012, **18**, 14805–14811.

173. L. Liu, D. A. Ruiz, F. Dahcheh, G. Bertrand, R. Suter, A. M. Tondreau and H. Grützmacher, *Chem. Sci.*, 2016, **7**, 2335–2341.

174. D. Heift, Z. Benkő and H. Grützmacher, *Chem. - A Eur. J.*, 2014, **20**, 11326–11330.

175. Y. W. Ge, F. Peng and P. R. Sharp, *J. Am. Chem. Soc.*, 1990, **112**, 2632–2640.

176. Z. Modarres Tehrani, D. Lucas, Y. Mugnier, A. Antiñolo, A. Otero, M. Fajardo, A. Garces and C. Lopez-Mardomingo, *J. Organomet. Chem.*, 1997, **548**, 309–313.

177. A. Trummal, L. Lipping, I. Kaljurand, I. A. Koppel and I. Leito, *J. Phys. Chem. A*, 2016, **120**, 3663–3669.

178. G. R. Desiraju and T. Steiner, *The Weak Hydrogen Bond: In Structural Chemistry and Biology*, Oxford University Press, Oxford, 2001.

179. M. Brookhart, B. Grant and A. F. Volpe, *Organometallics*, 1992, **11**, 3920–3922.

180. P. Müller, *Crystallogr. Rev.*, 2009, **15**, 57–83.

181. L. Carreras, L. Rovira, M. Vaquero, I. Mon, E. Martin, J. Benet-Buchholz and A. Vidal-Ferran, *RSC Adv.*, 2017, **7**, 32833–32841.

182. A. H. Gomes de Mesquita, C. H. MacGillavry and K. Eriks, *Acta Cryst.*, 1965, **18**, 437–443.

183. M. Finze, E. Bernhardt, M. Berkei, H. Willner, J. Hung and R. M. Waymouth, *Organometallics*, 2005, **24**, 5103–5109.

184. A. Hinz, R. Labbow, F. Reiß, A. Schulz, K. Sievert and A. Villinger, *Struct. Chem.*, 2015, **26**, 1641–1650.

185. G. Grötsch, R. Boese and W. Malisch, *Chem. Ber.*, 1986, **119**, 2367–2372.

186. S. J. Connelly, W. Kaminsky and D. M. Heinekey, *Organometallics*, 2013, **32**, 7478–7481.

187. M. Lehmann, A. Schulz and A. Villinger, *Angew. Chemie Int. Ed.*, 2009, **48**, 7444–7447.

188. C. Lindner, R. Tandon, B. Maryasin, E. Larionov and H. Zipse, *Beilstein J. Org. Chem.*, 2012, **8**, 1406–1442.

189. G. Ferguson, J. F. Gallagher, C. Glidewell, J. N. Low and S. N. Scrimgeour, *Acta Cryst. C*, 1992, **48**, 1272–1275.

190. D. Zhang, Y. Wen, Y. Xiao, G. Yu, Y. Liu and X. Qian, *Chem. Commun.*, 2008, 4777.

191. K. Semba, M. Shinomiya, T. Fujihara, J. Terao and Y. Tsuji, *Chem. - A Eur. J.*, 2013, **19**, 7125–7132.

192. A. J. Pell, G. Pintacuda and C. P. Grey, *Prog. Nucl. Magn. Reson. Spectrosc.*, 2019, **111**, 1–271.

193. Y. Su, X. Wang, X. Zheng, Z. Zhang, Y. Song, Y. Sui, Y. Li and X. Wang, *Angew. Chemie Int. Ed.*, 2014, **53**, 2857–2861.

194. A. E. Chichibabin, *Chem. Ber.*, 1907, **40**, 1810–1819.

195. L. K. Montgomery, J. C. Huffman, E. A. Jurczak and M. P. Grendze, *J. Am. Chem. Soc.*, 1986, **108**, 6004–6011.

196. E. A. Hauser and M. B. Leggett, *J. Am. Chem. Soc.*, 1940, **62**, 1811–1814.

197. S. Norrehed, C. Karlsson, M. E. Light, A. Thapper, P. Huang and A. Gogoll, *Monatshefte fur Chemie*, 2019, **150**, 77–84.

198. D. F. Evans, *J. Chem. Soc.*, 1959, 2003–2005.

199. S. Zheng, S. Barlow, C. Risko, T. L. Kinnibrugh, V. N. Khrustalev, S. C. Jones, M. Y. Antipin, N. M. Tucker, T. V. Timofeeva, V. Coropceanu, J.-L. Brédas and S. R. Marder, *J. Am. Chem. Soc.*, 2006, **128**, 1812–1817.

200. J. Gräfenstein and D. Cremer, *Phys. Chem. Chem. Phys.*, 2000, **2**, 2091–2103.

201. Y. Zhao and T. M. Swager, *European J. Org. Chem.*, 2015, **2015**, 4593–4597.

202. B. Fischer, J. Boersma, G. Van Koten, W. J. J. Smeets and A. L. Spek, *Organometallics*, 1989, **8**, 667–672.

203. U. Behrens and E. A. Dimos, *Zeitschrift fur Krist. - New Cryst. Struct.*, 2012, **227**, 509–510.

204. K. J. Miller, T. T. Kitagawa and M. M. Abu-Omar, *Organometallics*, 2001, **20**, 4403–4412.

205. V. Chandrasekhar, R. Boomishankar, R. Azhakar, K. Gopal, A. Steiner and S. Zacchini, *Eur. J. Inorg. Chem.*, 2005, **2005**, 1880–1885.

206. G. Bepete, F. Hof, K. Huang, K. Kampioti, E. Anglaret, C. Drummond and A. Pénicaud, *Phys. status solidi - Rapid Res. Lett.*, 2016, **10**, 895–899.

207. N. A. Yakelis and R. G. Bergman, *Organometallics*, 2005, **24**, 3579–3581.

208. R. B. King, F. G. A. Stone, W. L. Jolly, G. Austin, W. Covey, D. Rabinovich, H. Steinberg and R. Tsugawa, *Inorg. Synth.*, 1963, **7**, 99–115.

209. D. Heift, Z. Benkő and H. Grützmacher, *Dalton Trans.*, 2014, **43**, 831–840.

210. H. Schmidbauer and W. Wolfsberger, *Synth. React. Inorg. Met. Org. Chem.*, 1974, 149.

211. M. R. Mazieres, C. Roques, M. Sanchez, J. P. Majoral and R. Wolf, *Tetrahedron*, 1987, **43**, 2109–2118.

212. G. R. Fulmer, A. J. M. Miller, N. H. Sherden, H. E. Gottlieb, A. Nudelman, B. M. Stoltz, J. E. Bercaw and K. I. Goldberg, *Organometallics*, 2010, **29**, 2176–2179.

213. O. V. Dolomanov, L. J. Bourhis, R. J. Gildea, J. A. K. Howard and H. Puschmann, *J. Appl. Crystallogr.*, 2009, **42**, 339–341.

214. G. M. Sheldrick, *Acta Cryst.*, 2008, **A64**, 112–122.

215. G. M. Sheldrick, *Acta Cryst.*, 2015, **C71**, 3–8.

216. M. J. Frisch, G. W. Trucks, H. B. Schlegel, G. E. Scuseria, M. A. Robb, J. R. Cheeseman, G. Scalmani, V. Barone, B. Mennucci, G. A. Petersson, H. Nakatsuji, M. Caricato, X. Li, H. P.

Hratchian, A. F. Izmaylov, J. Bloino, G. Zheng, J. L. Sonnenberg, M. Hada, M. Ehara, K. Toyota, R. Fukuda, J. Hasegawa, M. Ishida, T. Nakajima, Y. Honda, O. Kitao, H. Nakai, T. Vreven, J. A. Montgomery Jr., J. E. Peralta, F. Ogliaro, M. Bearpark, J. J. Heyd, E. Brothers, K. N. Kudin, V. N. Staroverov, R. Kobayashi, J. Normand, K. Raghavachari, A. Rendell, J. C. Burant, S. S. Iyengar, J. Tomasi, M. Cossi, N. Rega, J. M. Millam, M. Klene, J. E. Knox, J. B. Cross, V. Bakken, C. Adamo, J. Jaramillo, R. Gomperts, R. E. Stratmann, O. Yazyev, A. J. Austin, R. Cammi, C. Pomelli, J. W. Ochterski, R. L. Martin, K. Morokuma, V. G. Zakrzewski, G. A. Voth, P. Salvador, J. J. Dannenberg, S. Dapprich, A. D. Daniels, O. Farkas, J. B. Foresman, J. V. Ortiz, J. Cioslowski and D. J. Fox, *Gaussian 09*, *Revision A.02*, Gaussian, Inc., Wallingford, CT, 2009.

217. C. Lee, W. Yang and R. G. Parr, *Phys. Rev. B*, 1988, **37**, 785–789.

218. A. D. Becke, *J. Chem. Phys.*, 1993, **98**, 5648–5652.

219. J. S. Binkley, J. A. Pople and W. J. Hehre, *J. Am. Chem. Soc.*, 1980, **102**, 939–947.

220. M. S. Gordon, J. S. Binkley, J. A. Pople, W. J. Pietro and W. J. Hehre, *J. Am. Chem. Soc.*, 1982, **104**, 2797–2803.

221. R. Dennington, T. A. Keith and J. M. Millam, *GaussView, Version 4.1*, Semichem Inc., Shawnee Mission, KS, 2007.

222. J. Tomasi, B. Mennucci and R. Cammi, *Chem. Rev.*, 2005, **105**, 2999–3094.

223. E. D. Glendening, A. E. Reed, J. E. Carpenter and F. Weinhold, *NBO Version 3.1*.

224. M. D. Hanwell, D. E. Curtis, D. C. Lonie, T. Vandermeersch, E. Zurek and G. R. Hutchison, *J. Cheminform.*, 2012, **4**, 17.

225. C. R. Groom, I. J. Bruno, M. P. Lightfoot and S. C. Ward, *Acta Crystallogr. Sect. B Struct. Sci. Cryst. Eng. Mater.*, 2016, **72**, 171–179.

226. I. J. Bruno, J. C. Cole, P. R. Edgington, M. Kessler, C. F. Macrae, P. McCabe, J. Pearson and R. Taylor, *Acta Cryst. B*, 2002, **58**, 389–397.

227. C. F. Macrae, P. R. Edgington, P. McCabe, E. Pidcock, G. P. Shields, R. Taylor, M. Towler and J. van de Streek, *J. Appl. Crystallogr.*, 2006, **39**, 453–457.

228. G. A. Bain and J. F. Berry, *J. Chem. Educ.*, 2008, **85**, 532.